SENSOR INTEGRATION IN PV DEVICES

STATE OF THE ART AND FUTURE OPPORTUNITIES

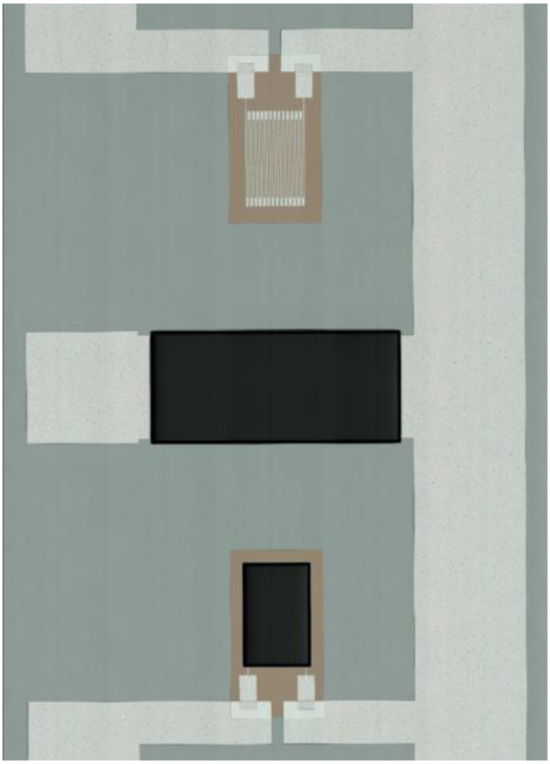

SENSOR INTEGRATION IN PV DEVICES

STATE OF THE ART AND FUTURE OPPORTUNITIES

by

VIERI SPINATELLI

To obtain the degree of

Master of Science

at the Delft University of Technology

to be defended publicly on Monday October 11th, 2021 at 11:00 AM.

Student number:	5142415	
Project duration:	November 2nd, 2020 – October 11, 2021	
Thesis commitee:	prof. dr. O. Isabella	TU Delft, Professor & Supervisor
	dr. P. Manganiello	TU Delft, Assistant Professor & Daily Supervisor
	dr. ir. S. Vollebregt	TU Delft, Assistant Professor

ACKNOWLEDGEMENTS

Science is a community-driven endeavour.

Over the course of this thesis, I have experienced first-hand the significance of such phrase. As I began, my knowledge on microfabricated sensors was limited, not to mention regarding their actual processing. While the scientific literature provided an extensive background knowledge, I have also relied on the experience, insights, and availability of numerous people within TU Delft. Here, I would like to acknowledge them.

I thank my supervisor, dr. Patrizio Manganiello, and the head of the PVMD group, prof. dr. Olindo Isabella, for allowing such research to take place by providing guidance and the required resources. I am also grateful towards the members of the PVMD group for their kind support. In particular, I thank dr. Guangtao Yang, dr. Gianluca Limodio, dr. Luana Mazzarella and Yifeng Zhao for their help in the development and execution of the cleanroom fabrication process, while I thank dr. Mirco Mutillo and Stefaan Heirman for their aid in the final manufacturing and measurement steps.

I am grateful to the EKL staff and Microelectronics team for their expertise and availability, especially during the device processing in the cleanroom. Here, I thank dr. Paolo Sberna and dr. Bruno Morana for their assistance in the moments of need during fabrication. I also appreciate the help provided by dr. Hitham M. Amin Hassan regarding the use and processing of polyimide, and by both Joost van Ginkel and Joost Romijn on the use of the Cascade probe station for automated measurements. Furthermore, I am thankful to other MSc EKL users for their moral support during the numerous hours spent working side by side in the laboratory.

Regarding the equipment related to the characterization of the sensors, I thank Lukasz Pakula for the access to the climate chamber of the Department of Microelectronics and his general suggestions, and Alexander Uithol from the Faculty of Aerospace Engineering for his expertise and support related to the three-point bending test. Furthermore, I highly appreciate the availability demonstrated by Martin Verwaal from the Faculty of Industrial Design: while I eventually did not require access to the climate chamber located in the Applied Labs, he welcomed the cooperation with the PVMD group.

During this journey, I also learned that “community-driven” does not only refer to the scientific community, but also to the people that supported my work by supporting me. Therefore, I am extremely thankful to my family, my partner, friends, and colleagues for their emotional support and keeping me motivated during trying times.

ABSTRACT

The on-field performance and lifespan of PV modules are affected by the interaction of numerous parameters, among which temperature, strain, and humidity. Among these parameters, only temperature is occasionally measured in PV installations, and such monitoring is often external to the module. This limits its use and does not provide accurate information on the conditions at cell level. The integration of different sensors on PV cells can improve the performance of PV devices and enable the early detection of faults and unwanted operating conditions, examples of which are PV module delamination and the occurrence of hotspots, respectively.

This thesis reports on the design, fabrication and testing of four types of sensors, as an initial step within the PVMD group towards sensor integration on PV cells. The devices considered for this work are the following: an aluminum-based resistive temperature sensor, a Boron-doped poly-silicon piezoresistive strain sensor, and two polyimide-functionalized humidity sensors – one capacitive, the other thermoresistive. Furthermore, these devices are combined into multi-sensing platforms with the aim to simultaneously sense sets of parameters (e.g. strain & temperature) to eventually compensate for their reciprocal interference.

The results of the electrothermal characterization of the non-laminated temperature and strain sensors reveal an overall linear response of the devices, with an average TCR of around $+3.75 \cdot 10^{-3}\ °C^{-1}$ and $-3.7 \cdot 10^{-3}\ °C^{-1}$, respectively; this translates into a change in resistance of approximately 22.2-22.5% over the temperature range under study ($30\ °C$-$90\ °C$). Meanwhile, the characterization with a climate chamber of a fabricated capacitive humidity sensor shows a significant increase in capacitance: when relative humidity changes between 20% and 80% at $30\ °C$, the measured capacitance rises from $6.86\ nF$ to $7.20\ nF$ – equivalent to a 5% increase. Furthermore, capacitance measurements performed at constant humidity ratio and varying temperatures indicate a substantial cross-sensitivity of the humidity sensor under test, resulting in an approximately linear capacitance increase between $20\ °C$ and $40\ °C$ with an average regression slope of $10\ pF/°C$.

Since the tested capacitive humidity sensor and piezoresistive strain sensor show a substantial response to temperature, temperature compensation is needed to ensure reliable and accurate measurements of both humidity and strain. To this regard, a simplified compensation based on the simultaneous interrogation of the resistive temperature sensor and capacitive humidity sensor is successfully performed, which highlights the importance of integrated multi-sensing platforms.

CONTENTS

Acknowledgements **v**

Abstract **vii**

1 Introduction **1**

1.1 Motivation and Objective 5

2 Background knowledge **9**

2.1 Sensing Techniques: State-of-the-Art 9
  2.1.1 Capacitive sensors 10
  2.1.2 Resistive sensors 11
  2.1.3 Optical sensors. 13
2.2 Sensor selection. 14
  2.2.1 Thermoresistive Temperature Sensor 15
  2.2.2 Piezoresistive Strain Sensor 18
  2.2.3 Capacitive Humidity Sensor 23
  2.2.4 Thermoresisitive Humidity Sensor 27

3 Modelling and Design **33**

3.1 Sensors 33
  3.1.1 Resistive Temperature Sensor 34
  3.1.2 Piezoresistive Strain Sensor 39
  3.1.3 Capacitive Humidity Sensor 41
  3.1.4 Thermoresistive Humidity Sensor 43
3.2 Wafer Overview 45
  3.2.1 Primary Connections 47
  3.2.2 Sensing Platforms 47
  3.2.3 Sensors Combinations 48

4 Device Fabrication **51**

4.1 MEMS Processing 51
  4.1.1 Zero Layer: Alignment Marks 52
  4.1.2 First Layer: Silicon oxide 52
  4.1.3 Second layer: Poly-Silicon 53
  4.1.4 Third Layer: Thin Metal 55
  4.1.5 Fourth Layer: Thick Metal 56
  4.1.6 Fifth Layer: Polyimide 58
4.2 Manufacturing 60
  4.2.1 Laser Cutting. 61
  4.2.2 Wiring 62
  4.2.3 Lamination 66

5 **Measurement and Results** **69**
5.1 Resistive and piezoresistive sensors 69
5.1.1 Measurement Setup and Device Characterization 69
5.1.2 Results and discussion 70
5.2 Humidity sensing platform 77
5.2.1 Measurement Setup and Device Characterization 77
5.2.2 Results and discussion 81
5.3 Strain sensing platform 87
5.3.1 Measurement Setup and Device Characterization 87
5.3.2 Results and discussion 88

6 **Conclusion and Future Work** **91**
6.1 Conclusion 91
6.2 Future Work. 95

A **Silicon-based Sensors Review: Table of Content** **97**

B **Mask Designs** **101**
B.1 Humidity Sensing Platform: T-Cell Code 102
B.2 Strain Sensing Platform: T-Cell Code 110

C **COMSOL simulations** **121**

D **Complete Processing Flowcharts** **129**
D.1 Flowchart with comb-finger capacitor 129

E **Data Processing** **141**

References **155**

ACRONYMS

AE Aerospace Engineering.

BoS Balance of System.

BSC Bifacial Solar Cell.

DASML Delft Aerospace Structures and Materials Laboratory.

DC Direct Current.

DI Deionized.

EEMCS Electrical Engineering, Mathematics and Computer Science.

EKL Else Kooi Laboratory.

EMR Electromagnetic Radiation.

ESP Electrical Sustainable Power.

EVA Ethylene-vinyl acetate.

FEA Finite Element Analysis.

GF Gauge Factor.

GPM Gain-Phase Meter.

IBC Interdigitated Back Contact.

IRENA International Renewable Energy Agency.

MEMS Micro-Electro-Mechanical System.

MPP Maximum Power Point.

MPPT Maximum Power Point Tracking.

MUT Material Under Test.

NMP N-Methyl-2pyrrolidone.

OM Object of Measurement.

PCR Positive Temperature Coefficient.

PV Photovoltaic.

PVMD Photovoltaic Materials and Devices.

RH Relative Humidity.

RTD Resistance Temperature Detector.

SIMS Secondary Ion Mass Spectrometry.

TCR Temperature Coefficient of Resistance.

1

INTRODUCTION

OVER the last decades, a growing sensitivity to environmental issues has significantly shifted society's perception of the fossil fuel based economy, whilst the increasing cost of climate change related events (extreme weather, desertification, flora & fauna extinction, agricultural losses, etc.) [1] and the dropping price for solar energy [2] [2–4] further convinced governments & industries to invest into PV. In fact, according to a recent report published by the International Renewable Energy Agency (IRENA), the cumulative installed capacity of solar PV has risen from just one GW in 2000 to 480 GW in 2018 [5]. Moreover, it is reported that PV is projected to grow sixfold by 2030, and then almost threefold again by 2050, hitting 8,519 GW of installed capacity, as illustrated in Fig. 1.1. As a result, solar PV will play a key role in the transition to clean power generation.

Since the first wafer fabrication, research was focused on increasing the achievable efficiency under nominal conditions, while the novel industry worked to decrease the cost of the modules. Nowadays, new records have been achieved as efficiency is nearing its physical maximum [6, 7], the so-called Shockley–Queisser limit, and solar energy has become cheaper than traditional fossil fuel based sources in certain energy markets [8]. However, little room is left in further development as the Shockley–Queisser limit cannot be surpassed without "cheating" [9] and the module price is increasingly dependent on

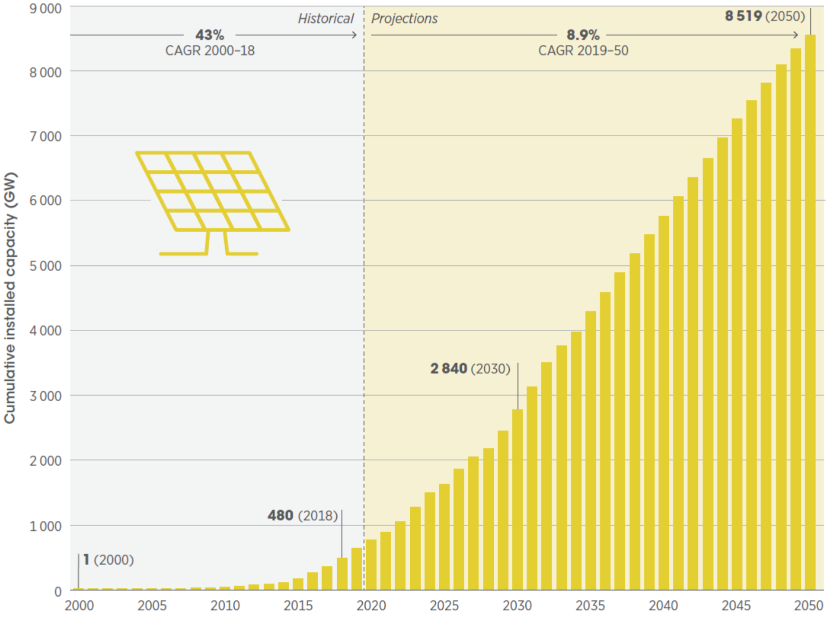

Fig. 1.1: Historical values of cumulative installed PV capacity (2000-2018) and future projections. *Reprinted from [5]*

costs not related to the actual silicon wafers and their processing [10, 11]. Meanwhile, in 2020 up to 65 % of the total costs involved in a PV systems concern the balance of system (BoS) on average [12], up from roughly 34 % in 2015 [13]. The BoS includes all the non-modular components, such as the cabling/wiring, the grid connection, the racking, the mounting and the inverter; however, both studies exclude the cost of the inverters, yet they consider the installation costs and the soft costs (i.e. permitting, financing, etc.).

In real world operating conditions, the efficiency depends on the combination of numerous parameters that, while perhaps insignificant on their own, have strong effects when acting together. Among these parameters, temperature and irradiance stand out [14]. The current-voltage profile, namely the *IV curve*, of a solar cell represents its behaviour under illumination and it typically has the outline of a "knee", the shape of which varies both with temperature and irradiance, as illustrated in Fig. 1.2(*a*). Meanwhile, the product of voltage and current defines the power output (P) of the cell, resulting in an associated PV curve. As Fig. 1.2(*b*) shows, such curve possesses a point where the power output is maximum, the Maximum Power Point (MPP), which represents the optimum operating point. Deployed PV systems aim to work at the MPP [15] to maximize the power generation; therefore, a MPP tracking system is implemented to shift the operating conditions of the solar cells (e.g. the voltage) to be as close as to the MPP. However, the inherent fluctuations in environmental conditions continuously shift the MPP, thus complicating the tracking of such point. When the PV system does not operate at the MPP, it incurs in generation losses, which can quickly become substantial at voltages

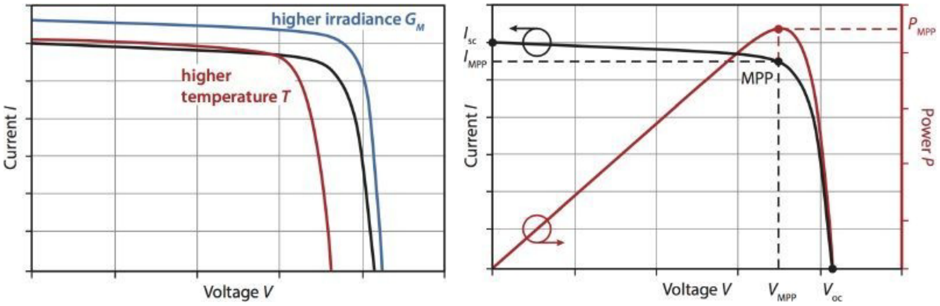

(a) *(b)*

Fig. 1.2: (a) Typical effects of temperature (T) and irradiance (G_M) on the I-V curve of a solar cell. *(b)* Example of an IV curve and its corresponding PV curve, including the MPP. *Reprinted from [14].*

higher than V_{MPP} (see Fig. 1.2, *b*). Since power is sold on the electricity market in advance [16], production forecasting is a fundamental aspect to ensure profits and security of supply; should this not be the case, dispatch issues may arise, while PV system owners observe less-than-expected production [17–19]. Consequently, it is important to gather as much data as possible to improve both the forecasting methods of power production and the control logic of the MPP trackers. Meanwhile, a rudimental health monitoring of the PV system can be performed based on the comparison between forecasted and achieved output [20]; however, this approach does not provide information on either the cause of the problem or the location where it will arise, as it considers the system as a whole. In this context, sensors represent a fundamental tool to improve the MPP tracking, the forecasting and the diagnostics, as they allow to evaluate the outdoor performance of solar PV and to promptly act upon the occurrence of anomalies. Ideally, these devices should be in direct contact with the solar cell for their optimal operation, as power is actively generated only at cell-level and the surrounding passive components of a PV module interfere with the reading of the sensors.

There are currently two common approaches to perform sensing in PV systems, both of which are external to the modules. The first simply consists in the attachment of the sensor onto the module [21, 22], often on the backside. This approach is too approximate as PV modules count numerous solar cells, which cannot be efficiently monitored by a localized point of measurement. Additionally, the interposed material between solar cell and sensor causes disturbances and errors in the measurements. For instance, the frame of the module acts as a heat-sink, thus leveling out the instantaneous temperature fluctuations of the solar cell; similarly, the degree at which deformation occurs depends on the position which is considered, thus the presence of layers between cell and sensor introduces inaccuracies. The other option is only applicable to temperature sensing and consists in the thermal imaging of the modules [23]. However, it is a rather expensive method which cannot be operated continuously [24]. Occasionally, sensors are integrated into the PV module itself [25–27], even in contact with the solar cell [28]. Yet, this approach is generally implemented for research purposes, rather than real applications. Considering all these aspects, it becomes clear that sensor integration within modules should be further developed to achieve lower costs, better module performance and improved control.

The power output of a solar cell is directly related to the surface exposed to the irradiation. Indeed, relative terms such as *irradiance* (W/m^2) and *current density* (A/cm^2) are preferably used in the PV field, rather than their absolute counterparts, power (W) and current (A). Not surprisingly, the drive to maximize the effective area of the solar cell is simultaneous to the efforts to improve its material properties. Most notably, the major advancements in surface-optimized solar cells are the development of Interdigitated Back Contact (IBC) cells and Bifacial Solar Cells (BSC). In fact, IBC cells and BSC rank among the highest performing devices, reaching an efficiency of around 26% and 34%, respectively, with the cells developed by Kaneka (single-junction crystalline cell) and Fraunhofer ISE (four-junction/bifacial c-Si hybrid module) [29]. Consequently, it is of great interest to limit the surface dedicated to the integration of sensors onto the solar cell itself, thus minimizing the loss of the active surface.

The problem of size reduction of electrical and mechanical components constitutes the basis of the Micro-Electro-Mechanical System (MEMS) technology since it was first conceived in 1960 and the first working MOSFET was manufactured [30]. Soon after, this peculiar technology was successfully applied by H.C. Nathanson to fabricate a resonant gate transistor in batches in 1964 [31]. Ever since, new developments, such as the ability to fabricate MEMS and integrated circuits simultaneously, have led to the increasing use of such technology to process components for countless electronic devices. In parallel to MEMS, the same drive for smaller devices has pushed the boundaries into the submicron scale already in the mid-1980's [32]. This milestone has helped fuelling the initial advancements in nanotechnology, a research field which took its first tangible steps with the invention of the scanning tunneling microscope in 1981 by G. Binning and H. Rohrer [33]. Indeed, such invention allowed the observation of a surface's features at the atomic level, as prominently demonstrated by IBM in 1990 (see Fig. 1.3).

Over the past decades, the market for electronic devices has been continuously growing to satisfy the increasing demand for both consumer and industrial electronics [35], as parts of the world population increasingly require access to the higher living stan-

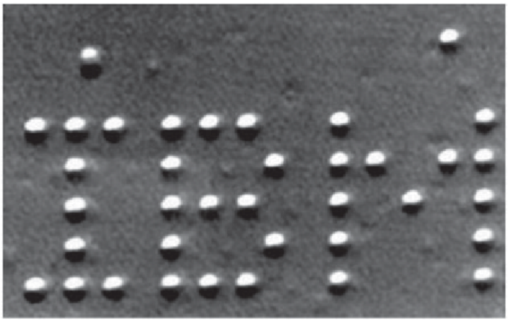

Fig. 1.3: IBM logo written in Xenon atoms. *Reprinted from [34]*

dards provided by such devices [36], and more mechanical systems are translated into an electronic version (e.g. the automotive industry [37]). As sensors play an essential role in any kind of system by providing the means to monitor an event or process, they are a common feature in devices, resulting in a multi-billion-dollar market that produces billions of units [35]. Furthermore, in recent years novel scientific advancements have been achieved in computer science, automation and telecommunication, leading to a thriving research on artificial intelligence [38, 39] – in particular, machine learning and neural networks –, on Big Data [40] and on the Internet of Things [41]. The common aspect among these technical developments is their strong dependence upon information. These innovative tools are already pervading real-world applications and the required supply of data can only be provided by a multitude of sensors and an appropriate communication system. Nowadays, numerous sensors are based on semiconductor materials, which are doped to fine-tune their electrical properties to best suit their intended purpose. Among semiconductor materials, silicon is the most widely implemented due to its abundance in the Earth's crust (2nd most common element), easy manufacturing & processing, solar-spectrum compatible bandgap, high refractive index and stable oxides [42, 43]. Hence, silicon-based sensors are expected to remain leading devices in the sensing field in the foreseeable future. Furthermore, the same material properties have made silicon a fundamental element in the PV field: as of 2019, Si-wafers account for about 95% of the total PV production – 66% of which for mono-crystalline Si [6]. Therefore, the integration of silicon-based sensors onto a PV cell represents the next logical step in the research effort for more efficient solar modules.

This thesis presents the entire integration process of a number of sensors, from their MEMS-based manufacturing to their wiring and lamination into a regular PV material stack.

- A metal resistor to measure temperature.
- A polyimide-functionalized capacitors for moisture detection.
- A doped poly-silicon piezoresistive strip sensitive to strain.
- A novel thermal-based moisture set-point detector.

The thesis includes the preliminary study, modelling, fabrication, design of testing procedure and characterization of all the devices. It is worth to mention that the last device in the previous list, namely the thermal-based moisture set-point detector is, to the best of my knowledge, a totally novel device, not available in any previous literature.

The project aims to develop a set of sensors that can be integrated on active solar cells to form a sensing platform capable of monitoring both the health, the operating conditions, and performance of solar panels during their operation.

1.1. MOTIVATION AND OBJECTIVE

Previous to this thesis, a literature review on general silicon-based sensors was undertaken, as part of an autonomous project. In such work, a multitude of sensing devices were outlined and their respective working principles were described, regardless of their field of use. Indeed, numerous sensors designed for medical, biological and chemical applications [44–55] were analyzed, among others. In the resulting report, the identified devices were categorized based on their sensing purpose (acceleration, force, chemicals, light intensity, etc.), as well as on their sensing approach (capacitive, resistive, optical, etc.). Appendix A provides an excerpt of the document - namely, the Table of Contents. The goal of the project was to outline the current status in sensors design, with a specific focus on the use of silicon - both as the active material and as the main support for processing. Additionally, the state-of-the-art overview served the purpose of scanning the available literature for publications specifically related to the integration of sensors into photovoltaic devices, the topic of this thesis. However, during this targeted inquiry only one relevant article could be detected [56].

The main motivation of this thesis is to expand the knowledge on the integration of monitoring systems directly onto photovoltaic devices by developing a selection of sensors with processes compatible with general cell manufacturing. The devices of interest target three of the major parameters for PV applications, namely temperature, humidity and strain. Bulk silicon can be regarded as a not-yet-activated solar cell and, therefore, the successful integration of sensing devices onto a simple wafer would already provide ample information on the feasibility of further developments in such research field. Furthermore, the realization of a working device could boost the effective performance of solar modules by providing localized data, which in turn has the potential to fine-tune the current monitoring algorithms and reduce losses through preemptive action. Another motivation is that the *in-house* development of sensors and their subsequent testing is *"uncharted territory"* within the Photovoltaic Materials and Devices (PVMD) research group at the Technical University Delft. As a result, the scope of this thesis is also to provide the PVMD group with fabrication-related know-how and inter-faculty testing blueprints, as well as a cross-faculty network for future sensor-related projects.

In view of the importance of the aforementioned parameters for both health monitoring and Maximum Power Point Tracking (MPPT) of PV modules, the objective of the thesis is to design, fabricate and test a sensor for each parameter. Furthermore, an additional thermal moisture set-point detector, a thermoresistive humistat, has been studied due to its novelty. To achieve the thesis objective, the following tasks have been performed:

1. Selection of the most suitable sensor for each parameter based on the available literature.

2. Design of each sensor and the related auxiliary structures considering the iterations of interest (e.g. size). Their design is based on mathematical models; in particular, COMSOL Multiphysics simulations were instrumental to the development of the humistat (see Appendix C).

3. Development of a micro-fabrication process which includes all the sensors of interest.

4. Lamination of the sensors into typical encasing materials used in photovoltaics.

5. Design of an *in-house* testing flowchart to schedule every step into a coherent timeline.
6. Development of a measurement system to reliably interrogate each sensor.
7. Characterization of the response of the manufactured devices within the ranges of interest. Namely, typical and extreme operating conditions of outdoor installed PV modules have been emulated.

All the above-mentioned tasks will be detailed in the remainder of this thesis, that is organized as follows. In Chapter 2, the sensing approaches most common within the scientific literature will be introduced, while the physics of the selected sensors will be detailed. Chapter 3 will describe the design process of the sensor and supporting structures, as well as of the overall wafer layout. The complete fabrication process of the devices, both within and outside the cleanroom, will be reported in Chapter 4. Chapter 5 will define the measurement setups and report the achieved results. Finally, a summary of the main aspects of this thesis and suggestions for future work will be presented in Chapter 6.

2

BACKGROUND KNOWLEDGE

THE purpose of this Chapter is to provide an overview on the topic of sensors, as well as a theoretical background. First, Section 2.1 will introduce the main sensing principles which are typically found in literature. Then, the physics behind the selected sensors will be outlined into more detail in Section 2.2. For further information, the interested reader is referred to the previous literature review on silicon-based sensors (see Appendix A).

2.1. SENSING TECHNIQUES: STATE-OF-THE-ART

The need of precise and real-time measurement data drives the continuous development of sensors, with the manufacturing of both innovative and more performing devices. Sensing can be achieved with various approaches, yet the most common methods that can be found in the literature are those that rely on capacitive, resistive and optical effects. Hereafter, each technique will be briefly introduced with reference to examples of their applications.

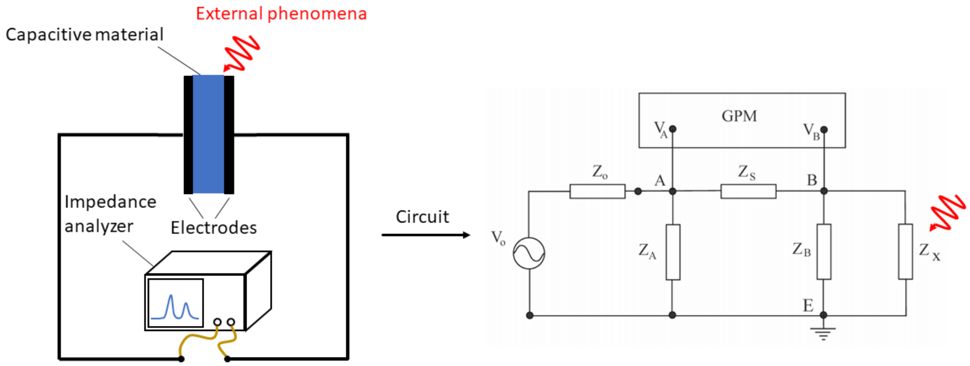

Fig. 2.1: Schematic representation of a simple capacitive sensing system with an illustrative circuit diagram. The equivalent circuit depicts an impedance analyzer which uses a modified Gain-Phase Meter (GPM) [64]. As reported in the article, in this device V_0, Z_0 are the voltage and impedance of the signal generator source, Z_A, Z_B are the input impedances of the GPM input channel, Z_S is the reference impedance and Z_X is the unknown device impedance. In the case of a capacitive sensor, Z_X is approximately equivalent to a pure capacitance. *Adapted from [64].*

2.1.1. CAPACITIVE SENSORS

Capacitive sensors are a class of devices that are able to translate external events into alterations of the measurable capacitance value, where *capacitance* describes the ability of a system to store energy under the form of electric charge [57]. Capacitive sensors are often adopted for their distinct qualities, such as low power consumption, high sensitivity to mechanical phenomena with low sensitivity to temperature, limited circuit requirements [58, 59], as well as fast response time, non-intrusive and non-invasive nature, no radiation and flexibility in electrode design [60, 61 in 62].

A capacitive device is primarily composed of a pair of electrodes in contact with a material perceptive to a certain physical quantity, as depicted in Fig. 2.1. This material – often referred to as material under test (MUT) – is commonly a *dielectric*, namely a substance which transmits an electric force without conduction [63]. Capacitive sensing is the result of the interaction between the MUT and an interrogating electric field. When an electric field is applied at the electrodes of the sensor, an opposing electric displacement occurs within the MUT that alters the charge accumulated between the electrodes. Eventually, conclusions regarding the system variables (e.g. moisture, strain, temperature, etc.) can be reached based on the variance of certain properties, such as permittivity and conductivity [62]. To measure the capacitance of the device, an electrical signal under the form of an alternating voltage is applied to the MUT, and the frequency of the electrical stimulus is evaluated by the impedance analyzer.

The operating principle of capacitive sensors can be designed to work solely based on geometrical features, or they may focus on the properties of the MUT. In fact, a change in

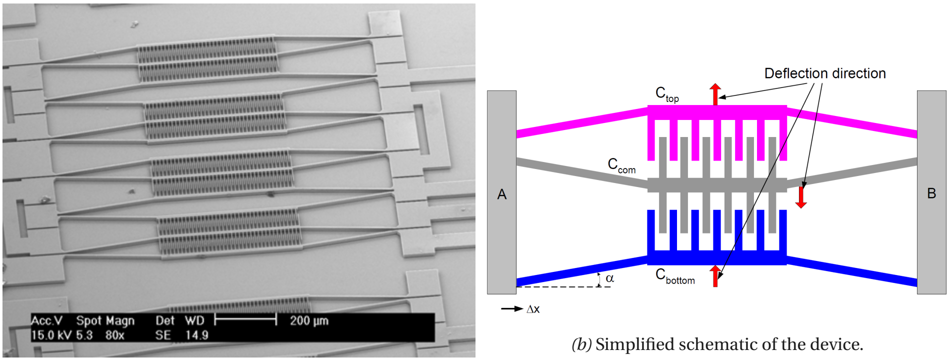

(a) Image of the capacitive strain sensor as captured by the Scanning Electron Microscope (SEM).

(b) Simplified schematic of the device.

Fig. 2.2: Example of a MEMS capacitive sensor with moving elements. Here, a displacement Δx causes a deflection of the suspended comb-finger electrodes that unbalances the system, resulting in an increased performance. *Reproduced from [72].*

shape or distance between electrodes with the same MUT induces a shift in capacitance as well. Consequently, capacitive sensors with either fixed or moving elements can be devised, thus enabling inventive approaches to sensing (see Fig. 2.2). Selecting the right MUT is another important design choice as it not only may increase the sensitivity of the device, but also *broaden* the selection of variables the system can be made sensitive to. For instance, capacitive humidity sensors have been developed by implementing moisture absorbing dielectrics such as polyimide [65–67] and porous aluminum oxide[68] . In addition to humidity, other designs of capacitive sensing systems allow the measurement of different variables, such as acceleration [65, 66], pressure [69, 70], and magnetic fields [66]. Furthermore, capacitive devices can be even adapted to sense and measure biomolecules in a solution by functionalizing the capacitor with biospecific binding agents [71].

2.1.2. RESISTIVE SENSORS

Sensing devices that operate by measuring the electrical resistance of a material are a preferred choice among consumers, as they are simple, low cost, and rather precise [73]. Furthermore, resistive sensors have other attractive qualities, such as good reliability and adjustable resolution [73].

As depicted in Fig. 2.3, resistive sensors are comprised of a portion of material sensitive to the target phenomena, and its connected electrodes (terminals), similarly to the capacitive sensors introduced in 2.1.1. However, the resistance value can be measured by directly analyzing the output in case of resistive sensors when a voltage or current signal is applied at the respective electrodes. When a phenomenon (e.g. applied strain, moisture absorption, temperature variations, induced magnetic fields, etc.) affects the sensitive material, its resistance varies and the resulting output signal changes. The intensity which the electrical resistance varies with depends primarily on the natural properties of the material: indeed, every substance exhibits a different sensitivity, ranging from virtually none to strongly susceptible [74]. For instance, diamagnetic materials such as wood and plastic are unresponsive to magnetic field alterations, as opposed to ferromagnetic objects.

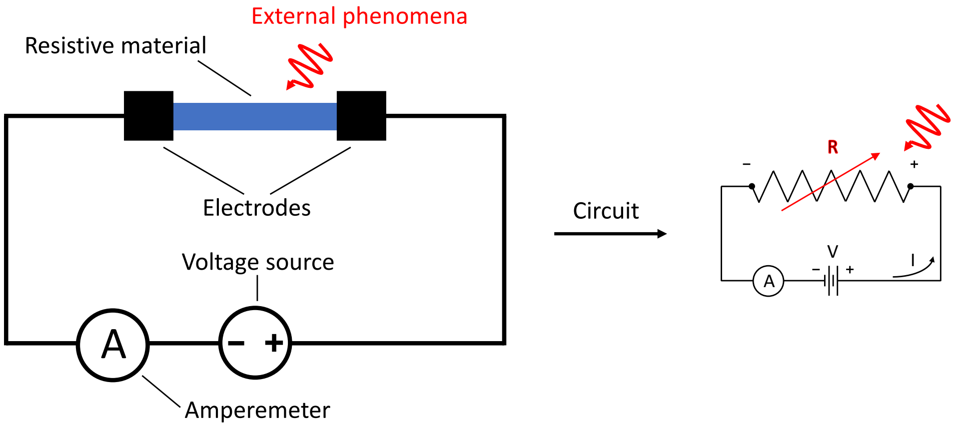

Fig. 2.3: Schematic representation of a simple resistive sensing system with its circuit diagram. Input signal: Voltage (V) - Measured output: Current (I).

While this class of sensors can be further sub-grouped into various categories depending on the applied sensing principles, piezoresistive and thermoresistive are the most prevalent forms of resistive sensors across the literature. The first sub-class is based on the piezoresistive effect, which defines the change in electrical resistivity of a material under applied strain [75]. This effect differs from the strain gauge effect universally experienced by materials under deformation, as it is not based on geometrical aspects, yet purely on material properties. Piezoresistive components find their natural application as strain [56], pressure [65, 76, 77], acceleration [65], force [78] and torque sensors [79], as well as for secondary functions such as aerosol [80] and temperature [81] sensors. Meanwhile, thermoresistive sensors are devices that vary their electrical resistance when their operating temperature changes. In principle, every substance observes a deviation in its resistance value when a temperature shift is recorded; however, certain materials display a substantial sensitivity [74], which makes them appealing for sensing purposes. Most commonly, thermoresistive sensors are implemented in temperature sensing systems [56, 65, 82] under the form of resistance temperature detectors (RTDs); in this case, the devices are discontinuously interrogated by short signal impulses to avoid self-heating of the resistive element. However, thermoresistive sensors can be adapted for other applications by slightly tweaking their core principle: for instance, hot-wire anemometers operate by exploiting the self-heating of a resistor in contact with a moving fluid to measure its speed or flow rate [65, 83].

2.1.3. OPTICAL SENSORS

In general terms, optical sensors are a class of electronic devices that convert the interaction between electromagnetic radiation (EMR) and matter into an electrical signal. In recent decades, the development of this type of sensors has surged due to the inherent qualities of this technology, which make them appealing to various applications. Among its advantages, an optical sensor counts a sensible size & weight reduction, the immunity to electromagnetic interference, its multiplexability, as well as the capability to operate remotely [84].

Depending on the origin of the radiation, optical sensors can be sub-grouped into passive and active sensors. In the first case, the electromagnetic radiation is generated outside of the device – generally, by the object of measurement (OM) – and is only quantified, thus the sensor is passively interacting with its environment. Contrarily, in an active optical sensor the radiation source is integrated within the device to interrogate the OM.

ACTIVE OPTICAL SENSORS

In its fundamental form, an active optical sensor is composed of an EMR source – typically, either a broadband light source or a tunable laser –, a sensing element which the radiation interacts with, and a detector sensitive to the radiation in the bandwidth of interest. The basic working principle of this type of sensors can be expressed as follows. The EMR source generates a beam with a specific electromagnetic spectrum which travels through a medium (e.g. a silica optical fiber) until it reaches the sensing element (e.g. fiber Bragg gratings). Here, the parameter of interest, such as temperature, interacts with the sensing element, causing a change in the spectral profile. Then, the altered laser beam is forwarded to a detector. Finally, variations such as intensity fluctuations or resonant wavelength shifts are analyzed and linked to alterations of the parameter. A diagram of a typical optical sensing system can be viewed in Fig. 2.4. Here, an optical circulator is used to redirect the radiation returning from the sensing element to a spectrometer only. However, other setups can be designed: for instance, Pang *et al.* opted for the combined use of an optical coupler and a photodetector to study the interfer-

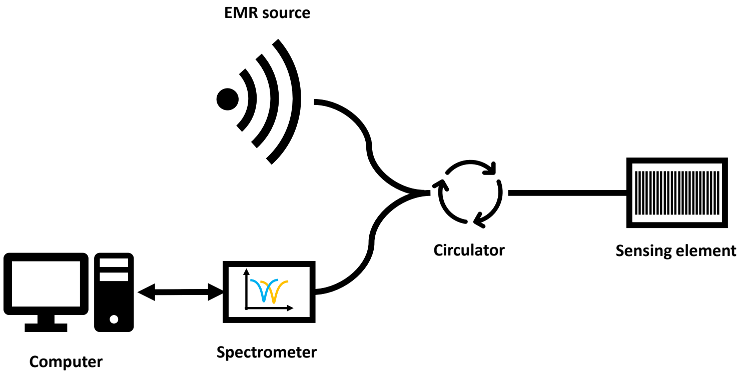

Fig. 2.4: Schematic representation of an optical sensing system. *Adapted from [85].*

ence of the electromagnetic waves [84]. Furthermore, in certain implementations it is not required to return the incoming beam through the same optical medium, yet it can be transmitted further after the interaction [86, 87].

A number of different sensing elements are currently implemented in active optical sensors, among which Micro-Ring Resonators, Fabry-Perot Interferometers and Photonic Crystal Nanobeam Cavities. As reported by the scientific literature, these structures are implemented in a wide range of applications to measure electric fields [88], biomolecules [44, 46, 47], various gases [48, 89, 90], strain [91], humidity [92–94] and temperature [87, 92].

PASSIVE OPTICAL SENSORS

Due to their nature, passive optical sensors can only detect events that generate sensitive radiation variations autonomously. As a result, these devices consist in simple photodetectors which are tuned to the wavelength band of interest. The most elementary design of a photodetector is a photodiode, namely a p-n junction semiconductor device where an internal electric field is used to collect charge carries generated by the material's photonic absorption [95]. As Fig. 2.5 depicts, when the incident light penetrates into the layers of the diode and its photon are absorbed, electron-hole pairs are generated. These pairs of free charge can then diffuse through the material and be swept apart by the electric field present in the depletion layer, thus generating a potential across the p-n junction. In case the electrodes are connected, then an external current flow can be induced. Normally, photodiodes operate under voltage bias condition - mainly reverse bias, yet self-powered forms can be found as well [96]; in either case, a light shining onto the device generates a measurable output current, which is then related to the value of the target parameter. Generally, photodetectors are implemented as light intensity sensors [97, 98]; in particular, these devices are a fundamental part of the optical spectrum analyzers commonly implemented in active optical sensing systems [99, 100], as they serve the purpose of collecting and quantifying the power levels of the generated and forwarded radiation by the EMR source and the sensing element, respectively. Nonetheless, photodetectors can have other applications such as temperature sensors [101] or as flame spectrum analysers [102].

2.2. SENSOR SELECTION

The scientific literature on sensing devices provides a great variety of fascinating designs and working principles, as evidenced by the preceding review on silicon-based sensors (see Appendix A). However, not every conceived solution is feasible for the purpose of this thesis, be it due to the inherent irrelevancy to the target application (PV), the incompatibility with the laboratory equipment and know-how available, or the limited time frame of a MSc thesis. Furthermore, the goal of this thesis is to integrate the sensors onto solar cells which eventually are laminated; therefore the devices must also be robust enough to sustain further aggressive manufacturing. Consequently, a number of sensors are considered based on a conscious selection, which weighted the aforementioned limitations. In total, four devices are devised: one thermoresistive sensor to measure temperature, one piezoresistive strain sensor, and two humidity sensors, one ther-

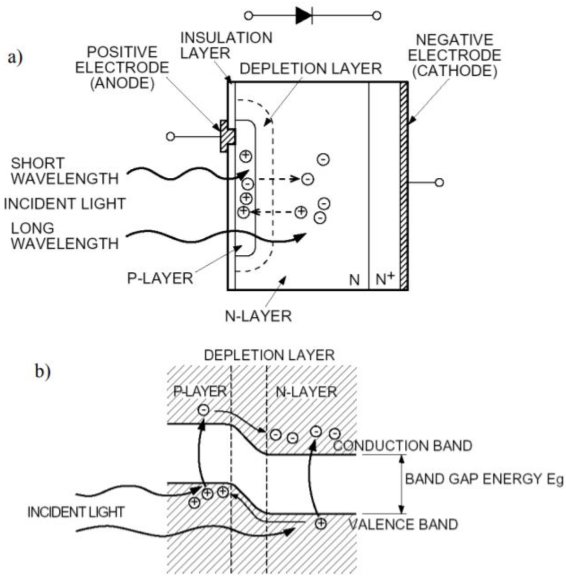

Fig. 2.5: Structural diagram of a silicon photodiode (a) and the energy level diagram of its p-n junction (b). In Fig. (b), the x-axis indicates the physical distance from the front surface, while the y-axis represents the energy levels of the charge carriers. *Reproduced from [95].*

moresistive and one capacitive. Hereafter, a compendium is provided that encompasses the further detailing of the principles upon which the chosen sensors operate.

2.2.1. THERMORESISTIVE TEMPERATURE SENSOR

The temperature dependence of a body's resistance ($R = R(T)$) – more properly, its resistivity (ρ) – is a well-known effect since its discovery in 1821 by sir H. Davy. In fact, as he wrote about his experiments, *"[...] the conducting power of metallic bodies varied with the temperature, and was lower, in some inverse ratio, as the temperature was higher."* [103]. This simple observation then paved the way for further research on the topic and, eventually, led to the envision of the first platinum RTD in 1860 by sir C. W. Siemens [104]. In 1887, H. L. Callendar patented the first reliable platinum RTD, consisting in a coil of platinum wire wrapped around a mica support, which is inserted in a glass tube to protect the fragile component [104]. In this case, platinum was the material of choice because it is a chemically inert metal with a strongly stable temperature-resistance relation ($\partial\rho \approx const.$), although very expensive. Nonetheless, other materials can be used in a RTD, if their aberration from linearity is accounted for. Typically, common metals such as aluminum, copper, nickel and silver [56, 65, 105–109] are implemented because they are cheap, easy to process and sensitive to temperature fluctuations.

As previously mentioned in Section 2.2.1, thermoresistive temperature sensors exploit the temperature dependence of a material's electrical resistance. Indeed, the electrical resistance increases or decreases when a temperature rise occurs, in accordance with

Davy's observation. The direction of the change depends on the material's temperature coefficient of resistance (TCR)[110], the most important property of an RTD. The TCR, α, is mathematically defined as the relative change in resistance, R, per unit change of temperature, T (see Eq. 2.1) [111]. If positive, the TCR expresses an incremental effect, whilst the opposite holds true if negative.

$$\alpha(T) = \frac{1}{R}\frac{\partial R}{\partial T} \tag{2.1}$$

Metals typically posses a *positive* temperature coefficient (PCR) and their resistance can be thoroughly modelled by the Callendar–Van Dusen equation [111], as reported in Eq. 2.2.

$$R(t) = \begin{cases} R_0(1 + At + Bt^2 + C(t-100)t^3) & \text{-200 °}C \le t \le 0\,°C \\ R_0(1 + At + Bt^2) & 0\,°C \le t < 850\,°C \end{cases} \tag{2.2}$$

Here, R is the sensor resistance at temperature t (°C), and R_0 is the sensor resistance at 0 °C, while A, B, C are the constants that depend on the considered material.

Generally, micro-fabricated RTDs present more defects in their metal crystal structure compared to their commercial macro-scale counterparts, which lead to a different T-R relation with respect to Eq. 2.2 [111]. Consequently, the calibration of the sensor must be performed before its use. Typically, the calibration procedure consists in comparing the sensor's temperature measurements at fixed points with those obtained by another temperature measurement system with trusted readings first, and then fitting the data with a continuous function. Commonly, the extrapolated function of a PCR RTD is expressed by a power series similar to Eq. 2.2, yet with different constants (c_1, c_2, ...). Furthermore, its shape depends on the order, n, at which the series is interrupted, which is related to the approximation error $e(t^n)$ (see Eq. 2.3) [111].

$$R(t) = R_0(1 + c_1 t + c_2 t^2 + ...) = R_0(1 + C_1 t + C_2 t^2 + e(t^3)) \tag{2.3}$$

Most metallic RTDs are well described by a third order function over their maximum range of operation, yet a linear approximation yields a limited error for small variations at low temperature [111]. As a result, Eq. 2.3 is often substituted by Eq. 2.4.

$$R(t) \approx R_0(1 + C_1 t) \tag{2.4}$$

By applying the derivative to Eq. 2.4 and inserting the result in 2.1, the following equation can be obtained

$$\alpha(t) = \frac{R_0 C_1}{R(t)} \tag{2.5}$$

The further evaluation at $t = 0°C$ leads to Eq. 2.6 and Eq. 2.7.

$$\alpha(t = 0°C) = \alpha_0 = \frac{R_0 C_1}{R_0} = C_1 \tag{2.6}$$

$$R(t) \approx R_0(1 + \alpha_0 t) \tag{2.7}$$

In case the calibration is performed with respect to a reference temperature, t_o, other than 0 °C ($t_o \neq t_0$), then Eq. 2.8 develops into the following

$$R(t) \approx R_o[1+\alpha_o(t-t_o)] = R_o[1+\alpha_o\Delta t] \tag{2.8}$$

while it is assumed that the device operates *within* its linearity conditions. By reformulating $\Delta R = R(t) - R_o$, the measured temperature value is obtained through the following formula

$$t = t_o + \left(\frac{\frac{\Delta R}{R_o}}{\alpha_o}\right) = t_o + \left(\frac{\Delta R_{rel.}}{\alpha_o}\right) \tag{2.9}$$

Section 2.2.1 mentioned the use of a voltage (current) source as the interrogation method of resistive sensors, while a returning current (voltage) is evaluated. The interchangeability between voltage, V, and current, I as input signals is ensured by Ohm's law, which relates the two parameters through the material's resistance, R (see Eq. 2.10).

$$V = RI \tag{2.10}$$

Assuming a constant current input, I_o, and neglecting other effects (e.g. Joule heating, thermal expansion, etc.), the electrical potential measured at the RTD electrodes is related to temperature t according to Eq. 2.11.

$$t = t_o + \left(\frac{\frac{\Delta R}{R_o}}{\alpha_o}\right) = t_o + \left(\frac{\frac{\Delta V}{R_o I_o}}{\alpha_o}\right) = t_o + \left(\frac{\frac{\Delta V}{V_o}}{\alpha_o}\right) = t_o + \left(\frac{\Delta V_{rel.}}{\alpha_o}\right) \tag{2.11}$$

The sensitivity of a sensor can be defined as the differential of its response to the quantity measured. Under such interpretation, the resulting sensitivity of an RTD is described by Eq. 2.12 & 2.13, expressed first in terms of resistance, S_R, and then of voltage, S_V.

$$S_R(t) = \frac{\partial R}{\partial t} \overset{2.1}{=} \alpha(t)\cdot R(t) \overset{\text{lin.}}{\approx} \alpha_o R_o \tag{2.12}$$

$$S_V(t) = \frac{\partial V}{\partial t} \overset{2.1\ \&\ 2.10}{=} \alpha(t)\cdot R(t) I_o \overset{\text{lin.}}{\approx} \alpha_o R_o I_o \tag{2.13}$$

So far, the working principle of a PCR RTD was described by exclusively taking into account the direct effect of the external temperature. In fact, self-generated effects resulting from the operation of this type of sensor are commonly neglected, as it is not interrogated by a continuous signal, but rather by impulses. Consequently, the interrogation time interval is so narrow that not enough energy is generated through Joule heating to sensibly impact the reading of the RTD. Nonetheless, other aspects of different nature are able to falsify the measurement of the thermoresistive sensor. In particular, parameters such as stress and strain dominate the cross-sensitivity spotlight of RTDs [112], as they induce resistance alterations due to the "strain gauge" effect (see Eq. 2.25 and 2.35). More information on this effect will be provided in Section 2.2.2.

2.2.2. PIEZORESISTIVE STRAIN SENSOR

The primitive notion that stress and strain are related effects dates back to 1678, when Robert Hooke published his observation that certain material demonstrate a linear relationship between displacement and force [113]. However, it was not before 1822, that a detailed mathematical formalism for stress was developed by Augustin-Louis Cauchy, as a result of centuries worth of work in mathematics, physics and engineering by other great minds, such as the Bernoulli family, Leonhard Euler, Thomas Young, Charles-Augustin Coulomb, Antoine Parent, and sir Isaac Newton [113]. Finally, by applying Cauchy's mathematical model, Hooke's law was generalized into the theory of linear elastic response for isotropic solids, which links stress and strain in general terms. In 1856, 35 years after the discovery of the temperature dependence of the electrical resistance, William Thomson, also known as Lord Kelvin, identified another fundamental electrical effect, namely the relation between strain and resistance [114]. According to his observations, copper wires which a longitudinal tension is applied to display a different galvanometric reading, compared to their unstretched condition. Eventually, Edward E. Simmons and Arthur C. Ruge devised the first commercial wire strain gauges in 1938 [115], which could be bonded reliably to a structure and consisted in a fine wire encapsulated in a flexible material (see Fig. 2.6).

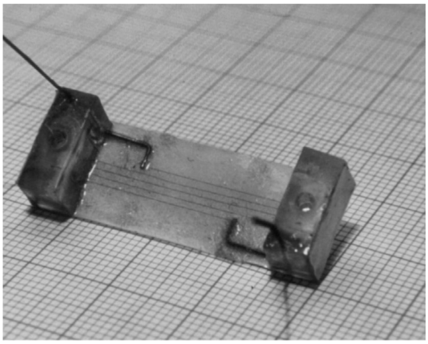

Fig. 2.6: Strain gauge as patented by Ruge in 1944, without the felt protection layer. Reproduced from [116].

The working principle of a strain gauge consists in an alteration of the electrical resistance value upon deformation, as introduced in Section 2.1.2. As shown in Eq. 2.14, the electrical resistance, R, has been experimentally proven to be a function of the material's resistivity, ρ, as well as the ratio between its length, L, and perpendicular cross-section, A. Consequently, when an object (e.g. a metal wire) is deformed, the geometrical ratio is likely to vary, which becomes certain in the case of an incompressible material. Furthermore, it has been observed that also the resistivity itself varies under deformation [117, 118]. Therefore, the electrical resistance of a substance is both a function of its pure geometry and its inherent nature.

$$R = \rho \frac{L}{A} \tag{2.14}$$

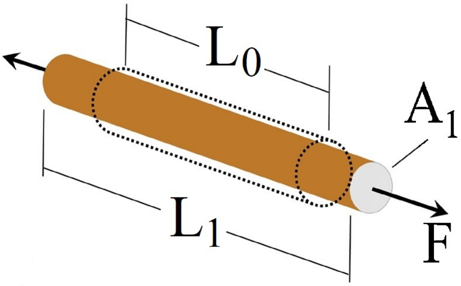

Fig. 2.7: Illustration of the deformation of a cylinder under a tensile load (F). *Adapted from [118]*

In their review, Fiorillo *et al.* thoroughly report on the piezoresistive effect in all its declinations, be it in case of metal, semiconductor or polymer composite materials [118]. Furthermore, they provide a detailed state-of-the-art on strain gauges and their implementations. To their credit, the derivation of the mathematical tools used to describe strain gauges will follow their rationale henceforth.

Under the assumption that an electric field, E, is applied to an isotropic electrically conductive bar with length, L, resistivity, ρ and cross-section, A, its resistance is still expressed by Eq. 2.14. Upon differentiation and division by the resistance value itself, such equation leads to an expression (Eq. 2.15) which defines the relative change in resistance as the sum of the relative change of its multiplication factors, where their respective sign is defined according to the differentiation power law.

$$\begin{aligned} \mathrm{d}R &= \frac{\partial R}{\partial \rho}\mathrm{d}\rho + \frac{\partial R}{\partial L}\mathrm{d}L + \frac{\partial R}{\partial A}\mathrm{d}A \\ &\Downarrow \cdot \frac{1}{R} \\ \frac{\mathrm{d}R}{R} &= \left(\frac{\partial R}{\partial \rho}\mathrm{d}\rho + \frac{\partial R}{\partial L}\mathrm{d}L + \frac{\partial R}{\partial A}\mathrm{d}A\right)\frac{1}{R} \\ &= \left(\frac{L}{A}\mathrm{d}\rho + \frac{\rho}{A}dL - \frac{\rho L}{A^2}\mathrm{d}A\right)\frac{A}{\rho L} \\ &= \frac{\mathrm{d}\rho}{\rho} + \frac{\mathrm{d}L}{L} - \frac{\mathrm{d}A}{A} \end{aligned} \tag{2.15}$$

Meanwhile, strain, ϵ, is defined as the variation in the dimension of interest, X, per unit dimension, namely as

$$\epsilon_X = \frac{\mathrm{d}X}{X}. \tag{2.16}$$

Generally, nine strain components grouped into a three-by-three tensor are required to describe the strain conditions of an infinitesimal cube of material, according to Cauchy's formalism. However, it can be demonstrated that every tensor can be reduced to three principal components, which are orthogonal to each other [119, 120]. For simplicity, a cylindrical bar (see Fig. 2.7), is considered and it is further assumed that the occurring deformation is the result of a purely tensile force applied at the circular sides. Consequently, the number of strain components can be reduced to only two due to symmetry: the longitudinal strain, ϵ_l, and diametral strain, ϵ_d. Eq. 2.17 shows their definition; here, L_0 and D_0 refer to the initial values of length and diameter.

$$\begin{aligned} \epsilon_l &= \frac{\mathrm{d}L}{L_0} \\ \epsilon_d &= \frac{\mathrm{d}D}{D_0} \end{aligned} \tag{2.17}$$

This simplification can be conveniently visualized when contemplating a wide rubber band that is pulled at both edges: in this case, as the cross-section is reducing, the length of the material increases. The extent of the arising contraction is a natural property of the material itself, and it is expressed by the Poisson's ratio, ν, as shown by Eq. 2.18. In the case of the axially stretched cylindrical bar, it follows that $\epsilon_{transverse} = \epsilon_d$, $\epsilon_{axial} = \epsilon_l$.

$$\nu = -\frac{\epsilon_{transverse}}{\epsilon_{axial}} \tag{2.18}$$

As a consequence of the definition of strain (Eq. 2.17), the final length, L_1, and diameter, D_1, are evaluated as follows

$$\begin{aligned} L_1 &= L_0(1+\epsilon_l) \\ D_1 &= D_0(1+\epsilon_d) \end{aligned} \tag{2.19}$$

while the new cross-section A_1 is expressed by Eq. 2.20.

$$\begin{aligned} A_1 &= \pi\left(\frac{D_0}{2}\right)^2(1+\epsilon_d)^2 \\ &= A_0(1+\epsilon_d)^2 \end{aligned} \tag{2.20}$$

Should a change in volume occur during the deformation of the bar, the incremental variation can be described as $dV_0 = V_1 - V_0$. By inserting Eq. 2.17, 2.19 and 2.20 into such expression and neglecting the higher order infinitesimals ($E(\epsilon^2) \approx 0$), a linear relation between the volumetric deformation and the arising strain can be determined. Eq. 2.21 illustrates the various steps of the derivation.

$$\begin{aligned} \mathrm{d}V_0 &= V_1 - V_0 \\ &= A_1L_1 - A_0L_0 \\ &= A_0(1+\epsilon_d)^2L_0(1+\epsilon_l) - A_0L_0 \\ &= A_0L_0[(1-\epsilon_l\nu)^2(1+\epsilon_l) - 1] \\ &= V_0[\epsilon_l(1-2\nu) + \epsilon_l^2(\nu^2 - 2\nu + \epsilon_l\nu^2)] \\ &= V_0\epsilon_l[1 - 2\nu + E(\epsilon_l^2)/\epsilon_l] \\ &\approx V_0\epsilon_l(1-2\nu) \end{aligned} \tag{2.21}$$

The incremental volume variation can be defined through its differential form as well, namely as $dV_0 = dA_0L_0 + A_0dL_0$. Consequently, Eq. 2.21 can be reformulated in relative terms as follows

$$\frac{\mathrm{d}V_0}{V_0} = \frac{\mathrm{d}A_0\cancel{L_0}}{A_0\cancel{L_0}} + \frac{\cancel{A_0}\mathrm{d}L_0}{\cancel{A_0}L_0} \approx \epsilon_l(1-2\nu) \tag{2.22}$$

Henceforth, the infinitesimals of higher order ($E(\epsilon^2)$) are now ignored for ease of discussion. Furthermore, since the initial condition regarded until this point (L_0, D_0, A_0 and V_0) possess no specificity, Eq. 2.17 and 2.22 can be expressed in all generality as

$$\begin{aligned}\epsilon_l &= \frac{\mathrm{d}L}{L}\\ \epsilon_d &= \frac{\mathrm{d}D}{D}\\ \frac{\mathrm{d}V}{V} &= \frac{\mathrm{d}A}{A} + \frac{\mathrm{d}L}{L} = \epsilon_l(1-2\nu)\end{aligned} \tag{2.23}$$

to which follows that Eq. 2.15 can be redefined as

$$\begin{aligned}\frac{\mathrm{d}R}{R} &= \frac{\mathrm{d}\rho}{\rho} + \frac{\mathrm{d}L}{L} - \left[\epsilon_l(1-2\nu) - \frac{\mathrm{d}L}{L}\right]\\ &= \frac{\mathrm{d}\rho}{\rho} + \epsilon_l - [\epsilon_l(1-2\nu) - \epsilon_l]\\ &= \frac{\mathrm{d}\rho}{\rho} + \epsilon_l(1+2\nu)\end{aligned} \tag{2.24}$$

Typically, a strain gauge sensitivity is outlined by its so-called *gauge factor* (GF), which is defined as the ratio between the relative change in electrical resistance and the relative change in dimension (see Eq. 2.25). Since strain in a complex system occurs in at least three directions – namely the principal directions of strain, the gauge factor is not an individual parameter and it can be define for each orientation. In the case of the here considered cylindrical bar under pure axial tension, only the longitudinal gauge factor GF_l is definable.

$$GF = \frac{\mathrm{d}R/R}{\mathrm{d}X/X} = \frac{\mathrm{d}R/R}{\epsilon} \tag{2.25}$$

By introducing Eq. 2.24 into the definition, the longitudinal gauge factor is then expressed as

$$GF_l = 1 + 2\nu + \frac{1}{\epsilon_l}\frac{\mathrm{d}\rho}{\rho} \tag{2.26}$$

With respect to Eq. 2.26, the change in resistivity, $\frac{d\rho}{\rho}$, upon material deformation is commonly understood as the piezoresistive effect, to differentiate it from the purely geometrical effect described by the term $1+2\nu$.

The principle behind this piezoresistive effect is explained in terms of amplitude variations of the vibrations taking place in the material lattice [112]. However, a further in-depth discussion requires mathematical tools and notions deriving from the study of solid-state physics, which adds excessive complexity to the description of a simple strain sensor. Therefore, it is referred to the work by Fiorillo *et al.* for further reading, as their review provides a rather concise elucidation on the topic [118]. In brief, when an external stress (or strain) is applied to a material, the energy gap that divides its conduction (energetically higher) and valence (energetically lower) bands varies, thus increasing or decreasing the chances that an electron bounces from its valence band into conduction band. Because the conduction band governs the *electrical conductivity* – which is the inverse of the electrical resistivity, the mechanical reduction of the energy gap leads to a decrease in resistivity. This particular effect becomes more prominent when a semiconductor is considered; in fact, by doping the semiconductor with other elements – typically phosphorus or boron, the concentration of free charges increases, and thus the electrical resistivity drops. Nonetheless, other effects influence the way resistivity varies with the doping of the material, leading to a non-linear relation between gauge factor and doping concentration [121, 122]. Furthermore, the stability of a piezoresistive semiconductor-based sensor generally increases with doping concentration, whilst its sensitivity declines [123].

The relative variation in resistivity can be expressed as a function of so-called *piezoresistive coefficients*, π_{ij}, which quantify the piezoresistive effect depending on the orientation and nature of the stress applied to the material (e.g. shear stress). As reported by Fiorillo *et al.*, these independent coefficients can be goniometrically combined to generate new comprehensive coefficients in the directions of interest. Hence, the term $\frac{d\rho}{\rho}$ of the cylindrical bar may now be expressed as the sum of the piezoresistive effects in the longitudinal and transverse directions, as shown in Eq. 2.27. Here, π_l, π_t and σ_l, σ_t are the piezoresistive coefficients and the applied stresses in the longitudinal and transverse directions, respectively.

$$\frac{\Delta\rho}{\rho} = \pi_t\sigma_t + \pi_l\sigma_l \tag{2.27}$$

Under the assumption that only an axial tension is applied to the considered bar ($\sigma_t = 0$), Eq. 2.24 may be reformulated as

$$\frac{\mathrm{d}R}{R} = \pi_l\sigma_l + \epsilon_l(1+2\nu) \tag{2.28}$$

As previously mentioned, Hooke's generalised law links stress and strain in case of linearly elastic materials, as shown in Eq. 2.29. In this case, $\underline{\underline{\sigma}}$ and $\underline{\underline{\epsilon}}$ denote two second order tensors, whilst **C** is a *forth* order matrix containing all the proportionality constants.

$$\underline{\underline{\sigma}} = \mathbf{C}\underline{\underline{\epsilon}} \tag{2.29}$$

Due to its length and complexity, the complete derivation of Hooke's generalized law is out of the scope of this thesis. Nonetheless, the interested reader is referred to [124] for further information. Generally, piezoresistive strain sensors are designed to be sensitive almost exclusively to a single direction, as simultaneous deformations in multiple orientations introduce signal noise which interferes with the reading of the sensor. Hence, the simplified discussion on the strain gauge's working principle introduced by Fiorillo *et al.*

is sufficient for the intended purpose of this thesis. Under these circumstances, Eq. 2.29 is reduced to

$$\sigma_l = E\epsilon_l \tag{2.30}$$

where E is the Young modulus, which represents a material's natural resistance to deformation under applied forces. When this expression is inserted in Eq. 2.24, the relative change in resistance can be formulated in either strain or stress terms, as reported in Eq. 2.31

$$\begin{aligned} \frac{\mathrm{d}R}{R} &= \epsilon_l(\pi_l E + 1 + 2\nu) \\ \frac{\mathrm{d}R}{R} &= \sigma_l\left(\pi_l + \frac{1+2\nu}{E}\right) \end{aligned} \tag{2.31}$$

As previously discussed, the piezoresistivity of a semiconductor such as silicon is affected by the doping concentration, N. Yet, temperature plays a key role too, as it also affects the energy gap between the valence and conductance bands [125]. According to Kanda, the overall effect of these variables on the piezoresistive coefficient can be accounted for with the introduction of a dimensionless factor P, as in Eq. 2.32 [126].

$$\pi_l(N,T) = P(N,T)\pi_{l,ref} \tag{2.32}$$

Finally, the gauge factor of a silicon rod under pure tension may be expressed as

$$GF_l = P(N,T)E\pi_l + 1 + 2\nu \tag{2.33}$$

Commonly, the term $1+2\nu$ is neglected, as the maximum value for the Poisson's ratio in absolute terms is one and the piezoresistive effect can account for as high as two orders of magnitude [112, 127].

In the case of metals, the change in resistivity depends in almost its entirety on volumetric arguments. Indeed, P. W. Bridgman discovered that the relative variations of resistivity and volume are directly proportional, as illustrated by Eq. 2.34 [112].

$$\frac{\mathrm{d}\rho}{\rho} = C\frac{\mathrm{d}V}{V} \tag{2.34}$$

In such expression, C indicates the Bridgman's constant of metals, whose value lies between 1.13 and 1.15 for typical strain gauge alloys. By subsequently substituting Eq. 2.23 into 2.34 and then the resulting expression into 2.26, the longitudinal gauge factor of a metallic cylindrical bar is expressed as follows

$$GF_l = 1 + 2\nu + C(1-2\nu) = 1 + C + 2\nu(1-C) \tag{2.35}$$

2.2.3. CAPACITIVE HUMIDITY SENSOR

Similarly to the case of the piezoresistive effect described in the previous Section, the process of developing a complete formalism to describe the notion of capacitance spanned over centuries, with numerous scientists studying the bizarre electrical phenomena. In fact, the origin of the capacitor is credited to Ewald Georg von Kleist, who invented in 1745 a device capable of providing electrical shocks [128]. This rudimentary capacitor consisted in a jar partially filled with water and an cork-isolated electrical lead in contact with the liquid, whilst the hand holding the glass was the outer electrode. In the meantime, new exciting discoveries were fuelling the interest into this field, such as Benjamin Franklin's finding that true nature of lightning is electrical [129]. In 1776, Henry Canvendish defined the concept of electric potential and its link to current, whilst investigating how electric fishes could deliver electric shocks. His work then paved the way for Luigi Galvani's experiments with electricity on dead frogs a decade later, which in turn inspired Alessandro Volta's experiments and led to the invention of the first electric battery in 1800. Twenty years later, Hans Cristian Øersed discovered that electricity and magnetism are related effects, and already in 1831 the first induction-based electric generator was introduced by Michael Faraday. However, it was only with James Maxwell in the mid-19th century that a mathematical model was developed to unify electricity, magnetism and optics into the study of electromagnetism [129]. Through this synthesis, the complete theory of capacitors could be finally formally derived.

The capacitive humidity sensor considered in this thesis is an example of a device with fixed elements, and it is based on a moisture sensitive MUT. As such, when water vapor is absorbed into the MUT, a capacitance alteration is measured. For ease of discussion, the working principle will be described considering now an ideal parallel plate capacitor, as shown in Fig. 2.8.

The capacitance between the two electrodes can be mathematically described in its simplest form as the ratio between the accumulated charge (Q) of a conductor and the generated electric potential (V) (see Eq. 2.36).

$$C = \frac{Q}{V} \tag{2.36}$$

By considering an elementary geometry such as the ideal plate capacitor (see Fig. 2.8), the capacitance formula can be rewritten as in Eq. 2.37 [131]. Here, ϵ_r and ϵ_0 express,

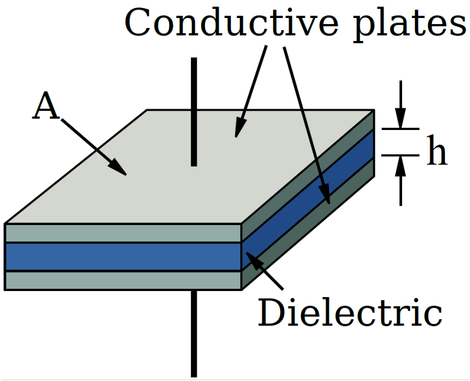

Fig. 2.8: Schematic diagram of a parallel plate capacitor. *Adapted from [130].*

respectively, the dielectric constant of the material between the plates – the dielectric – and the permittivity of space. Meanwhile, A and h indicate the surface of the plates and their distance.

$$C = \frac{\epsilon_r \epsilon_0 A}{h} \tag{2.37}$$

This equation exemplifies the direct dependence of the capacitance to the two defining aspects of a capacitor: its geometry and the material properties of the dielectric. As a result, the development of capacitive sensors relies on these parameters. When moisture diffuses from the environment into the MUT, the water molecules swell the absorbing layer and interfere with its properties. In particular, the relative permittivity of the MUT changes with the amount of moisture absorbed ($\epsilon_r = \epsilon_r(m_{moist.})$), leading to a variation in measured capacitance.

Moisture diffusion is a topic of obvious importance in the field of humidity sensors, as it outlines the governing equations of the interaction between environmental humidity and the absorbed moisture in materials. However, a thorough discussion of the matter in this thesis is not necessary and would result cumbersome to the reader. Therefore, for further details on the general subject of diffusion, it is referred to the book *"Diffusion in Solids: Fundamentals, Methods, Materials, Diffusion-Controlled Processes"* authored by Mehrer [132]. Hereafter, the topic is briefly introduced according to the simplified analysis reported by Jansen *et al.* [133].

The standard diffusion theory is based on Fick's laws. For an isotropic medium, the first law postulates that the diffusion flux vector, **J**, is proportional to the concentration gradient vector, ∇X, and it is directed in the opposite direction of the gradient (see Eq. 2.38) [132]. Here, the diffusion flux is expressed, in all generality, as the number of particles crossing a unit area per unit time. Meanwhile, the proportionality factor, D, also known as *diffusivity*, represents the rate at which the particles can diffuse through the medium, and X is the scalar concentration field expressed as the number of particles within a unit volume, which is a function of position and time ($X = X(x, y, z, t)$).

$$\mathbf{J} = -D\nabla X \tag{2.38}$$

Considering the case where diffusion occurs only in one direction (x-axis), the first law becomes

$$J = -D\frac{\partial X}{\partial x} \tag{2.39}$$

Meanwhile, Fick's second law states that diffusion induces a concentration change in time proportional the second-order spacial derivative of the concentration itself [132], as shown in Eq. 2.40.

$$\frac{\partial X}{\partial t} = -D\frac{\partial^2 X}{\partial x^2} \tag{2.40}$$

When a material is exposed to a stable environment with constant relative humidity (RH), it is assumed that an exposed first layer of infinitesimal thickness is instantly permeated by the water molecules, and thus *saturated.* Subsequently, the moisture slowly

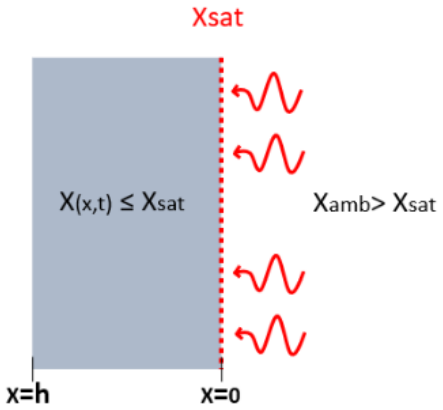

Fig. 2.9: Schematic representation of the moisture diffusion into a material.

diffuses and migrates further into the material. The saturation concentration, X_{sat}, describes the maximum concentration of moisture that can be absorbed by a material, and it represents the boundary condition to the problem of diffusion illustrated by Eq. 2.40. Fig. 2.9 reports a schematic representation of the considered diffusion problem. Under these circumstances, the solution to the differential equation is determined by

$$\frac{X(x,t)-X_0}{X_{sat}-X_0} = 1 + \frac{4}{\pi}\sum_{n=0}^{\infty}\frac{(-1)^n}{2n+1}\cos\left(\frac{(2n+1)\pi x}{2h}\right)\exp\left(-\frac{(2n+1)^2\pi^2 Dt}{4h^2}\right) \tag{2.41}$$

where h and X_0 are, respectively, the thickness and the initial uniform concentration of the material considered [134]. By introducing the term $B_n = (2n+1)\pi/2$, Eq. 2.41 can be reformulated as follows

$$X(x,t) = X_0 + 2(X_{sat}-X_0)\sum_{n=0}^{\infty}\frac{(-1)^n}{B_n}\cos\left(\frac{B_n x}{h}\right)\exp\left(-\frac{B_n^2 Dt}{h^2}\right) \tag{2.42}$$

and by integrating the previous relation over the sample volume ($\mathrm{d}V = A\mathrm{d}h$), the mass of absorbed moisture is evaluated according to Eq. 2.43.

$$\begin{aligned} m(t) &= WL\int_0^h C(x,t)\mathrm{d}x \\ &= WL\left[hX_0 + 4(X_{sat}-X_0)\sum_{n=0}^{\infty}\frac{(-1)^n}{B_n}\exp\left(-\frac{B_n^2 Dt}{4h^2}\right)\int_0^h\cos\left(\frac{B_n x}{2h}\right)\mathrm{d}x\right] \\ &= V\left[X_0 + 8(X_{sat}-X_0)\sum_{n=0}^{\infty}\frac{(-1)^n}{B_n^2}\exp\left(-\frac{B_n^2 Dt}{4h^2}\right)\sin\left(\frac{B_n}{2}\right)\right] \end{aligned} \tag{2.43}$$

Following Jansen *et al.*'s indication, such relation results in

$$m(t) = m_0 + (m_{sat}-m_0)[1-f(t)] \tag{2.44}$$

where $f(\tau) = \sum_{n=0}^{\infty} \frac{8}{B_n^2} \exp(-B_n^2 \tau)$ and $\tau = \frac{Dt}{4h^2}$. Additionally, the authors report that the relationship between saturation mass and relative humidity is typically estimated to be linear; however, Jansen *et al.* prefer a second-order approximation to account for both non-linear and temperature dependent effects, as outlined in Eq. 2.45.

$$m_{sat} = a_1 RH + a_2 RH^2 \tag{2.45}$$

Here, a_1, a_2 are two coefficients whose value varies with temperature and which can be determined through empirical data. Regarding the temporal coefficient, $f(t)$, breaking the summation at $n = 0$ means introducing an error which is less than 2%. Should this be the case, then, in view of Eq. 2.44, the absorbed mass of moisture is reformulated as

$$m(t) = m_0 + (a_1 RH + a_2 RH^2 - m_0) \left[1 - \frac{8}{\pi^2} \exp\left(-\pi \frac{Dt}{4h^2} \right) \right] \tag{2.46}$$

According to Schubert and Nevin, no comprehensive theoretical or empirical formula describing the permittivity of a mixture of immiscible dielectrics properly represents all experimental data [135]. However, they argue that the relative absorption of water in a polymer such as polyimide is low, and thus all equations show a linear profile . One of these formulas is Looyenga's semi-empirical equation described in Eq. 2.47. Here, γ is the volume fraction of water in the polymer film, $\epsilon_{polymer}$ the relative dielectric constant of the polymer, ϵ_{H2O} that of water, whilst ϵ_{mix} outlines the resulting relative permittivity of the mixture.

$$\epsilon_{mix} = \left[\gamma \left(\epsilon_{H_2O}^{\frac{1}{3}} - \epsilon_{MUT}^{\frac{1}{3}} \right) + \epsilon_{MUT}^{\frac{1}{3}} \right]^3 \tag{2.47}$$

The volume fraction is defined as the ratio of the volume occupied by the absorbed water molecules within the polymer and the total volume. By introducing the density of water, ρ_{H_2O}, mass and volume become related terms, and the volume fraction can then be expressed as

$$\gamma = \frac{V_{H_2O}}{V_{H_2O} + V_{MUT}} \overset{\cdot\frac{\rho_{H_2O}}{\rho_{H_2O}}}{=\!=} \frac{m_{H_2O}}{m_{H_2O} + \rho_{H_2O} V_{MUT}} \tag{2.48}$$

2.2.4. THERMORESISITIVE HUMIDITY SENSOR

Heat transfer between bodies is a salient aspect of thermodynamics, a science which studies the relationship between heat and other forms of energy. The use of heat for human industry has been an extraordinary development in the early history of mankind, as it provided access to new temperature-controlled processes such as cooking, metallurgy and numerous material transformations [136]. As Dixit *et al.* argue in their book *"A Brief History of Mechanical Engineering"*, while heat was exploited throughout the millennia for various purposes and devices, it was not until the Industrial Revolution (1750-1850) that their working principles were understood. In fact, the name *thermodynamics* itself was only coined by Lord Kelvin around 1854 after major discoveries, such as the general gas equation, the conduction and convection laws, the Carnot efficiency, the mechanical equivalent of heat, the first two laws of thermodynamics and the definition of an *absolute* temperature scale. Meanwhile, M. Planck's black body radiation law, which defines how ideal bodies irradiate power based on their temperature, was published only in 1901, and the third principle of thermodynamics was only postulated in 1906 by W. Nernst.

The concept of the here proposed thermoresistive humidity sensor is based on the differential heat dissipation of an electric heat source through a humidity-sensitive layer, which varies its thermal conductivity when moisture is absorbed. In this case, the internal heat generation is achieved through Joule heating by a metal resistor. This effect occurs whenever a current flows through an electric conductor, and it is described by the so-called Joule-Lenz law illustrated in Eq. 2.49.

$$P = VI = RI^2 \tag{2.49}$$

Here, V indicates the voltage at the conductor's extremities, R its electrical resistance, and I the current flowing through. Furthermore, direct current (DC) conditions and an ohmic conductor, namely a conductor that follows Eq. 2.10, are assumed.

In thermodynamics, heat is the energy that is being transferred between a system and its surroundings as a result of a temperature difference. Meanwhile, the second law of thermodynamics declares that the transfer always occurs in the direction of the lower temperature, unless another process is added to generate a net increase in entropy [137]. The exchange of thermal energy between an object and its surrounding is governed by two main mechanisms:

- *Conduction.* Conduction is the mechanism which describes how heat is transferred from one body *in contact* to another, or from one body part to another, in case of the presence of a temperature gradient [138]. Such process can be described by the kinetics of molecules, electrons and atoms. Indeed, temperature can be broadly regarded as an indicator of the average kinetic energy of these particles in the considered volume: the more energetic the particles in a region, the higher its temperature. When high-energy particles randomly collide with lower energy ones – or vibrate in locked crystal or lattice structures, their energy and momentum is partially ceded, according to their respective conservation principles. This trickle-down effect then continues until all particles *statistically* possess the same energy level and no preferred reaction direction can be distinguished. In electrically conductive solids, the motion of free electrons contributes the most to the heat exchange, whereas in nonconductors the lattice vibration mechanism governs the process; as a result, electric insulators are generally thermal insulators, too.

- *Convection.* In the case of fluids, the kinetic energy of atoms or molecules becomes predominant, and a different effect adds to heat transfer properties: *convection.* Convection describes the energy which is additionally exchanged through the *macroscopic* movement of the fluid itself [139], and it can be free or forced, depending on whether the flow is a result of an internal density or external pressure difference [140].

- *Thermal radiation.* This mechanism expresses the energy transfer as the emission (or absorption) of electromagnetic radiation as a function of the body's temperature, thus reducing (or increasing) its internal energy [138]. Contrarily to conduction, thermal radiation does not require any transmission medium and it is *always* present for any body at a temperature above absolute zero. Furthermore, its physical principle cannot be fully understood with auxiliary models based on classical mechanics, as is the case of the aforementioned kinetic model of temperature. According to quantum mechanics, atoms absorb and emit only discrete amounts of energy, called *quanta*; when this occurs, atoms undergo transitions between different energy states. On the atomic scale, energy is transmitted by photons and phonons, where the first represent quanta of electromagnetic radiation and the latter quanta of atomic lattice vibration [141]. In line with the thermodynamic energy minimum principle [142], the energy level of an atom spontaneously decreases to its minimum level, although in probabilistic terms [143]. Consequently, when an atom does return to its reference state, it may emit a photon in an arbitrary direction under spontaneous emission conditions.

The exhaustive introduction of the thermodynamic and quantum aspects of heat transfer is out of the scope of this thesis; therefore, the interested reader is referred to the related technical literature for further information [137, 139, 144, 145]. Furthermore, the complete thermal analysis of heat generation and transfer within a multi-object system exposed to an unstable environment under transient conditions is a very complex and strongly non-linear problem – and an outdoor photovoltaic module is an example of this. To study such thermodynamic systems, a finite element analysis (FEA) is commonly performed on a realistic model through solver and simulation software such as COMSOL, which already includes the entire set of equations and mathematical tools necessary to describe the process and approximate the solution. To provide a general understanding of how the thermoresitive humidity sensor operates, the discussion hereafter will be limited to a simplified one-dimensional model under steady-state conditions.

In all generality, the conduction of heat from a material to another is expressed by Fourier's law [139]

$$\dot{\mathbf{q}} = -\lambda(T,p)\, grad(T) = -\lambda(T,p)\left(\frac{\partial T}{\partial x}\mathbf{e_x} + \frac{\partial T}{\partial y}\mathbf{e_y} + \frac{\partial T}{\partial z}\mathbf{e_z}\right) \tag{2.50}$$

where $\dot{\mathbf{q}}$ defines the heat flux, T, p are temperature and pressure, $\mathbf{e_x}$, $\mathbf{e_y}$, $\mathbf{e_z}$ are the unit vectors in the three coordinate directions, and λ is a constant of proportion of the material named *thermal conductivity*. When solids are considered, the effect of pressure on the proportionality constant is disregarded, thus Eq. 2.50 is simplified as follows for the one-dimensional model (y-oriented)

$$\dot{q}_{cond.} = -\lambda(T)\frac{\mathrm{d}T}{\mathrm{d}y} \tag{2.51}$$

Similarly, the convective heat transfer from solid to fluid is described by another coefficient of proportionality: the local *heat transfer coefficient*, α [139]. As shown in Eq.

2.52, the heat flux is evaluated through a *finite* temperature difference between the surface temperature of the solid, T_S, and the fluid temperature, T_F, measured outside of the *boundary layer*. The boundary layer describes a film of a certain thickness, δ, that coats the solid, where the profile of the velocity component of the fluid parallel to the solid's surface is not uniform due to viscous effects between the static object and the moving fluid. In a similar manner to the velocity boundary layer, δ, a temperature boundary layer, δ_{th}, may be defined as well, thus expressing the spacial confinement of the heat flux. Indeed, at a distance $\Delta y > \delta_{th}$, the temperature gradient is virtually zero, meaning that no further relevant heat exchange occurs within the fluid.

$$\dot{q}_{conv.} = \alpha(T_S - T_F) \tag{2.52}$$

Contrarily to conduction and convection, thermal radiation is not proportional to a temperature gradient; instead, it possesses a fourth order temperature dependency, as discovered by J. Stefan and L. Boltzmann. In the simplest of cases, a body at temperature T interacts with a surrounding environment at T_E by absorbing and emitting radiation – here, the temperatures are expressed in Kelvin. The net radiative heatflux, $q_{rad.}$, resulting from this exchange is described by Eq. 2.53, where σ, a and ϵ are, respectively, the Stefan-Boltzman constant, the *absorptivity* and the *emissivity*. The emissivity represents a correction factor that accounts for the *selective* spectrum of emission of real bodies, while the absoptivity is a coefficient that considers other aspects – such as material and surface properties, as well as the source and type of the incident radiation [138].

$$\dot{q}_{rad.} = \sigma(\epsilon T^4 - a T_E^4) \tag{2.53}$$

Furthermore, Kirchhoff's law states that emissivity and absorptivity must be equal at the thermal equilibrium ($\epsilon = a$) [146], which results in

$$\dot{q}_{rad.} = \sigma\epsilon(T^4 - T_E^4) \tag{2.54}$$

Generally, conduction, convection and thermal radiation take place simultaneously in a system, and their effects superimpose, resulting in the total transferred heat being defined as the sum each component.

$$\dot{q}_{tot.} = \dot{q}_{cond.} + \dot{q}_{conv.} + \dot{q}_{rad.} \tag{2.55}$$

Assuming overall system uniformity, the heat flux can be described in finite terms as the ratio between the heat flow, $\dot{Q}$, and the cross-section normal to the flow, A. In case of constant coefficients, the respective heat flow components are expressed as in Eq. 2.56, where $\overline{t}$ is the thickness of the solid layer through which heat conduction occurs.

$$\begin{aligned}
\dot{Q}_{cond.} &= A\frac{\int_{T_0}^{T_1} -\lambda \, \mathrm{d}T}{\int_{y_0}^{y_1=y_0+\overline{t}} 1 \, \mathrm{d}y} \\
&= \left[\frac{A\lambda}{\overline{t}}\right](T_1 - T_0) \\
\dot{Q}_{conv.} &= [A\alpha]\,(T_S - T_F) \\
\dot{Q}_{rad.} &= A\sigma\epsilon(T^4 - T_E^4) \\
&= \left[A\sigma\epsilon(T + T_S)(T^2 + T_E^2)\right](T - T_S)
\end{aligned} \tag{2.56}$$

As can be noted, the flow term, $\dot{Q}$, is related to a difference in state variable, T. Translated into general terms, the quantities reported in Eq. 2.56 have the following shape

$$\dot{Y} = K\Delta X \Longrightarrow \Delta X = \frac{1}{K}\dot{Y} \tag{2.57}$$

which strongly resembles Eq. 2.10. Indeed, V expresses a difference in electric potential, a state variable, while I describes a flow of electric charge. In agreement with the analogy, it follows that the inverse of K indicates a resistive term. Consequently, the thermal resistances for conduction, convection and thermal radiation are defined as

$$\begin{aligned} R_{cond.} &= \frac{\overline{t}}{A\lambda} \\ R_{conv.} &= \frac{1}{A\alpha} \\ R_{rad.} &= \frac{1}{A\sigma\epsilon(T+T_S)(T^2+T_E^2)} \end{aligned} \tag{2.58}$$

and a *thermal circuit* can be drawn, which may be solved observing the same methods applied for electric circuits. An example of a thermal circuit is illustrated in Fig. 2.10, which represents a simplified one-dimensional model of an embedded heater. Here, three layers (two over, one under) encapsulate a heating layer with negligible thickness, while air at ambient temperature flows at both sides of the solid and represents its surrounding. Furthermore, it is assumed that only conduction occurs within the solid layers. In accordance to Eq. 2.58, the thermal resistance of thermal radiation is depicted as a variable element, due to its dependence on the temperature of the external surfaces ($T_{1/air}$ and $T_{3/air}$). In view of the introduced non-linearity, the complexity of the heat transfer problem becomes evident already in this simplified model. Consequently, when increasing the dimensions, considering secondary effects, and analysing transient conditions, a FEA is necessary to properly estimate the response of the system.

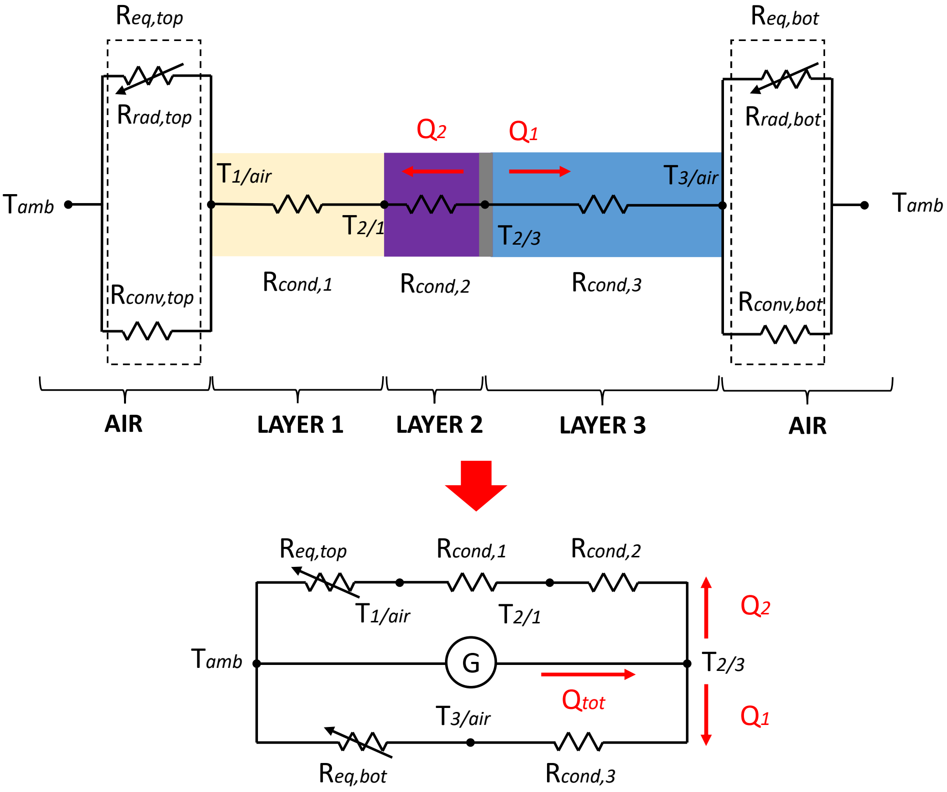

Fig. 2.10: Example of a one-dimensional heat transfer process through multiple layers and materials. On the right, the equivalent thermal circuit is shown, where G represents the joule heating element operated by a constant current, I_0. Meanwhile, $R_{eq,top}$ and $R_{eq,bot}$ indicate the thermal resistances which vary as a result of a changes in temperature.

3

MODELLING AND DESIGN

THE purpose of this Chapter is to introduce the final design of the sensors selected for fabrication over the course of this thesis, as well as to motivate the design choices made. Generally, the design phase is not a linear process, and often requires to adapt previous solutions to new choices and constraints. However, for sake of clarity, the actual sensors will be first introduced in this thesis in Section 3.1, with reference to their geometry, constitutive materials, layers and photomasks. Then, an overview of the structures generated on the wafer will be provided first in Section 3.2, as well as a detailed description of the devised macro-structures, namely the primary connections and the sensing platform.

3.1. SENSORS

Over the course of this thesis, four different types of sensors were selected to be fabricated and tested. To design these, one of three main approaches can be followed:

- Each sensor is designed on its own, as a single entity. This approach maximizes the customizability of the devices, as only the constraints specific to one type of sensor apply. On the negative side, it requires more materials (e.g. photomasks) and fabrication steps, thus resulting more time-consuming and expensive.

- All sensors are designed together. Here, customization is limited, but it might significantly reduce the fabrication steps as certain processes are performed simultaneously (e.g. all metal components that have the same thickness can be deposited in one step).

- Sets of sensors are designed together. This solution is a compromise between the previous ones, resulting in both moderate initial expenses and processing times whilst providing an intermediate level of customization. For instance, when the effect of a layer's thickness is investigated for three resistors with different target resistance, these could be designed in a way that two have the same thickness yet different dimension. Hence, only two – rather than three – photomasks are required; however, at least one additional lithography step is necessary to process the three structures compared to the case where all resistors are designed with the same thickness, and thus with a single photomask.

As the goal of this work is to study the integration of sensors *and* their combined operation as *sensor platforms* within the time-frame of a master thesis, the second approach was deemed suitable.

In the following subsections, the design of each sensor is presented. Once all the geometries of the devices were defined, the planar masks required for the photolithography steps during MEMS fabrication (see Section 4.1) were developed using L-EDIT. L-EDIT is a hierarchical physical layout editor typically used for projects within the Else Kooi Laboratory (EKL). L-EDIT allows users to code geometries, thus to insert variables and create parametric structures. As it will be described into more detail in Section 3.2.3, photolitography masks with numerous sensor variations were developed; therefore, this feature was exploited to automatically place all the relevant structures as certain parameters are varied during the instancing of a cell. However, the tool uses many software-specific commands which are insufficiently described in the documentation for the first-time user. As a courtesy, Appendix B is added with the generating code of the here presented sensors, for the reader searching for a template.

3.1.1. RESISTIVE TEMPERATURE SENSOR

The importance of temperature sensing devices for PV applications has already been underlined in Chapter 1. In view of its ease of fabrication and great compatibility with standard processing within the EKL, a temperature sensor based on a metallic RTD was selected.

The design of the temperature sensor is mainly based on the device fabricated by Beinert *et al.* [56] and it consists in a meander-shaped resistor with multiple parallel fingers, as depicted in Fig. 3.1. Additionally, this device counts two pads for the input and output of the interrogating signal – current or voltage –, and a number of end-loops that interconnect the fingers. The pads represent the *secondary contact pads*, in contrast to the *primary contact pads* described in Section 3.2.1. The difference between these set of

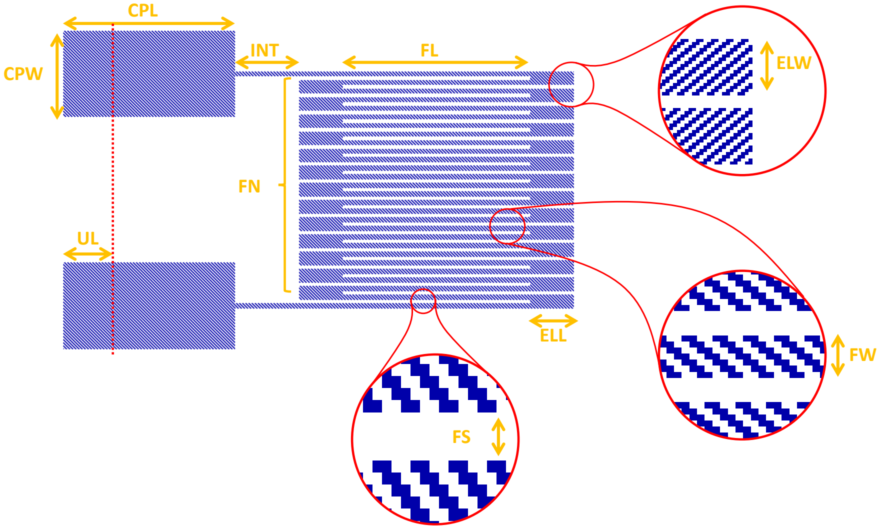

Fig. 3.1: Example of a resistor as designed on L-EDIT.

pads lies in their intended purpose: the primary contacts are interrogated *after* the full fabrication of the sensors, while the secondary contacts may be used to characterize the devices *during* their processing. Table 3.1 reports the dimensions of the various features with reference to the figure. Here, the finger length and spacing are indicated as *variable (VAR)*, as the examined variations of the RTDs will only affect these parameters. In Section 3.2.3, an overview of all the sensor variations will be provided. Meanwhile, the *underlap* parameter in the table represents the amount by which the secondary contact pads underlay other structures, such as the primary connections.

Contrarily to the work of Beinert *et al.* [56], where a silver-based RTD is fabricated, the

Table 3.1: Planar geometry of the resistor depicted in Fig. 3.1.

Parameter	**Abbreviation**	**Value**
Contact Pad Length	CPL	400 μm
Contact Pad Width	CPW	200 μm
Finger Length	FL	*VAR*
Finger Width	FW	10 μm
Finger Spacing	FS	*VAR*
Finger Number	FN	28
End-loop Length	ELL	100 μm
End-loop Width	ELW	30 μm
Interconnection	INT	250 μm
Underlap	UL	100 μm

Table 3.2: Material properties: Silver vs Aluminum.

Properties	Silver	Aluminum	Unit
Density	10.5 [147]	2.7 [147]	g/cm^3
Electrical Resistivity (@20 °C)	$1.59 \cdot 10^{-8}$ [118]	$2.65 \cdot 10^{-8}$ [118]	Ωm
Thermal Conductivity	420 [147]	237 [147]	W/mK
Thermal Expansion Coefficient (0-100 °C)	$19.1 \cdot 10^{-6}$ [147]	$23.5 \cdot 10^{-6}$ [147]	K^{-1}
Temperature Coefficient of Resistance (@20 °C)	$3.8 \cdot 10^{-3}$ [148]	$3.9 \cdot 10^{-3}$ [148]	$°C^{-1}$
Gauge Factor	3.35 [118]	3.1 [118]	-

use of aluminum is investigated, due to its very low cost and wide-spread use within the PV sector. A quick comparison of the material properties of the two metals is provided in Table 3.2. As it can be seen, silver has a lower coefficient of thermal expansion and electrical resistivity, yet a higher thermal conductivity: these properties are commonly advantageous for sensing applications, as they reduce the interfering effects of temperature. Furthermore, silver is more resistant to oxidation compared to aluminum, which facilitates its processing. Nonetheless, in this thesis it is argued that aluminum is still suitable for PV applications, where both the temperature range and exposure to environmental conditions (e.g. moisture) is limited during normal operation.

As sensor fabrication is a novel topic within the PVMD group, no prior knowledge was available regarding the optimal parameters for integration onto PV devices. Hence, the design of the RTD began with the design of a reference sensor, which eventually was varied by modifying the variable parameters. Among these, the reference thickness of the metal layer needed to be identified first, since this dimension is set for all the structures processed with metal sputtering (see Section 4.1.4). Meanwhile, the resistance of the end-loops is much lower than that of the fingers, since the end-loops are much wider than the fingers, as illustrated in Fig. 3.1; consequently, the finger spacing has a lower impact on the RTD's resistance, and thus is set equal to the finger width for the reference resistor. Then, a target reference resistance of 95 Ω was chosen, and Eq. 2.14 was applied to approximately evaluate the resistance of the various combinations of the remaining variables. The target value is slightly lower than what implemented by Beinert *et al.* (100 Ω) as only the resistor fingers were considered in the evaluation, therefore underestimating the actual nominal value. Due to the planned parameter variations and fabrication-dependent results, precision in designing the reference resistor is not a key priority at this stage. Eventually, the reference values reported in Table 3.3 were selected, which result in a resistance value of 93.28 Ω. As mentioned, this value represents the estimation of the *minimum* value, as other features were not included.

Previously, the effect of the finger spacing was ignored as it bears little importance in the resistance calculation. However, the reason behind the choice of the finger spacing as a variable under study is due to the fact that the same resistor also represents the base component of the thermoresistive humidity sensor described in Section 3.1.4. In fact,

Table 3.3: Summary of the parameter values set for the reference resistor.

Parameter	**Value**
Reference finger length	440 μm
Reference finger spacing	10 μm
Reference aluminum thickness	350 nm

the spacing between the fingers affects the surface occupied by the resistor, which in turn defines the surface density of the thermal power generated through ohmic heating – and thus the maximum temperatures reached at the center of the resistor. As the thermoresistive humidity sensor senses a change in moisture as a difference in the thermal resistance of a moisture-sensitive material, it is advantageous to simultaneously operate a second reference heater that is not functionalized with the same material. Since a metal resistor can operate both as a heater and as a temperature sensor [82], it follows that the aluminum RTD must be identical to the aluminum heater of the thermoresistive humistat. For the same reason, the considered RTD is placed on top of a 300 nm thick silicon oxide layer, which acts as a thermal insulator. The addition of the insulator is not a necessary element of the temperature sensor, yet it represents an example of converging design: the design choices of one sensor affect those of others, and a compromise must be found. Nonetheless, some resistors have been placed directly onto the bare substrate. As it will be described in Section 3.2.2, a sensing platform containing sets of perpendicular strain and temperature sensors is devised. Since no humistat is present on such platform, the silicon oxide structure is not added to the design. Generally, the inclusion of an insulating layer between the resistor and the substrate affects the reading of the temperature sensors. However, during fabrication it is possible to simply disregard the steps related to the development of such layer, and obtain the same structures on the substrate. With this approach, more scenarios could potentially be studied.

In Table 3.1, the dimensions of the secondary contact pads, namely the pads that are in direct contact with both the sensor and the primary connections (see Section 3.2.1), are reported. Here, "primary connections" refers to the complete auxiliary structure that includes both the primary contact pads and the conductive traces that link them to the secondary contact pads. The secondary pads were defined to provide compatibility with both the Cascade automatic probe station and screen printing processes. As it will be outlined in Section 5.1, the Cascade probe station is used to interrogate the bare sensors, and it requires a minimum contact pad of 80-100 μm in side length for a reliable automatic operation. Meanwhile, screen printing represents an alternative to the MEMS processing of the primary connections for certain sensors, as well as being commonly used to produce the top electrodes of solar cells; in this case, the minimum suggested gap is also around 100-120 μm to ensure that no short-circuiting occurs due to the relative inaccuracy of the process. Overall, the features of this sensor are big in comparison with typical MEMS devices, and could be further reduced to have a lesser impact on the performance of a solar cell when integrated – as well as to use less material. However, in this initial work the focus is on the proof of concept, as well as on the compatibility with solar cell processing tools; therefore, features no smaller than five microns were adopted

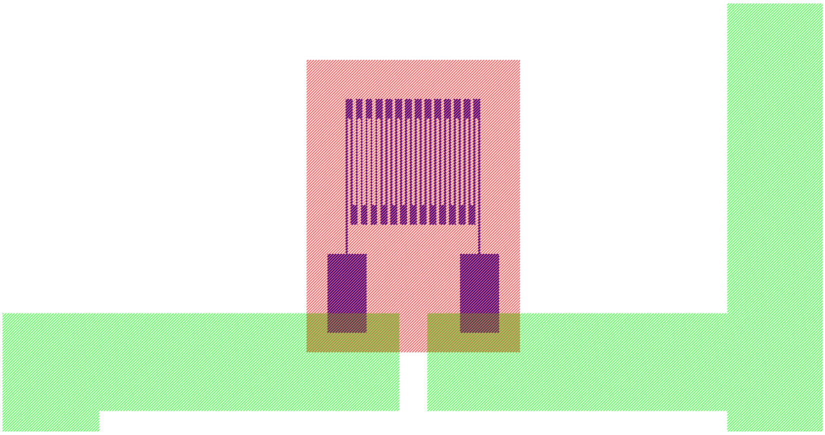

Fig. 3.2: Example of the completed design of an RTD on L-EDIT. Here, the light red, purple and light green areas represent the thermal insulator, the aluminum RTD and the primary connections, respectively. Each color defines both a layer and a photolithography mask, while the specified color sequence outlines the processing order followed.

to ensure the reliable and standard-compatible processing of the sensors, thus reducing the number of fabrication-related unknowns. The selected resistor thickness (350 nm) is relatively large, which leads to a greater total resistor length than what is technically attainable: in fact, a very thin and short metal sheet could achieve the same resistance value, and be similarly implemented as a temperature sensor. However, ensuring a certain toughness of the RTDs during all the fabrication, handling and measurement steps is a priority in this study, thus a sturdy design was selected.

As mentioned in Section 2.2.2, metals are strain sensitive materials, and they obey Eq. 2.35, which quantifies the strain gauge effect *in the direction of* the applied deformation. When a temperature sensor is made more compact by increasing the number of finger whilst reducing their length, the total line length of the interconnecting elements placed between the fingers increases. Consequently, the amount of material which is sensitive to strain perpendicular to the preferential direction defined by the fingers of the sensors increases, thus introducing an additional noise component during measurement. This effect can be reduced by lengthening the end-loops, as their resistance decreases in accordance with Eq. 2.14; therefore, at constant strain and gauge factor, the change in resistance in the transverse direction drops according to Eq. 2.25. In case the longitudinal resistance is much greater than the transverse resistance of the end-loops, it can be assumed that only strain in the longitudinal direction can cause perturbation during the temperature reading. When the reference resistor is considered, it can be observed that the width of the end-loop is ten times that of a single finger, while its length is only roughly 7% . By applying Eq. 2.14, it can be estimated that the resistance of an end-loop is less than 1% of the resistance of a finger, and the resistor can be assumed to not possess any transverse strain sensitivity.

In Fig. 3.2, an overview of the complete design of an RTD is provided, with reference to its constitutive layers. As it can be noted, three photolithography steps are required to generate the complete device. First, the insulating layer is deposited and patterned; then, the actual resistor is processed; finally, the main connections are generated – more information on the MEMS fabrication steps is given in Chapter 4.

3.1.2. PIEZORESISTIVE STRAIN SENSOR

The scientific literature reports numerous examples of strain sensors that exploit piezoresistive materials for various purposes, as mentioned in Section 2.1.2. These devices possess an inherently larger sensitivity to stresses and deformations compared to the metal-based RTDs described in the previous Section. Hence, a smaller line-shaped piezoresistive sensor might already offer a sufficient response when interrogated.

The design of the strain sensor fabricated for the purpose of this thesis takes inspiration from the publication by Beinert *et al.*, as it consists in a strip of doped piezoresistive material. However, a number of differences can be spotted. Firstly, the piezoresistors are made of polycristalline silicon, rather than monocrystalline. This choice was made as the devised sensor is deposited on top of the substrate, and not embedded into it – which already represents a second distinction. Consequently, more degrees of freedom are left to the selection of the substrate. Another difference is the lack of a shielding guard ring: indeed, when the sensor is processed *into* the prospective solar cell, a highly doped ring surrounding the device must be added to shield it from the generated electrons. Finally, Beinert *et al.* perform Phosphorous implantation of the mono-silicon to generate an n-type piezoresistor, while in this work the poly-silicon is implanted with Boron (p-type piezoresistor). Here, Boron was chosen as it maximized the gauge factor in poly-silicon, as reported by French [122]. In particular, the article states that a doping concentration of approximately $1.7 \cdot 10^{-19}\ cm^{-3}$ corresponds to the maximum gauge factor achievable. Furthermore, the electrical resistivity of doped poly-silicon is reported to be larger than its monocrystalline counterpart, which then strongly rises as the doping concentration decreases [149]. At the optimal concentration corresponding to the highest gauge factor, the resistivity is expected to be roughly equal to $0.09\ \Omega \cdot cm$.

The active part of the sensor consists in the aforementioned strip of piezoresistive material defined by three geometrical features: length (aspect ratio), width and thickness. Similarly to the design of the metal resistor, the thickness of the layer was defined first, and was set to $250\ nm$. This layer thickness was selected with the idea to facilitate processing, since an in-house flowchart was used as template for the steps involving poly-silicon. Meanwhile, the planar dimensions represent the variables that are modified to generate variations of the sensor, as will be further outlined in Section 3.2.3. An overview of the sensor is provided in Fig. 3.3, where it can be observed that an additional metal structure joins the piezoresistive strip to the primary connections. This structure serves as the secondary contact pad of the sensor, and it possesses the same thickness of the metal resistor described in the previous Section. As such, it is designed on the same photomask, with the same constraints in place for the contact pads of the resistor. These secondary contact pads are not necessary for the operation of the piezoresistive strain sensor, therefore their fabrication might seem like an additional unnecessary processing step. However, they allow for interrogation of the device even without the large primary

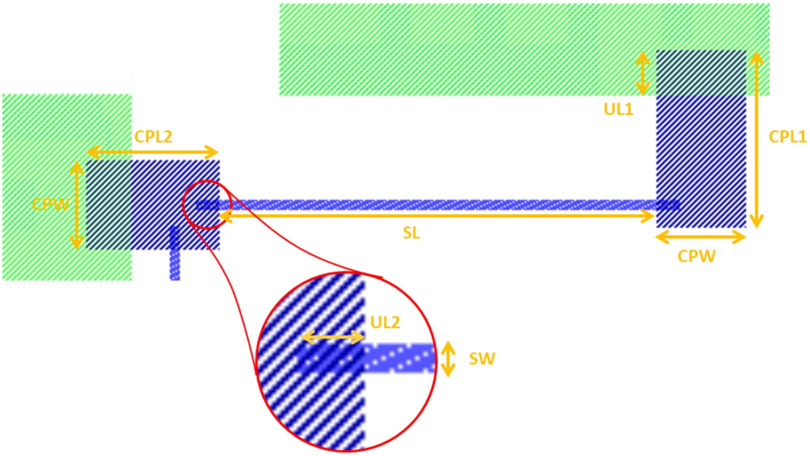

Fig. 3.3: Example of the completed design of a piezoresistive strain sensor on L-EDIT. Here, the blue, light blue and light green areas represent the poly-silicon strip, the aluminum secondary contact pad, and the primary connections, respectively. Each color defines both a layer and a photolithography mask, while the specified color sequence outlines the processing order followed.

connection, e.g. with the Cascade probe station. Moreover, all sensors are fabricated at the same time, therefore these secondary contact pads do not require a real additional processing step, since they are realized with the same photomask of the RTDs' secondary contact pads. Furthermore, the use of secondary contact pads supports an overall greater customization of the structures. Indeed, the primary connections are fixed, and not adapted to fit specific sensors, as will be further described in Section 3.2.1. Hence, new structures could be designed in the future, without the need to redesign the primary contacts. In Table 3.4, a recap of the different sensor's features is provided.

In a similar fashion to the previously described temperature sensor, these strain sensors form the other main component of the sensing platform. As will be illustrated in

Table 3.4: Piezoresistor geometry with reference to its planar design shown in Fig. 3.3.

Parameter	**Abbreviation**	**Value**
Contact Pad Length 1	CPL1	400 μm
Contact Pad Length 2	CPL2	300 μm
Contact Pad Width	CPW	200 μm
Strip Length	SL	*VAR*
Strip Width	SW	*VAR*
Underlap 1	UL1	100 μm
Underlap 2	UL2	50 μm
Contact Pad Thickness		350 nm
Strip Thickness		250 nm

Section 3.2.2, these devices are introduced in sets of two perpendicular sensors, and are paired with a respective temperature sensor each. Because of their elongated shape, these strain sensors are expected to be sensitive almost exclusively to longitudinal strain.

3.1.3. CAPACITIVE HUMIDITY SENSOR

The measurement of capacitance is a common method to determine the presence of specific compounds, as certain materials are – or can be made – sensitive to them. Some examples of capacitive sensors are provided in Section 2.1.1. In case of a humidity sensor, the target substance is water, which easily penetrates various materials and affects their material properties – in particular, their relative permittivity. In the instance of this thesis, a comb-finger capacitor is designed with polyimide as the dielectric, taking inspiration from the work on Multifunctional Integrated Sensors (MFISES) by Roozeboom *et al.* [65, 66]. In their work, the comb-fingers were directly etched into the substrate (buried oxide) in 8.5 μm deep trenches, while aluminum bond pads were placed adjacent to these. In line with the focus on substrate-independent sensors, the capacitor of this thesis was designed as a directly deposited metal layer. Another advantage of this solution consists in keeping the fabrication simple, as additional etching steps would inflate the total number of processing steps and introduce further complexities. The downside of this approach is that the maximal achievable layer thickness is more strongly limited by its processing, which directly affects the obtainable capacitance value (see Eq. 2.37). Regarding the moisture-sensitive polymer, Roozeboom *et al.* selected the commonly used SPR220 photoresist to functionalize their sensor as a proof-of-concept, and they manually deposited it onto the comb-fingers. Meanwhile, the polyimide Durimide 7020 produced by Fujifilm is considered for the purpose of this thesis. This material is both moisture sensitive and photosensitive, thus it is compatible with photolithographic processing. Furthermore, Durimide 7020 was readily available within the EKL. In view of these qualities and the fact that other types of Durimide – or polyimides in general – were already implemented for moisture sensing purposes [150, 151], the use of this polymer was investigated first. Contrarily to Roozeboom *et al.*, the polyimide was spin-coated and patterned to generate regular structures with a greater degree in repeatability. More information on the MEMS fabrication of this sensors will be provided in Chapter 4. The main properties of the selected polyimide, as outlined in its datasheet, are reported in Table 3.5. As can be noted, this polymer can fully sustain high temperature processes – such as the planned lamination ($T_{max.} = 145\,°C$) or the silver paste curing ($T_{max.} = 185\,°C$) illustrated in Section 4.2.

Table 3.5: Material properties of Durimide 7020 by Fujifilm

Properties	**Value**	**Unit**
Glass Transition Temperature	>350	$°C$
Thermal Decomposition Temperature	>510	$°C$
Dielectric Constant	3.3	-
Moisture Absorption (@50% RH)	1.3	%

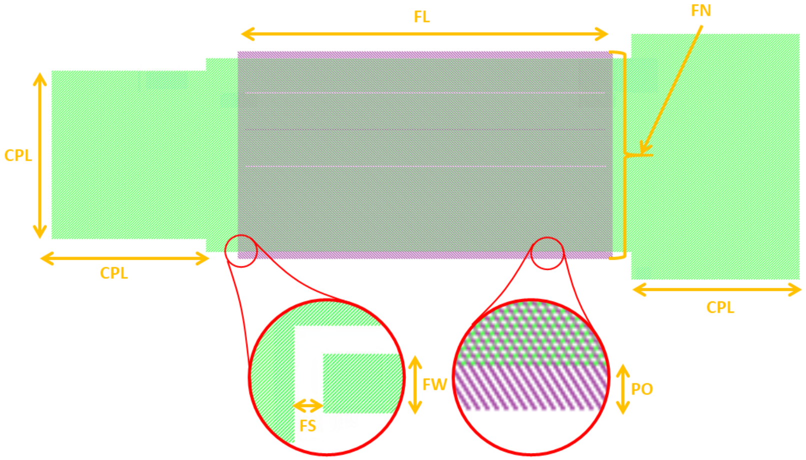

Fig. 3.4: Example of the completed design of a capacitive humidity sensor on L-EDIT. Here, the light green and light purple areas represent the capacitor structure as integrated with the primary connections, and the polyimide covering, respectively. Each color defines both a layer and a photolithography mask, while the specified color sequence outlines the processing order followed. The bottom-left enlargement shows a detail of the tip of a capacitor finger without the addition of polyimide, while the bottom-right magnification indicates the additional polymer at the capacitor's edges.

An example of the designed comb-finger capacitor can be viewed in Fig. 3.4. Meanwhile, Table 3.6 reports the planar dimensions of the structures. As illustrated, the device has a simple geometry consisting in repeated parallel fingers which are connected alternatively to the contact pads, while the polyimide covers the entire surface defined by the fingers with the addition of a surrounding perimeter of constant width. This "polyimide overflow" serves as a buffer zone during fabrication, as to reduce the risk of erroneous uncovering of the marginal fingers. Meanwhile, the width, number and spacing of the fingers are chosen as variables ("VAR") due to their effect on the capacitance value of the device. In particular, the finger width is varied to potentially investigate the effect of the *fringing fields*, namely the non-uniform electric fields formed at the sidewalls of a capacitor's electrodes, on the total capacitance: in fact, the capacitor fingers are buried in a thick polymer layer (aspect ratio > 15) and their width is comparable with the distance between them, which might result in a capacitance larger than what expected from Eq. 2.36 [152]. Contrarily, the finger length has a well-known impact on capacitance (see Eq. 2.37), and thus has been set to a constant value, which corresponds to the maximum which could be achieved on a single die considering the other structures present (see Section 3.2).

The capacitor is the only sensor that does not possess secondary contact pads, as it has been fully merged with the design of the primary contacts. This choice is a result of the ambition to reduce the fabrication steps of all the devices, and the contrasting aspirations between the metal RTDs and the capacitors. Indeed, from the comparison of Eq. 2.14 and Eq. 2.37, it follows that to reduce the size of the sensors at set values of capac-

Table 3.6: Planar geometry of the capacitor depicted in Fig. 3.4.

Parameter	**Abbreviation**	**Value**
Finger Length	FL	2.8 mm
Finger Width	FW	*VAR*
Finger Number	FN	*VAR*
Finger Spacing	FS	*VAR*
Polyimide Overflow	PO	50 μm
Contact Pad Length	CPL	1300 μm

itance and resistance, respectively, the thickness of the metal layer should be increased for the capacitor, and reduced for the resistor. On the other hand, the goal of the primary connections is to deliver the interrogating signals from the contact pads to the sensors with the least amount of parasitic resistance. This is achieved with thicker connections. Therefore, the design target of the capacitor is aligned with that of the primary connections and these two structures are combined into a single layer. A disadvantage of the merging of these structure is represented by the thickness limitations set by the implemented processes: in fact, the actual thickness of the capacitor eventually achieved with lift-off is about 1 μm, as detailed in Section 4.1.5.

Regarding the polyimide layer, a similar reasoning is followed to define its thickness. In fact, another humidity sensor is designed in this thesis, namely a thermoresistive device (humistat) based on a metal resistor covered in the same polyimide (see Section 3.1.4); to curtail the fabrication length and the number of photomasks, it was of interest to combine the polymer layer of the two devices into a single process. On one side, the main purpose of the capacitor is to measure the change in capacitance of the polymer *between* the fingers; therefore, any additional polymer on top of the capacitor represents a barrier for moisture penetration that is expected to increase the response time of the sensor. On the other hand, the humistat relies on a substantial layer to increase the relative value of the variable thermal resistance within the laminated system. Eventually, priority was given to the latter sensor due to its novelty, in order to ensure that it could be tested in its ideal conditions. As a result, the target thickness was set above 15 μm; however, the actually achieved value during MEMS fabrication deviates sensibly. More information on the processing of this layer can be found in Section 4.1.6.

3.1.4. THERMORESISTIVE HUMIDITY SENSOR

The thermoresistive humidity sensor conceived in this thesis is a device which analyses how heat is dissipated from a resistive heat source under varying humidity conditions. The concept of this device originated while studying the implementation feasibility of a set of suspended diodes as humidity sensing device, as proposed by Okcan and Akin [153]. In their article, the diodes are first formed in the substrate, and then excavated with an etching step to leave their structure suspended. Finally, a cap is attached on one diode to operate it as a reference sensor immersed in an atmosphere with fixed absolute humidity. This type of processing is invasive, as it introduces indentations in the sub-

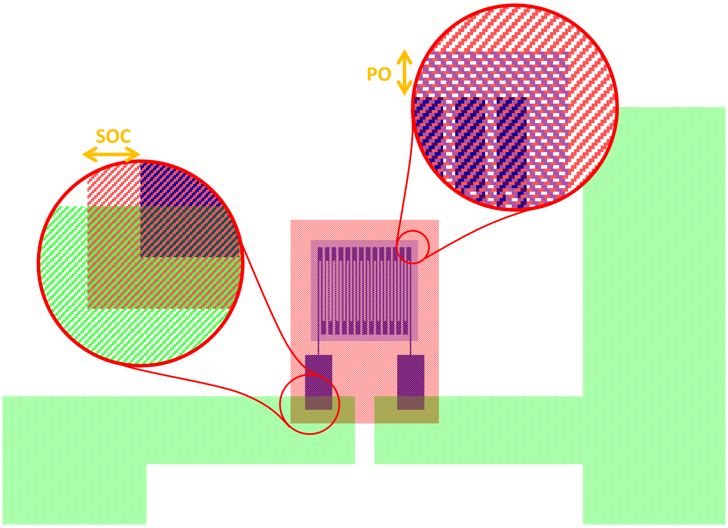

Fig. 3.5: Example of the completed design of a humistat on L-EDIT. Here, the light red, purple, light green and ligth purple areas represent the thermal insulator, the aluminum RTD, the primary connections, and the polyimide, respectively. Each color defines both a layer and a photolithography mask, while the specified color sequence outlines the processing order followed.

strate; furthermore, it presents multiple challenges (e.g. the manual attachment of the cap), which makes such solution less compatible with traditional PV processing. Therefore, the suspended diode is replaced by a resistive heater that is deposited *on top* of the substrate. However, this approach erases the almost isotropic conditions ensured by the suspension of the device, and it reduces the impact of moisture onto the heat transfer coefficient, as only one side of the sensor is effectively sensitive to water. To improve the design of thermoresistive sensors, a moisture absorbing layer and an insulating layer are added above and below the heater, respectively. The reasoning behind these additions is that on one side the moisture absorber withholds a larger amount of moisture in proximity of the heater, while on the other the insulator enhances the directionality of the heat transfer through the moisture absorbing material. Eventually, the purpose of this sensor is not to accurately measure each variation in absorbed moisture, but rather detect the presence of moisture once a certain level is reached; in this sense, the device is more of a thermoresistive humistat.

The literature on thermoresistive humidity sensors is generally quite sparse, and no specific article on this approach was found. To remedy the lack of proven knowledge, a simplified simulation was undertaken through COMSOL Multiphysics to gather some initial observations useful for its design. Here, a multiscale model of a sensor laminated into typical PV module layers was generated, and a number of parameter variations were simulated. For further information on the model, the interested reader is referred to Appendix C. The final design of the humistats consists in resistors identical to the ones

Table 3.7: Partial geometry of the humistat with reference to its planar design, as shown in Fig. 3.5. The dimensions of the resistor's features are already reported in Table 3.1.

Parameter	Abbreviation	Value
Silicon Oxide Overflow	SOC	100 μm
Polyimide Overflow	PO	*VAR*
Silicon Oxide Thickness		300 nm
Aluminum Thickness		350 nm
Polyimide Thickness		>15 μm
Primary Connections Thickness		~1 μm

defined for the aluminum RTDs in Section 3.1.1, placed on top of the same 300 nm thick silicon oxide structure. However, in this instance a layer of polyimide (Durimide 7020 by Fujifilm, >15 μm) is added, as already mentioned in Section 3.1.3. According to this configuration, the aluminum resistor operates as the heater through ohmic heating when current is applied to its electrodes; meanwhile, the silicon oxide and polyimide represent the insulators and moisture absorbers, respectively. An example of the full device is shown in Fig. 3.5, while Table 3.7 summarizes all the related parameters which have not been considered in Table 3.1.

3.2. WAFER OVERVIEW

The standard wafers used within the EKL for MEMS processing are generally circular wafers measuring 10 cm in diameter. As the size of the devices is very small in comparison to the available surface, the sensors are typically not directly positioned across the wafer, but rather collected in sets within self-contained single rectangular dies, which are then repeated over the plane. These units contain both the actual devices, as well as the supporting elements (primary connections and contact pads, auxiliary structures, etc.). Consequently, the design is simplified into a grid of repetitive elements.

Following numerous discussions with process experts and technicians, various technical requirements and constraints were identified. These not only result from the fabrication steps, but also from the planned measurement phase of the sensors. For instance, to asses the strain sensors with a three-point bending test (see Section 5.3.1), the dies containing such devices must be placed at the center of an elongated sample to sustain the maximal deformation. However, the maximum width of the sample cannot exceed the width of the sample holder (~3 cm). Simultaneously, to achieve a satisfactory lamination of the wafer sample, it is suggested to leave around 1 cm at each side. Furthermore, if a buffer zone of ~3 mm in width is considered between each die to account for possible misalignment during laser cutting, the maximum width of a die is already limited to roughly 7 mm. Eventually, the final width of the die is set to 6 mm, that allows for eight dies to be fitted at the center of the wafer – rather than seven. As the samples containing the strain sensors must have the same length, the optimal length of a single die was found to be 1 cm, thus obtaining a total of seven rows of dies. Additionally, space

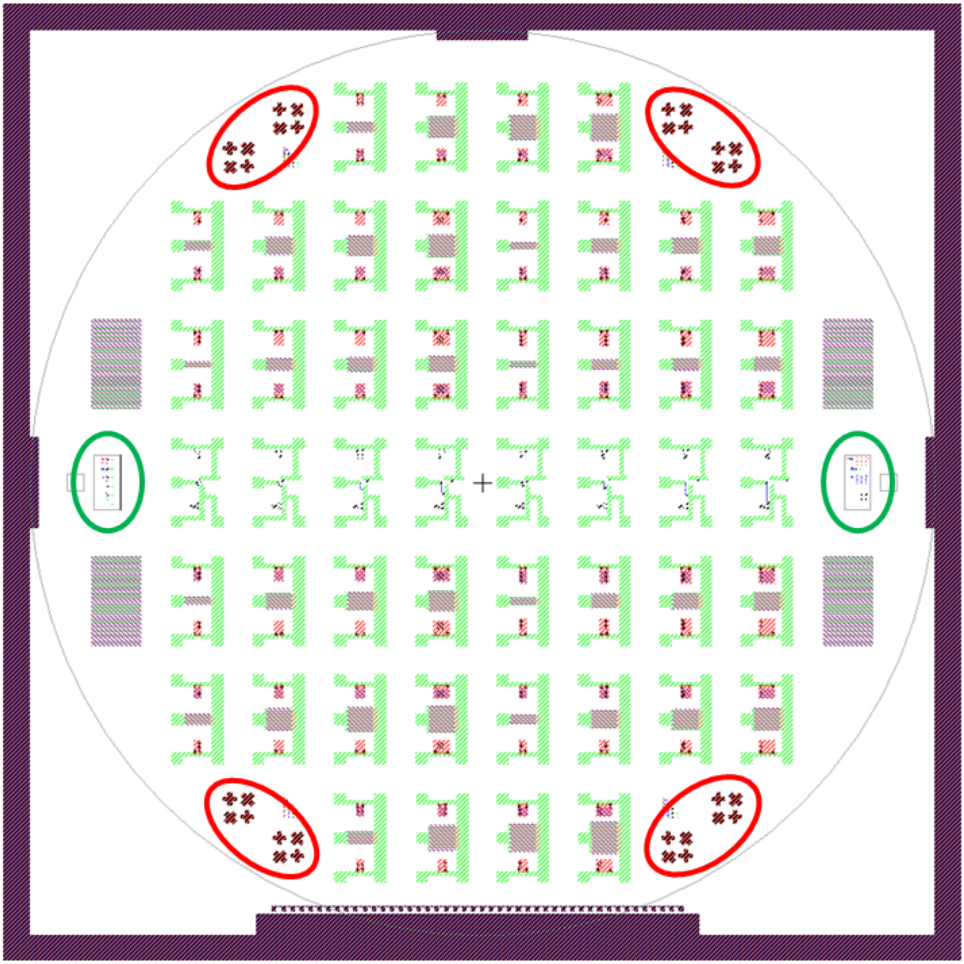

Fig. 3.6: Overview of all the structures present on the wafer, as an overlap of the complete set of photomasks. The positioning of the auxiliary structures, such as the alignment marks for the contact aligner (green circle) and screen printing (red circle), can be observed.

for other four dies is present right above and below the alignment marks for the contact aligner. However, these were not utilized to produce sensors, but rather to test the filling properties of the polyimide (Durimide 7020). In fact, a sequence of parallel metal fingers with decreasing gaps (1.5-45 μ*m*) is produced concurrently with the primary connections; these are then covered with the polymer. An overview of the wafer is given in Fig. 3.6.

3.2.1. PRIMARY CONNECTIONS

The primary connections are metal structures that generate the primary contact pads, and the lines linking these to the devices. While various metals are potential candidates, aluminum was selected due to its common use in PV devices. Nonetheless, other materials, such as silver and copper, could eventually be studied. Regarding the dimensions of the lines, the minimum feature, namely their width, is 500 μ*m*; meanwhile, an aluminum of 1 μ*m* was selected for the primary connections to ensure a reliable lift-off, as reported in Section 4.1.5.

In order to test the sensors within a typical PV laminate, metal wires or tabs must be soldered to the sensors themselves. These wires must then be connected to measurement equipment to interrogate the sensors. To allow for proper soldering of such wires, a minimum feature size of 1.3 *mm* has been advised for the contact pad, with a minimum distance between pads of 2 *mm*; this means that the length of the die could not be reduced to less than 7.9 *mm*. As it will be described later on in Section 4.2.2, soldering was not feasible due to the poor solderability of aluminum and the level of precision and care required by the ultrasonic soldering. Eventually, a different approach was used to achieve the primary connection, which is based on gluing flat tabs to the contacts. Nonetheless, the substantial size of the pads, as well as their spacing, facilitated processing under this new approach.

The design of the primary connection pursues the general aim of inter-compatibility of the structures with future designs. To this end, the primary connections are not adapted to the shape and position of the sensors; indeed, the link between primary connections and devices is achieved through secondary connections. Consequently, new designs can be fitted within the pattern of the primary connections and the related photomask can be reused.

3.2.2. SENSING PLATFORMS

Four different sensors were designed to sense three different quantities: temperature, strain, and humidity. However, each device can be sensitive to the other quantities to a certain degree. Therefore, it is of interest to simultaneously interrogate these sensors to compensate for their mutual effects by processing their respective readings. Due to size and positioning constraints, not all sensors could be fit into a single die. As a result, two types of sensing platforms were devised: one focused on humidity sensing, and one on strain sensing. Examples of these are shown in Fig. 3.7. The first contains both types of humidity sensors (capacitive and thermoresistive), as well as a temperature sensor. As already mentioned in Section 3.1.1, the added metal resistor operates as the reference

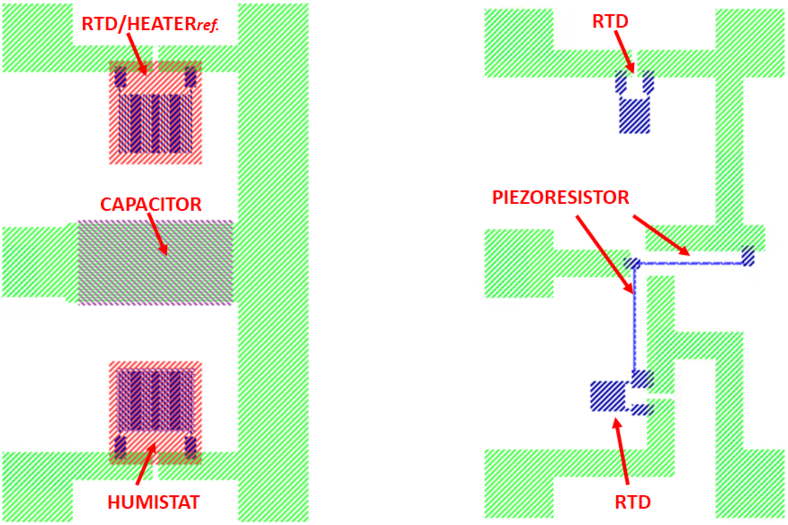

(a) (b)

Fig. 3.7: Examples of the completed design of a humidity (a) and strain (b) sensing platform on L-EDIT.

for the thermoresistive device: by interrogating both resistors simultaneously, a sensible difference in their operation after calibration would then be linked to a moisture ingress, thus triggering a prospective monitoring system. Furthermore, the resistor represents a temperature sensor that can be used to offset the thermal effects that might affect the operation of the capacitor. The second platform consists in the dual use of temperature and strain sensors. Here, the perpendicular strain sensors measure strain occurring in any direction as the vector sum of the sensed orthogonal components. Meanwhile, the RTDs measure approximately the same temperature, as this quantity is isotropic and the distance between the sensors is relatively small. Since the temperature sensors are less sensitive to strain, their reading could potentially be used to compensate the thermal effects onto the strain sensors.

3.2.3. SENSORS COMBINATIONS

In Section 3.1, the main aspects regarding the design of the sensors were detailed. It was mentioned which parameters would be varied, but the variations were not quantified. Here, brief considerations on the matter will be introduced.

In total, 52 dies could be fitted onto the wafer after the various constraints were considered. Of these, only 8 are centered onto the wafer and may generate the samples for the three-point bending test, thus they are the sole dies that may contain the strain sensors. As outlined in Table 3.4, the parameters selected as variable for the piezoresistors are the width and length (aspect ratio); this implies that the maximum number of variations that can be fitted in the available dies is 2x4. In this case, more length variations were desired, thus only two widths were considered. Similarly, two 4x2x5 combinations

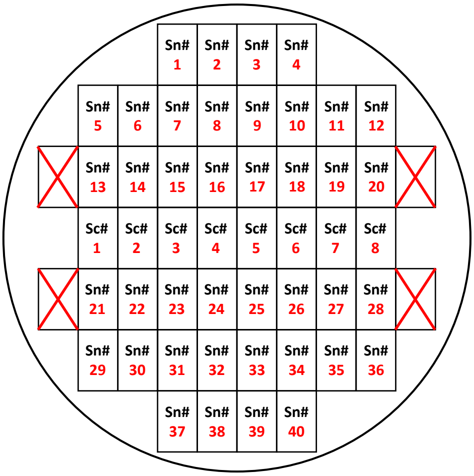

Fig. 3.8: Overview of the positioning and numbering of the on-silicon reference resistors (Sc#= R#), piezoresistors (Sc#= P#), capacitors (Sn#= C#), and resistors (Sn#= R#). *Sc: centered sensor; Sn: not centered sensor.*

were deemed suitable for the capacitors (*finger number* x *finger width* x *finger spacing*) and the resistors (*finger spacing* x *polyimide overflow* x *finger length*), respectively. As already mentioned in Section 3.1.1, the aluminum resistors of the RTDs and humistats are identical; since the polyimide overflow defined in Table 3.7 only affects the latter sensors and two variations are considered (50 µm & 100 µm) for such parameter, it follows that two sets of identical RTDs are present on the wafer. Fig. 3.8 portraits how the dies are numbered on the wafer, while Fig. 3.9 provides a complete overview of the parameter variations of the sensors, as well as their selected values.

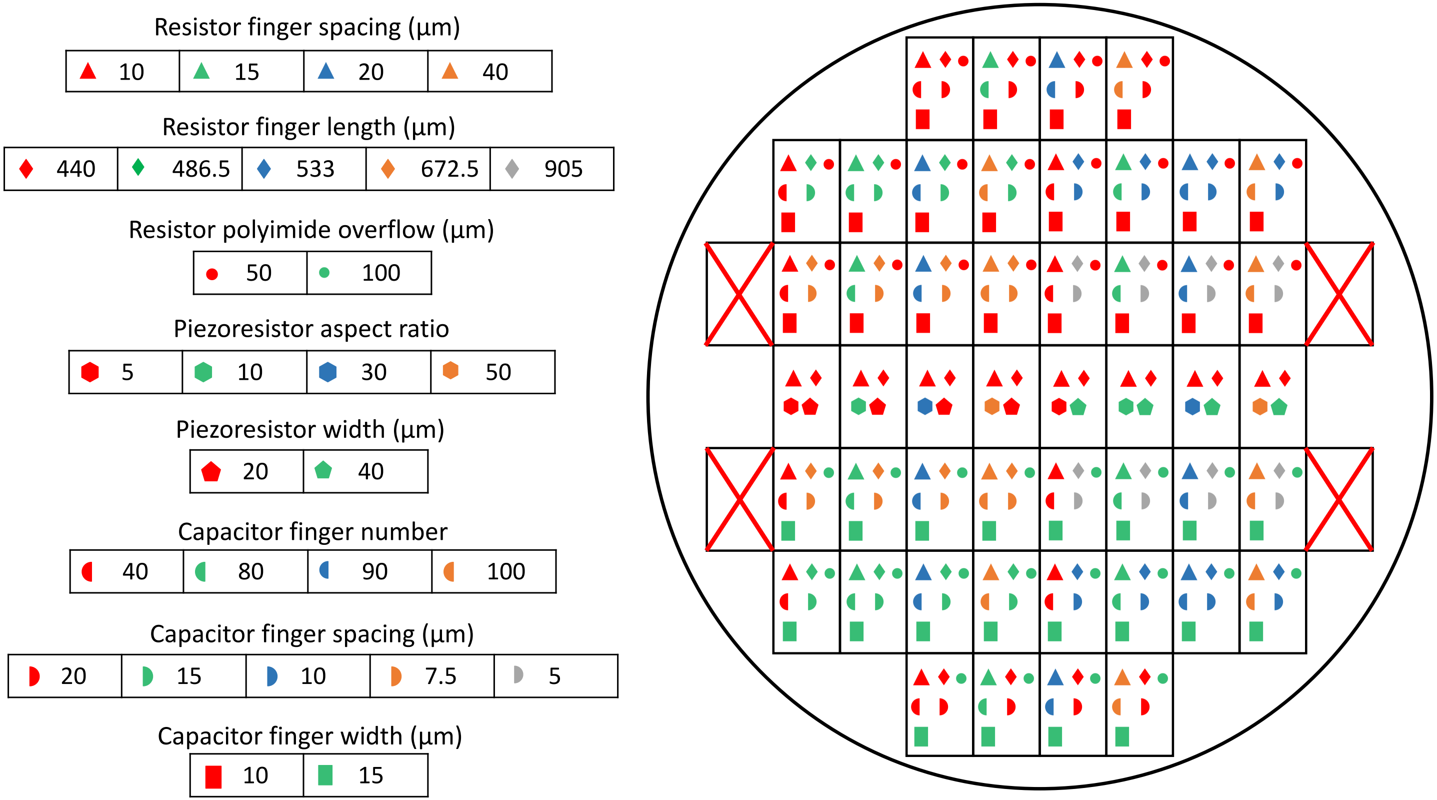

Fig. 3.9: Complete overview of the parameter variations considered for each sensor, including their location on the wafer and their combinations.

4

DEVICE FABRICATION

In this Chapter, the complete fabrication process of the designed sensors will be detailed. First, the performed MEMS processes will be described in Section 4.1. Here, the steps followed for each layer will be detailed and justified. The full flowchart can be viewed in Appendix D. Then, Section 4.2 will outline the additional processes external to the cleanroom environment, which are required to complete the fabrication of the samples.

4.1. MEMS PROCESSING

The fabrication phase begins with polished n-type (100) mono-crystalline silicon wafers of 10 cm in diameter and 260~300 μm in thickness. However, the type of wafer has limited relevance to the processing of sensors, as they are only deposited onto the substrate. The main aspects to consider are the thickness of the substrate and the adhesion quality of the structures to its surface. In fact, the thickness of the wafer directly affects its mechanical properties during the prospective three-point bending test, while a strong adhesion ensures that the devices are able to withstand aggressive fabrication steps, such as lamination (see Section 4.2.3). Nevertheless, this type of wafer has been selected as it is generally used to realize c-Si solar cells within the PVMD group.

4.1.1. ZERO LAYER: ALIGNMENT MARKS

The new wafers first undergo the standard EKL process to form the so-called "zero layer", which generates on their surface the 120 nm-deep alignment marks required for photolithography steps performed with the contact aligner. This process starts with a cleaning step to remove any undesired particles (e.g. dust) which might have collected onto the wafer. Within the EKL, a standard cleaning procedure for non-contaminated wafers is present, which consists in two ten-minute-long nitric acid (HNO_3) baths, followed by a five minute rinsing with deionized water (DI water) and a spin-drying step. The first acid bath is at room temperature (~20 °C) and contains a 99% solution of HNO_3, while the second is at 110 °C with a concentration of 69.7%. Following this cleaning step, the wafers are coated with a 1.4 µm thick layer of positive resist (SPR3012) through the automatic coating station; then, the resist is patterned by the wafer stepper (exposure energy: 120 mJ/cm^2), developed within the automatic developing station, inspected, and plasma etched. Ultimately, the remaining photoresist is removed by the means of plasma stripping, and the wafers go through the standard cleaning process anew.

4.1.2. FIRST LAYER: SILICON OXIDE

Next is the processing of the first layer, where the insulating structures of the humistat are created. Here, the wafers are placed into a furnace to thermally grow a 300 nm silicon oxide (SiO_2) layer through wet oxidation. Following the indication by the online calculator provided by Brigham Young University [154], the approximate time to achieve the target thickness is set to 16 minutes and 26 seconds at 1100 °C. The actual achieved thickness was measured with an ellipsometer, which resulted in an average value around 312 nm. The difference between the expected and achieved values can be explained by taking into account the intrinsic fluctuations in the operating conditions of the furnace. Nonetheless, the importance of this "error" is limited, as the difference is less than 4%; hence, the performance of the humistat is expected to be slightly improved, while that of the RTDs that will be postitioned on SiO_2 marginally deteriorated. Furthermore, the Marangoni cleaning described in Section 4.1.3 will remove few nanometers of the oxide, thus the difference is expected to be further reduced. Following the oxide growth, the layer is then coated similarly to the case of the "zero layer", but the patterning of the first structures is achieved through exposure by the contact aligner in soft contact mode (exposure energy: 127.8 mJ/cm^2). Once developed and inspected, wet etching is performed to obtain the structures. This etching step is achieved by rinsing the wafers in a bath containing Triton X-100 (ratio: 1:5000), then dipping them in a buffered hydrofluoric (BHF) solution (ratio: 1:7) at ambient temperature for 4 minutes and 30 seconds. Wet etching is successful when all windows have been opened, and the underlying hydrophobic silicon is exposed. To remove the remaining resist from the structures, the wafers are placed in an acetone bath at 40 °C for approximately one minute. The actual time generally depends on the type of resist, as well as its thickness. Nonetheless, the complete removal of the resist can be visually verified. Finally, a standard cleaning step is performed, which removes both undesired particles and possible remaining resist.

4.1.3. SECOND LAYER: POLY-SILICON

The processing of the second layer consists in the deposition, patterning, doping and annealing of poly-silicon, the constituent material of the piezoresistive strain sensors. The first step in its processing is a so-called *Marangoni cleaning*, where the Marangoni effect is applied to thoroughly dry the wafer and delay the re-development of the native oxide on its surface, thus ensuring a better adherence of the poly-silicon to the silicon wafer during its deposition. This special cleaning step consists in a four-minute-long 0.55% HF bath at room temperature, followed by a four-minute-long DI water rinsing. The wafers are then dried with a flow of isopropanol (IPA) while they slowly emerge from the bath. The Marangoni cleaning is best performed right after a standard cleaning, and right before the actual deposition. On the downside, the HF solution etches away some nanometers of the patterned SiO_2; however, during processing of the previous layer, more oxide than intended was thermally grown, which can be assumed to have been compensated for.

After cleaning, the wafers are placed into the LPCVD furnace for 1 hour and 54 minutes to deposit 250 nm of poly-silicon. At this stage, dummy wafers should be added to verify the actual achieved layer thickness at the end of the deposition; unfortunately, this step was mistakenly skipped. Nonetheless, the logbook of the furnace records previous users targeting the same layer thickness using similar settings (±1-2 minutes), leading to the assumption that the target thickness has been approximately achieved. Following deposition, the poly-silicon layer is subject to Boron doping through ion implantation. To achieve this, an implantation dose and energy of $5{\cdot}10^{14}$ $ions/cm^2$ and 5 keV are used, respectively. The implantation dose was selected with the aim to approximately achieve the ion concentration corresponding to the maximum gauge factor ($N_{opt}{\sim}1.7{\cdot}10^{19}$ $ions/cm^3$), as shown in Fig. 4.1. Indeed, the ratio between implantation dose and poly-silicon thickness results in an ideal concentration of $2{\cdot}10^{19}$ $ions/cm^3$ under uniform dopant distribution. However, the profile of the actual doping concentration is not uniform, as reported by Nedelec *et al.* [155]. In fact, the Boron concentration peaks within the first 250 nm of poly-silicon after implantation with a $5{\cdot}10^{14}$ $ions/cm^2$ dose, with an average approximately equal to $4.5\ {\cdot}10^{19}$ $ions/cm^3$, as illustrated in Fig. 4.2. Furthermore, the figure indicates that a subsequent annealing step is able to reduce the non-uniformity of the doping concentration along the poly-silicon thickness. In view of the limited time, the optimization of the implantation dose was not feasible, thus the same dose implemented by Nedelec *et al.* was applied during the fabrication of the first sensors, with the goal to further study this topic in a second batch of devices. Unfortunately, over the course of this thesis the implanter present in the EKL abruptly became inoperative, preventing any further experimental investigation. Regarding the implantation energy, half the energy utilized by Nedelec *et al.* was selected for the purpose of this thesis, 5 keV, to reduce the risk of undesired implantation of the substrate: in fact, the poly-silicon layer studied by Nedelec *et al.* is approximately four times thicker, and it presents a considerable ion concentration after the initial 250 nm. Furthermore, contrarily to the piezoresistor considered in this thesis, Nedelec *et al.* cover the poly-silicon with a PECVD SiO_2 layer to prevent Boron out-diffusion during annealing, which represents an additional barrier to implantation.

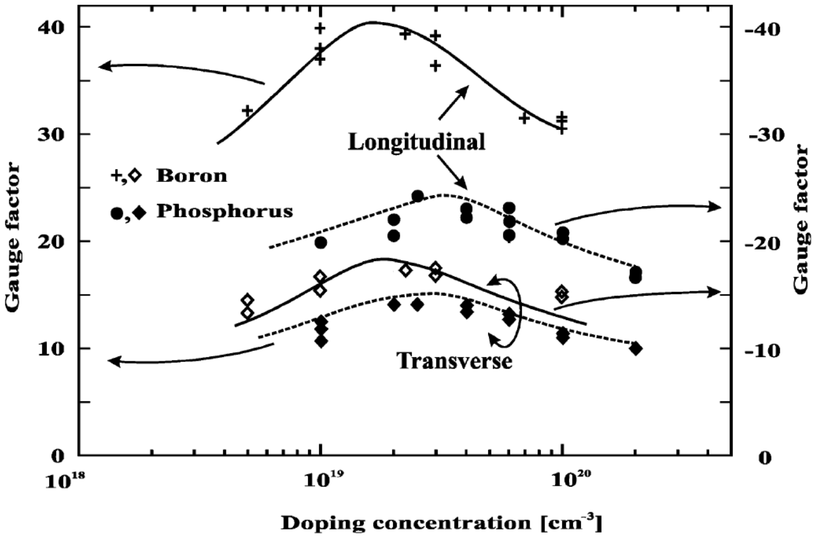

Fig. 4.1: Gauge factor profile of poly-silicon as a function of doping concentration. *Reproduced from [122].*

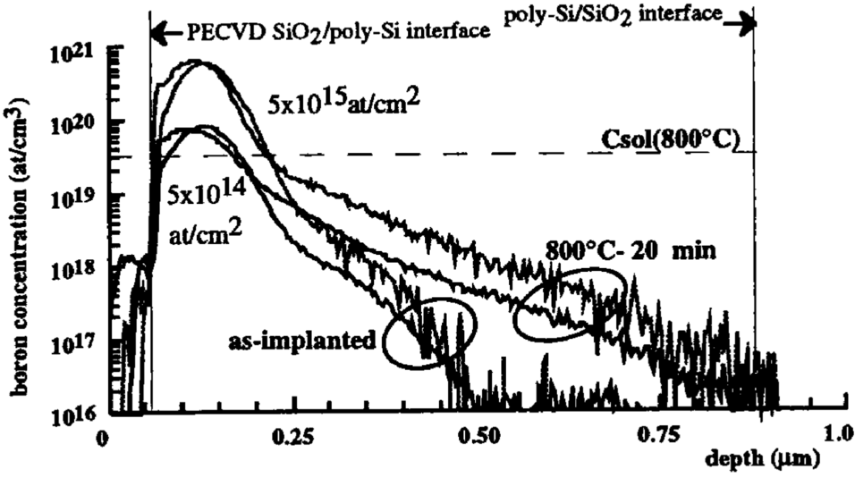

Fig. 4.2: Boron concentration profile in poly-silicon after implantation with $5 \cdot 10^{14}$ at/cm^2 and $5 \cdot 10^{15}$ at/cm^2 doses (energy: 10 keV) and after a *twenty-minute-long* annealing step at 800 °C. Here, a PECVD SiO$_2$ encapsulation is added to prevent Boron out-diffusion during annealing. *Reproduced from [155].*

After the implantation, a standard cleaning step must be performed to remove undesired particles, which might flake off the furnace walls and be deposited onto the wafers by the gas flow. Then, an annealing step is executed to promote ion migration, and to relieve the internal stresses accumulated by the poly-silicon during its deposition and implantation [156]. To achieve this, annealing is performed for one hour at 850 $°C$ in an oxygen atmosphere to obtain a more stable concentration across the section of the piezoresistor. Unfortunately, there was no chance to verify the obtained doping profile. After the necessary standard cleaning step has been performed anew, the poly-silicon is coated by a 3.1 μm layer of positive photoresist (SPR3012), which is then patterned (exposure energy: 426 mJ/cm^2) and developed; then, the structures are again defined by plasma etching. Finally, the remaining resist is stripped through plasma resist stripping, and the wafers are standard cleaned and visually inspected.

4.1.4. THIRD LAYER: THIN METAL

The third layer generates the first metal structures, namely the aluminum resistors and secondary contact pads. Hence, this layer defines the first sets of sensors which could already be operated. However, the secondary contact pads can be interrogated only through special precision equipment, such as the Cascade probe station.

The processing of the third layer begins with a full wafer metallization, achieved through sputter coating of 425 nm of an aluminum alloy at 350 $°C$. This thickness is larger than the 350 nm set during the design phase outlined in Section 3.1.1. This choice was made to account for the removal of the so-called "aluminum fences", namely the vertical structures which are formed when material is deposited onto the lateral walls of the photoresist, and are not removed during the subsequent resist stripping. Meanwhile, the alloy consists of aluminum with a 1% addition of silicon, which was strongly advised by the cleanroom operators due to its superior adhesion quality to the substrate.

Following the sputtering of the aluminum, the wafers are coated with 1.4 μm of positive resist (SPR3012), aligned and exposed (exposure energy: 142 mJ/cm^2), developed, and then inspected. Then, the wafers are prepared for the aluminum fence removal by clearing the structures from the remaining resist through plasma etching (1000 W with 2 minutes overetch). Next, the wafers are moistened by a one minute rinse in a Triton X-100 bath (ratio: 1:5000), and etched for 30 seconds in an aluminum etch fluid to remove 75 nm from the surface of the metal. This fluid is a mix of various acids, and it contains 770 ml of concentrated phosphorus acid (H_3PO_4, 85%), 19 ml of concentrated nitric acid (HNO_3, 65%), 140 ml of concentrated acetic acid (CH_3COOH, 100%), and 71 ml of DI water. Once etching has been achieved, the wafers are promptly rinsed with DI water, then spin-dried. According to the internal EKL rules regarding contamination, aluminum is considered a "green-metal", which is compatible with processing in most equipment. However, the wet benches are split into those dedicated to wafers not contaminated by metals, and those designed for green metals only. In latter case, the standard cleaning is reduced to a single HNO_3 99% bath at room temperature, lasting 10 minutes with subsequent DI water rinsing (5 minutes) and spin drying. Other metals have other status and follow different rules. For instance, silver is considered a "red metal", and thus cannot be further processed with the majority of tools present in the cleanroom 100. Hence, the use of aluminum was also preferred for fabrication as it facilitates the processing of the sensors: indeed, the presence of silver does not allow the use of the automatic coater/developer, the standard wet benches and the plasma etcher. However, this choice came with its limitations, as aluminum oxidizes very quickly and can become difficult to solder; contrarily, more noble metals, like silver, are typically chosen both as a sensor's constitutive material and contacting metal, as show-cased in the work by Beinert *et al.* [56].

4.1.5. FOURTH LAYER: THICK METAL

Following the first metallization, a second aluminum layer is deposited to generate the capacitors and the primary connections simultaneously, as already introduced in Section 3.1.3. Ideally, the layer should be as thick as possible; however, the thickness was eventually set to 1 μm in view of the delicate lift-off process. Due to contamination issues, the wafers cannot be sputter coated again; therefore, metal PVD coating is performed with the Provac evaporator as the alternative processing. This tool is the only one located in the cleanroom 10000 and it is a highly contaminating tool: indeed, wafers are regarded as contaminated by "red metals" as soon as they are inserted. It follows that the wafers cannot be placed in the automatic coater and developer. Since each wafer contains unique dies (see Section 3.2.3), numerous wafers were processed to account for possible defective devices; as a result, it was convenient to operate the automatic equipment, both from the perspective of repeatability and time. Consequently, the immediate solution was to process the fourth layer through lift-off. This method inverts the steps related to the photoresist processing with those associated with the material deposition, and it switches the etching step with a solvent bath. Following this approach, the material on top of the existing resist is peeled off, leaving behind the part which filled the patterned openings.

In this work, lift-off was performed manually within the Special Applications Laboratory (SAL) by immersing the developed wafers one at a time into glassware containing the solvent, which is subsequently placed into an ultrasonic bath. Every five minutes the processed wafer is visually inspected and rotated, while occasionally the peeling of the metal is promoted by removing the wafer from the bath and spraying DI water onto it. Once lift-off is completed on the wafer dies, traces of the metal may still stick to the substrate at its edges; these are gently scraped off with a pair of tweezers, and the wafer is dipped into the solvent for another 30 seconds. With this method, the duration of the ultrasonic bath is reduced, thus lessening possible detrimental effects of the ultrasound onto the metal-to-substrate bond. Finally, the wafer is rinsed with DI water, spin-dried for 60 seconds and cleaned by completing the metal standard cleaning process within SAL.

The first action required to fabricate the fourth layer is the coating of the wafers. After initial discussions with experienced EKL users, various attempts were made on dummy wafers to achieve a very thick coating (>7μm) to ensure a satisfactory metal lift-off. In fact, increasing the lateral surface of the resist exposed to the solvent corresponds to slashing the duration of the ultrasound bath, as a wider cross-section is available for the solvent to dissolve the resist.

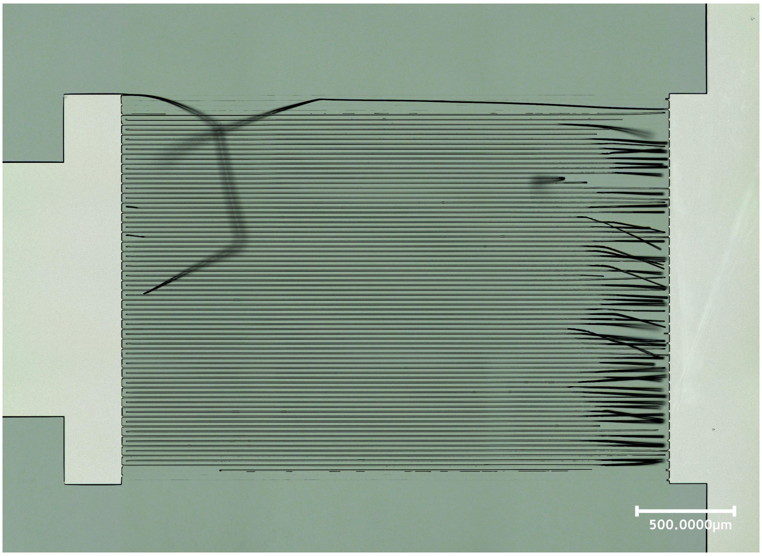

Fig. 4.3: Digital microscope image of an over-developed comb-finger capacitor. The structures with the highest aspect ratio, namely the capacitor fingers, are detached during development by the centrifugal forces exerted by the automatic developer.

While the suggested thickness was about 10-12 μm for a 2 μm aluminum layer (aspect ratio ~ 6), the automatic coater/developer has no standard process for such thickness. Nonetheless, tests were carried out with 7 μm, which were spin coated and developed as two times a single 3.5 μm layer. At this point, manual coating and development were not tested because of the latter's aggressiveness, especially when performed by an inexperienced person. In fact, the smallest features, namely the capacitor fingers, were not able to resist the forces exerted onto them during development because of their high aspect ratio. Different development times were tested, yet even the slightest over-development damaged the delicate structures, as shown in Fig. 4.3. Rather than reducing the metal thickness to 500 μm to obtain the suggested aspect ratio with a 3 μm coating, additional tests were carried out by coating the maximum standard negative photoresist (AZ-nLOF2020) thickness, 3.5 μm, patterning (exposure energy: 73 mJ/cm^2), development, and evaporating both 1 and 2 micrometers of aluminum – thus more than halving the ratio. Remarkably, lift-off was successful, although slow and burdensome. An example of an obtained capacitor is shown in Fig. 4.4 with an aluminum thickness of 1 μm. Here, it can be observed that all fingers are properly attached to the substrate; nonetheless, a tape-test was performed to verify the adhesion quality of the layer. Such test consists in placing a piece of strong tape onto the smallest features and pulling it off with force; it resulted successful for both thicknesses.

An initial lift-off test was performed utilizing an acetone bath at room temperature. However, the process was very slow (>1 hour) and it led to poor results, as the aluminum easily peeled off during the tape test. Unfortunately, it cannot be concluded with certainty that the prolonged ultrasonic bath is the major cause of the weak layer bonding,

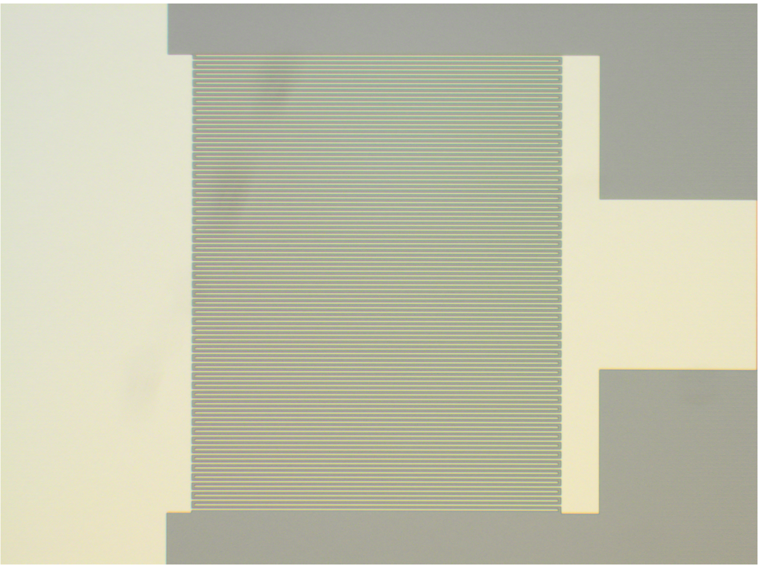

Fig. 4.4: Optical microscope image of a successful capacitor (C40 in Fig. 3.8) before the processing of the fifth layer, namely the polyimide (see Section 4.1.6).

as a previous underdevelopment of the photoresist might also explain the result. Due to time constraints, no further test on this specific issue was performed, and the acetone was replaced by N-Methyl-2pyrrolidone (NMP), a more aggressive solvent. The use of acetone was initially investigated, as it is a relatively safe and inexpensive solvent, which are important qualities when continuously handling large quantities. Nonetheless, the processing time was reduced to less than half an hour by performing lift-off with NMP at 75 °C, and a excellent adhesion quality was achieved. Regarding the effect of the aluminum thickness onto the lift-off process, a 1 μm thick layer appears to have an overall slightly shorter processing time compared to a thickness of 2 μm – not quantifiable as it depends on the "freshness" of the solvent bath. As the effect of prolonged exposure to ultrasounds could not be studied due to time constraints, the layer thickness was eventually set to 1 μm to conservatively ensure that both the integrity of the wafers and the processing of the following layer would not be affected.

4.1.6. FIFTH LAYER: POLYIMIDE

The last material to be added onto the wafers is the moisture absorbing polyimide. As discussed in Section 3.1.3, Durimide 7020 is used due to its photosensitivity, moisture absorbing capability and immediate availability within the EKL; however, it is not a commonly used polymer. Moreover, only manual coating and development can be performed. Therefore, a number of preparatory tests were done to develop an acceptable process. Furthermore, the processed wafers are considered contaminated at this stage, thus dedicated equipment must be used and good practices must be followed.

As the first step, the polymer is coated by the means of manual spin-coating. For this, the polyimide must be at room temperature when poured onto the wafer, and the amount used is enough to generate a circle of 2.5-3 cm in diameter. As a result of the performed tests, it was eventually found that an initial seven seconds spin at 1000 RPM, followed by another ten seconds spin at 1900 RPM, leads to a coating layer ranging between 20-22 μm *after* its curing, in line with what is indicated on the technical datasheet of the polyimide; in both cases, and additional second is considered to accelerate the wafer to the set RPM. Other tests were then executed to define an operational baking procedure. Indeed, the datasheet reports an approximate shrinkage of 45% during curing, which places the initial thickness to roughly 36-40 μm *before* curing. Given the substantial thickness of the polyimide layer, a long baking step was expected and had to be determined. Initially, the soft baking suggested in the datasheet was followed; this process consists in two six-minute-long baking steps at 70 $°C$ and 100 $°C$. However, the obtained polyimide layer was deemed too soft to be further processed, as it was easily sticking to a Q-tip when probed. By varying both time and temperature, it was eventually found that two twelve-minute-long baking steps at 70 $°C$ and 100 $°C$ provided satisfactory results. The reason for this difference might be related to the way baking is performed (hotplate vs oven): in fact, the suggested process did not specify which method should be used. Eventually, a hotplate was utilized for the purpose of this thesis.

After baking, the wafers are exposed for patterning with an energy of ~250 mJ/cm^2 (contact mode: proximity), and stored at room temperature for at least 30 minutes as Post-Exposure Delay (PED). The next step consists in the manual development with HTR-D2 (developer) and RER600 (rinser), as indicated in the datasheet. For this, each wafer is first placed into a shallow beaker containing HTR-D2, and development is promoted by the manual sloshing of the liquid. Subsequently, the wafer is dried with the nitrogen gun and inspected by eye: if "shadows" are observed on the bare silicon, the wafer is placed back into the developer and the step is restarted. Once the development is deemed visually sufficient, the *dry* wafer is placed in the other beaker containing the rinser (RER600) for about a minute. Finally, the wafer is rinsed with acetone, spin-dried for a minute, and inspected under the microscope. Should the structures be still under-developed, the full process is started over. Unfortunately, due to the amount of polyimide to be developed, no approximate development time can be recommended: in fact, the solvent had to be replaced at least once during processing of each wafer, as the polymer quickly saturated the solution. Nonetheless, it is estimated by experience that the full development with an unsaturatable amount of solvent would take 3-5 minutes per wafer. Meanwhile, the minimum time required for the entire process – development, rinsing, drying and inspecting – is expected to be around 10-15 minutes per wafer in the best scenario.

The last step planned for the polyimide layer – and thus the last process of the MEMS fabrication of the sensors – consists in the curing of the polymer. To achieve this, the wafers are placed in an oven to cure the polyimide at 350 $°C$ for 60 minutes, as suggested in the datasheet. During such process, the thick layer shrinks by roughly 45% and blackens, as shown in Fig. 4.5.

As final remark, the drying step between dipping the samples from one bath to another is of great importance. Indeed, during the first attempts, the wafers were directly transferred from one solution to the other, and eventually an unexpected reaction occurred

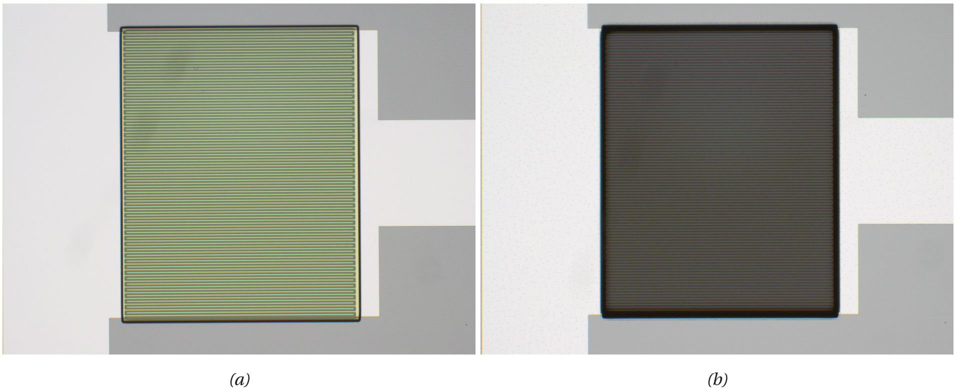

(a) (b)

Fig. 4.5: Optical microscope image of the capacitor C#40: before (a) and after (b) curing of the polyimide.

with the polyimide on the wafer; as Fig. 4.6 illustrates, white slime formed on the wafer. With the assistance by a senior EKL engineer, it was determined that this effect resulted from the interaction between the two chemicals and the significant amount of polymer, which could be conveniently prevented by reducing the amount of HTR-D2 dripping from the wafer.

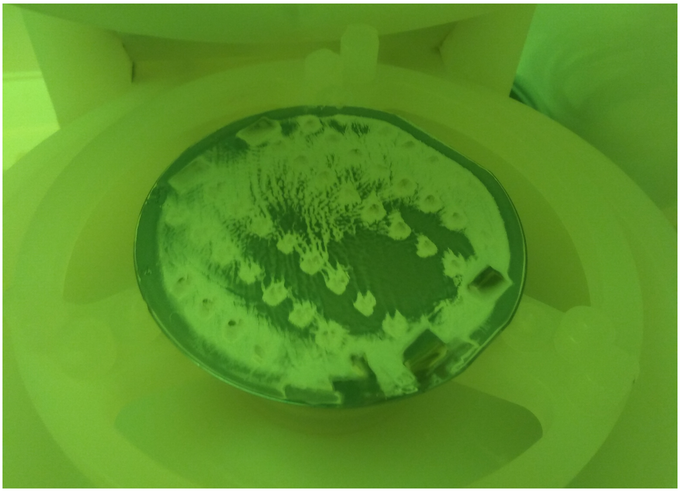

Fig. 4.6: Unexpected reaction of the polyimide layer when the drying step is disregarded during wafer transfer from HTR-D2 to RER600

4.2. MANUFACTURING

The wafers fully processed within the cleanroom are not yet complete, as samples still need to be cut out, wired and laminated. This second fabrication phase is carried out within the Electrical Sustainable Power (ESP) laboratory and the Phovoltatronics Lab, where the tools and material required are located.

4.2.1. LASER CUTTING

Laser cutting is the first operation performed on the wafers. In this process, the profile of the desired structures is first laser engraved into the wafer, and then fractured along the obtained grooves by manually applying pressure. Table 4.1 reports the configurations set for the laser cutter.

Table 4.1: Laser cutter configurations.

Parameter	Value
Power level	100 % (~ 30 W)
Speed	300 mm/s
Frequency	150 Hz
Repetitions	35 rep./segment

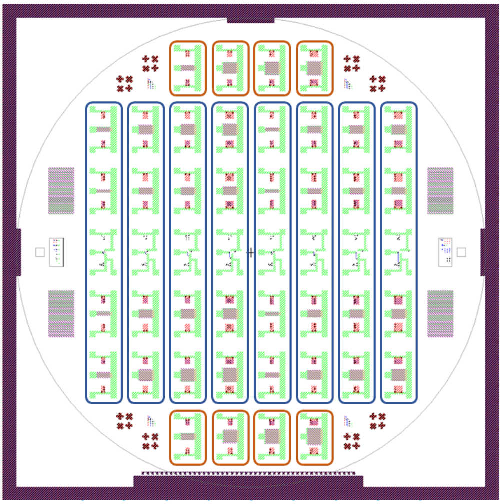

Fig. 4.7: Scheme of the samples obtained through laser cutting as located on the wafer. For a larger depiction of the designed wafer, it is referred to Fig. 3.6.

The full design of the structures is detailed in Chapter 3, where the size, positioning and spacing of the dies on the wafer are defined (see Section 3.2). In particular, the dimensions of a single die is set to 6x10 mm^2, while the die-to-die distance counts 3 mm. The spacing serves the purpose of reducing the consequences of a misalignment (e.g. a slight rotation of the wafer), as well as the risk of re-deposition of the material evaporated by the laser onto the sensing platforms. To prepare the samples for lamination, the wafer cannot be cut into a grid of single dies, as this is not compatible with a three-point bending test. Indeed, to appropriately investigate whether the piezoresistive device is capable of sensing strain applied to the substrate, namely the prospective solar cell, the sample should have an elongated shape. With reference to Fig. 4.7, the optimum aspect ratio of the samples containing the strain sensors is achieved when a column contains five dies. Considering a 1.5 mm wide perimeter around the edges, a final sample measuring 9x65 mm^2 is obtained. As a result, a total of eight dies, four on top and four on the bottom, are not included in the aforementioned samples, as shown in Fig. 4.7. However, these contain only humidity sensing platforms, which are not bound to any specific sample geometry – and thus can be divided into single dies. Consequently, a total of nine through-all cuts perpendicular and two parallel to the primary flat of the wafer are sufficient to carve out all the samples.

4.2.2. WIRING

The original idea regarding the connection of external devices to the sensors was to first solder general purpose wires onto the primary contact pads. However, the choice of pure aluminum as the metal of the pads introduced further complexities: indeed, aluminum quickly forms an oxide layer, which both acts as an electrical insulator and prevents the pure metal from soldering. Generally, ultrasonic soldering can be performed with aluminum, as the ultrasonic cavitation generated by the ultrasonic waves is able to remove the oxide film on the material. Additionally, active solders can be used, which are filler materials that react with the aluminum to promote the ultrasonic soldering. However, during initial dry-runs, it was determined that this process is not appropriate given the scale and fragility of the devices. In fact, the ultrasonic solder iron is difficult to handle during operation due the combined effect of its oscillation and pressurized gas stream, thus, without an experienced hand it becomes virtually impossible to reliably solder without scratching the wafer and the sensors. Furthermore, the added solder forms a considerable dome around the wires, which acts as a point of pressure. Consequently, it becomes unfeasible to further process any soldered sample due to the high risk of fracturing it, as shown in Fig. 4.8.

Fig. 4.8: Example of a soldered wafer sample which broke due to the points of pressure. The sample was being prepared for lamination as it fractured, and only ordinary forces were applied during handling. More information on the lamination process is provided in Section 4.2.3.

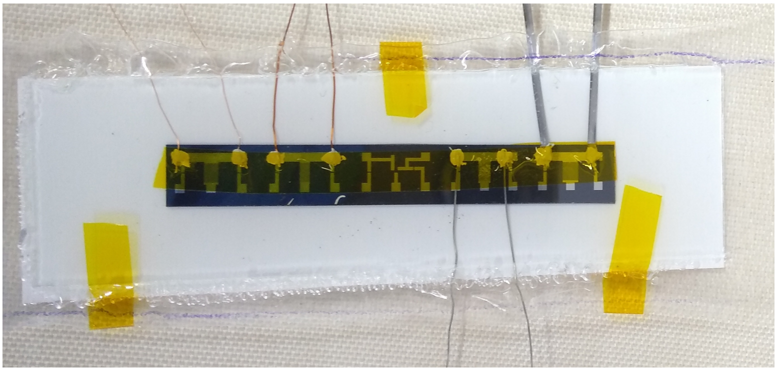

Fig. 4.9: Laminated test sample with wires and tabs attached to the contact pads. This sample does not contain any sensor, but only the primary connections. *From left to right*: two types of copper wires, aluminum wires, aluminum tabs.

Eventually, a process involving the silver paste (DuPont Solamet PV416) used for screen printing was developed. First, the contact pads are coated with the paste, while avoiding any erroneous drip which could short-circuit the devices. Then, their surface is scratched with a needle – or similar – to ensure a better ohmic contact, since the superficial aluminum oxide is partially removed. Then, the tips of the wires are placed on top the contact pads, while further paste is added to fully incorporate them. Once all the wires have been processed, the sample is placed onto a hot plate set to 185 °*C* for 20 minutes.

Tests were performed to determine which wiring solution would suit best the devised process. The wiring solutions under test, namely aluminum wires, aluminum tabs, and coated copper wires, were connected to the sensors using the above described procedure, based on the use of the silver screen printing paste, followed by the lamination of the samples. The purpose of such test was both to verify whether the connections of the wires/tabs achieved with the use of the silver paste could sustain the heat and pressure treatment which occurs during lamination, as well as to determine the electrical resistance introduced by each wiring solution. Fig. 4.9 shows the test sample after lamination. This investigation demonstrated that all processed components show good resilience to lamination, independently of the used wiring solution. However, the used copper wires did not provide any resistance reading, probably because the insulating coating was not fully removed from their ends. On the other hand, both the aluminum tabs and wires presented good conductivity, with a total resistance of no more than 1.6 Ω. In view of the bigger surface area available for the contact and the negligible increase in handling complexity, the aluminum tabs are the preferred choice as connectors for the sensors. Unfortunately, only one test sample could be laminated, since the available laminator broke due to short-circuiting of its heater and was not repaired in time for further processing.

The screen printing paste method eventually implemented was an immediately available alternative, yet it is not the best solution as it is a very delicate process that requires

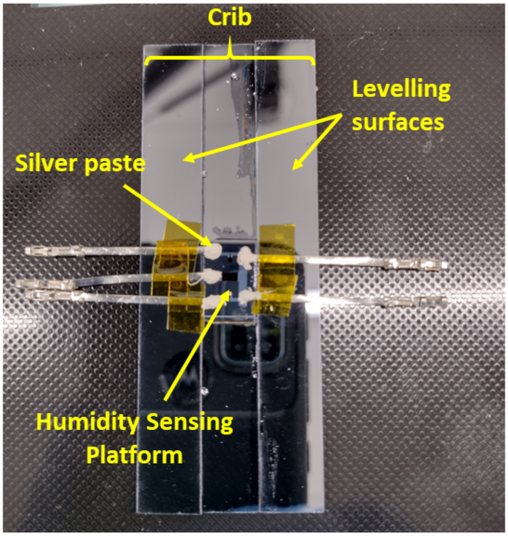

Fig. 4.10: A humidity sensing platform processed with the aid of the "crib".

a high degree of care, resulting in a long assembly time (~1-1.5 hour/sample) and a limited number of samples prepared. Various attempts were made to expedite the assembly and to compensate the fragility of the connections by fabricating supporting components. For instance, two pieces of wafer with the same thickness of the sample's substrate were glued to another entire wafer, leaving a gap wide enough to place the sample in it – a sort of "crib" for the samples, as shown in Fig. 4.10. This way, the tabs could be taped to a level surface, thus reducing any torque at the tab's tip and improving the adherence between the silver paste and the tab. Meanwhile, a "tab-holder" was designed and 3D-printed to correctly space out the tabs (see Fig. 4.11), all of which are subsequently secured at once with a long strip of heat resistant tape and properly attached to the contact pads.

Regarding the external connection of the various measurement equipment, the intention was to use simple crocodile clips; yet, the silver paste connections are too delicate to sustain the expected stress deriving from the handling and measurement of the samples without the planned lamination. In fact, the bare weight of the clips can be enough to detach the tabs from the contacts. Nonetheless, the aluminum tabs are of the right size (width: ~1.3 mm) for a different approach, namely the use of crimp-on connectors (see Fig. 4.11) that are compatible with jump wires. Furthermore, these connectors facilitate the electrical interconnection between the aluminum tabs and the measuring equipment, as the counter connector can be crimped on the wires of a low resistance ribbon cable; as a result, the operation range and cable slack can be increased according to the needs of the experiment. Another effort to reduce the mechanical stress sustained by the connection between tabs and contact pads in case of non-laminated samples is represented by two 3D-printed sample holders – one designed for static operation in a climate chamber, the other for strain tests. As shown by Fig. 4.12, these holders are based

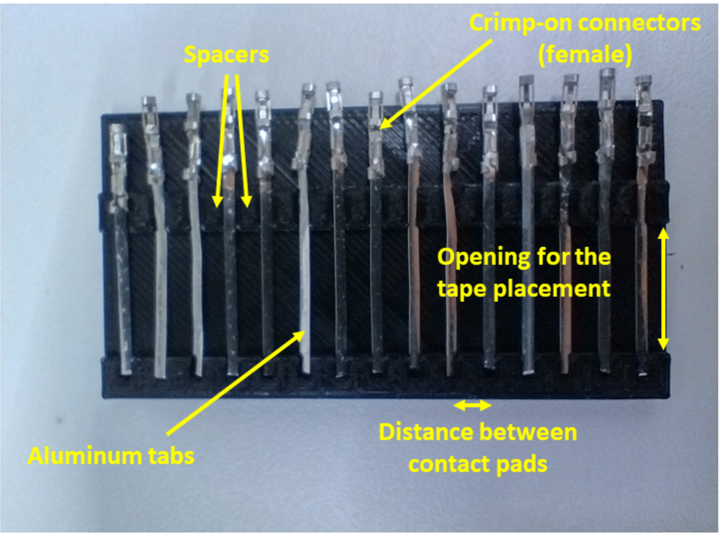

Fig. 4.11: Example of the second version of the 3D-printed tab-holder. As opposed to the original version, one side (top in the figure) is left open to accommodate different tab lengths and the subsequently added crimp-on female connectors.

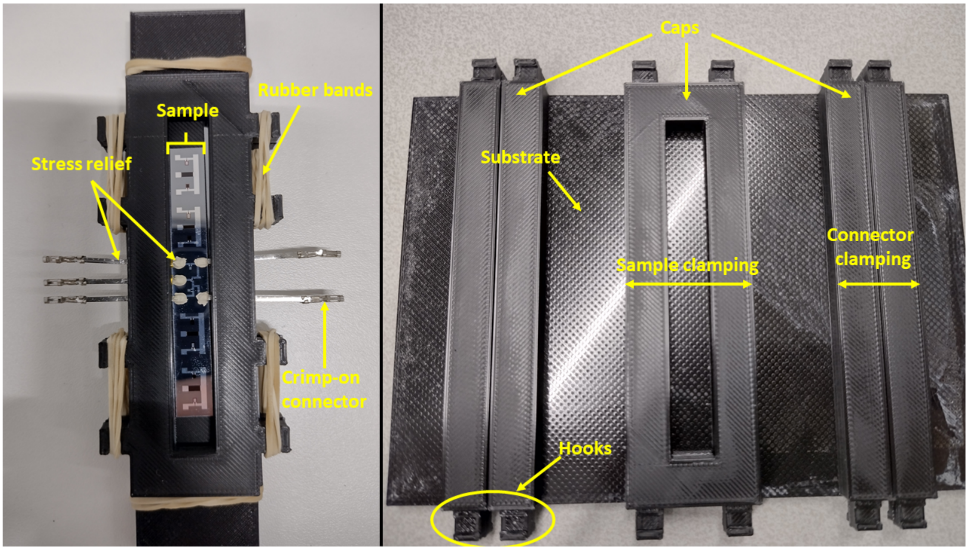

Fig. 4.12: 3D-printed sample holders. *Left*: loaded sample holder as conceived for the three-point bending test. *Right*: unloaded sample holder for static operation.

on the same core principles: the samples must be exposed and any pressure acting on the aluminum tabs must be applied at a certain distance from the contact pads. As a result, the tip of the aluminum tabs is more firmly secured without any pressure on the irregular surface of the cured silver paste, thus eliminating the risk of sample fracture due to the points of pressure (see Fig. 4.8). Furthermore, the clamping of the tabs acts as a stress relief, since the torque transmitted to the contact pads is limited; hence, the portion of the aluminum tabs which protrudes from the clamp can be handled with a lesser risk of damage to the connections. To achieve this, the sensor is centered onto a platform together with the aforementioned "crib" (see Fig. 4.10), and a cap with a centered hole is fixed on top through rubber-bands anchored to hooks at its edges. In the case of the platform for the three-point bending test, the design had to be adapted to stay within 3 cm width. In the other design, the platform is bigger and accommodates other caps to potentially anchor the crimp connectors as well, thus further decoupling the forces applied by the external connection.

4.2.3. LAMINATION

Following the wiring of the connections, the wafer samples needed to be sandwiched among typical solar module lamination materials in the following top-to-bottom order: glass, encapsulant, sample, encapsulant and backsheet. Unfortunately, the laminator broke before the completed devices – with the sensing platforms and interconnecting tabs – could be processed, thus only dummy samples were laminated during initial dry-runs of the process. In Table 4.2 the materials and thicknesses of each layer are reported for the samples which were laminated.

Table 4.2: Materials used during lamination.
EVA: Ethylene Vinyl Acetate, F-coated PET: fluoro-coated Polyethylene Terephthalate.

Component	Material	Thickness [μm]
Glass (Corning EAGLE XG)	Borosilicate glass	700
Encapsulant (3M EVA9110T)	EVA	500
Wafer stripe	Silicon	500
Encapsulant (3M EVA9110T)	EVA	500
Backsheet (ICOSOLAR PPF)	F-coated PET	310

Given the small non-standard size of the samples with respect to the usual solar cells, the materials must to be manually cut. To cut the glass into 2.9x10 cm^2 rectangular pieces, a groove is first scored onto the available 10x10 cm^2 glasses with a glass cutter; then the glass is broken along that line. The other components can be cut with scissors along previously drawn lines. This way, 11x4 cm^2 and 10.2x3.1 cm^2 rectangular foils are obtained for the encapsulant and the backsheet, respectively. Once the materials are stacked and hold in place with Kapton tape, the sandwiched samples are placed into the laminator. Table 4.3 summarizes the configurations set for the various lamination steps operated by the laminator. In particular, the first and last steps describe the pre- & post-processing, namely the heating up and cooling down of the machine. An example of a successful lamination result can be seen in Fig. 4.9, although in this specific case a 3 mm thick glass layer was used due to a lack of thinner glass. Finally, the excess material is removed from the edges.

Table 4.3: Lamination process configurations.

Step [#]	**Time** [s]	**Temperature** [$°C$]	**Vacuum up** [$mBar$]	**Vacuum down** [$mBar$]	**Vacuum Pins**
#1	-	80	1000	1000	up
#2	120	80	0	0	up
#3	480	145	0	0	up
#4	60	145	400	0	down
#5	600	145	400	0	down
#6	60	145	0	1000	down
#7	30	145	0	1000	up
#8	-	-	1000	1000	up

Various issues can arise during lamination, as a substantial level of manual work is involved. Typically, the most troublesome steps are the breaking of the glass and the correct handling of the pre-laminated layer stack. For instance, in the first case, if the surface of the glass is not sufficiently scored, then the glass might not break along the intended line; in the latter, the layers might slide on top of each other when not enough clamping pressure is applied during handling, resulting in a misalignment which cannot be corrected after lamination. Additionally, if the thermal tape is applied too loosely, then the wafer samples can slide during lamination while the polymeric encapsulant melts.

5

MEASUREMENT AND RESULTS

THE purpose of this Chapter is to describe how the testing and characterization of the sensors is performed and to show, analyze and discuss the results eventually achieved. First, Section 5.1 will outline the electrothermal characterization of the resistive temperature and piezoresistive strain sensors by means of the Cascade probe station. Then, the characterization of the humidity sensing platform will be analysed in Section 5.2 at various humidity and temperature conditions within a climate chamber. Finally, Section 5.3 will report on the characterization of the piezoresistive strain sensors through a three-point bending test. In each Section, the measurement equipment and setup will be detailed first, following which the results will be presented and discussed.

5.1. RESISTIVE AND PIEZORESISTIVE SENSORS

5.1.1. MEASUREMENT SETUP AND DEVICE CHARACTERIZATION

The thermal response of the RTDs and the piezoresistive strain sensors *prior* to lamination is investigated with the Cascade Summit probe station (CAS33), which allows to determine the current-voltage characteristics of the devices – and thus their resistance value – at different temperatures. The Cascade system consists in a 6-needles probe station where the processed wafers are placed onto a gold chuck and secured with vacuum. Additionally, a temperature controller is connected to the chuck, by the means of which it becomes possible to regulate the temperature of the chuck. Since only the end temperature is set and the needles are placed *after* such value is reached, only the static response of the sensors is studied with the Cascade probe station. To interrogate a sensor, the appropriate number of probes needles (e.g. four needles for four-point measurements) need to be placed onto the relative contact pads, while the settings (e.g. voltage or current bias range, number of sweep points) for each must be specified in the software. The advantage of the Cascade probe station consists in the option to perform automatic measurements, both within and across dies. To this end, however, the dies on the wafer and the contact pads within each die must be at fixed repeated intervals in both planar directions – although the distance can be different for each direction –, as the probes automatically move by pre-determined amounts. Consequently, this aspect must be taken into account during the design phase of the devices. Contrarily to the secondary pads, the primary connections do not change shape nor shift across dies of the same type (e.g. dies containing the humidity sensing platform), as detailed in Section 3.2.1; therefore, the needles can be placed on such structures. Furthermore, to benefit from the automation, the tool requires a file containing the complete instructions of the process, which must be coded as a system of macros containing both custom functions and tool-specific commands. Starting from the knowledge and templates provided by other users, the automatic process could be programmed, thus sensibly reducing the total time for the characterization of the sensors. Nonetheless, the complete measurement campaign is still time-consuming. In fact, the software must be rebooted and the probes *manually* reset to the initial position at any completed round of wafer measurements.

Given the simplicity of the sensors and the limited resistance added by the probe system, a two-point measurement is performed by applying an input voltage to the temperature and strain sensors, and measuring the occurring current flowing through the two needles. Here, the sensors are interrogated with a voltage sweep over four different chuck temperatures, ranging from 30 °C to 90 °C with 20 °C intervals. The eventually adopted parameters set for the voltage bias sweep used to characterize the thermal behavior of both the RTDs and the piezoresistive strain sensors are summarized in Table 5.1.

Table 5.1: Sweep parameters set for the two-point measurements.

Sensor	**Device**	**Voltage Range [V]**	**Number of Points**
Temperature	Aluminum resistor	[-5, +5]	401
Strain	poly-Si piezoresistor	[-20, +20]	401

5.1.2. RESULTS AND DISCUSSION

Four non-laminated wafers were characterized according to the process described in Section 5.1.1, for a total of 160 aluminum on-oxide RTDs, 64 aluminum on-silicon RTDs and 64 piezoresistors. Despite the automatic measurement, some outliers and unreliable measurements are present; these are likely the result of non-working devices and measurement errors (e.g. unexpected loss of contact of the probe needles). To draw conclusions on the working sensors that have been processed, pre-processing of the measurement results has been performed to remove the outliers and unreliable measurements. This step consists in the removal of all results that fall outside a certain range, which boundaries are shown in Table 5.2, as well as those that both show a clear deviation from overall trends and are not supported by literature. Since the sensors based on the aluminum resistors and poly-silicon piezoresistors would eventually be operated at an optimal (fixed) bias voltage, or current, *after calibration*, the analysis in this Section is narrowed down to a specific voltage value, as shown in Table 5.2. The full data processing is described in Appendix E, which the reader is referred to for further details. In the following discussion, all the results considered are referred to the values obtained *after* the data processing.

Table 5.2: Boundaries applied during the processing of the data resulting from the measurements of the temperature and strain sensors using the Cascade probe station.

Sensor	**Device**	**Resistance Limits** [Ω]	**Voltage** [V]
Temperature	Aluminum resistor	[0, 300]	-1.5
Strain	poly-Si piezoresistor	[0, 10^6]	+7.5

TEMPERATURE SENSOR

The results obtained from the characterization of the aluminum RTDs are shown in Fig. 5.1 and 5.2, for the resistors on insulator and on silicon respectively. Here, an overall strongly linear trend can be observed in the evaluated electrical resistance of the sensors over the range of temperatures tested, in line with the considerations expressed in Section 2.2.1. Based on the observed resistance at 30 $°C$ and 90 $°C$, the TCR of each resistor, which identifies its sensitivity in terms of normalized resistance (see Eq. 2.8), can be determined according to Eq. 2.1; the resulting TCR values are in the range of 3.6-3.9 $\cdot 10^{-3}$ $°C^{-1}$, which is similar to what is found in literature (see Table 3.2).

Since measurements were performed with the Cascade probe station only at steady-state conditions and the thermal insulation by the 300 nm silicon oxide layer is negligible at such conditions, it can be assumed that the on-oxide and on-silicon structures are at identical temperatures. In both cases, however, the measured resistance of the reference resistors, namely the resistors with a finger length of 440 μm (see Table 3.3), are larger than expected compared to the resistance value of 95 Ω estimated in Section 3.1.1. Considering Eq. 2.8 and the TCR of aluminum (see Table 3.2), the resistance of the reference resistor is expected to vary from 95 Ω to 98.7 Ω between 20 $°C$ and 30 $°C$, in contrast with the obtained average values of approximately 110 Ω and 122 Ω at 30 $°C$ for the RTD on silicon oxide and on the bare wafer, respectively. To achieve this, the initial resistance at 20 $°C$ of the on-oxide and on-silicon devices must be roughly equal to about 106 Ω and 117 Ω, thus 11.6 % and 23.2 % higher than the estimated value; furthermore, by evaluating the overall TCR of the aluminum resistors based on the difference in average resistance between 30 $°C$ and 90 $°C$ – namely 110 Ω & 135 Ω and 122 Ω & 150 Ω –, similar results are obtained. The achieved higher resistance is likely the result of a combination of factors, such as a too approximate evaluation of the reference resistance during the

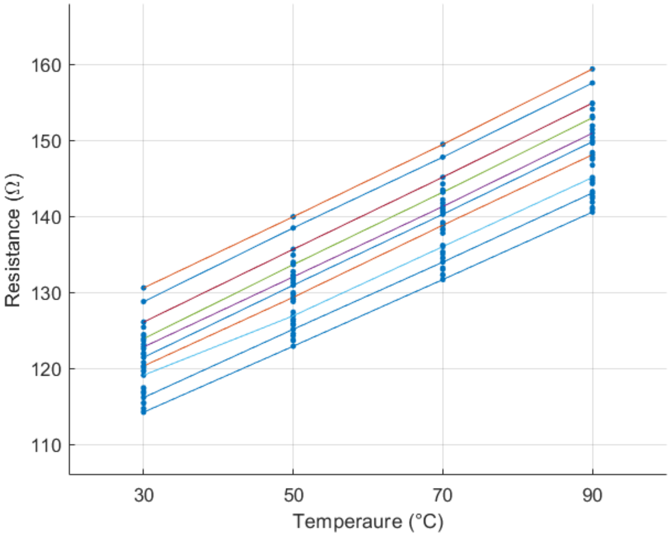

Fig. 5.1: Scatter plot of the results deriving from the thermal characterization of the on-silicon reference RTDs (see Fig. 3.8 and 3.9), which shows the change in resistance at increasing temperatures. Each point at each temperature represents the measured resistance at -1.5 *V* bias voltage of a sensor belonging to a specific die of specific wafer tested. A number of colored lines, each connecting the markers related to a specific RTD, are drawn to better visualize the response of the devices.

design phase (see Section 3.1.1), a size reduction due to over-development of the resist patterns, or over-etching of the aluminum. Furthermore, in view of the two-point measurement performed with the Cascade probe station, additional electrical resistance is introduced by the probes, in the order of few Ohms. However, this error is systematic and it causes a constant offset of the resistance reading when devices at the same temperature are compared.

Another interesting aspect to observe is the difference in resistance between the reference resistors on-oxide and those on-silicon, as the latter have an approximately 11 % higher average resistance at 30 °*C*. In view of the identical processing steps, the difference is likely due to an effect introduced by the silicon oxide underneath during etching (e.g. a local decrease in the etch rate of the aluminum). Unfortunately, these aspects could not be further studied as a second batch of devices could not be fabricated.

Based on the response of the aluminum RTDs shown in Fig. 5.1 and 5.2, it can be concluded that, although many working RTDs have been obtained, no clear reproducibility of the sensors is achieved. Indeed, the resulting electrical resistance of the on-silicon *reference* temperature sensors varies significantly in a range between 115 Ω and 135 Ω at 30 °*C* (± 6.6%). The cause of the lack in consistency across the numerous identical devices can be linked to the MEMS fabrication phase. Here, issues may have occurred that resulted in a sensible detrimental effect onto the operation of the device. For instance, during the processing of the fourth layer, the wafers were coated with the wrong

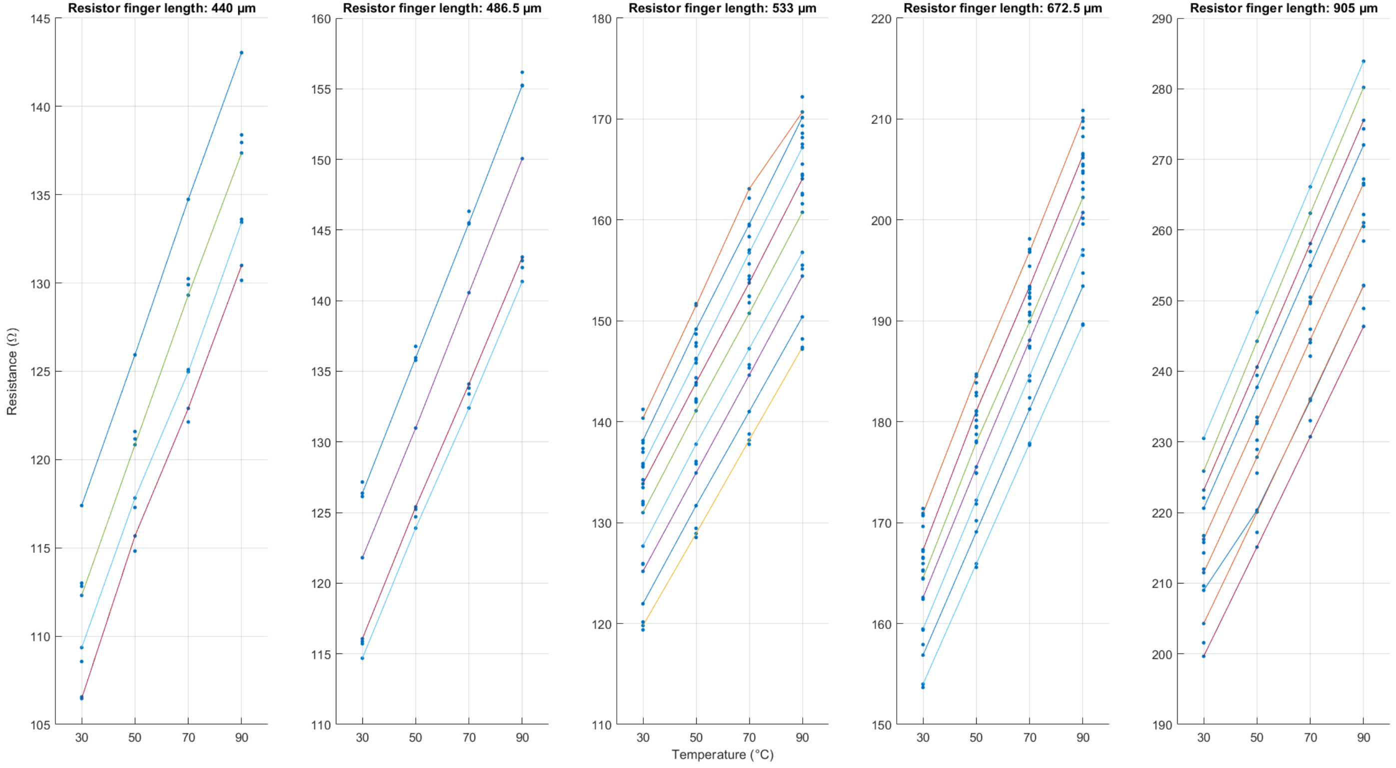

Fig. 5.2: Scatter plot of the results deriving from the thermal characterization of the on-oxide RTD variations divided based on the resistor finger length (see Fig. 3.8 and 3.9), showing the change in resistance at increasing temperatures. Each point at each temperature represents the measured resistance at -1.5 V bias voltage of a sensor belonging to a specific die of specific wafer tested. A number of colored lines, each connecting the markers related to a specific RTD, are drawn to better visualize the response of the devices.

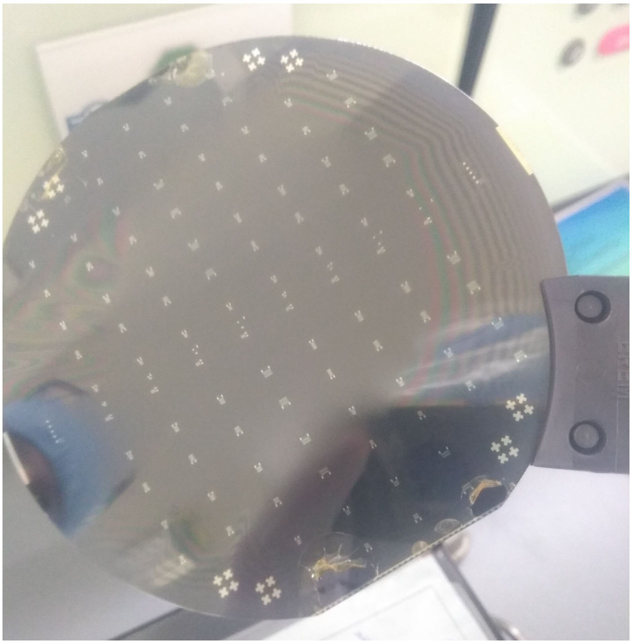

Fig. 5.3: Example of a wafer after the hardening and cracking of resist during plasma stripping. The resistors and piezoresistors are visible.

resist thickness, which had to be subsequently removed; to achieve this, plasma stripping of the resist was performed. However, during such step the resist was burned onto the wafers (see Fig. 5.3) and then more aggressive stripping steps were required to remove the polymer from the surface, which might have affected the structures present on the wafer. However, other less noticeable mistakes might have occurred, e.g. slightly prolonged etching times at the wet benches.

STRAIN SENSOR

Similarly to the case of the metal resistors, the resistance values and temperature responses of the poly-silicon strain sensors were assessed through automatic probing with the Cascade probe station. In this instance, however, the inconstant nature of the obtained measurements is more pronounced, and the results had to be processed as well to draw conclusions. More information on the data processing is reported in Appendix E, while Table 5.2 reports the parameters considered for such preprocessing step. The achieved results are plotted in Fig. 5.4, which illustrates how the resistance varies with temperature for each combination of piezoresistor width and aspect ratio. After processing of the results, an overall steadily decreasing trend of the electrical resistance can be observed, which reflects a negative TCR of the material. Based on the results shown in 5.4, the an average TCR of -3.7 $\cdot 10^{-3}$ $°C$ is estimated, which implies a 22.2 % drop in resistance between 30 $°C$ and 90 $°C$. This is in accordance with the experimental study by Lu *et al.*, where the effect of doping on the TCR of poly-silicon films is investigated

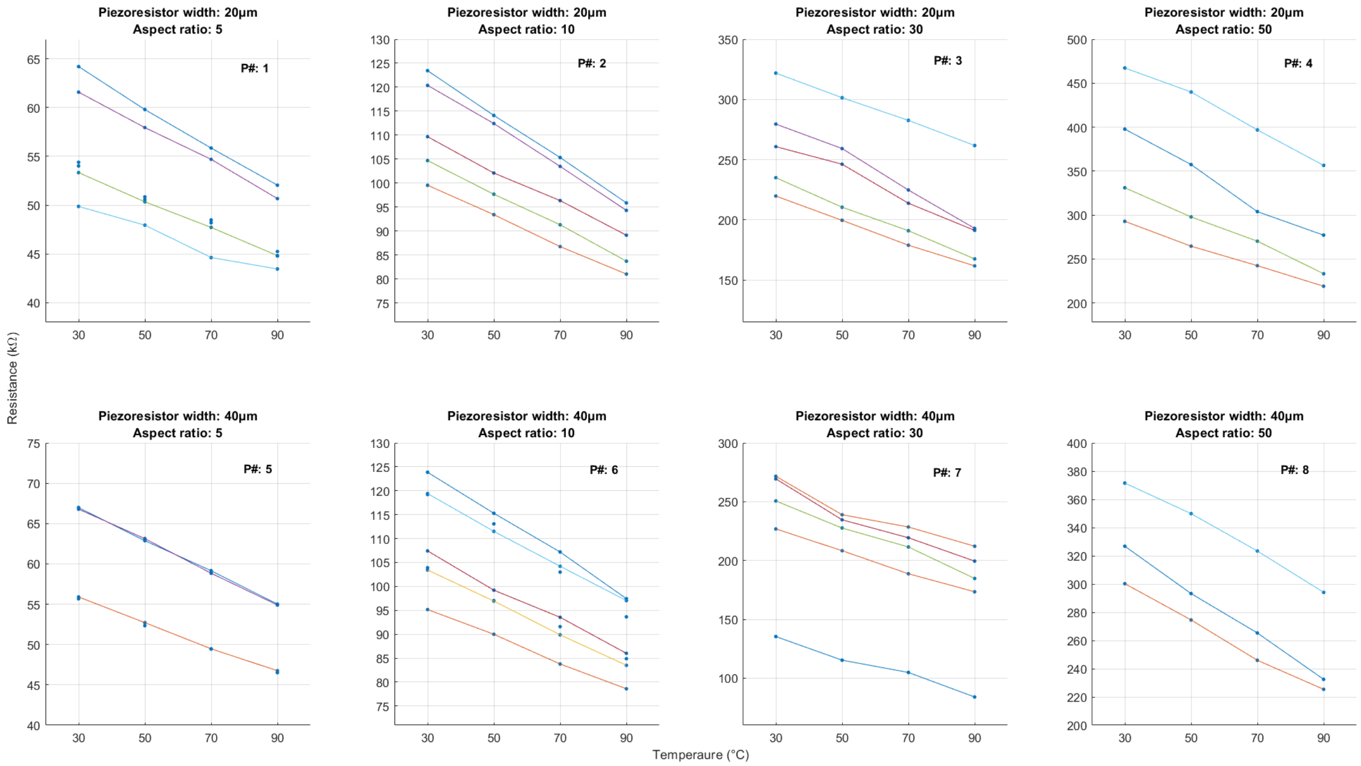

Fig. 5.4: Scatter plot of the results deriving from the thermal characterization of the strain sensor variations divided based on the width and aspect ratio (see Fig. 3.8 and 3.9), showing the change in resistance at increasing temperatures. Each point at each temperature represents the measured resistance at +7.5 V bias voltage of a sensor belonging to a specific die of specific wafer tested. A number of colored lines, each connecting the markers related to a specific sensor, are drawn to better visualize the response of the devices.

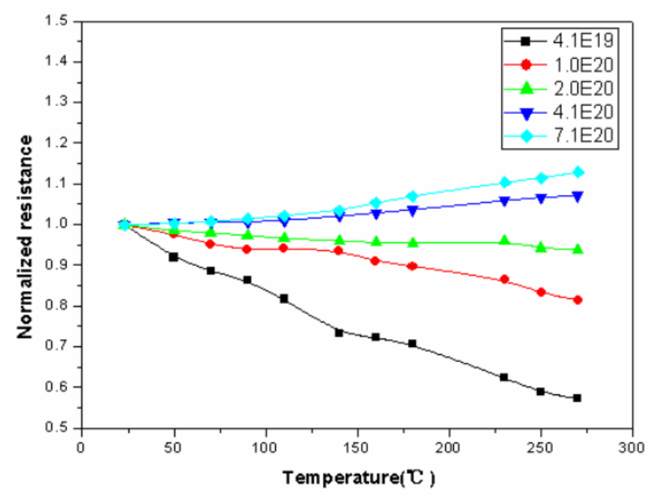

Fig. 5.5: Measured normalized resistance of a 80 nm thick poly-silicon film versus temperature at different doping concentrations (Boron), expressed in at/cm^{-3}. *Reprinted from [157].*

[157]: according to their results, the TCR of poly-silicon increases with the doping concentration and may range from negative (low doping) to positive (high doping) values, as shown in Fig. 5.5. Based on observations made in Section 4.1.3 regarding Boron implantation, the*expected* doping concentration of the piezoresistor fabricated in this thesis ($4.5 \cdot 10^{19}$ at/cm^3) is slightly higher than the minimum concentration tested by Lu *et al.* ($4.1 \cdot 10^{19}$ at/cm^3). Assuming that such concentration has been achieved during processing, an approximate 13% decrease in resistance between 30 °C and 90 °C can be estimated from Fig. 5.5; however, this is less than the 22.2 % average drop of the fabricated devices. Therefore, the real doping concentration achieved is likely less than $4.1 \cdot 10^{19}$ at/cm^3.

While a number of piezoresistors exemplified in Fig. 5.4 display a comparablly consistent drop, the thermal effect is generally not consistent across the devices; furthermore, identical piezoresistors have electrical resistances which vary significantly, even more than in case of the aforementioned aluminum RTDs. Consequently, no sensor reproducibility is attained in this case as well, most likely due to the same processing-related issues that affected the metal resistors. However, in this thesis the piezoresistive strain sensor is the most complex device under study in terms of fabrication, as it consists of three layers and is subject to ion implantation; hence, other scenarios cannot be excluded, especially due to the lack of knowledge regarding the real ion concentration achieved within the poly-silicon layer. Therefore, a further investigation involving targeted tests is required to investigate the quality of the sensor fabrication. Unfortunately, this were not possible as the implanter was out of order.

Overall, the graphs displayed in Fig. 5.4 show a substantial change as a result of temperature alone within the range under test, with variations in the order of tens of kilo-Ohms.

Therefore, the main conclusion which can be drawn is that to operate the piezoresistors for strain measuments, the thermal effect must be properly compensated for – and this can be achieved with the devised strain sensing platform (see Section 3.2.2).

5.2. HUMIDITY SENSING PLATFORM

5.2.1. MEASUREMENT SETUP AND DEVICE CHARACTERIZATION

The capacitive and thermoresistive humidity sensors are constitutive elements of the humidity sensing platform, as seen in Section 3.2.2. Furthermore, both types of devices are functionalized with the same polyimide with identical thicknesses. To test the humidity sensors, a climate chamber is required, as this equipment is capable of simultaneous temperature and humidity control. Eventually, the Angelantoni DY110C climate chamber of the Department of Micro-Electronics within the EEMCS faculty was operated.

Regarding the thermoresistive humidity sensor, a sourcemeter was not available when the climate chamber could be operated; therefore, the humistat could not be tested. Nonetheless, a complete procedure for the characterization of the humistat has been developed and is now described. The two heaters, one sensitive to moisture and the other operated as the reference, would be connected to a sourcemeter each. Both sourcemeters would then apply incremental DC currents within a maximum value of 0.2 A, which has been determined through the simulations described in Appendix C. Simultaneously, the output voltage of the the resistors with and without polyimide – the two heaters – would be recorded by a multimeter and compared: a discrepancy of the measured output difference of the two heaters between "dry" and "moist" conditions would imply that moisture has been absorbed by the polymer. Contrarily to the capacitive humidity sensor, this device cannot operate continuously, as the heat dissipated through the polyimide layer would cause moisture out-diffusion. Consequently, heating cycles that account for moisture re-absorption must be considered at every change in bias current, e.g. when shifting from 0.18 A to 0.2 A at constant ambient conditions; it also follows that the time required to characterize the thermoresistive humidity sensor is expected to be longer than the one of the capacitive sensor.

As opposed to the humistat, the interrogation of the capacitive humidity sensor only requires an LCR meter. Therefore, characterization of a capacitive humidity sensor has been possible, since the LCR meter (Hameg HM8118) was readily available.. Additionally, the RTD of the humidity sensing platform could also be simultaneously operated by the means of the Keithley 2000 multimeter. The climate chamber already includes a set of temperature and humidity sensors, with which it measures the ambient conditions of the chamber for its own control logic; however, these are placed at the back of the chamber, thus at a distance from the sample. To gather more information about the established local ambient conditions in direct proximity of the sample, additional reference temperature and humidity sensors were included. For this purpose, the commercially available Adafruit AM2315 dual sensor was deployed.

The complete measurement setup devised for the purpose of the combined character-

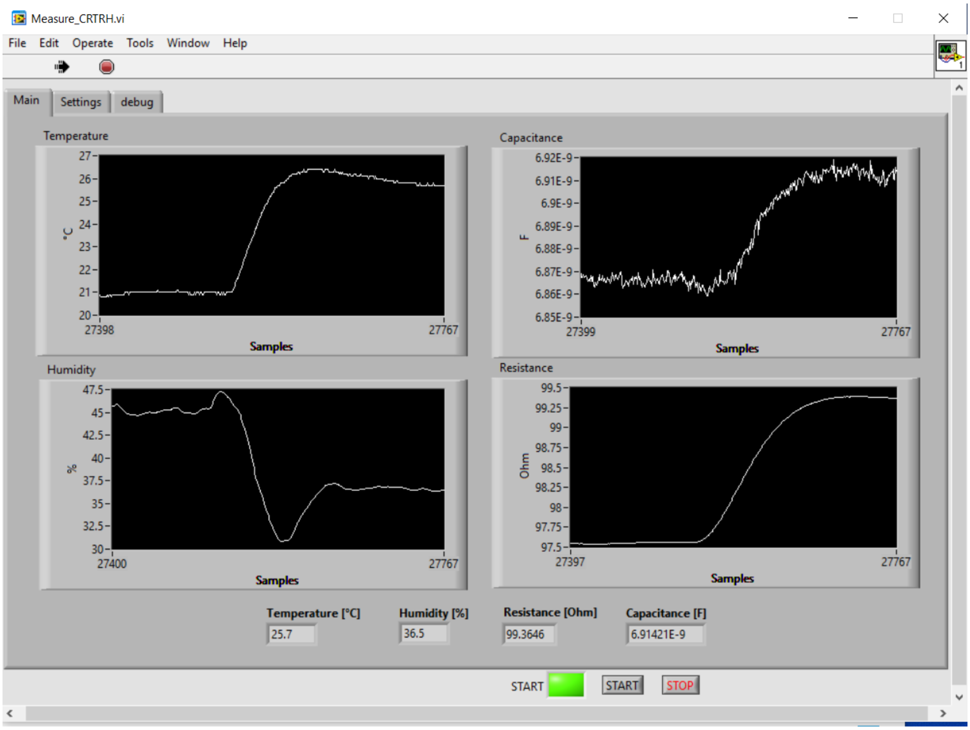

Temperature [°C] 25.7

Humidity [%] 36.5

Resistance [Ohm] 99.3646

Capacitance [F] 6.91421E-9

Fig. 5.6: LabView interface. The plots show the live data acquisition over a customizable interval of recorded samples. *Clockwise from the bottom left:* relative humidity, temperature, capacitance, and resistance as measured by the reference humidity & temperature sensors (Adafruit AM2315) and by the fabricated capacitive humidity sensor and aluminum RTD.

ization of the resistive temperature and capacitive humidity sensors is as follows. The non-laminated sample containing the humidity sensing platform, placed in its "crib" and clamped by the 3D-printed support (see Section 4.2.2), is placed within the climate chamber. Through jump wires and ribbon cables, the crocodile clips of the LCR meter and multimeter are connected to the protruding tabs without exerting any significant torque to the delicate connections. Meanwhile, the reference sensors are placed directly on top of the sample at a distance of about 1.5 cm, and are connected to an Arduino board (Arduino Uno). Finally, the entire measurement equipment is connected to a computer set up with the required drivers. Furthermore, a LabView-based application and interface were developed to centralize the control of the data acquisition of the four sensors, allowing to specify the settings of each measurement equipment, to log and synchronize the readings, and to visualize the results over an adjustable interval (max. 1000 sampled measurements, ~1.5 h) while these are recorded, as illustrated in Fig. 5.6. The resulting measurement setup is shown in Fig. 5.7, while Table 5.3 provides an overview of the settings applied for each tool, as well as the operation range and accuracy of the reference sensors.

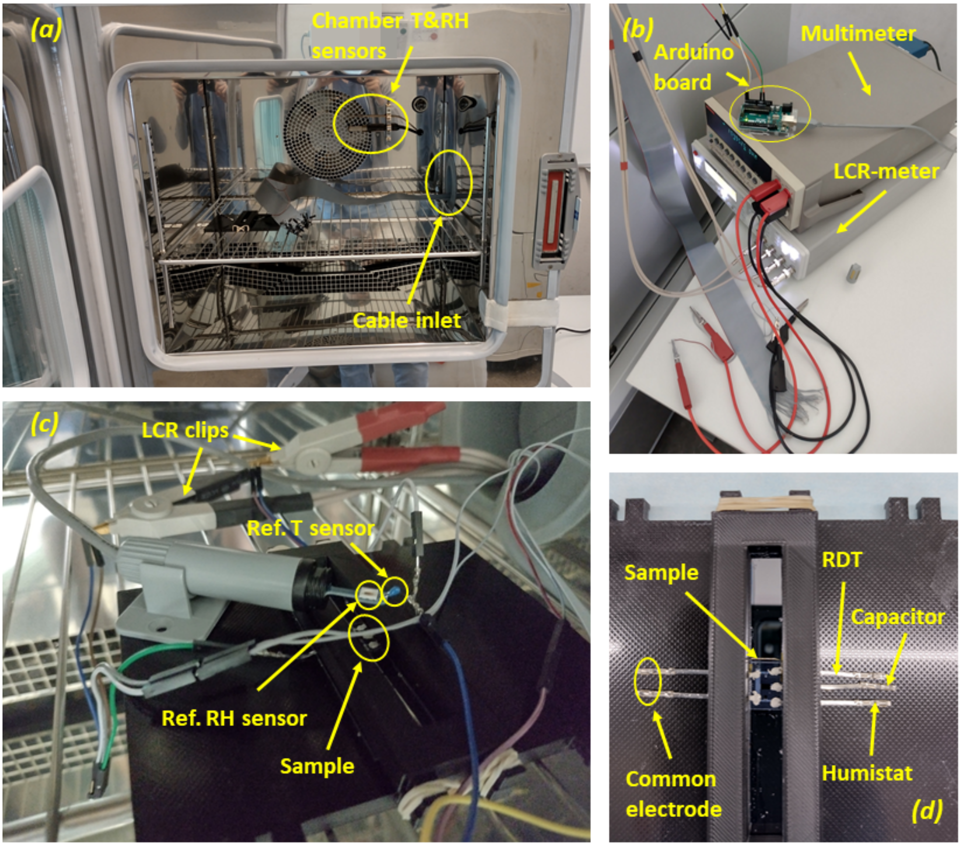

Fig. 5.7: Overview of the complete measurement setup. *(a)* Depiction of the interior of the climate chamber. *(b)* Detail of the external setup of the implemented measurement system. *(c)* Detail of internal setup. *(d)* Detail of the static sample holder, inclusive of the sample and the connections to the sensors.

Table 5.3: List of tools and reference sensors implemented in the measurement setup involving the climate chamber. The used settings of the equipment and the main details of the sensors are reported.

Equipment	**Name**	**Settings**
Multimeter	Keithley 2000	auto-range (4 wires)
LCR meter	HM8118	frequency: 1 kHz, amplitude: 1 V
Arduino board	Arduino Uno	–
Reference Sensor	**Name**	**Details**
Temperature sensor	AM2315	range: [-20 °C, +80 °C], accuracy: ±0.1 °C
Humidity sensor	AM2315	range: [0 %, 100 %], accuracy: ±2 %

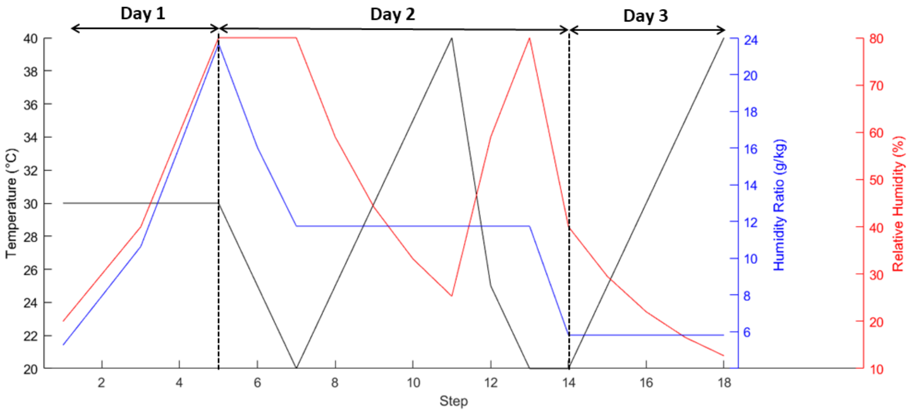

Fig. 5.8: Order of settings of the climate chamber. The humidity ratio of each step is determined based on a free interactive online calculator [158]. The vertical lines identify the settings of the climate chamber during its overnight operation.

The general procedure followed during the actual testing of the sensors is as follows. First, the climate chamber is set to the initial temperature and relative humidity values; since no prior knowledge regarding the response time of the sensors is available, the profile of the measured quantities, namely the capacitance of the capacitive humidity sensors and the resistance of the aluminum RTD, is observed on the LabView interface (see Fig. 5.6). Once the measured profiles that are visible in the LabView interface suggest that the devices operate in steady-state conditions, the settings of the climate chamber are *manually* varied and time is given to the sensors under analysis to reach the new steady-state. This process is then repeated until the end of the measurements, when the climate chamber is opened. The values of temperature and relative humidity set over the course of the measurements are reported in Fig. 5.8. In particular, steps 1-5 show a change in RH at constant temperature, while in steps 14-18 the humidity ratio, namely the mass ratio between water vapor and air, is maintained approximately constant. To determine the values of the humidity ratio at the set temperature and RH conditions, a psychrometric chart was utilized [158].

When the laminated devices are considered, the testing in the climate chamber should be performed twice for a better overview of the operation of the sensors: the first time with intact samples, the second with delaminated ones. With this approach, reference values for the capacitors and humistats would be obtained, which might differ from what is established during the pre-lamination tests. Indeed, the amount of moisture which might be trapped within the sample during lamination is not known beforehand. Regarding the subsequent delamination step, one possibility is to test the humidity sensors *after* the three-point bending test, as this step is likely to damage the sample and to create openings through which moisture can penetrate. However, this approach reduces the overall reproducibility of the measurements, as it is unknown beforehand whether the fractures introduced are sufficient for moisture penetration. Furthermore, the humidity sensors themselves – or their connections – could get damaged during the three-point bending test. Therefore, a repeatable procedure should be performed, such as perforating the encapsulant with a needle at certain locations.

5.2.2. RESULTS AND DISCUSSION

As opposed to the thermal characterization of the strain and temperature sensors achieved with the probe station, the devised measurement setup for the testing of the RTD and the capacitive humidity sensor allows for continuous data acquisition. Therefore, information regarding the transient response of these devices can be gathered. However, the increased complexity of the measurement setup does not allow the interrogation of multiple samples at once. Indeed, the equipment implemented has a limited number of input/output channels through which it can communicate with the sensors; meanwhile, the climate chamber should not be opened during operation to switch the sample under test. For this reason and owing to the fact that a single sample of the humidity sensing platform was readily available when the test in the climate chamber was performed – and no further sample could have been prepared and tested within the remaining time available for this thesis –, only one capacitor and the related RTD were characterized within the climate chamber using the procedure described before. The main results of this experiment are presented in Fig. 5.9 and 5.11.

Fig. 5.9 compares the results of the measurements performed at constant *set* temperature (30 °C) and varying relative humidity levels – namely steps 1 to 5 in Fig. 5.8 –, which implies a continuous rise in humidity ratio. Here, it can be observed that the response of the aluminum RTD is relatively stable over the course of the test with negligible oscillations ($\ll$1%) and that it follows the general trend registered by the reference temperature sensor (see Fig. 5.9, *bottom*). Meanwhile, regarding the fabricated capacitive humidity sensor, a clear surge in capacitance is observed, rising from the initial 6.86 nF to above 7.2 nF over the course of the test. These values are substantially larger than any capacitance values estimated using Eq. 2.37, which were in the order of tens of picofarad. The addtional capacitance at constant temperature may be a result of the fringing fields mentioned in Section 3.1.3: as the width of the capacitor's fingers is much larger than their thickness (15-10 µm to 1 µm), a wide top surface is in contact with the thick polyimide layer and the fringing electric fields may become predominant (see Fig. 5.10). Consequently, the device may operate as a *coplanar* capacitor capable of interacting with the *entire* polyimide layer, rather than only with the portion of polymer present between the comb-fingers. Furthermore, Fig. 5.9 shows that the largest surge in measured capacitance occurs when the *set* relative humidity of the climate chamber is increased from 60% to 80%, resulting in the highest capacitance increase (>100 pF) within an hour from the change of the climate chamber settings. This increase is much larger than that achieved when the settings are shifted from 40% to 60% (~60 pF), despite the change in both relative humidity and humidity ratio is approximately equal (see steps 3 to 5 in Fig. 5.8). Meanwhile, the shifts from 20% to 30% and from 30% to 40% yield similar changes in capacitance. This discrepancy may be the outcome of local effects occurring at humidity levels closer to the saturation point of water vapor in air, such as a local water condensation on the exposed polyimide layer. For instance, when the relative humidity is raised at constant temperature, the water vapor introduced through a nozzle above the

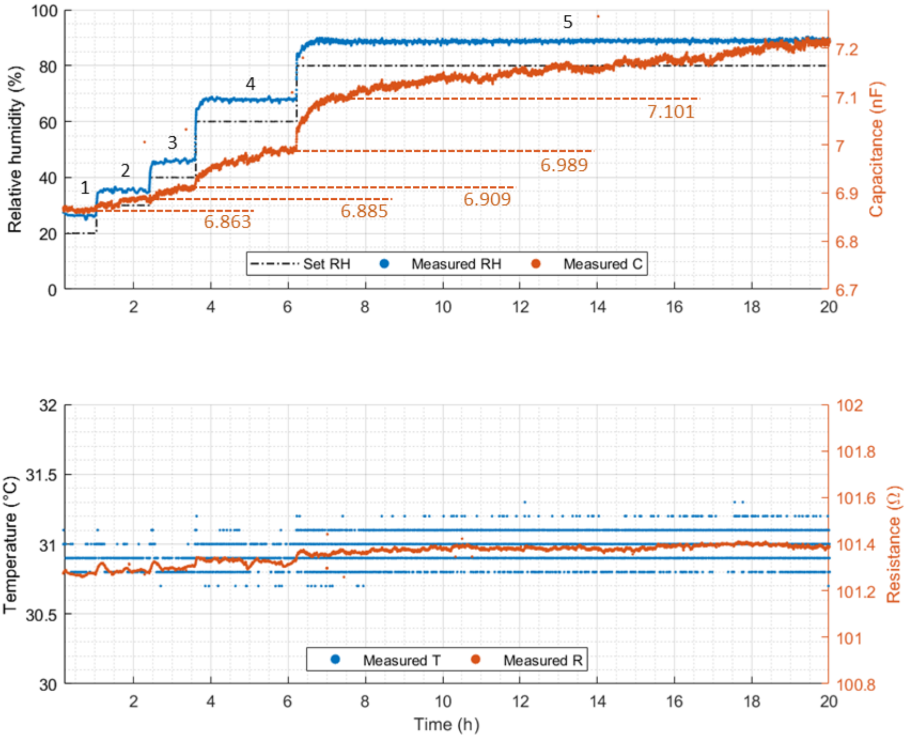

Fig. 5.9: Measurement results of the four sensors interrogated, namely the fabricated (capacitive) humidity and temperature sensors and their respective reference sensors, at varying relative humidity and constant temperature. *Top:* Overlay of the relative humidity measured by the reference sensor and the capacitance sensed by the fabricated humidity sensor. *Bottom:* Overlay of the temperature recorded by the reference sensor and the resistance of the aluminum RTD. The numbers in black within the top graph refer to the step numbering considered in Fig. 5.8, thus indicate the settings of the climate chamber. Meanwhile, the orange numbers show the values where the response of the fabricated humidity sensor appeared to have reached a steady-state during the in-person observation of the capacitance readings.

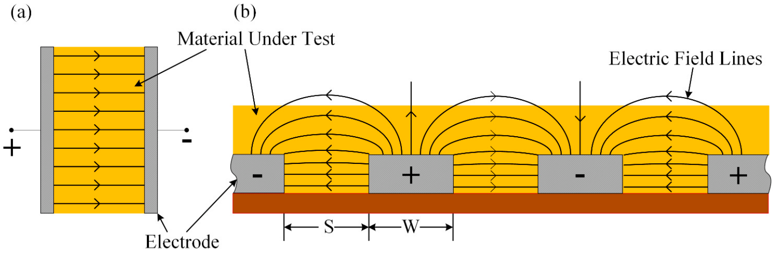

Fig. 5.10: Comparison between the electric fields of a parallel plate capacitor *(a)* and a coplanar interdigitated capacitor *(b)*. *S:* (finger) spacing, *W:* (finger) width. *Reprinted from [159].*

sample may deposit onto its surface; as the evaporation rate decreases with increasing relative humidity, the local condensation might linger longer and increase the moisture absorption rate of the polymer.

Another interesting aspect shown by Fig. 5.9 arises when looking at the overnight data acquisition which took place during step 5 (30 $°C$ & 80% set). Here, the collected measurements indicate that the actual response time of the capacitive humidity sensors is extremely long (>14 h), contrarily to what was assumed based on the *real-time* profile seen in the charts of the LabView interface (see Fig. 5.6). In particular, the overall profile recorded over the course of the prolonged transient has an unusual shape, consisting of an initial pronounced curvature followed by an almost linear increase. In fact, the curvature is so conspicuous that a capacitance spike of about 40 pF occurs within five minutes from the change in the psychrometric conditions within the climate chamber from step 4 to step 5. To achieve the same capacitance increase during the linear trend of the transient, more than three hours are required. This unexpected response of the capacitive humidity sensor may be linked anew to the effect of the fringing fields, further supporting the hypothesis that a coplanar capacitor was effectively achieved. Indeed, if the fringing fields allow the capacitor to detect moisture throughout the polyimide layer, then the initial almost-instantaneous moisture ingress in proximity of the surface is immediately detected; as the absorbed moisture saturates the outer portion of the moisture-sensitive material, only the slow moisture diffusion from the surface to the embedded fingers drives the rise in measured capacitance, resulting in the almost linear increase observed in Fig. 5.9.

The second figure, namely Fig. 5.11, shows the response of both the capacitive humidity sensor and the RTD to the increase in temperature at an approximately constant humidity ratio (~5.819 g/kg), while the relative humidity drops (see steps 14 to 18 in Fig. 5.8). Here, the four temperature steps can be clearly identified in both temperature and humidity sensors' response, resulting in variations of around 1.9 Ω and 50 pF, respectively, for each 5 $°C$ increase. When compared to the results obtained during the characterization at constant temperature and variable humidity, the shift in capacitance which occurs for a 5 $°C$ temperature rise is slightly larger than the shift that results when the set relative humidity is increased from 20% to 40% (approx. 43 pF). Therefore, the sensor is highly sensitive to thermal effects. However, from the available data, it cannot be deter-

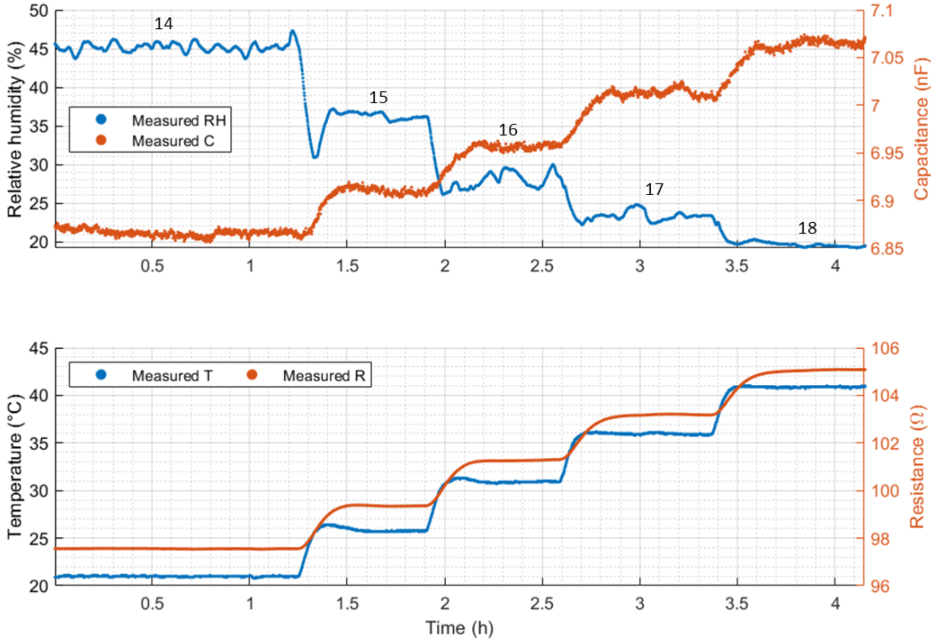

Fig. 5.11: Measurement results of the four sensors interrogated, namely the fabricated (capacitive) humidity and temperature sensors and their respective reference sensors. *Top:* Overlay of the relative humidity measured by the reference sensor and the capacitance sensed by the fabricated humidity sensor. *Bottom:* Overlay of the temperature recorded by the reference sensor and the resistance of the aluminum RTD. The numbers in black within the top graph refer to the step numbering considered in Fig. 5.8, thus indicate the settings of the climate chamber.

mined whether the device is more sensitive to temperature than to humidity, since no steady-state conditions were reached over the course of the measurements at different relative humidity levels. Such sensitivity to temperature is likely due to the simultaneous occurrence of three different effects. First, the geometry of the capacitor's fingers varies due to the thermal expansion of the metal, leading to thicker fingers with less spacing in between; therefore, the capacitance between fingers is increased in accordance with Eq. 2.37. Second, both the diffusion coefficient and the saturation concentration of moisture within the polymeric material increase with temperature, thus increasing the dielectric constant of the material [133]. Third, the dielectric constant of the polyimide may vary at different temperatures [160–162].

Another aspect which is revealed in Fig. 5.11 is represented by the slow and slightly delayed response of the devices to the set temperature steps. However, as opposed to the inherently slow moisture absorption withing the thick polyimide layer, the cause of such outcome lies in the measurement setup and not necessarily in the fabricated sensors: as shown in Fig. 5.7, the reference sensors are suspended and surrounded by air within the climate chamber, whereas the sensors under test are in contact with a considerable thermal mass, namely the 3D-printed support structure. Indeed, the climate chamber does not immediately reach the correct settings, yet it first overshoots the target value and then cools the system to the right temperature; while the reference temperature sensor is quick enough to detect such event – a slight temperature spike can be observed in the related graph (Fig. 5.11, *bottom*)–, the thermal mass of the 3D-printed support dampens any oscillation in the response of the fabricated temperature sensor as the system, which is composed of the support structure and the sensor's sample, slowly reaches the thermal equilibrium.

In view of the relatively regular response of the fabricated sensors observed in Fig. 5.11, a simple temperature compensation can be performed. Assuming that the plateaus represent steady-state conditions, the temperature, capacitance and resistance values of each plateau can be evaluated as the average between all the measurement points belonging to the plateau. First, the fabricated temperature sensor is calibrated with respect to its reference sensor through a linear regression of the average temperature and resistance values (average regression slope: 0.38 $\Omega/°C$); this results in the conversion of the measured resistance into the temperature profile of the sensor. The following stage consists in the actual compensation of the effect of temperature onto the capacitor. To achieve this, the device is calibrated with respect to the aluminum RTD of the humidity sensing platform, resulting in an average regression slope of 10 $pF/°C$. Finally, the simplified temperature compensation is achieved by subtracting the additional thermal capacitance from the capacitance measured at a temperature T ($C_{meas.,T}$), which is estimated through the regression slope (K_{slope}) and the temperature difference between the temperature measured by the RTD (T) and a reference temperature (T_0 = 20 $°C$), as shown in Eq. 5.1. The result of the simplified temperature compensation is outlined in Fig. 5.12, which also reports the difference between the average plateau values. Here, the thermal delay and dampening by the thermal mass can be better viewed as the measured and estimated temperatures are noticeably different only during the transient of each temperature step.

$$C_{corr.,T_0} = C_{meas.,T} - K_{slope} \cdot (T - T_0) \qquad \text{where} \qquad K_{slope} = \left(\frac{\Delta C_{meas.,step}}{\Delta T_{step}} \right)_{avg.} \tag{5.1}$$

A final aspect revealed by Fig. 5.9 and 5.11 is the significant difference between the values of the parameters set for the climate chamber and the quantities measured by the reference sensors. In fact, the reference humidity and temperature sensors determine a systematic upward shift of the values – approximately 4-10% and 0.5-1.3 $°C$, respectively – as stable operating conditions of the climate chamber, which is greater than the accuracy of the devices (see Table 5.3). As the quality of the calibration of the built-in sensors located in the chamber is unknown, it cannot be ascertained which set of sensors provides the most reliable reading of the psychrometric conditions; when this is known, the calibration of the fabricated sensors must be repeated if necessary, following a procedure to the one presented above. Nonetheless, the fabricated devices show a positive response to the quantities they aim to sense, which demonstrates their potential to operate as integrated sensors. Furthermore, the considerable noise introduced by thermal effects on the measured capacitance and the successfully applied temperature compensation, as outlined in Fig. 5.12, highlight the importance of the humidity sensing

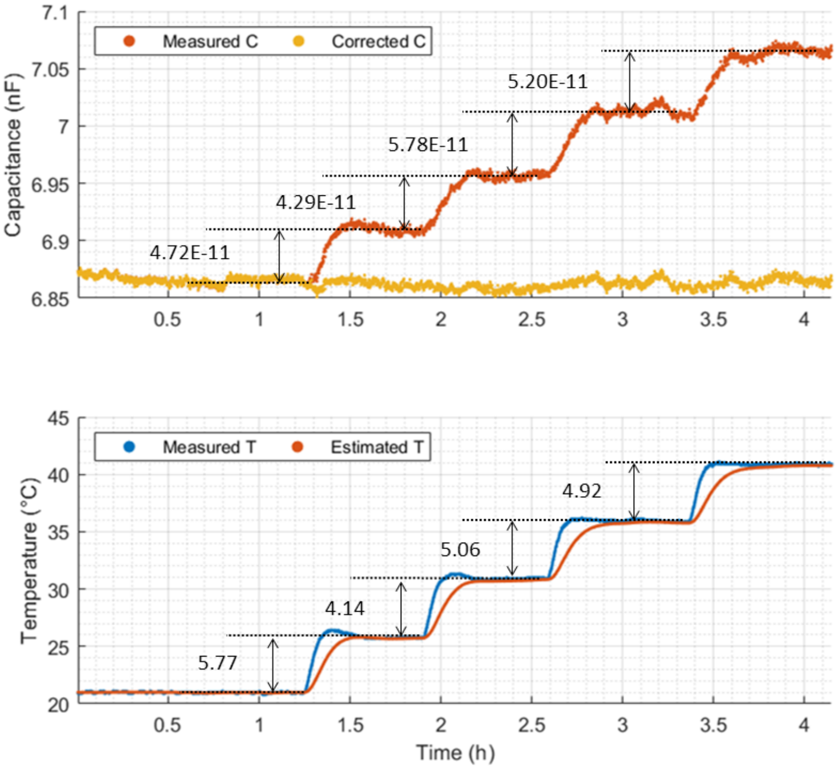

Fig. 5.12: Top: Thermal compensation for the capacitive humidity sensor. *Bottom:* The result of the calibration of the aluminum RTD.

platform, that combines both temperature and humidity sensors, in real applications.

5.3. STRAIN SENSING PLATFORM

5.3.1. MEASUREMENT SETUP AND DEVICE CHARACTERIZATION

The strain analysis of the piezoresistive devices is more difficult to undertake compared to thermal characterization previously outlined in Section 5.1.1, as the equipment available within the Faculty of Electrical Engineering, Mathematics and Computer Science (EEMCS) is unsuitable for the required strain test of the sensors; therefore, other faculties were contacted. Eventually, access to the Delft Aerospace Structures and Materials Laboratory (DASML) of the Faculty of Aerospace Engineering (AE) was granted. Here, a 3 kN load cell is readily available to perform three-point bending tests onto the samples. Furthermore, a smaller load cell is also at disposal, yet it requires customized components (e.g. the supports for the sample) which would be manufactured specifically for the purpose of this thesis. After initial tests with laminated strips of unprocessed wafers, it was determined that the 3 kN load cell is sufficient to test the strain sensors' proof-of-concept, as shown in the following Section 5.3.2.

The three-point bending test consists in a rig where the specimen is placed onto two supports at its extremities and a third component applies pressure to its center, as shown in Fig. 5.13. In this case, the system operates by imposing an incremental displacement of the central element, whilst measuring its reactive force. Generally, the deflection and force are then linked to the internal mechanical conditions, namely strain and stress. When a sample consists in an assembly of materials, relations between the parameters are more complex and require a detailed model. However, for the purpose of this thesis it is sufficient to verify that the devices are functional and have a clear, measurable and consistent response to the deformation of the sample.

As mentioned in Section 4.2.3, the lamination of the sensors could not be achieved, which halted this measurement step. In the devised test, the laminated strain sensors would be externally interrogated by a voltage (or current) signal in a two-point measurement with the same sampling frequency of the force measurement performed by the load cell. Hence, the results obtained by both samplings could then be compared

Fig. 5.13: Three-point bending test performed on bare (*left*) and laminated (*right*) wafer samples.

to extract initial information on the devices' response. To interrogate the piezoresistive strips, the same multimeter (Keithley 2000) operated for the resistance reading of the aluminum RTD during the tests in the climate chamber could be used (see Section 5.2.1), while the developed LabView software could be adapted to log the data concerning both the piezoresistor and the bending rig. Furthermore, additional multimeters could be connected to the RTDs of the strain sensing platform to record the ambient temperature surrounding the bending rig.

5.3.2. RESULTS AND DISCUSSION

As previously mentioned in Section 4.2.3, lamination could not be achieved as the laminator was inoperative, leaving the delicate tab-to-pad connections (see Section 4.2.2) susceptible to any torque applied to the aluminum tabs. Furthermore, only a single tab-connected non-laminated strain sensing platform was eventually obtained. Unfortunately, this sample broke during an initial test aimed at investigating whether the specifically designed sample holder (depicted in Fig. 4.12, *left*) would be able to transmit a central deflection to the contained sample; in this case, the sample was glued to to its "crib" (see Fig. 4.10). In view of the time constraints of this MSc thesis, no further sample containing the sensors could be processed. Fortunately, a number of samples made with wafer cut-outs – both laminated and bare – were prepared at the initial stage of this thesis following to the fabrication process described in Section 4.2.1 and 4.2.3. These dummy samples were then used to verify whether the available three-point bending rig could be potentially operated for the strain characterization of the piezoresistive strain sensors.

In total, seven laminated and ten non-laminated samples were examined, measuring 29x100 mm^2 and 9x65 mm^2 respectively. The results obtained with this preliminary test are illustrated in Fig. 5.14 for the bare (*left*) and laminated (*right*) samples. These plots show the force measured by the testing rig itself, while a deflection at the center of the sample is imposed. As can be noted, the measured force rises linearly with the increasing centre deflection until the *fracture point* of the samples; this point corresponds to the sudden drop visible in the graphs and indicates the moment when the sample stops exerting a reactive force in response to the imposed deflection. The profiles shown in Fig. 5.14 reflect the mechanical properties of a brittle materials, where little strain relief is provided as no permanent deformation of the material occurs before their fracture [163]. Fig. 5.14 also reveals that the maximum deformation the samples can sustain varies significantly, roughly ranging between 1 mm & 3.5 mm and 1.5 mm & 4 mm for the non-laminated and laminated samples, respectively. Consequently, when the risk reduction of a *destructive* test is a key priority, the samples must be subjected to a deflection lower that the minimum indicated in the graphs – approximately lower than 1 mm for the non-laminated samples and 1.2 mm for the laminated ones. Nonetheless, while the two types of samples display a similar minimum deflection, their length is different (non-laminated: 65 mm, laminated: 100 mm), as visible in Fig. 5.13. Consequently, distinct strain levels are sustained at the center of each sample type.

The results shown in Fig. 5.14 (*right*) do not represent the instant where the silicon wafer breaks, but rather when the whole assembled sample fails. This corresponds to

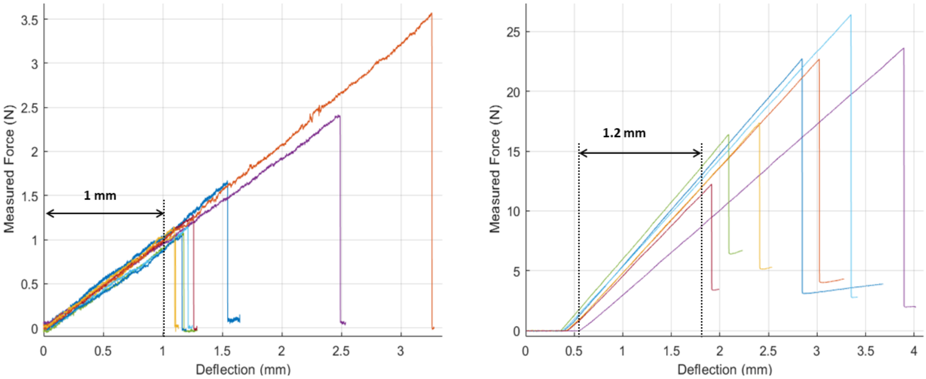

Fig. 5.14: Three-point bending test results of the bare (*left*) and laminated (*right*) dummy samples. Each color identifies a different dummy sample under test, while the sudden drop corresponds to the breaking of the sample.

the cracking of the glass, as this layer provides most of the rigidity. Contrarily to the case of the bare samples (see Fig. 5.14, *left*), a first range of deflection without any sensible force measurement can be observed here for the laminated components. This is due to the wider initial gap between the top component of the three-point bending rig and the sample, as it is observable in Fig. 5.13. Another difference between the two graphs depicted in Fig. 5.14 is represented by the different smoothness of the force-deflection profiles; however, this is a consequence of the fact that the forces measured in the case of the non-laminated samples are smaller (max: ~3.5 N) compared to the laminated one (max: ~25 N) and closer to the resolution of the load cell. Nonetheless, from the preliminary tests it follows that the 3 kN load cell can be operated for both laminated and non-laminated samples to investigate the operation of the piezoresistive strain sensors.

6

CONCLUSION AND FUTURE WORK

The work presented in this thesis represents the initial step in the direction of sensor integration in PV devices within the PVMD group. In this final Chapter, various aspects and future implications regarding the performed work will be addressed. In Section 6.1 the different steps undertaken during this thesis project will be outlined and the obtained results will be discussed. Then, Section 6.2 will draw recommendations for future efforts on the topic of sensor integration into PV devices.

6.1. CONCLUSION

The accurate assessment of parameters such as temperature, strain and humidity at cell-level plays an important role in the on-field operation of photovoltaic solutions, in terms of performance, reliability and lifetime. However, the literature regarding the integration of sensing devices directly onto solar cells is scarce; indeed, a single source regarding on-cell integration was identified over the course of a literature review undertaken prior to this thesis [56]. Here, a temperature sensor and a strain sensor are separately studied, which are based on a silver RTD and a doped strip of mono-crystalline silicon, respectively. Recently, other authors within the same research team have published a conference paper on the integration of both a capacitive moisture sensor and a resistive temperature sensor onto solar cells [164]. The devices presented in this paper are fabricated by means of a silver-paste-based screen-printing process, while the encapsulating EVA is used as the dielectric of the capacitor. The objective of the here presented thesis is aligned with the available literature, yet the proposed solutions are different. Among the interests of this thesis is the combined use of multiple types of sensors to form multi-functional sensing platforms capable of monitoring the status of the PV device. The type of sensors considered for such purpose reflect some of the main parameters of interest in the PV field – namely temperature, strain and humidity –, while four different sensing methods are investigated in total: resistive temperature sensing, piezoresistive strain sensing, capacitive humidity sensing and thermoresistive humidity sensing. To achieve that, the sensors, processes and measurement setups had to be devised.

The first concrete phase of the thesis consists in the design of the devices, as described in Chapter 3. Here, attention is simultaneously given to the single sensors, the complete sensing platforms, and the arrangement of the dies onto the silicon wafer to obtain a compromise among various aspects, such as ease of fabrication, cost of the materials, compatibility with the prospective measurement equipment and flexibility to future sensor variations. Both the designed temperature sensors and thermoresistive humidity sensors consist in aluminum meander-shaped resistors, yet the latter is embedded in a moisture-absorbing polyimide layer. Similarly, the capacitive humidity sensors, which are based on comb-finger capacitors, are functionalized to moisture sensing by means of the same polyimide layer. Meanwhile, the piezoresistive strain sensors consist of deposited poly-silicon strips which are Boron-doped to improve their gauge factor. The design choices are generally supported by the available literature, and occasionally based on the experience of researchers and technicians. Yet, the thermoresistive humidity sensor, also referred to as *humistat*, required an additional simulation step with COMSOL Multiphysics (outlined in Appendix C) to gather initial insights about its operation and its performance within a typical PV module. Eventually, the outcome of the COMSOL model revealed that an input DC current of 0.2 A would provide a resulting output voltage difference of 1.63 mV when polymer absorbs 1 % of its mass as moisture. Furthermore, the expected maximum temperature within the laminated cell is expected to be less than 75 $°C$ when the humistat is operated overnight. The planar architecture of the devices and the correspondent lithographic masks were designed with L-EDIT, a hierarchical physical layout editor with a lesser-known feature: the coding of the structures (see the code in Appendix B). This aspect of the software allows the parameterization of the geometries and their positioning, therefore facilitating the mask design process in case of numerous variations of the devices. Furthermore, the knowledge gathered on the topic was eventually shared within the PVMD group and has already been used for the design of lithographic masks in other projects related to the research field of Photovoltatronics.

During the fabrication phase, described in Chapter 4, the sensors were first processed in the EKL cleanroom – mainly cleanroom 100 – following a newly designed flowchart, which is reported in Appendix D. While the processing of the first three layers (300 nm SiO_2, 250 nm poly-Si and 350 nm Al), described in Section 4.1.2, 4.1.3 and 4.1.4, consists in a sequence of relatively standard steps, the fourth and fifth layer, namely the second aluminum film (1 μm) and the Durimide 7020 polyimide cover (~22 μm), involved a number of tests to determine the proper settings for their successful development. Eventually, it was determined that lift-off could be achieved using a coating thickness of 3.5 μm with an aluminum layer thickness of both 1 μm and 2 μm, in spite of the low aspect ratio (see Fig. 4.4). Regarding the adopted Durimide 7020 polyimide, such polymer is generally not used within the EKL processing, in particular at the thickness adopted for the purpose of this thesis. As a result of the initial processing tests, it was established that the duration of the baking step should be twice as long as the time suggested in the technical datasheet; moreover, when working with thick layers such as those adopted here, an additional drying step is necessary between the HTR-D2 development and RER600 rinsing, to avoid the development of the unusual slime shown in Fig. 4.6. Unfortunately, the processes could not be optimized and no second batch of sensors could be fabricated in view of the constraints set by the timeline of a MSc thesis and the equipment availability.

In order to test the different sensors and sensing platforms, the wafers fabricated in the cleanroom required additional manufacturing steps, as described in Section 4.2. First, the wafers needed to be cut into smaller samples complying with the requirements set by measurement setups; second, wires had to be connected to the sensing platforms; finally, the samples needed to be laminated as usually done with PV cells to create PV modules. The wiring of the sensors should have been achieved through wire-soldering, as initially planned. However, the ultrasonic soldering of aluminum wires to the aluminum contact pads of the sensors resulted more complex and harmful to the devices than expected, as shown in Fig 4.8. Eventually, an alternative solution was devised to form the connections, which consists in the use of the silver paste for PV screen-printing processes to attach aluminum tabs to the contact pads, as depicted in Fig. 4.10. The connections formed with this approach are delicate and can break during handling, yet they are able to sustain the lamination process (see Fig. 4.9) and become very durable once laminated. Unfortunately, the only laminator at disposal for PV module manufacturing broke. To compensate the lack of mechanical strength of the connections formed with the alternative process, sample holders were designed and 3D-printed: as illustrated in Fig. 4.12, these holders consist in a clamping system that reduces the torque transmitted to the tab-pad connections during handling.

The final stage of this thesis is the testing of the sensors and the analysis of the achieved results, as presented in Chapter 5. Since the development of sensors has not been a research subject within the PVMD group until recently, measurement setups and characterization methods had to be conceived based on the equipment available, which often required the support of other departments and faculties. Eventually, the Cascade probe station and the climate chamber owned by the Department of Microelectronics within the EEMCS faculty were identified as solutions to characterize the temperature-dependence of the non-laminated temperature and strain sensors and to test both laminated humidity sensors, respectively. Meanwhile, a three-point bending rig with a 3 kN load cell present in the DASML of the AE faculty was determined an initial option to investigate whether the strain sensors can be effectively interrogated – and to characterize them. Ultimately, only the characterization with the Cascade probe station could be performed as planned, as the lack of laminated samples and the time constraints of this thesis limited the characterization by means of the other measurement setups. Fortunately, the operation of a single non-laminated sample containing a functioning temperature sensor and capacitive humidity sensor could be analysed by the means of the climate chamber.

The raw data obtained from two-point IV measurements performed by the Cascade probe station on the aluminum resistors (temperature sensors) and poly-silicon piezoresistors (strain sensors) contains numerous failed measurements and outliers, which were removed according to the process described in Appendix E. The processed results of the on-silicon reference resistors, the on-oxide resistors and the piezoresistors are depicted in Fig. 5.1, 5.2 and 5.4, respectively. As shown in such figures, the response to the changes in temperatures of identical devices across dies and wafers is similar, e.g. the resistance increase with temperature is linear and with a similar slope for all working reference resistors. As expected for a metal resistor (see Eq. 2.8), the achieved slope in terms of normalized resistance is similar to the TCR of aluminum found in literature ($3.9 \cdot 10^{-3}\ °C^{-1}$). However, the actual resistance values of the same devices vary significantly at constant temperature, with differences above 6% for the aluminum resistors and more than 30 % for certain polysilicon piezoresistors. These results imply that no reproducibility is attained for this first batch of sensors, the likely cause of which are errors and accidents which occurred during the fabrication phase, as well as inherent processing differences that result from the spacial distribution of the dies across the wafers. For instance, during wet etching steps the first dies to enter the etching bath are also the last to exit, which slightly increases their etching time. Nonetheless, the data demonstrate that the fabricated aluminum resistors can be operated as temperature sensors, while the piezoresistors show a substantial sensitivity to temperature as well, with an average resistance drop of 22.2 % between 30 $°C$ and 90 $°C$. Furthermore, this latter result supports the need for a sensing platform containing both temperature and strain sensing devices, as devised in this thesis, in order to compensate for the effects of temperature on the operation of the strain sensors.

Regarding the characterization of the fabricated resistive temperature sensors and capacitive humidity sensors, this is achieved with a measurement setup that consists in a climate chamber, an LCR meter, a multimeter and two reference sensors (temperature & relative humidity), as depicted in Fig. 5.7; meanwhile, Fig. 5.6 shows the interface of a LabView application that was developed to centrally control the data acquisition. Here, the LCR meter is used to interrogate the capacitive devices, while the multimeter measures the resistance of the resistive sensors. Unfortunately, a single sample containing these devices was available when their characterization could be achieved. The results obtained by varying the humidity at constant temperature are illustrated in Fig. 5.9, while Fig. 5.11 shows the data recorded at constant humidity ratio and varying temperatures. With respect to the fabricated capacitive humidity sensor, the achieved capacitance values are much larger than expected – nF rather than pF –, and a sharp initial surge followed by a linear transient with a moderate slope occurs at every change in humidity, in spite of a response time of the sensor longer than 14 hours. This suggests that a coplanar capacitor might have been fabricated in reality, which would allow the sensor to be sensitive to moisture absorption within the entire volume of the covering moisture-sensitive polymer, rather than only between the thin comb-fingers. Therefore, the moisture ingress at the surface of the polymer might be immediately detected, while the further moisture diffusion would slowly increase the capacitance. Overall, the observed change in capacitance at 30 °C is significant as the relative humidity incrementally rises from 20% to 80%, resulting in an increase of 340 pF (5 %) over the course of the measurements. However, the capacitive humidity sensor displays a great sensitivity to temperature variations as well. Indeed, the measured capacitance increases by about 200 pF (3 %) at a constant humidity ratio of 5.819 g/kg. As the shift in the capacitance value due to the applied 5 °C temperature steps is approximately constant (~10 $pF/°C$), a successful simplified temperature compensation is performed based on the readings of the fabricate temperature sensor, as shown in Fig. 5.11. A comprehensive and accurate characterization of the sensor is necessary to define a correct and complete compensation procedure. However, the obtained results and the developed temperature compensation technique represent a further argument in support for the development of an integrated humidity sensing platform.

To conclude, this thesis reports the full development of four different sensors, from their conception and design, through their fabrication and ultimately to their testing. Regardless of the unforeseeable circumstances (e.g. unavailable equipment) and the limited amount of samples which could be characterized, this work provides tools, experience and insights on the various development steps in the hopes that it will support future work concerning sensor integration in PV devices within the PVMD group.

6.2. FUTURE WORK

Future work should address the process optimization first, to ensure a greater consistency of the fabricated devices across wafers. An improvement example might be the removal of the aluminum oxide layer, which quickly forms after the first aluminum deposition (see Section 4.1.4) and acts as an electrical insulator, by means of an additional Marangoni cleaning step prior to the deposition of the second aluminum layer, which constitutes the primary connections (see Section 3.2.1 and 4.1.5); as a result, a better contact between the two metal layers would be achieved. The optimization should also entail a detailed study of the material properties of the deposited layers; in particular, the achieved profile of the doping concentration in the poly-silicon stripe should be analyzed, e.g. by means of Secondary Ion Mass Spectrometry (SIMS). Meanwhile, the here presented sensors should be finally laminated and characterized to investigate their response in PV module-like conditions, as planned at the beginning of this project. In fact, in case the unusual response of the capacitor under test in the climate chamber described in Section 5.2.2 is related to an interaction with the setup (i.e. a capacitance added by the sample holder shown in Fig. 4.12 or by a local moisture condensation), laminating the device would ensure a more protected environment – as well as a test scenario closer to real conditions. Apart from these obvious improvements, the following ideas could be tested:

- The humidity sensing platform containing the capacitive and resistive humidity sensors, as well as the resistive temperature sensor, could be integrated into a single device by connecting another contact pad at one of the electrodes of the capacitor, opposite to the already existing pad.

- The capacitors could be screen-printed as in the work by [164]; in this case, however, further tests would be required to develop a reliable process to add a moisture-sensitive material.
- Regarding the capacitor, other moisture-sensitive dielectrics could be tested, as well as other thicknesses. In fact, a thinner layer could sensibly reduce the total response time of the sensor as moisture would have to diffuse through less material to reach the fingers of the capacitor.
- The effect of moisture on the electrical conductivity of the Durimide 7020 polyimide could be studied to investigate whether such material could be implemented to fabricate a resistive humidity sensor.
- To improve the solderability of the thick aluminum layer, a thin top layer of silver can be added during the metal evaporation. This would simplify the wiring step of the samples.
- Previous to the three-point bending test and after lamination, the resistance of the piezoresistors could be measured again – although not with the Cascade probe station – to investigate whether the sensors are sensitive enough to detect any residual strain after lamination.

Since the scientific research on sensors is a thriving field, this work could be adapted in the future to new improved designs – or even different types of sensors.

A

SILICON-BASED SENSORS REVIEW: TABLE OF CONTENT

In this first Appendix, a glimpse into the report of the state-of-the-art on silicon-based sensors is offered. Such work is the result of a three-month long autonomous project undertaken previous to the start of the activities related to the here presented dissertation.

In the following pages, the Table of Contents of the report is first disclosed to the interested reader. As it can be noted in the Table of Contents, the sensors deemed appealing are grouped based upon their sensing purpose affinity into so-called *sensing groups*, and an acronym is given to each group - for instance, *BC*, *FF* and *LI* stand for *Biochemical/Chemical*, *Fluid Flow* and *Light Intensity*, respectively. As an exception to the rule, certain types of sensors do not fit properly into any of the sensing groups, and thus are gathered under the umbrella-group *Other Sensors*.

CONTENTS

1 Introduction 1

2 AFT Sensing Group 5
2.1 Acceleration sensors (accelerometers) 5
2.1.1 Capacitive accelerometers 6
2.1.2 Piezoresistive accelerometers 7
2.1.3 Optical accelerometers. 8
2.2 Force sensor (piezoresistive) 11
2.3 Torque sensor (piezoresistive). 12

3 BC Sensing Group 15
3.1 Biological sample sensors (optical) 16
3.2 Flame sensor (optical) 22
3.3 Gas sensors 23
3.3.1 CO_2 sensors (optical) 23
3.3.2 H_2 sensors (optical) 26
3.3.3 NH_3 sensors (optical) 27
3.4 Ion concentration sensor 28
3.4.1 F^- ion concentration sensors (ISFET) 28
3.4.2 H^+ ion concentration sensors (ISFET) 29
3.5 Solvent sensors (optical) 32

4 EMF Sensing Group 37
4.1 Electric Field sensor (optical) 38
4.2 Electromagnetic Field sensors (optical) 40
4.3 Magnetic Field sensors 44

5 FF Sensing Group 47

6 H Sensing Group 55
6.1 Capacitive humidity sensors 56
6.2 Thermal humidity sensors 57
6.3 Optical humidity sensors 60

7 LI Sensing Group 69

8 P Sensing Group 75
8.1 Capacitive pressure sensors. 75
8.2 Piezoresistive pressure sensors 78
8.3 Resonant pressure sensors 82
8.4 Optical pressure sensors 84

9 SS Sensing Group **89**
9.1 Optical strain sensors 90
9.2 Resonant strain sensors 92
9.3 Piezoresistive stress sensors 94

10 T Sensing Group **97**
10.1 Optical temperature sensors 97
10.2 Photoelectric temperature sensors 105
10.3 Thermoresistive temperature sensors 106

11 Other Sensors **113**
11.1 Aerosol sensor 114
11.2 Current sensor 115
11.3 Reaction heat sensors (calorimeters) 119

12 Conclusion **123**
12.1 Discussion 125
12.2 Concluding remarks 127

References **129**

B

MASK DESIGNS

B.1. HUMIDITY SENSING PLATFORM: T-CELL CODE

Table B.1: L-EDIT T-Cell parameters and variables of the humidity sensing platform. *Lengths are expressed in nanometers.*

PARAMETERS		
Name	**Type**	**Default Value**
Connection_width	Double	500000
Pad_length	Double	1300000
Pad_height	Double	1300000
x_side	Double	6000000
y_side	Double	10100000
freespace	Double	100000
Connection_distance	Double	140000
Finger_length	Double	2800000
Resistor_width	Double	10000
Resistor_interconnection_length	Double	100000
Resistor_lead	Double	150000
Element_number	Integer	28
junction_width_small	Double	200000
junction_length_small	Double	300000
Overflow_small	Double	50000
Overflow	Double	100000
Polyimide_overflow_Capacitor	Double	50000
Insulation_overflow	Double	200000
VARIABLES		
Finger_number	Integer	
Finger_distance	Double	
Finger_width	Double	
Resistor_side_length	Double	
Resistor_interdistance	Double	
Polyimide_overflow_Resistor	Double	

```
/*******************************************************************************
 * Cell Name: Cell1
 * Creator  : L-Edit Tcell Builder
 *
 *******************************************************************************/

#include <cstdlib>
#include <cmath>
#include <cstring>
#include <cstdio>
#include <string>
```

```
#define EXCLUDE_LEDIT_LEGACY_UPI
#include <ldata.h>


/* Begin -- Uncomment this block if you are using L-Comp. */
//#include <lcomp.h>
/* End */

/* TODO: Put local functions here. */
void Cell1_main(void)
{
  int iTmpUpiReturnCode = LUpi_GetReturnCode();
  /* Begin DO NOT EDIT SECTION generated by L-Edit */
  LCell     cellCurrent     = (LCell)LMacro_GetNewTCell();
  double    Connection_width = LCell_GetParameterAsDouble(cellCurrent,
                "Connection_width");
  double    Pad_length = LCell_GetParameterAsDouble(cellCurrent, "Pad_length");
  double    Pad_height = LCell_GetParameterAsDouble(cellCurrent, "Pad_height");
  double    x_side = LCell_GetParameterAsDouble(cellCurrent, "x_side");
  double    y_side = LCell_GetParameterAsDouble(cellCurrent, "y_side");
  double    freespace = LCell_GetParameterAsDouble(cellCurrent, "freespace");
  double    Connection_distance = LCell_GetParameterAsDouble(cellCurrent,
                        "Connection_distance");
  int       Finger_number = LCell_GetParameterAsInt(cellCurrent, "Finger_number");
  double    Finger_width = LCell_GetParameterAsDouble(cellCurrent, "Finger_width");
  double    Finger_distance = LCell_GetParameterAsDouble(cellCurrent,
                "Finger_distance");
  double    Finger_length = LCell_GetParameterAsDouble(cellCurrent, "Finger_length");
  double    Resistor_side_length = LCell_GetParameterAsDouble(cellCurrent,
                        "Resistor_side_length");
  double    Resistor_width = LCell_GetParameterAsDouble(cellCurrent,
                "Resistor_width");
  double    Resistor_interconnection_length = LCell_GetParameterAsDouble(cellCurrent,
                        "Resistor_interconnection_length");
  double    Resistor_lead = LCell_GetParameterAsDouble(cellCurrent, "Resistor_lead");
  int       Element_number = LCell_GetParameterAsInt(cellCurrent, "Element_number");
  double    Resistor_interdistance = LCell_GetParameterAsDouble(cellCurrent,
                        "Resistor_interdistance");
  double    junction_width_small = LCell_GetParameterAsDouble(cellCurrent,
                        "junction_width_small");
  double    junction_length_small = LCell_GetParameterAsDouble(cellCurrent,
                        "junction_length_small");
  double    Overflow_small = LCell_GetParameterAsDouble(cellCurrent,
                "Overflow_small");
  double    Overflow = LCell_GetParameterAsDouble(cellCurrent, "Overflow");
  double    Polyimide_overflow_Resistor = LCell_GetParameterAsDouble(cellCurrent,
                "Polyimide_overflow_Resistor");
  double    Polyimide_overflow_Capacitor = LCell_GetParameterAsDouble(cellCurrent,
                "Polyimide_overflow_Capacitor");
  double    Insulation_overflow = LCell_GetParameterAsDouble(cellCurrent,
                        "Insulation_overflow");
  /* End DO NOT EDIT SECTION generated by L-Edit */

    if(LUpi_GetReturnCode())
    {
        LDialog_MsgBox("Error:␣Tcell␣failed␣to␣read␣parameters.");
        return;
```

```
}
LUpi_SetReturnCode(iTmpUpiReturnCode);


/* Begin -- Uncomment this block if you are using L-Comp. */
//LC_InitializeStateFromCell(cellCurrent);
/* End */
LFile pFile = LCell_GetFile( cellCurrent );

/* Clear out existing ports */
LPort pPort, pPort_next;
for ( pPort = LPort_GetList( cellCurrent ); pPort; pPort = pPort_next )
{
    pPort_next = LPort_GetNext( pPort );
    LPort_Delete( cellCurrent, pPort );
}
/* Clear out existing elements */
LLayer pLayer;
for ( pLayer = LLayer_GetList( pFile ); pLayer; pLayer =
                1LLayer_GetNext( pLayer ) )
{
    LObject pObj;
    LObject pObj_next;
    for ( pObj  = LObject_GetList( cellCurrent, pLayer ); pObj; pObj = pObj_next)
    {
            pObj_next = LObject_GetNext( pObj );
            LObject_Delete( cellCurrent, pObj );
    }
}
/* Clear out existing instances */
LInstance pInst;
LInstance pInst_next;
for ( pInst = LInstance_GetList( cellCurrent ); pInst; pInst = pInst_next )
{
    pInst_next = LInstance_GetNext( pInst );
    LInstance_Delete( cellCurrent, pInst );
}

/* TODO: Put local variables here. */

/* TODO: Begin custom generator code.*/
double x_start = Connection_distance/2;
double y_start = - y_side/2 + freespace + Pad_height - Connection_width;
double x_end = x_side/2 - freespace - Pad_length + Overflow;
double y_end = y_start + Connection_width;
int i = 0;
int l = Element_number/2;
int m = l - 1;

LCoord x;
LCoord y;
LCoord xcount;
LCoord ycount;

pLayer = LLayer_Find( pFile, "1normal␣Layer" );

x_start = - (Element_number * Resistor_width + (Element_number - 1)*
```

```
                    * Resistor_interdistance)/2 - Insulation_overflow;
    x_end = - x_start;
    y_start = - y_side/2 + freespace + Pad_height - Insulation_overflow;
    y_end = y_start + Resistor_side_length + 2*Insulation_overflow +
                    + junction_length_small + Resistor_lead;

    LBox_New( cellCurrent, pLayer, x_start, y_start, x_end, y_end);
    LBox_New( cellCurrent, pLayer, x_start, - y_start, x_end, - y_end);


    pLayer = LLayer_Find( pFile, "3normal␣Layer" );

    for (i=0; i < Element_number; i++){

    x_start = - (Element_number * Resistor_width + (Element_number - 1) *
                    * Resistor_interdistance)/2 + i*(Resistor_width +
                    + Resistor_interdistance);
    x_end = x_start + Resistor_width;
    y_start = - y_side/2 + freespace + Pad_height + junction_length_small +
                    + Resistor_lead;
    y_end = y_start + Resistor_side_length;

    LBox_New( cellCurrent, pLayer, x_start, y_start, x_end, y_end);
    LBox_New( cellCurrent, pLayer, x_start, - y_start, x_end, - y_end);
    }

    for (l=0; l< Element_number/2; l++){
    x_start = - (Element_number * Resistor_width + (Element_number - 1) *
                    * Resistor_interdistance)/2 + 2*l*(Resistor_width +
                    + Resistor_interdistance);
    x_end = x_start + 2*Resistor_width + Resistor_interdistance;
    y_start = - y_side/2 + freespace + Pad_height + junction_length_small +
                    + Resistor_lead + Resistor_side_length;
    y_end = y_start - Resistor_interconnection_length;

    LBox_New( cellCurrent, pLayer, x_start, y_start, x_end, y_end);
    LBox_New( cellCurrent, pLayer, x_start, - y_start, x_end, - y_end);
    }

    for (m=0; m< Element_number/2 - 1; m++){
    x_start = - (Element_number * Resistor_width + (Element_number-1) *
                    * Resistor_interdistance)/2 + 2*m*(Resistor_width +
                    + Resistor_interdistance) + Resistor_width +
                    + Resistor_interdistance;
    x_end = x_start + 2*Resistor_width + Resistor_interdistance;
    y_start = - y_side/2 + freespace + Pad_height + junction_length_small +
                    + Resistor_lead;
    y_end = y_start + Resistor_interconnection_length;

    LBox_New( cellCurrent, pLayer, x_start, y_start, x_end, y_end);
    LBox_New( cellCurrent, pLayer, x_start, - y_start, x_end, - y_end);
    }


    x_start = - (Element_number * Resistor_width + (Element_number - 1) *
                    * Resistor_interdistance)/2;
    x_end = x_start + Resistor_width;
```

```
y_start = - y_side/2 + freespace + Pad_height + junction_length_small - Overflow;
y_end = y_start + Resistor_lead + Overflow_small + Overflow;

LBox_New( cellCurrent, pLayer, x_start, y_start, x_end, y_end);
LBox_New( cellCurrent, pLayer, - x_start, y_start, - x_end, y_end);
LBox_New( cellCurrent, pLayer, x_start, - y_start, x_end, - y_end);
LBox_New( cellCurrent, pLayer, - x_start, - y_start, - x_end, - y_end);

pLayer = LLayer_Find( pFile, "4normal␣Layer" );

x_start = - x_side/2 + freespace + Pad_length  - Overflow;
y_start = Finger_number * 2*(Finger_width + Finger_distance)/2;
x_end = x_start + Overflow + (x_side - 2*(Pad_length + freespace) +
                - Finger_length - Finger_distance)/2;
y_end = - y_start;

LBox_New( cellCurrent, pLayer, x_start, y_start, x_end, y_end);
LBox_New( cellCurrent, pLayer, - x_start, y_start, - x_end, y_end);


for (i = 0; i < Finger_number; i++) {

x_start = - x_side/2 + freespace + Pad_length - Overflow + (x_side +
                - 2*(Pad_length + freespace) - Finger_length +
                - Finger_distance)/2;
y_start = (Finger_number - i) * (Finger_width + Finger_distance) +
                - (Finger_width + Finger_distance)*i ;
x_end = x_start + Overflow + Finger_length;
y_end = y_start - Finger_width;

LBox_New( cellCurrent, pLayer, x_start, y_start, x_end, y_end);

x_start = - x_start;
x_end = - x_end;
y_start = y_start - (Finger_width + Finger_distance);
y_end = y_end - (Finger_width + Finger_distance);


LBox_New( cellCurrent, pLayer, x_start, y_start, x_end, y_end);

}

pLayer = LLayer_Find( pFile, "3normal␣Layer" );

x_start = - (Element_number * Resistor_width + (Element_number - 1) *
                * Resistor_interdistance)/2 - junction_width_small/2 +
                + Resistor_width/2;
x_end = x_start + junction_width_small;
y_start = - y_side/2 + freespace + Pad_height - Overflow;
y_end = y_start + junction_length_small + Overflow;

LBox_New( cellCurrent, pLayer, x_start, y_start, x_end, y_end);
LBox_New( cellCurrent, pLayer, - x_start, y_start, - x_end, y_end);
LBox_New( cellCurrent, pLayer, x_start, - y_start, x_end, - y_end);
LBox_New( cellCurrent, pLayer, - x_start, - y_start, - x_end, - y_end);
```

```
pLayer = LLayer_Find( pFile, "4normal␣Layer" );

x_start = Connection_distance/2;
y_start = - y_side/2 + freespace + Pad_height - Connection_width;
x_end = x_side/2 - freespace - Pad_length + Overflow;
y_end = y_start + Connection_width;

LBox_New( cellCurrent, pLayer, x_start, y_start, x_end, y_end);
LBox_New( cellCurrent, pLayer, - x_start, y_start, - x_end, y_end);

LBox_New( cellCurrent, pLayer, x_start, - y_start, x_end, - y_end);
LBox_New( cellCurrent, pLayer, - x_start, - y_start, - x_end, -y_end);


x_start = - x_side/2 + freespace;
y_start = - y_side/2 + freespace;
x_end = x_start + Pad_length;
y_end = y_start + Pad_height;

LBox_New( cellCurrent, pLayer, x_start, y_start, x_end, y_end);
LBox_New( cellCurrent, pLayer, x_start, - y_start, x_end, - y_end);

x_start = x_side/2 - freespace;
y_start = - y_side/2 + freespace;
x_end = x_start - Pad_length;
y_end = - y_start;

LBox_New( cellCurrent, pLayer, x_start, y_start, x_end, y_end);

x_start = - x_side/2 + freespace;
y_start = - Pad_height/2;
x_end = x_start + Pad_length;
y_end = - y_start;

LBox_New( cellCurrent, pLayer, x_start, y_start, x_end, y_end);

pLayer = LLayer_Find( pFile, "5inverse␣Layer" );


x_start = - (Element_number * Resistor_width + (Element_number - 1) *
                * Resistor_interdistance)/2 - Polyimide_overflow_Resistor;
x_end = - x_start;
y_start = - y_side/2 + freespace + Pad_height + junction_length_small +
                + Resistor_lead - Polyimide_overflow_Resistor;
y_end = y_start + Resistor_side_length + 2*Polyimide_overflow_Resistor;

LBox_New( cellCurrent, pLayer, x_start, y_start, x_end, y_end);


x_start = - x_side/2 + freespace + Pad_length + Connection_width + (x_side +
                - 2*(Pad_length + Connection_width + freespace) - Finger_length +
                - Finger_distance)/2 - Polyimide_overflow_Capacitor;
y_start = Finger_number * (Finger_width + Finger_distance) +
                + Polyimide_overflow_Capacitor;
x_end = x_start + Finger_length + 2*Polyimide_overflow_Capacitor;
y_end = - y_start;
```

```
LBox_New( cellCurrent, pLayer, x_start, y_start, x_end, y_end);


pLayer = LLayer_Find( pFile, "6normal␣Layer␣SP" );


for (i=0; i < Element_number; i++){

x_start = - (Element_number * Resistor_width + (Element_number - 1) *
                * Resistor_interdistance)/2 + i*(Resistor_width +
                + Resistor_interdistance);
x_end = x_start + Resistor_width;
y_start = - y_side/2 + freespace + Pad_height + junction_length_small +
                + Resistor_lead;
y_end = y_start + Resistor_side_length;

LBox_New( cellCurrent, pLayer, x_start, y_start, x_end, y_end);
LBox_New( cellCurrent, pLayer, x_start, - y_start, x_end, - y_end);
}

for (l=0; l< Element_number/2; l++){
x_start = - (Element_number * Resistor_width + (Element_number - 1) *
                * Resistor_interdistance)/2 + 2*l*(Resistor_width +
                + Resistor_interdistance);
x_end = x_start + 2*Resistor_width + Resistor_interdistance;
y_start = - y_side/2 + freespace + Pad_height + junction_length_small +
                + Resistor_lead + Resistor_side_length;
y_end = y_start - Resistor_interconnection_length;

LBox_New( cellCurrent, pLayer, x_start, y_start, x_end, y_end);
LBox_New( cellCurrent, pLayer, x_start, - y_start, x_end, - y_end);
}

for (m=0; m< Element_number/2 - 1; m++){
x_start = - (Element_number * Resistor_width + (Element_number - 1) *
                * Resistor_interdistance)/2 + 2*m*(Resistor_width +
                + Resistor_interdistance) + Resistor_width +
                + Resistor_interdistance;
x_end = x_start + 2*Resistor_width + Resistor_interdistance;
y_start = - y_side/2 + freespace + Pad_height + junction_length_small +
                + Resistor_lead;
    y_end = y_start + Resistor_interconnection_length;

LBox_New( cellCurrent, pLayer, x_start, y_start, x_end, y_end);
LBox_New( cellCurrent, pLayer, x_start, - y_start, x_end, - y_end);
}


x_start = - (Element_number * Resistor_width + (Element_number - 1) *
                * Resistor_interdistance)/2;
x_end = x_start + Resistor_width;
y_start = - y_side/2 + freespace + Pad_height + junction_length_small - Overflow;
y_end = y_start+Resistor_lead + Overflow_small + Overflow;

LBox_New( cellCurrent, pLayer, x_start, y_start, x_end, y_end);
LBox_New( cellCurrent, pLayer, - x_start, y_start, - x_end, y_end);
LBox_New( cellCurrent, pLayer, x_start, - y_start, x_end, - y_end);
```

```
    LBox_New( cellCurrent, pLayer, - x_start, - y_start, - x_end, - y_end);

    x_start = - (Element_number * Resistor_width + (Element_number - 1) *
                * Resistor_interdistance)/2 - junction_width_small/2 +
                + Resistor_width/2;
    x_end = x_start + junction_width_small;
    y_start = - y_side/2 + freespace + Pad_height - Overflow;
    y_end = y_start + junction_length_small + Overflow;

    LBox_New( cellCurrent, pLayer, x_start, y_start, x_end, y_end);
    LBox_New( cellCurrent, pLayer, - x_start, y_start, - x_end, y_end);
    LBox_New( cellCurrent, pLayer, x_start, - y_start, x_end, - y_end);
    LBox_New( cellCurrent, pLayer, - x_start, - y_start, - x_end, - y_end);

    x_start = - x_side/2 + freespace + Pad_length + Connection_width + (x_side +
                - 2*(Pad_length + Connection_width + freespace) - Finger_length +
                - Finger_distance)/2 + Insulation_overflow/2;
    y_start = Finger_number * (Finger_width + Finger_distance) +
                - Insulation_overflow/2;
    x_end = x_start + Finger_length + Finger_distance + Overflow + Connection_width +
                - Insulation_overflow;
    y_end = - y_start;

    LBox_New( cellCurrent, pLayer, x_start, y_start, x_end, y_end);

    /* End custom generator code.*/
}

extern "C" int UPI_Entry_Point(void)
{
    Cell1_main();
    return 1;
}
```

B.2. STRAIN SENSING PLATFORM: T-CELL CODE

Table B.2: L-EDIT T-Cell parameters and variables of the strain sensing platform.
Lengths are expressed in nanometers.

PARAMETERS		
Name	**Type**	**Default Value**
Connection_width	Double	500000
Pad_length	Double	1300000
Pad_height	Double	1300000
x_side	Double	6000000
y_side	Double	10100000
freespace	Double	100000
Connection_distance	Double	140000
Resistor_side_length	Double	640000
Resistor_width	Double	10000
Resistor_interconnection_length	Double	100000
Resistor_lead	Double	150000
Element_number	Integer	28
Resistor_interdistance	Double	10000
junction_width_small	Double	200000
junction_length_small	Double	300000
junction_width_big	Double	200000
junction_length_big	Double	200000
Overflow_small	Double	50000
Overflow	Double	100000
VARIABLES		
Piezoresistor_aspect_ratio	Double	
Piezoresistor_width	Double	

```
/*******************************************************************************
 * Cell Name: Cell1
 * Creator  : L-Edit Tcell Builder
 *
 *******************************************************************************/

#include <cstdlib>
#include <cmath>
#include <cstring>
#include <cstdio>
#include <string>

#define EXCLUDE_LEDIT_LEGACY_UPI
#include <ldata.h>
```

```
/* Begin -- Uncomment this block if you are using L-Comp. */
//#include <lcomp.h>
/* End */

/* TODO: Put local functions here. */
void Cell1_main(void)
{
    int iTmpUpiReturnCode = LUpi_GetReturnCode();
    /* Begin DO NOT EDIT SECTION generated by L-Edit */
    LCell    cellCurrent = (LCell)LMacro_GetNewTCell();
    double   Connection_width = LCell_GetParameterAsDouble(cellCurrent,
                        "Connection_width");
    double   Pad_length = LCell_GetParameterAsDouble(cellCurrent, "Pad_length");
    double   Pad_height = LCell_GetParameterAsDouble(cellCurrent, "Pad_height");
    double   x_side = LCell_GetParameterAsDouble(cellCurrent, "x_side");
    double   y_side = LCell_GetParameterAsDouble(cellCurrent, "y_side");
    double   freespace = LCell_GetParameterAsDouble(cellCurrent, "freespace");
    double   Connection_distance = LCell_GetParameterAsDouble(cellCurrent,
                "Connection_distance");
    double   Resistor_side_length = LCell_GetParameterAsDouble(cellCurrent,
                        "Resistor_side_length");
    double   Resistor_width = LCell_GetParameterAsDouble(cellCurrent,
                "Resistor_width");
    double   Resistor_interconnection_length = LCell_GetParameterAsDouble(cellCurrent,
                        "Resistor_interconnection_length");
    double   Resistor_lead = LCell_GetParameterAsDouble(cellCurrent, "Resistor_lead");
    int      Element_number = LCell_GetParameterAsInt(cellCurrent, "Element_number");
    double   Resistor_interdistance = LCell_GetParameterAsDouble(cellCurrent,
                "Resistor_interdistance");
    double   junction_width_small = LCell_GetParameterAsDouble(cellCurrent,
                "junction_width_small");
    double   junction_length_small = LCell_GetParameterAsDouble(cellCurrent,
                "junction_length_small");
    double   junction_width_big = LCell_GetParameterAsDouble(cellCurrent,
                "junction_width_big");
    double   junction_length_big = LCell_GetParameterAsDouble(cellCurrent,
                "junction_length_big");
    double   Overflow_small = LCell_GetParameterAsDouble(cellCurrent,
                "Overflow_small");
    double   Overflow     = LCell_GetParameterAsDouble(cellCurrent, "Overflow");
    double   Piezoresistor_aspect_ratio = LCell_GetParameterAsDouble(cellCurrent,
                "Piezoresistor_aspect_ratio");
    double   Piezoresistor_width = LCell_GetParameterAsDouble(cellCurrent,
                "Piezoresistor_width");
    /* End DO NOT EDIT SECTION generated by L-Edit */

    if(LUpi_GetReturnCode())
    {
        LDialog_MsgBox("Error:␣Tcell␣failed␣to␣read␣parameters.");
        return;
    }
    LUpi_SetReturnCode(iTmpUpiReturnCode);


    /* Begin -- Uncomment this block if you are using L-Comp. */
    //LC_InitializeStateFromCell(cellCurrent);
    /* End */
```

```
LFile pFile = LCell_GetFile( cellCurrent );

/* Clear out existing ports */
LPort pPort, pPort_next;
for ( pPort = LPort_GetList( cellCurrent ); pPort; pPort = pPort_next )
{
    pPort_next = LPort_GetNext( pPort );
    LPort_Delete( cellCurrent, pPort );
}
/* Clear out existing elements */
LLayer pLayer;
for ( pLayer = LLayer_GetList( pFile ); pLayer; pLayer = LLayer_GetNext(pLayer))
{
    LObject pObj;
    LObject pObj_next;
    for ( pObj  = LObject_GetList( cellCurrent, pLayer ); pObj; pObj = pObj_next)
    {
            pObj_next = LObject_GetNext( pObj );
            LObject_Delete( cellCurrent, pObj );
    }
}
/* Clear out existing instances */
LInstance pInst;
LInstance pInst_next;
for ( pInst = LInstance_GetList( cellCurrent ); pInst; pInst = pInst_next )
{
    pInst_next = LInstance_GetNext( pInst );
    LInstance_Delete( cellCurrent, pInst );
}

/* TODO: Put local variables here. */

/* TODO: Begin custom generator code.*/
double x_start = Connection_distance/2;
double y_start = - y_side/2 + freespace + Pad_height - Connection_width;
double x_end = x_side/2 - freespace - Pad_length+Overflow;
double y_end = y_start + Connection_width;
int i = 0;
int l = Element_number/2;
int m = l - 1;
double Piezoresistor_length = Piezoresistor_aspect_ratio * Piezoresistor_width;

LCoord x;
LCoord y;
LCoord xcount;
LCoord ycount;

pLayer = LLayer_Find( pFile, "2normal␣Layer" );


x_start = - Piezoresistor_width/2;
y_start = - junction_length_big/2 + Overflow_small;
x_end = - x_start;
y_end = y_start - Piezoresistor_length - 2*Overflow_small;

LBox_New( cellCurrent, pLayer, x_start, y_start, x_end, y_end);
LBox_New( cellCurrent, pLayer, - y_start, x_start, - y_end, x_end);
```

```
pLayer = LLayer_Find( pFile, "3normal␣Layer" );

for (i=0; i < Element_number; i++){

x_start = - (Element_number * Resistor_width + (Element_number - 1) *
                * Resistor_interdistance)/2 + i*(Resistor_width +
                + Resistor_interdistance);
x_end = x_start + Resistor_width;
y_start = - y_side/2 + freespace + Pad_height + junction_length_small +
                + Resistor_lead;
y_end = y_start + Resistor_side_length;

LBox_New( cellCurrent, pLayer, x_start, - y_start, x_end, - y_end);

y_start = junction_width_small/2 + (- junction_length_big/2 +
                - Connection_distance + (- y_side/2 + freespace +
                + Pad_height))*2/3 - (Element_number * Resistor_width +
                + (Element_number - 1) * Resistor_interdistance)/2 +
                - junction_width_small/2 + i*(Resistor_width +
                + Resistor_interdistance);
y_end = y_start + Resistor_width;
x_start = - junction_width_big/4 - Resistor_lead;
x_end = x_start - Resistor_side_length;

LBox_New( cellCurrent, pLayer, x_start, y_start, x_end, y_end);
}

for (l=0; l< Element_number/2; l++){

x_start = - (Element_number * Resistor_width + (Element_number - 1) *
                * Resistor_interdistance)/2 + 2*l*(Resistor_width +
                + Resistor_interdistance);
x_end = x_start + 2*Resistor_width + Resistor_interdistance;
y_start = - y_side/2 + freespace + Pad_height + junction_length_small +
                + Resistor_lead + Resistor_side_length;
y_end = y_start - Resistor_interconnection_length;

LBox_New( cellCurrent, pLayer, x_start, - y_start, x_end, - y_end);

y_start = junction_width_small/2 + ( - junction_length_big/2 +
                - Connection_distance + (- y_side/2 + freespace +
                + Pad_height))*2/3 - (Element_number * Resistor_width +
                + (Element_number - 1) * Resistor_interdistance)/2 +
                - junction_width_small/2 + 2*l*(Resistor_width +
                + Resistor_interdistance);
y_end = y_start + 2*Resistor_width + Resistor_interdistance;
x_start = - junction_width_big/4 - Resistor_lead - Resistor_side_length;
x_end = x_start + Resistor_interconnection_length;

LBox_New( cellCurrent, pLayer, x_start, y_start, x_end, y_end);

}

for (m=0; m< Element_number/2 - 1; m++){

x_start = - (Element_number * Resistor_width + (Element_number - 1) *
```

```
                * Resistor_interdistance)/2 + 2*m*(Resistor_width +
                + Resistor_interdistance) + Resistor_width +
                + Resistor_interdistance;
x_end = x_start + 2*Resistor_width + Resistor_interdistance;
y_start = - y_side/2 + freespace + Pad_height + junction_length_small +
                + Resistor_lead;
y_end = y_start + Resistor_interconnection_length;

LBox_New( cellCurrent, pLayer, x_start, - y_start, x_end, - y_end);

y_start = junction_width_small/2 + Resistor_width + Resistor_interdistance +
                + (- junction_length_big/2 - Connection_distance + (- y_side/2 +
                + freespace + Pad_height))*2/3 - (Element_number *
                * Resistor_width + (Element_number - 1) *
                * Resistor_interdistance)/2 - junction_width_small/2 +
                + 2*m*(Resistor_width + Resistor_interdistance);
y_end = y_start + 2*Resistor_width + Resistor_interdistance;
x_start =  - Resistor_interconnection_length - junction_width_big/4 +
                - Resistor_lead;
x_end = x_start + Resistor_interconnection_length;

LBox_New( cellCurrent, pLayer, x_start, y_start, x_end, y_end);
}

y_start = ( - junction_length_big/2 - Connection_distance + ( - y_side/2 +
                + freespace + Pad_height))*2/3 - (Element_number *
                * Resistor_width +(Element_number - 1) *
                * Resistor_interdistance)/2;
y_end = y_start + Resistor_width;
x_start = - junction_width_big/4 + Overflow;
x_end = x_start - Resistor_lead - Overflow - Overflow_small;


LBox_New( cellCurrent, pLayer, x_start, y_start, x_end, y_end);

y_start = (- junction_length_big/2 - Connection_distance + (- y_side/2 +
                + freespace + Pad_height))*2/3 + (Element_number *
                * Resistor_width + (Element_number - 1) *
                * Resistor_interdistance)/2 - Resistor_width;
y_end = y_start + Resistor_width;
x_start = - junction_width_big/4 + Overflow;
x_end = x_start - Resistor_lead - Overflow - Overflow_small ;


LBox_New( cellCurrent, pLayer, x_start, y_start, x_end, y_end);

x_start = - (Element_number * Resistor_width + (Element_number - 1) *
                * Resistor_interdistance)/2;
x_end = x_start + Resistor_width;
y_start = - y_side/2 + freespace + Pad_height + junction_length_small - Overflow;
y_end = y_start + Resistor_lead + Overflow_small + Overflow;

LBox_New( cellCurrent, pLayer, x_start, - y_start, x_end, - y_end);
LBox_New( cellCurrent, pLayer, - x_start, - y_start, - x_end, - y_end);

pLayer = LLayer_Find( pFile, "3normal␣Layer" );
```

```
x_start = - junction_width_big/4;
x_end = x_start + junction_length_small + Overflow;
y_start = - Piezoresistor_length - junction_width_big/2 - junction_width_small;
y_end = y_start + junction_width_small;

LBox_New( cellCurrent, pLayer, x_start, y_start, x_end, y_end);
LBox_New( cellCurrent, pLayer, - y_start, x_start, - y_end, x_end);


x_start = junction_width_big/2;
x_end = - x_start - Overflow;
y_start = junction_length_big/2;
y_end = - y_start;

LBox_New( cellCurrent, pLayer, x_start, y_start, x_end, y_end);

x_start = - (Element_number * Resistor_width + (Element_number - 1) *
                * Resistor_interdistance)/2 - junction_width_small/2 +
                + Resistor_width/2;
x_end = x_start + junction_width_small;
y_start = - y_side/2 + freespace + Pad_height - Overflow;
y_end = y_start + junction_length_small + Overflow;

LBox_New( cellCurrent, pLayer, x_start, - y_start, x_end, - y_end);
LBox_New( cellCurrent, pLayer, - x_start, - y_start, - x_end, - y_end);

y_start = (- junction_length_big/2 - Connection_distance + (- y_side/2 +
                + freespace + Pad_height))*2/3 - (Element_number *
                * Resistor_width + (Element_number - 1) *
                * Resistor_interdistance)/2 - junction_width_small/2 +
                + Resistor_width/2;
y_end = y_start + junction_width_small;
x_start = - junction_width_big/4;
x_end = x_start + junction_length_small + Overflow;

LBox_New( cellCurrent, pLayer, x_start, y_start, x_end, y_end);

y_start = (- junction_length_big/2 - Connection_distance + (- y_side/2 +
                + freespace + Pad_height))*2/3 + (Element_number *
                * Resistor_width + (Element_number - 1) *
                * Resistor_interdistance)/2 - junction_width_small/2 +
                - Resistor_width/2;
y_end = y_start + junction_width_small;
x_start = - junction_width_big/4;
x_end = x_start + junction_length_small + Overflow;

LBox_New( cellCurrent, pLayer, x_start, y_start, x_end, y_end);


pLayer = LLayer_Find( pFile, "4normal␣Layer" );

x_start = - x_side/2 + freespace;
y_start = - y_side/2 + freespace;
x_end = x_start + Pad_length;
y_end = y_start + Pad_height;

LBox_New( cellCurrent, pLayer, x_start, y_start, x_end, y_end);
```

```
LBox_New( cellCurrent, pLayer, x_start, - y_start, x_end, - y_end);
LBox_New( cellCurrent, pLayer, - x_start, y_start, - x_end, y_end);
LBox_New( cellCurrent, pLayer, - x_start, - y_start, - x_end, - y_end);

x_start = - x_side/2 + freespace;
    y_start = - Pad_height/2;
x_end = x_start + Pad_length;
y_end = - y_start;

LBox_New( cellCurrent, pLayer, x_start, y_start, x_end, y_end);

x_start = Connection_distance/2;
y_start = - y_side/2 + freespace + Pad_height - Connection_width;
x_end = x_side/2 - freespace - Pad_length + Overflow;
y_end = y_start + Connection_width;

LBox_New( cellCurrent, pLayer, x_start, - y_start, x_end, - y_end);
LBox_New( cellCurrent, pLayer, - x_start, - y_start, - x_end, - y_end);

x_start = - x_side/2 + freespace + Pad_length - Overflow;
y_start = - Connection_width/2;
x_end = - junction_width_big/2;
y_end = - y_start;

LBox_New( cellCurrent, pLayer, x_start, y_start, x_end, y_end);

x_start = - x_side/2 + freespace + Pad_length - Overflow;
y_start = - y_side/2 + freespace + Pad_height - Connection_width;
x_end = - junction_width_big/4 + junction_length_small + Connection_distance +
                + Overflow;
y_end = y_start + Connection_width;

LBox_New( cellCurrent, pLayer, x_start, y_start, x_end, y_end);

x_start = - junction_width_big/4 + junction_length_small;
x_end = x_start + Connection_width;
y_start = - junction_length_big/2 - Connection_distance;
y_end = (y_start + (- y_side/2 + freespace + Pad_height))*2/3 +
                + Connection_distance/2;

LBox_New( cellCurrent, pLayer, x_start, y_start, x_end, y_end);
LBox_New( cellCurrent, pLayer, - y_start, x_start, - y_end, x_end);


x_start = - junction_width_big/4 + junction_length_small;
y_start = - y_side/2 + freespace + Pad_height - Connection_width;
x_end = x_start + Connection_width;
y_end = (- junction_length_big/2 - Connection_distance + (- y_side/2 +
                + freespace + Pad_height))*2/3 - Connection_distance/2;

LBox_New( cellCurrent, pLayer, x_start, y_start, x_end, y_end);

x_start = x_side/2 - freespace - Pad_length;
y_start = - y_side/2 + freespace + Pad_height - Overflow;
x_end = x_start + Connection_width;
y_end = (- Connection_width/2 - Connection_distance + ( - y_side/2 + freespace +
                + Pad_height))/3;
```

```
LBox_New( cellCurrent , pLayer , x_start , y_start , x_end, y_end);

x_start = x_side/2 - freespace - Pad_length;
y_start = y_side/2 - freespace - Pad_height + Overflow;
x_end = x_start + Connection_width;
y_end = junction_length_small - junction_length_big/4  + Connection_width +
                - Overflow;

LBox_New( cellCurrent , pLayer , x_start , y_start , x_end, y_end);

x_start = - junction_width_big/4 + junction_length_small + Connection_width +
                - Overflow;
x_end =  x_side/2 - freespace - Pad_length + Overflow;
y_start = (- Connection_width/2 - Connection_distance + (- y_side/2 + freespace +
                + Pad_height))/3 - Connection_width;
y_end = + Connection_width/2 + Connection_distance + Connection_width;
y_end = y_start + Connection_width;

LBox_New( cellCurrent , pLayer , x_start , y_start , x_end, y_end);

pLayer = LLayer_Find( pFile , "6normal␣Layer␣SP" );

for (i=0; i < Element_number; i++){

x_start = - (Element_number * Resistor_width + (Element_number - 1) *
                * Resistor_interdistance)/2 + i*(Resistor_width +
                + Resistor_interdistance);
x_end = x_start + Resistor_width;
y_start = - y_side/2 + freespace + Pad_height + junction_length_small +
                + Resistor_lead;
y_end = y_start + Resistor_side_length;

LBox_New( cellCurrent , pLayer , x_start , - y_start , x_end, - y_end);

y_start = junction_width_small/2 + ( - junction_length_big/2 +
                - Connection_distance + (- y_side/2 + freespace +
                + Pad_height))*2/3 - (Element_number *
                * Resistor_width + (Element_number - 1) *
                * Resistor_interdistance)/2 - junction_width_small/2 +
                + i*(Resistor_width + Resistor_interdistance);
y_end = y_start + Resistor_width;
x_start = - junction_width_big/4 - Resistor_lead;
x_end = x_start - Resistor_side_length ;

LBox_New( cellCurrent , pLayer , x_start , y_start , x_end, y_end);
}

for (l=0; l< Element_number/2; l++){

x_start = - (Element_number * Resistor_width + (Element_number - 1) *
                * Resistor_interdistance)/2 + 2*l*(Resistor_width +
                + Resistor_interdistance);
x_end = x_start + 2*Resistor_width + Resistor_interdistance;
y_start = - y_side/2 + freespace + Pad_height + junction_length_small +
                + Resistor_lead + Resistor_side_length;
y_end = y_start - Resistor_interconnection_length;
```

```
LBox_New( cellCurrent, pLayer, x_start, − y_start, x_end, − y_end);

y_start = junction_width_small/2 + (− junction_length_big/2 +
               − Connection_distance + (− y_side/2 + freespace +
               + Pad_height))∗2/3 − (Element_number ∗
               ∗ Resistor_width + (Element_number − 1) ∗
               ∗ Resistor_interdistance)/2 − junction_width_small/2 +
               + 2∗l∗(Resistor_width + Resistor_interdistance);
y_end = y_start + 2∗Resistor_width + Resistor_interdistance;
x_start = − junction_width_big/4 − Resistor_lead − Resistor_side_length;
x_end = x_start + Resistor_interconnection_length;

LBox_New( cellCurrent, pLayer, x_start, y_start, x_end, y_end);

}

for (m=0; m< Element_number/2 − 1; m++){

x_start = − (Element_number ∗ Resistor_width + (Element_number − 1) ∗
               ∗ Resistor_interdistance)/2 + 2∗m∗(Resistor_width +
               + Resistor_interdistance) + Resistor_width +
               + Resistor_interdistance;
x_end = x_start + 2∗Resistor_width + Resistor_interdistance;
y_start = − y_side/2 + freespace + Pad_height + junction_length_small +
               + Resistor_lead;
y_end = y_start + Resistor_interconnection_length;

LBox_New( cellCurrent, pLayer, x_start, − y_start, x_end, − y_end);

y_start = junction_width_small/2 + Resistor_width + Resistor_interdistance +
               + (− junction_length_big/2 − Connection_distance + (− y_side/2 +
               + freespace + Pad_height))∗2/3 − (Element_number ∗
               ∗ Resistor_width + (Element_number − 1) ∗
               ∗ Resistor_interdistance)/2 − junction_width_small/2 +
               + 2∗m∗(Resistor_width + Resistor_interdistance);
y_end = y_start + 2∗Resistor_width + Resistor_interdistance;
x_start =  − Resistor_interconnection_length − junction_width_big/4 +
               − Resistor_lead;
x_end = x_start + Resistor_interconnection_length;

LBox_New( cellCurrent, pLayer, x_start, y_start, x_end, y_end);
}

y_start = (− junction_length_big/2 − Connection_distance + (− y_side/2
               + freespace + Pad_height))∗2/3 − (Element_number ∗
               ∗ Resistor_width + (Element_number − 1) ∗
               ∗ Resistor_interdistance)/2;
y_end = y_start + Resistor_width;
x_start = − junction_width_big/4 + Overflow;
x_end = x_start − Resistor_lead − Overflow − Overflow_small  ;


LBox_New( cellCurrent, pLayer, x_start, y_start, x_end, y_end);

y_start = (− junction_length_big/2 − Connection_distance + (− y_side/2 +
               + freespace + Pad_height))∗2/3 + (Element_number ∗
```

```
                * Resistor_width + (Element_number - 1) *
                * Resistor_interdistance)/2 - Resistor_width;
y_end = y_start + Resistor_width;
x_start = - junction_width_big/4 + Overflow;
x_end = x_start - Resistor_lead - Overflow - Overflow_small;

LBox_New( cellCurrent, pLayer, x_start, y_start, x_end, y_end);

x_start = - (Element_number * Resistor_width + (Element_number - 1) *
                * Resistor_interdistance)/2;
x_end = x_start + Resistor_width;
y_start = - y_side/2 + freespace + Pad_height + junction_length_small - Overflow;
y_end = y_start + Resistor_lead + Overflow_small + Overflow;

LBox_New( cellCurrent, pLayer, x_start, - y_start, x_end, - y_end);
LBox_New( cellCurrent, pLayer, - x_start, - y_start, - x_end, - y_end);

x_start = - junction_width_big/4;
x_end = x_start + junction_length_small + Overflow;
y_start = - Piezoresistor_length - junction_width_big/2 - junction_width_small;
y_end = y_start + junction_width_small;

LBox_New( cellCurrent, pLayer, x_start, y_start, x_end, y_end);
LBox_New( cellCurrent, pLayer, - y_start, x_start, - y_end, x_end);


x_start = junction_width_big/2;
x_end = - x_start - Overflow;
y_start = junction_length_big/2;
y_end = - y_start;

LBox_New( cellCurrent, pLayer, x_start, y_start, x_end, y_end);

x_start = - (Element_number * Resistor_width + (Element_number - 1) *
                * Resistor_interdistance)/2 - junction_width_small/2 +
                + Resistor_width/2;
x_end = x_start + junction_width_small;
y_start = - y_side/2 + freespace + Pad_height - Overflow;
y_end = y_start + junction_length_small + Overflow;

LBox_New( cellCurrent, pLayer, x_start, - y_start, x_end, - y_end);
LBox_New( cellCurrent, pLayer, - x_start, - y_start, - x_end, - y_end);

y_start = (- junction_length_big/2 - Connection_distance + (- y_side/2
                + freespace + Pad_height))*2/3 - (Element_number **
                Resistor_width + (Element_number - 1) *
                * Resistor_interdistance)/2 - junction_width_small/2 +
                + Resistor_width/2;
y_end = y_start + junction_width_small;
x_start = - junction_width_big/4;
x_end = x_start + junction_length_small + Overflow;

LBox_New( cellCurrent, pLayer, x_start, y_start, x_end, y_end);

y_start = (- junction_length_big/2 - Connection_distance + (- y_side/2 +
                + freespace ++ Pad_height))*2/3 + (Element_number *
                * Resistor_width + (Element_number - 1) *
```

```
                    * Resistor_interdistance)/2 - junction_width_small/2 +
                    - Resistor_width/2;
    y_end = y_start + junction_width_small;
    x_start = - junction_width_big/4;
    x_end = x_start + junction_length_small + Overflow;

    LBox_New( cellCurrent, pLayer, x_start, y_start, x_end, y_end);

    /* End custom generator code.*/
}

extern "C" int UPI_Entry_Point(void)
{
    Cell1_main();
    return 1;
}
```

C

COMSOL SIMULATIONS

THE physics and the design of the thermoresistive humidity sensor are described in Sections 2.2.4 and 3.1.4, where it is mentioned that initial COMSOL Multiphysics simulations were undertaken. These simulations were necessary as little information was available in literature to support the design of such sensor. In the time frame of this *experimental* MSc thesis, only a simplified model could be studied; therefore, the results obtained are exclusively estimations and represent guidelines followed during the design phase outlined in Section 3.1.4. The purpose of this Appendix is to introduce the implemented model and the achieved results.

The model begins with a 1.20 mm by 1.65 mm cutout of a simplified PV module, where the cell is laminated in layers of glass, ethylene-vinyl acetate (EVA), aluminum and tedlar, as shown in Fig. C.1. Table C.1 reports the order, from top to bottom, and the thicknesses of the various materials considered for the model. These values are an estimation based on the literature regarding thermal FEA of PV modules [165–171] and on the materials datasheets available. Since the resistive humistat is an active sensor that generates heat, it is of interest to keep the maximum temperatures reached within the laminate close to the typical operating temperatures of a solar cell (~50 $°C$ [165]), thus avoiding the introduction of significant recurring thermal stresses that could affect the health of the laminate in the long term. As the focus of this work is to study the humidity sensor, the opera-

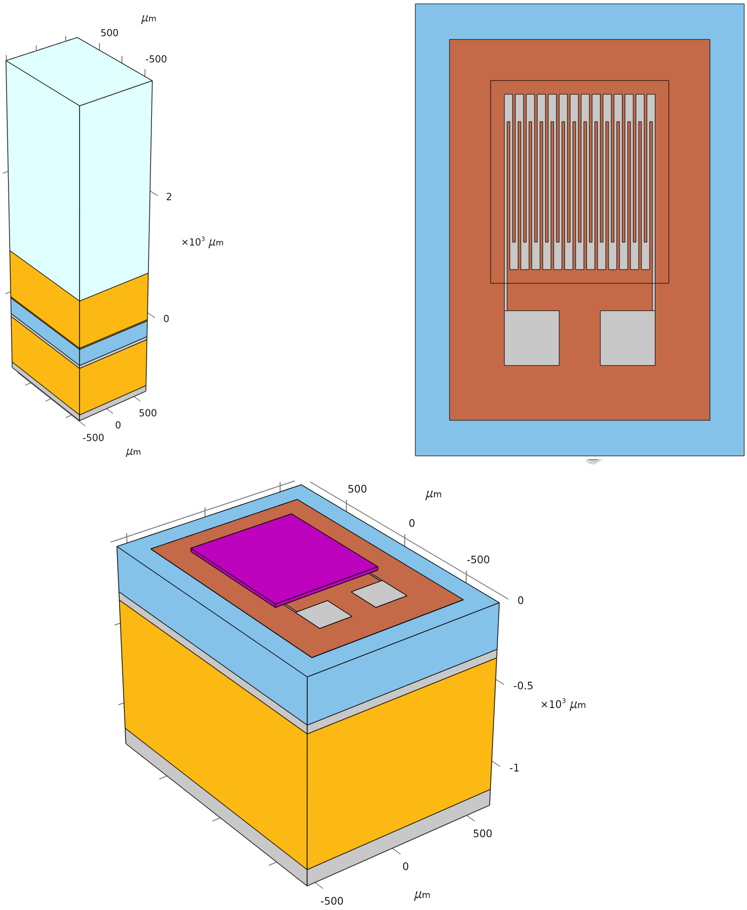

Fig. C.1: Top-left: Isometric view of the whole COMSOL model. Order of *visible* materials from top to bottom: glass, EVA, silicon, aluminum, EVA, and Tedlar. *Top-right*: Top view of the resistor. The rectangular perimeter indicates the profile of the polymer layer. *Bottom*: Isometric view of the partial COMSOL model. Order of *visible* materials from top to bottom: polyimide (purple), aluminum (light gray), silicon oxide (red), silicon (light blue), aluminum (light gray), EVA (orange), and Tedlar (gray). The aluminum layer between the silicon cell and the EVA encapsulant represents the backside contact of the cell.

Table C.1: Thicknesses of the constitutive materials of the PV laminate and their top-to-bottom order with reference to Fig. C.1 (top-left).

Material	Thickness
Glass	3 mm
EVA	800 μm
Silicon	270 μm
Aluminum	50 μm
EVA	800 μm
Tedlar	100 μm

tion of the PV cell is neglected and thus approximated as a plain silicon layer. In the center of the cutout and on top of the silicon layer, the sensor is then modelled as a sequence of a silicon oxide insulation, the meander-shaped aluminum resistor, and the polyimide covering, as illustrated in Fig. C.1 (bottom & top-right). The main dimensions of the metal resistor (e.g. finger length & width) are the same as those for the reference resistor described in Section 3.1.1, thus a thickness of 350 nm was set and a resistance of about 95-100 Ω is expected at ambient temperature. Meanwhile, the thickness of the polyimide layer is set to 20 μm, in accordance with the example process for thick layers provided in the Durimide 7020 (Fujifilm) polyimide datasheet. Contrarily, the thickness of the insulation is left as a variable of the simulation. The properties of the materials considered in the model are estimated through the combined use of the available COMSOL material library, material datasheets and the related literature [74, 118, 147, 148, 165–174]. In particular, the electrical conductivity of the polyimide layer ($\sigma_{poly.,moist}$) is set as the weighted average of the conductivity of water (σ_{water}) and dry polymer ($\sigma_{poly.,dry}$), as outlined by Eq. C.1; hence, an increase in the mass ratio between absorbed moisture ($m_{water,abs.}$) and polyimide ($m_{poly.,dry}$) results in a change in this property.

$$\sigma_{poly.,moist} = \frac{m_{poly.,dry} \cdot \sigma_{poly.,dry} + m_{water,abs.} \cdot \sigma_{water}}{m_{water,abs.} + m_{poly.,dry}} \tag{C.1}$$

As mentioned in Section 3.1.1, a second identical resistor is operated as the reference heater of the thermoresistive humidity sensor. The heat generated during the operation of this reference heater is dissipated through the same layers as in the cased of the humidity sensor, yet with the exception of the polyimide cover. Consequently, once the output difference between the two heaters at dry conditions is known ($m_{water,abs.} = 0$), any further change in output is related to the moisture absorption in the polyimide layer, as this represents the only difference between the set of heaters. To finalize the geometry of the model, 200 μm of silicon oxide are left around the edges of the resistor, while 50 μm of additional polyimide encompass the perimeter of its fingers, as illustrated in Fig. C.1 (top-right). Hence, the model created is of multiscale nature, since the dimensions of the structures range from centimeters to micrometers.

The meshing step of the model is complex in view of the wide range of dimensions. In fact, without any local submeshing of certain critical parts, the total number of nodes would have exceeded 20 million, which would have required too much computational memory and time. Therefore, top and bottom surfaces of the PV laminate were first meshed by the means of a regular planar quadrilateral mesh, which is then swept through the layers. Exceptions to the initial sweep are layers in direct contact with the sensor, namely the silicon cell and the top EVA encapsulant. The next node-reducing step consists in dividing the layers containing the sensor elements into sublayers, in a way that keeps the planar cross-section of the model remains constant along the vertical direction, as shown in Fig. C.2. In such figure, it can be better observed how the EVA layer is adaptively sectioned, as the three sublayers in Fig. C.2 (a) reflect the thickness of the bottom silicon oxide insulator, the thin center metal resistor, and the thick top polymer cover. Additionally, the portion of the polyimide layer above the aluminum layer is hidden in Fig. C.2 (b) to display the corresponding EVA sublayer and the resulting mesh sweep. In fact, the profile of the contact pads that lie under the EVA sublayer can be observed as a consequence of the mesh sweep. Following the subsectioning of the EVA, another quadrilateral mesh was first generated at the interface between resistor and insulation, since the metal structure has the smallest planar features. Then, a free triangular mesh is added to finalize the mesh on the same plane of the resistor/insulator interface, as visualized in Fig. C.3 (a); the resulting pattern is then swept through the sublayers containing the sensor's components. Finally, the nodes belonging to the remaining parts are generated with free tetrahedrals, which gradually reduce the mesh feature size of the first quadrilateral mesh to the finer mesh of the sensor's components. An overview of the final results is given in Fig. C.3 (b). The total amount of mesh nodes was reduced to less than four million.

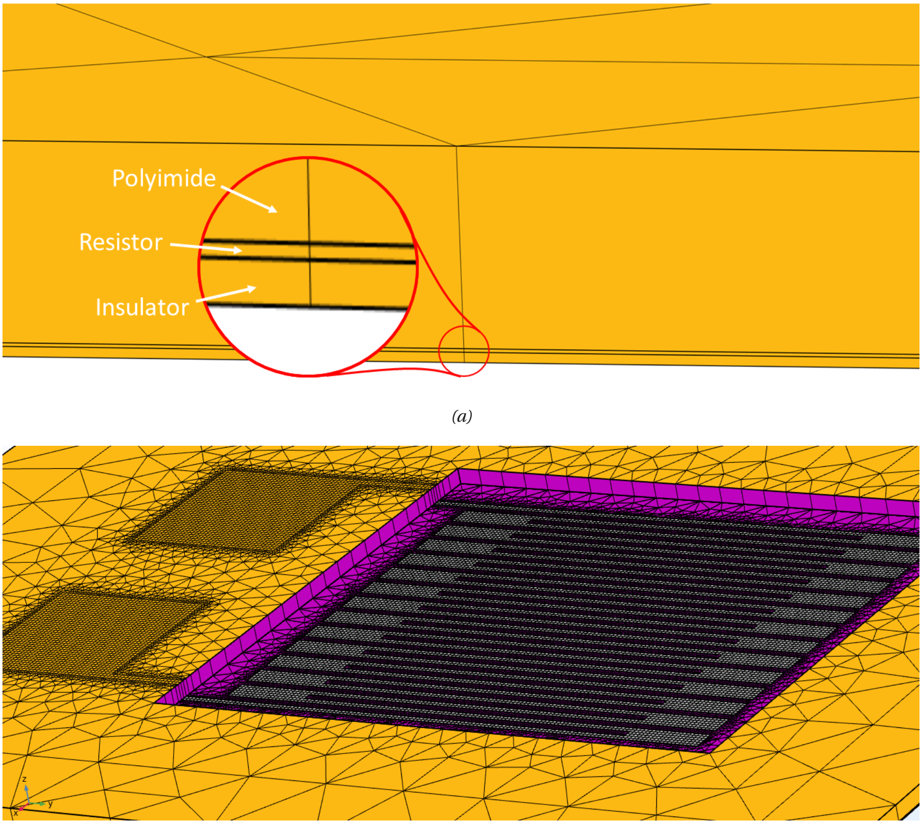

(a)

(b)

Fig. C.2: (a) Mesh detail of the EVA sublayers containing the humistat. *(b)* Detail of the layer sectioning and its meshing.

The physics defined for the model is also simplified to reduce the number of FEA variables. In fact, only the heat transfer in solids, the electric currents and the resulting electromagnetic heating are considered to account for the joule heating of the resistor and

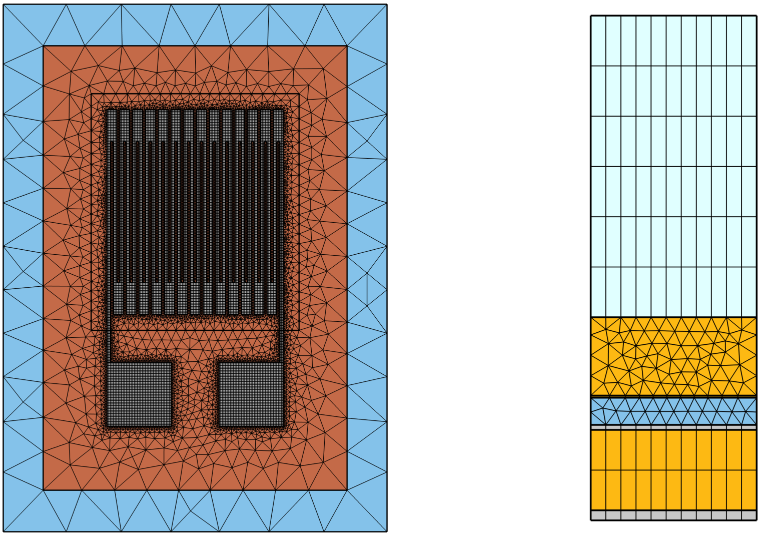

(a) *(b)*

Fig. C.3: (a) Top view of the resistor with the resulting planar mesh. (b) Mesh overview of the model (side view).

the subsequent heat dissipation through the materials. As such, a constant DC current is applied to one contact pad, while the other is set as ground (0 V). Meanwhile, only heat conduction is considered between layers, while only convection occurs at the top and bottom surface. Regarding heat convection, the top and bottom heat transfer coefficients were estimated following the approach implemented by Armstrong and Hurley [171] at a wind speed of 0.77 m/s, which results in an almost double coefficient at the top surface compared to the bottom surface. Regarding the boundary conditions, it is assumed that the sensor is operated at night time when the module is in thermal equilibrium with its surroundings at ambient temperature (20 °C), therefore no internal heat source other than the resistor is present. By considering the small cutout (<4 mm^2) as centered on the module – thus at the furthest point from the module's edges –, it can be assumed that the internal lateral surfaces remain at constant ambient temperature, in view of the substantial thermal mass of the full module: indeed, the mass of the cutout is less than 3 ppm when a 1.661 m by 0.997 m module [175] is considered.

To further reduce the complexity of the FEA, a steady-state analysis is performed, since an estimation of the maximal achievable response of the device is sufficient for the purpose of this model. As previously mentioned, the physics of moisture absorption and diffusion is not contemplated; nonetheless, the effect of moisture on the sensor can be evaluated by simulating each scenario (e.g. different driving current and insulation thickness) twice, once in dry and once in wet conditions. Based on the material datasheet of the Durimide 7020 polyimide by Fujifilm, the dry and wet conditions are defined by a water-polymer mass ratio of 0% and 1%, respectively. Finally, a simulation was carried out by varying the bias current ([0.16, 0.18, 0.20] A), the insulation thicknesses ([0.3, 0.6, 1] μ*m*), and the water mass ratio (0% & 1%). Table C.2 reports the obtained results, where the voltage difference (ΔV) refers to the difference between the achieve output voltages at dry and wet conditions – thus between reference heater and thermoresistive humidity sensor. As can be observed, the response of the sensor does not sensibly change with the thickness of the silicon oxide insulator *in steady-state conditions*, yet increases with the bias current and ranges between 0.75 mV and 1.63 mV in a non-linear fashion. Nonetheless, the insulator with its thickness might affect the reading of the sensor in a *transient state*, potentially reducing the response time of the device. Hence, this feature is still considered in the design of the humistat to be experimentally investigated.

Table C.2: Simulation results.

SiO_2 Thickness [μm]	**Bias current** [A]	**ΔV** [mV]
0.3	0.16	0.75
0.3	0.18	1.12
0.3	0.20	1.63
0.6	0.16	0.75
0.6	0.18	1.12
0.6	0.20	1.63
1.0	0.16	0.75
1.0	0.18	1.12
1.0	0.20	1.63

Regarding the heat dissipation, Fig. C.4 and Fig. C.5 depict the temperature profile at a centered cross-section of the resistor under a 0.16 A and 0.2 A bias current, respectively. As shown, the maximum temperature significantly rises with the increasing bias, surging from about 51 °C to above 70 °C. Due to time constraints and in view of the achieved results, an insulator thickness of 300 nm was selected for the first batch of fabricated sensors to proceed to the subsequent design phase of the devices, with the intention to vary such thickness in the following batches.

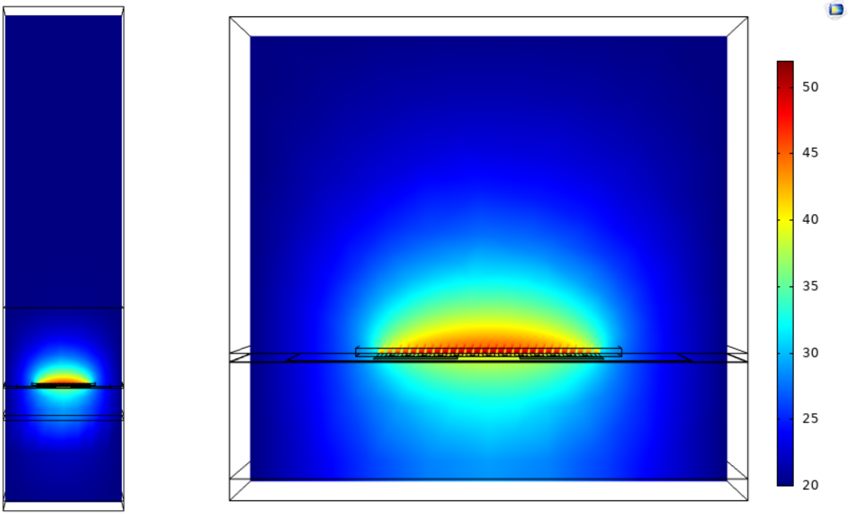

Fig. C.4: Temperature profile along the cross-section centered on the resistor at 0.16 *A* current bias. *Left*: overview – *Right*: detail.

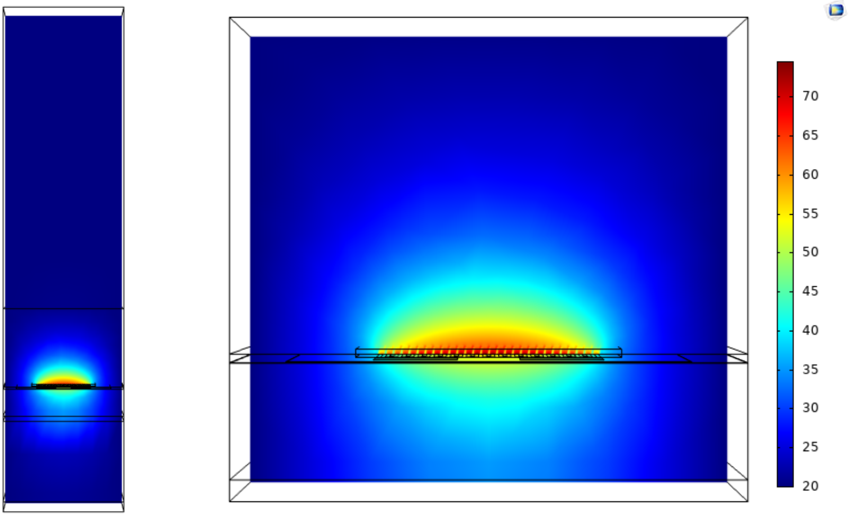

Fig. C.5: Temperature profile along the cross-section centered on the resistor at 0.2 *A* current bias. *Left*: overview – *Right*: detail.

D

COMPLETE PROCESSING FLOWCHARTS

D.1. FLOWCHART WITH COMB-FINGER CAPACITOR

STARTING MATERIAL

Table D.1: Silicon wafer specifications

Parameter	**Value**
Diameter	99.7 - 100.3 [mm]
Method/Dopant/Type:	PV-FZ/Phos/N
Thickness	255 - 305 [μm]
Finish	Polished
Orientation	(100) ± 1°
Resistivity	1 - 5 [Ωcm]

ZERO LAYER: ALIGNMENT MARKS

1. **Coating**

   Use the coater station of the EVG120 system to coat the wafers with photoresist.

   Use programm “1 - Co - 3012 – zero layer”. No EBR alternative: "1 - Co - 3012 – 1,4µm -NoEBR"

2. **Alignment and exposure**

Processing will be performed on the ASML PAS5500/80 automatic wafer stepper. Expose mask COMURK with job Litho\FWAM (note: choose Layer 1).

Exposure Energy: 120 mJ/cm^2

3. **Developing**

   Use the developer station of the EVG120 system to develop the wafers.

   Use program “1-Dev - SP”.

4. **Inspection**

   Visually inspect the wafers through a microscope:

   - No resist residues are allowed
   - Check the linewidth of the structures
   - Check the overlay of the exposed pattern if the mask was aligned to a previous pattern on the wafer

5. **Plasma etching: Alignment markers into Silicon**

   Use the Tricon Ωmega 201 plasma etcher.
   Use sequence URK_NPD (with a platen temperature of 20 °C) to etch 120 nm deep alignment markers into the Si.

6. **Layer stripping: Photoresist**

   Strip resist: Use the Tepla Plasma 300 system to remove the photoresist in an oxygen plasma.

   Follow the instructions specified for the Tepla stripper, and use the quartz carrier.

   Use program 1: 1000 Watts power and automatic endpoint detection + 2 min. overetching.

7. **Standard cleaning: HNO_3 99% and 69.5%**

   Equipment: Cleaning bench - HNO_3 99% Si (RT) and HNO_3 69.5% Si (110 °C) Ahead of cleaning, check if heating of HNO_3 69.5% is on.

   Clean: Cleaning 10 minutes in fuming nitric acid (99%) at ambient temperature.
   Use wet bench "HNO_3 (99%)" and the carrier with the white dot.

   Rinse: Rinsing in the DI water with the standard program until the resistivity is 5 MΩ or duration of 5’.

   Clean: Cleaning 10 minutes in concentrated nitric acid (69.5%) at 110 °C.
   Use wet bench “HNO_3 (69.5%)” and the carrier with the white dot.

   Rinse: Rinsing in the DI water with the standard program until the resistivity is 5 MΩ or duration of 5’.

Dry: Use the Spin Rinse Dryer (SRD) - “Avenger Ultra-Pure 6” rinser/dryer - with the standard program, and the carrier with a red dot.

FIRST LAYER: INSULATION LAYER

9. **Wet oxidation: 300 nm thermal SiO_2**

   Place the wafers in the furnace tube C1.

   Use program "WETOX".

   Oxidation time: 16’ 29" (expected thickness: $300nm$)

10. **Measurement: Oxide thickness**

    Use the Leitz MPV-SP measurement system for layer thickness measurements.

    Use program: Th. SiO2 on Si, >50nm auto5pts

11. **Coating**

    Use the coater station of the EVG120 system to coat the wafers with photoresist.

    Use programm “1 - Co - 3012 - 1,4μm”. No EBR alternative: "1 - Co - 3012 – 1,4µm -NoEBR"

12. **Alignment and exposure**

    Processing will be performed on the SUSS contact aligner.

    Expose mask "INSULATOR" with the recipe "2_FSA_soft_contact".

    Exposure energy: $127.8mJ/cm^2$

13. **Developing**

    Use the developer station of the EVG120 system to develop the wafers.

    Use program “1-Dev - SP”.

14. **Inspection**

    Visually inspect the wafers through a microscope:

    - No resist residues are allowed.
    - Check the linewidth of the structures.
    - Check the overlay of the exposed pattern if the mask was aligned to a previous pattern on the wafer.

15. **Wet etching: 300 nm oxide**

    Moisten: Rinse for 1 minute in wet bench “H_2O/Triton X-100 tbv BHF 1:7”. Use the carrier with the blue dot. The bath contains 1 ml Triton X-100 per 5000 ml deionized water.

    Etch: Use wet bench “BHF 1:7 (SiO_2 ets)” at ambient temperature, and the carrier with the blue dot. The bath contains a buffered HF solution.

    Time: Etch until the windows on the front side are hydrophobic, plus an extra 30 seconds. The required etch time depends on the layer thickness and composition. The etch rate of thermally grown oxide is 1.3 ± 0.2 nm/s at 20 °*C*. Total time: 4’ 30"

    Rinse: Rinse in the Quick Dump Rinser with the standard program until the resistivity is 5 MΩ.

    Dry: Use the “Avenger Ultra-Pure 6” rinser/dryer with the standard program, and the white carrier with a black dot.

    Inspection (microscope): All the windows must be open and the hydrophobic test may be applied.

16. **Acetone stripping: Photoresist**

    Remove the photoresist by placing the wafers into the wet bench "Acetone" and use the carrier with the two red dots.

    Time: 1’ approx.

    Temperature: 40 °*C*

17. **Standard cleaning: HNO_3 99% and 69.5%**

    Equipment: Cleaning bench - HNO_3 99% Si (RT) and HNO_3 69.5% Si (110 °*C*)
    Ahead of cleaning, check if heating of HNO_3 69.5% is on.

    Clean: Cleaning 10 minutes in fuming nitric acid (99%) at ambient temperature.
    Use wet bench "HNO_3 (99%)" and the carrier with the white dot.

    Rinse: Rinsing in the DI water with the standard program until the resistivity is 5 MΩ or duration of 5’.

    Clean: Cleaning 10 minutes in concentrated nitric acid (69.5%) at 110 °*C*.
    Use wet bench “HNO_3 (69.5%)” and the carrier with the white dot.

    Rinse: Rinsing in the DI water with the standard program until the resistivity is 5 MΩ or duration of 5’.

    Dry: Use the Spin Rinse Dryer (SRD) - “Avenger Ultra-Pure 6” rinser/dryer - with the standard program, and the carrier with a red dot.

SECOND LAYER: POLY-SI LAYER

17. **Marangoni cleaning / HF 0.55%**

    Time: ~4’ (etching) + 4’ (rinsing)

    Note: Some nm of the patterned SiO_2 layer will be etched away. Most of the area of the wafer will be hydrophobic, except the small parts covered with SiO_2.

18. **Deposition: 250 nm Poly-Si**

    Deposit 250 nm of poly-silicon by operating the E3 furnace.

    Recipe: LPOLYBIN

    Time: 1h 54’

    Use two additional test wafers for inspection.

19. **Ion Implantation: Boron (B)**

    Equipment: Varian Implanter E500HP

    Ion Species: Boron (B)

    Ion Energy: 5 keV

    Dose: 5e14 $ions/cm^2$

    Use the two additional test wafers too.

20. **Standard cleaning: HNO_3 99% and 69.5%**

    Equipment: Cleaning bench - HNO_3 99% Si (RT) and HNO_3 69.5% Si (110 °C) Ahead of cleaning, check if heating of HNO_3 69.5% is on.

    Clean: Cleaning 10 minutes in fuming nitric acid (99%) at ambient temperature.
    Use wet bench "HNO_3 (99%)" and the carrier with the white dot.

    Rinse: Rinsing in the DI water with the standard program until the resistivity is 5 MΩ or duration of 5’.

    Clean: Cleaning 10 minutes in concentrated nitric acid (69.5%) at 110 °C.
    Use wet bench “HNO_3 (69.5%)” and the carrier with the white dot.

    Rinse: Rinsing in the DI water with the standard program until the resistivity is 5 MΩ or duration of 5’.

    Dry: Use the Spin Rinse Dryer (SRD) - “Avenger Ultra-Pure 6” rinser/dryer - with the standard program, and the carrier with a red dot.

21. **Annealing: B-Implanted Poly-Si**

    Anneal the boron implanted wafers in the B1 furnace.

    Recipe: OXVAR

Time: 1h

Temperature: 850 °C

22. **Standard cleaning: HNO_3 99% and 69.5%**

    Equipment: Cleaning bench - HNO_3 99% Si (RT) and HNO_3 69.5% Si (110 °C)
    Ahead of cleaning, check if heating of HNO_3 69.5% is on.

    Clean: Cleaning 10 minutes in fuming nitric acid (99%) at ambient temperature.
    Use wet bench "HNO_3 (99%)" and the carrier with the white dot.

    Rinse: Rinsing in the DI water with the standard program until the resistivity is 5 MΩ or duration of 5'.

    Clean: Cleaning 10 minutes in concentrated nitric acid (69.5%) at 110 °C.
    Use wet bench "HNO_3 (69.5%)" and the carrier with the white dot.

    Rinse: Rinsing in the DI water with the standard program until the resistivity is 5 MΩ or duration of 5'.

    Dry: Use the Spin Rinse Dryer (SRD) - "Avenger Ultra-Pure 6" rinser/dryer - with the standard program, and the carrier with a red dot.

23. **Coating**

    Use the coater station of the EVG120 system to coat the wafers with photoresist.

    Use programm "1 - Co - 3027 - 3μm". No EBR alternative: "1 - Co - 3027 - 3μm - NoEBR".

24. **Alignment and exposure**

    Processing will be performed on the SUSS contact aligner.

    Expose mask "POLYSILICON" with the recipe "2_FSA_soft_contact".

    Exposure energy: 426 mJ/cm^2

25. **Developing**

    Use the developer station of the EVG120 system to develop the wafers.

    Use program "1 - Dev – DP 1".

26. **Inspection**

    Visually inspect the wafers through a microscope:

    - No resist residues are allowed.
    - Check the linewidth of the structures.

  - Check the overlay of the exposed pattern if the mask was aligned to a previous pattern on the wafer.

27. **Plasma etching: 250 nm Poly-Si**

    Use the Tricon Ωmega 201 plasma etcher.

    Use sequence "Poly2500" (with a platen temperature of 25 °*C*) to etch 250 nm of poly-silicon.

28. **Layer stripping: Photoresist**

    Strip resist: Use the Tepla Plasma 300 system to remove the photoresist in an oxygen plasma.

    Follow the instructions specified for the Tepla stripper, and use the quartz carrier.

    Use program 1 (Recipe 01): 1000 Watts power and automatic endpoint detection + 2 min. overetching.

29. **Standard cleaning: HNO_3 99% and 69.5%**

    Equipment: Cleaning bench - HNO_3 99% Si (RT) and HNO_3 69.5% Si (110 °*C*)
    Ahead of cleaning, check if heating of HNO_3 69.5% is on.

    Clean: Cleaning 10 minutes in fuming nitric acid (99%) at ambient temperature.
    Use wet bench "HNO_3 (99%)" and the carrier with the white dot.

    Rinse: Rinsing in the DI water with the standard program until the resistivity is 5 MΩ or duration of 5'.

    Clean: Cleaning 10 minutes in concentrated nitric acid (69.5%) at 110 °*C*.
    Use wet bench "HNO_3 (69.5%)" and the carrier with the white dot.

    Rinse: Rinsing in the DI water with the standard program until the resistivity is 5 MΩ or duration of 5'.

    Dry: Use the Spin Rinse Dryer (SRD) - "Avenger Ultra-Pure 6" rinser/dryer - with the standard program, and the carrier with a red dot.

THIRD LAYER: THIN METAL LAYER

30. **Metallization: 425 nm Al (with 1% Si) at 350** °*C*

    Use the Trikon Sigma 204 sputter coater for the deposition of an aluminum metal layer on the wafers.

    Use recipe AlSi_425nm_350C to obtain a 475 nm thick layer.

    Visual inspection: The metal layer must look shiny.

31. **Coating**

    Use programm "1 - Co - 3012 - 1.4μm". No EBR alternative: "1 - Co - 3012 - 1.4μm - NoEBR"

32. **Alignment and exposure**

    Processing will be performed on the SUSS contact aligner.

    Expose mask "METAL1" with the recipe "2_FSA_soft_contact".

    Exposure energy: 142 mJ/cm^2

33. **Developing**

    Use the developer station of the EVG120 system to develop the wafers.

    Use program “1-Dev – SP”.

34. **Inspection**

    Visually inspect the wafers through a microscope:

    - No resist residues are allowed.
    - Check the linewidth of the structures.
    - Check the overlay of the exposed pattern if the mask was aligned to a previous pattern on the wafer.

35. **Plasma etching: 425 nm Aluminum (sputtered at 350 °C)**

    Use the Trikon Ωmega 201 plasma etcher.

    Use sequence "al05_350" (with a platen temperature of 25 °C) to etch 425 nm of Aluminum.

36. **Aluminum fence removal**

    Plasma strip: Use the Tepla plasma system to remove the photoresist in an oxygen plasma. Follow the instructions specified for the Tepla stripper, and use the quartz carrier. Use program 1: 1000 watts power and automatic end point detection + 2 min. overetching.

    Moisten: Rinse for 1 minute in wet bench “H_2O/Triton X-100 tbv AL. Ets”. Use the carrier with the yellow dot. The bath contains 1 ml Triton X-100 per 5000 ml deionized water.

    Etching: Use wet bench “Al. ets 35 °C”, and the carrier with the yellow dot. 1 liter buffered aluminium etch fluid contains: 770 ml concentrated phosphorus acid (H_3PO_4 85%), 19 ml concentrated nitric acid (HNO_3 65%), 140 ml concentrate acetic acid (CH_3COOH 100%) and 71 ml deionized water.

    Etch time: 30". 75 nm of aluminium will be lost.

    QRD: Rinse in the Quick Dump Rinser with the standard program until the resistivity is 5 MΩ.

Drying: Use the “Avenger Ultra-Pure 6” rinser/dryer with the standard program, and the white carrier with a black dot.

37. **Cleaning: HNO_3 99% metal**

Clean: 10’ in fuming nitric acid at ambient temperature. This will dissolve organic materials. Use wet bench “HNO3 99% (metal)” and the carrier with the red and yellow dot.

Rinse: Rinse in Quick Dump Rinser with the standard program until the resistivity is 5 MΩ.

Dry: Use the “Avenger Ultra-Pure 6” rinser/dryer with the standard program, and the white carrier with a black dot.

Note: Do not perform a “HNO3 69.5% 110C Si” cleaning step!

FOURTH LAYER: THICK METAL LAYER

38. **Coating**

Use the coater station of the EVG120 system to coat the wafers with photoresist.

Use programm “Co - Nlof - 3.5μm”. No EBR alternative: “Co - Nlof - 3.5μm - NoEBR”

39. **Alignment and exposure**

Processing will be performed on the SUSS contact aligner.

Expose mask "METAL2" with the recipe "2_FSA_soft_contact".

Exposure energy: 73 mJ/cm^2

40. **Developing**

Use the developer station of the EVG120 system to develop the wafers.

Use program “1-Dev – DP 2”.

41. **Inspection**

Visually inspect the wafers through a microscope:

- No resist residues are allowed.
- Check the linewidth of the structures.
- Check the overlay of the exposed pattern if the mask was aligned to a previous pattern on the wafer.

42. **Metal evaporation (@CR10,000): 1000 nm Aluminum**

    Equipment: Provac Evaporator in CR10,000

    Use recipe: Al-Ag-Al-1000

    Note: Precautions for contaminated wafers must be taken from now on

43. **Lift-off (@SAL)**

    Equipment: Ultrasonic cleaner with NMP in SAL

    Time: until no metal residue is present on the wafer (30" approx).

    Check if the photoresist is removed under a microscope.

44. **Cleaning: HNO_3 (@SAL)**

    Clean: 10’ in fuming nitric acid at ambient temperature. This will dissolve organic materials. Use wet bench for contaminated wafers in SAL.

    Rinse: Rinse for 5’.

    Dry: Spin dry for 1’.

FIFTH LAYER: POLYIMIDE LAYER

Note #1: Should be finished in half a day

Note #2: Precautions for contaminated wafers must be taken

46. **Manual coating (@PolymerLab)**

    Use the Brewer Science manual coater system to coat the wafers with Polyimide (Durimide 7020 by Fujifilm).

    Use the membrane chuck for non-contaminated wafers.

    Pour enough polyimide in the center of the wafer to obtain a circle of 2.5-3 cm in diameter.

    Spin coat for 7" at 1000 RPM with an added second for ramp-up, then for 10" at 1900 RPM with an added second for ramp-up.

    Note: The polyimide must be at room temperature before pouring.

47. **Manual baking (@PolymerLab)**

    Use the hotplate for contaminated wafers to soft bake the spin-coated Polyimide (Durimide 7020 by Fujifilm).

    Bake for 12’ at 70 $°C$ first, then 12’ at 100 $°C$.

48. **Inspection and cleaning (@PolymerLab)**

    Visually inspect the back side of the wafers and clean with acetone.

    Also clean the edge of the wafer with a Q-tip with HTRD2 developer.

    No polyimide residues are allowed.

49. **Alignment and exposure**

    Processing will be performed on the SUSS contact aligner.

    Expose mask "POLYIMIDE" with the recipe "6_FSA_proximity".

    Exposure energy: 250 mJ/cm^2

50. **Post Exposure Delay (PED)**

    Perform Post-Exposure Delay for approx. 30’ at ambient temperature.

51. **Manual developing (@PolymerLab)**

    Use the developer red room.

    Develop the polyimide with HTRD2, dry the wafers with the nitrogen gun, rinse with RER600 (approx. 2’) and spin-dry for 1’ .

52. **Final cure (@PolymerLab)**

    Equipment: Koyo oven

    Cure: 1h at 350 °C and under low N_2 flow (standard)

    Programme: 7.

E

DATA PROCESSING

THE aluminum resistors and the doped poly-silicon piezoresistors are interrogated after their processing in the cleanroom (see Section 4.1) by means of the Cascade probe station to investigate their resistive response at varying temperatures. To achieve this, two-point measurements are performed at four different temperatures (30 °*C*, 50 °*C*, 70 °*C*, and 90 °*C*) by biasing the devices with a symmetric voltage sweep – 401 linearly-spaced points between ±5 *V* and ±20 *V* for the resistors and the piezoresistors, respectively. From the output current, the resistance of the devices is evaluated in accordance with Eq. 2.10.

Fig. E.1, E.2 and E.3 show the measurement results of the same eight dies on different wafers each as an example. As can be observed, the results are tainted by failed measurements. For instance, resistor R#:17 in Fig. E.1 indicates a likely loss in contact between the probe needles and the contact pads, since the resulting resistance is orders of magnitude larger than what expected at 90 °*C* only. In another instance, resistor R#:1 in Fig. E.3 clearly displays a faulty device due to the inconsistent reading at various temperature levels, in particular when compared to the other devices on the same wafer. Meanwhile, Fig. E.1 shows an unexpected behaviour of the resistors: at temperatures above 50 °*C* and for positive voltage values only, the resistance drops. Considering that this issue only arises when the *first* tested wafer is considered and is systematically present for *all* the dies, the likely explanation is the occurrence of processing issues or mistakes in the execution of measurements of this specific wafer. However, given the asymmetric nature of the device failure, it is difficult to define which measurement error might have caused it. As these errors are limited to one specific wafer, the related results are neglected in the data analysis of Section 5.1.2. Overall, the working devices display a profile analogous to that shown in Fig. E.2. For low bias values in absolute terms, the output current is too small to be accurately measured by the probe station, which explains the increasing oscillations and thus can be neglected. While stable within a small range, the measured resistance shows a slight upward curvature with increasing absolute bias. This effect is the result of the self-heating of the connections (see Eq. 2.49); however, the portion of the resistance increase that is related to the fabricated devices cannot be determined, since the performed 2-point measurement does not compensate for the electrical resistance of the probes. In any case, this systematic error is limited (<2%) and it affects similarly each device, thus it does not hinder the drawing of conclusions regarding the operation of the aluminum resistors as temperature sensors.

While the resistive temperature sensors can be operate at a fixed bias, the analysis over a voltage range is useful to determine which bias value should be considered; for the analysis of the achieved results in Section 5.1.2, a bias of -1.5 *V* is selected, which corresponds to a bias value where the effect of self-heating is negligible ($\ll$2%) and no accuracy-related issues arise. In Fig. E.4 the resistance profile of the resistors at constant bias and varying temperatures is depicted. Here, each plot combines the results of the various resistors fabricated on different wafers and with different finger spacing, in view of the negligible electrical resistance offered by the end-loops described in Section 3.1.1. In such figure, each color indicates a distinct spacing value; as can be noted, no color separation occurs, which implies that the measured electrical resistance of the resistors with different finger spacing is similarly distributed. Consequently, no sensible systematic shift in resistance due to the added resistance of the different resistor end-loops is observed, which confirms that their resistance can be neglected. Furthermore, an upper resistance limit of 300 Ω is considered in Fig. E.4 which discards any wrong measurement that may result from a loss of contact of the probes. However, this is not sufficient to remove all outliers, as demonstrated by a number of "rogue" zig-zag lines shown in the figure; by removing these and the imposed color sequence, Fig. E.5 is finally obtained. The measurement data of the reference temperature sensors is processed similarly and the results are shown in Fig. E.6

The data obtained from the poly-silicon piezoresistors can be processed similarly to the metal resistors. However, the response of the devices is less stable in this case across the voltage sweep, as depicted in Fig. E.7. Profiles similar to P#:1 and P#:8 in the figure may be a result of the inherent inaccuracy at low absolute bias voltage: as the resistance is 2-3 orders of magnitude larger than the one of the metal resistors, the output current is much lower. This type of profile seems to reach an approximately stable region at a certain bias. Meanwhile, no reasonable explanation can be found for profiles such as the case of P#:4 and P#:5 in Fig. E.7, especially when these are compared to their respective counterparts on other wafers, e.g. P#:4 and P#:5 in Fig. E.8. In fact, such type of profile displays a sudden drop in resistance (up to ~60 %) at a certain absolute bias voltage, followed by a region of highly unstable readings; additionally, such profile is neither consistent across wafers, nor symmetrical, nor necessarily occurring in both identical piezoresistors present on the same strain sensing platform. Most likely, the inconsistent resistance reading is a result of a fabrication-related issue. Nonetheless, an overall stable interval can be observed between 5 V and 7.5 V bias voltage, as illustrated in Fig. E.9. Therefore, in an analogous manner to the case of the metal resistor, a bias potential of +7.5 V is selected for the result discussion in Section 5.1.2, while all the data series with measured resistance above 1 $M\Omega$ are discarded. Unfortunately, no clear trend emerges out of the remaining plots of the devices, as shown in Fig. E.10. Nonetheless, based on the results achieved by Lu *et al.* in their analysis of the effects of doping on poly-silicon films [157], it is assumed that an approximately linear decrease in resistance represents the profile of a functioning piezoresistor within the temperature range under study. Consequently, Fig. E.11 is obtained by removing the data which strongly differs from a linear trend.

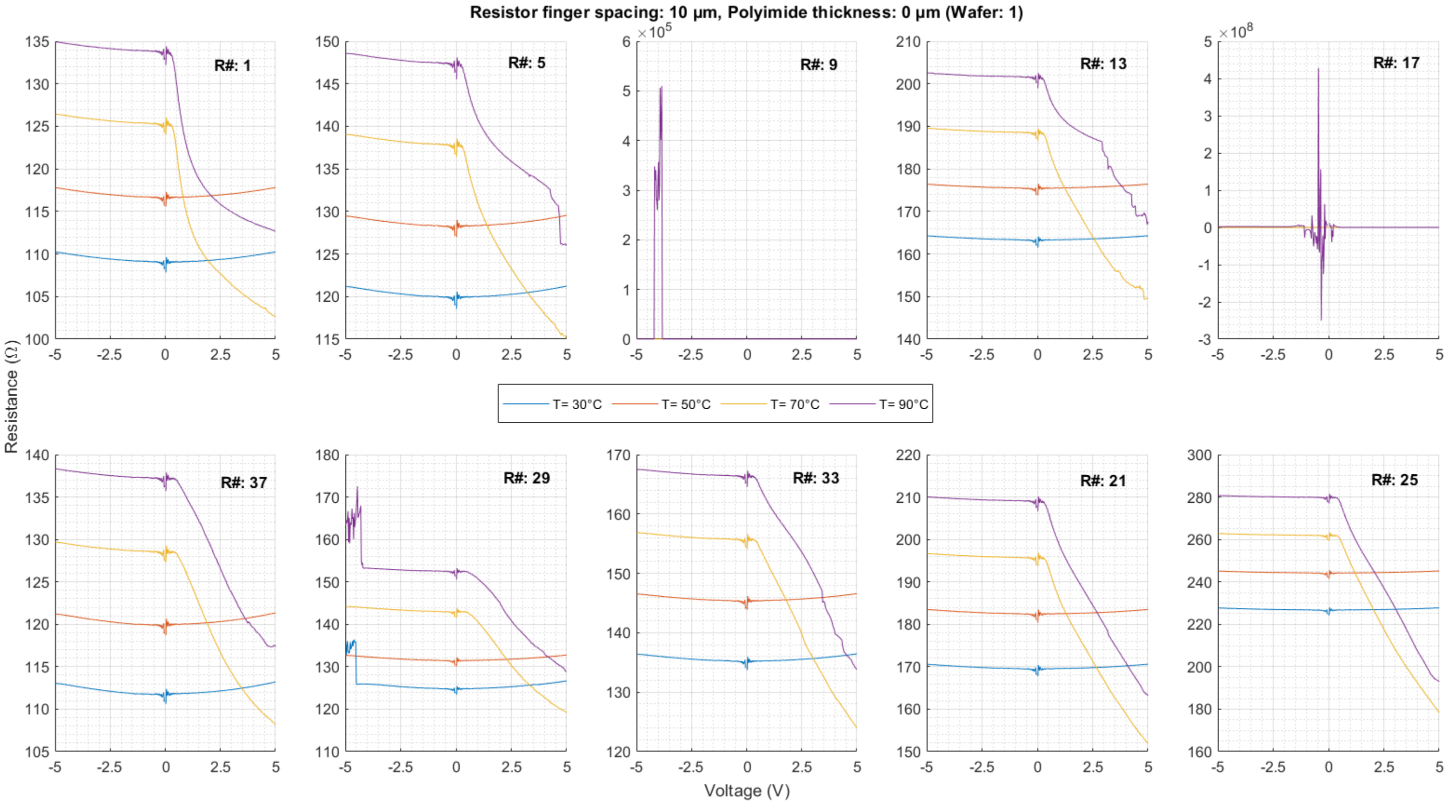

Fig. E.1: Resistance values vs input voltage at various temperatures for each resistor finger length of the RTDs with no polyimide and a finger spacing of 10 μ*m* on the *first* wafer tested, and over the full voltage sweep. The first row is dedicated to the resistors located on the top side of the wafer, while the second to those on the bottom side. The resistor number (R#) follows the order outlined in Fig. 3.8.

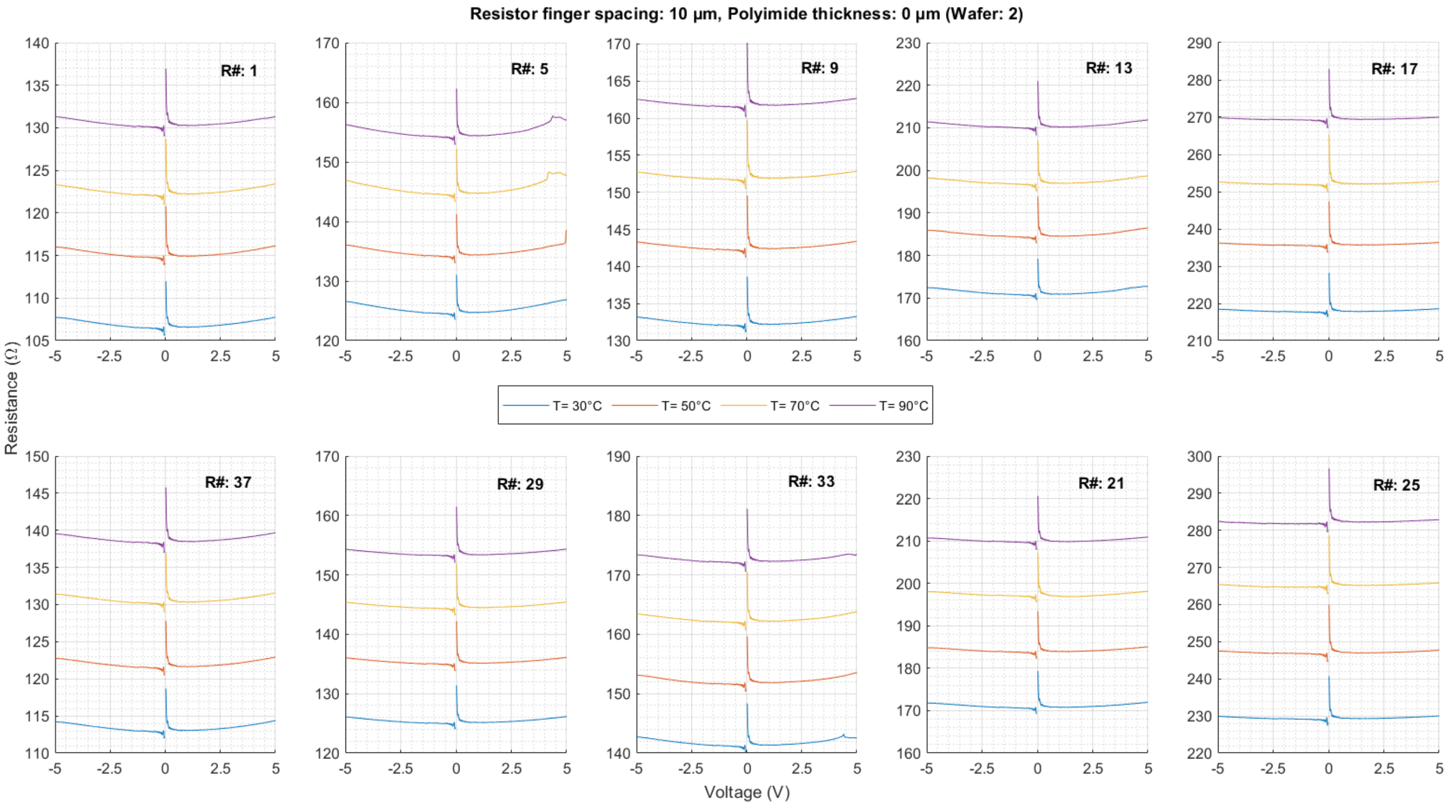

Fig. E.2: Resistance values vs input voltage at various temperatures for each resistor finger length of the RTDs with no polyimide and a finger spacing of 10 µ*m* on the *second* wafer tested, and over the full voltage sweep. The first row is dedicated to the resistors located on the top side of the wafer, while the second to those on the bottom side. The resistor number (R#) follows the order outlined in Fig. 3.8.

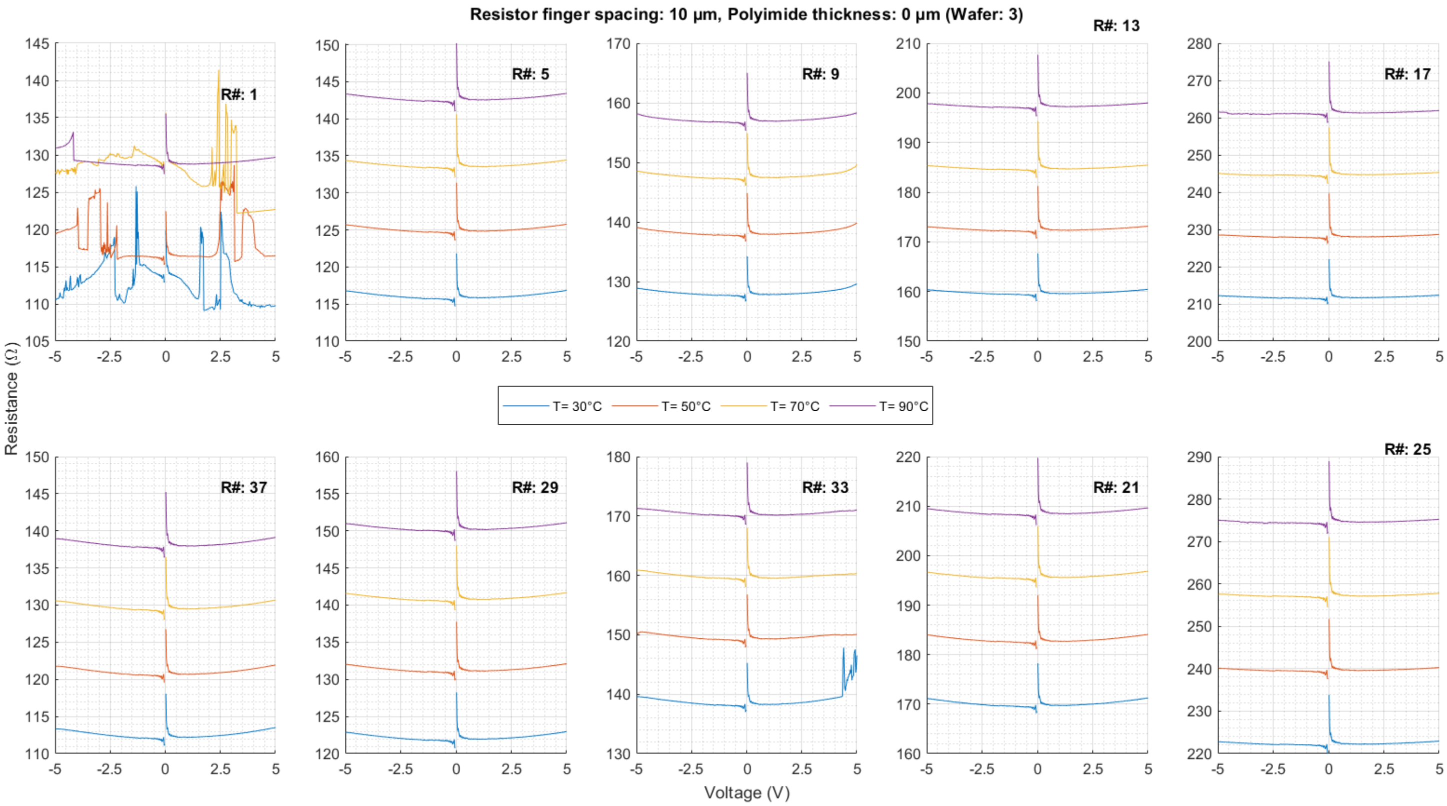

Fig. E.3: Resistance values vs input voltage at various temperatures for each resistor finger length of the RTDs with no polyimide and a finger spacing of 10 μm on the *third* wafer tested, and over the full voltage sweep. The first row is dedicated to the resistors located on the top side of the wafer, while the second to those on the bottom side. The resistor number (R#) follows the order outlined in Fig. 3.8.

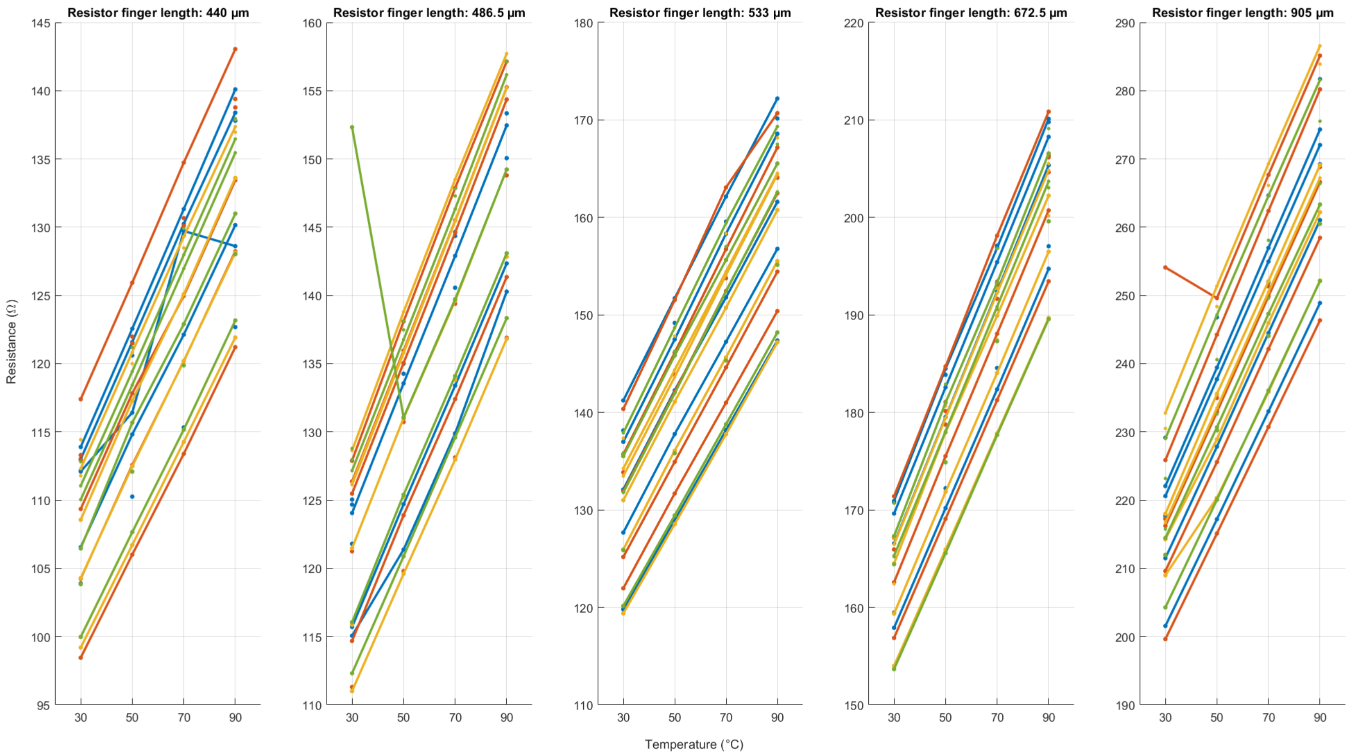

Fig. E.4: Resistance vs. temperature profile of all the resistors with the same finger length. Here, each color represents a different spacing between fingers and a number of lines have been hidden to make the image clearer.

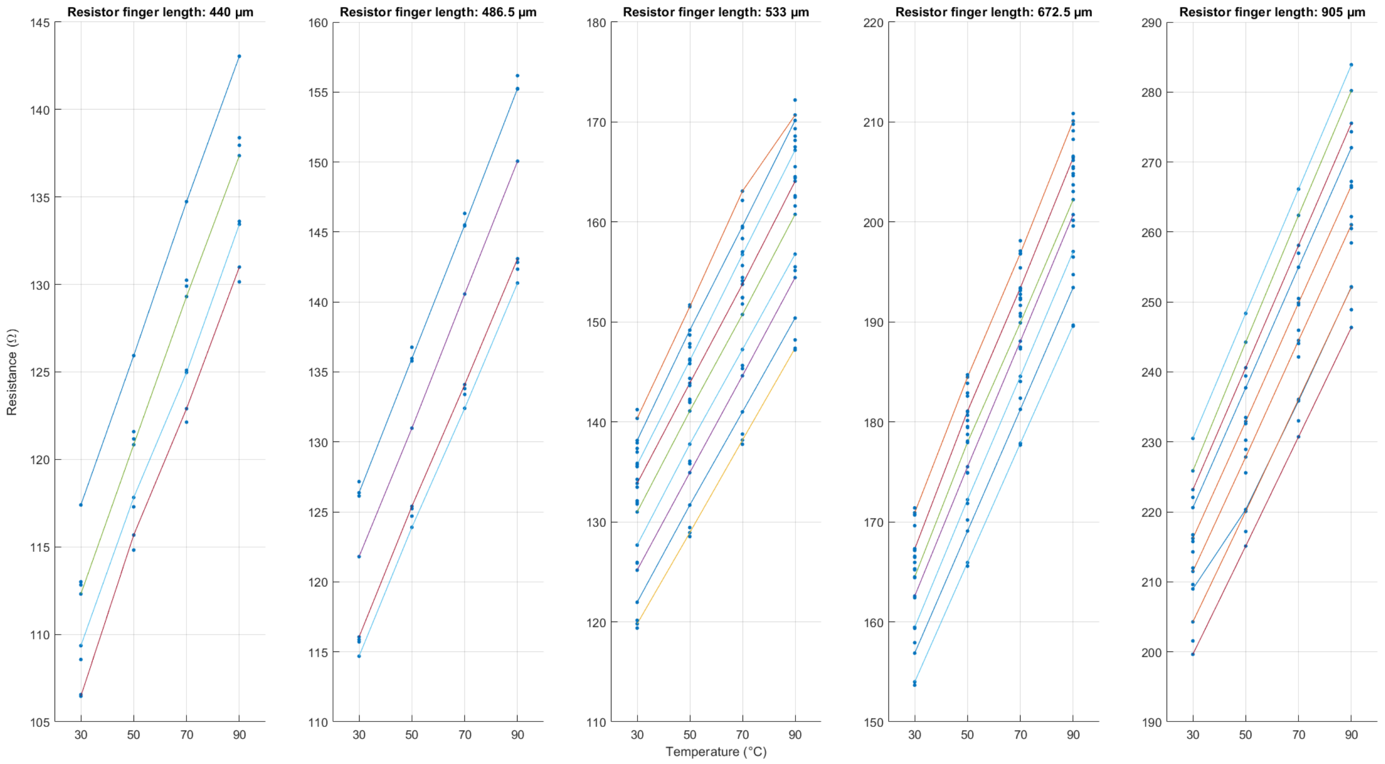

Fig. E.5: Scatter plot of the results deriving from the thermal characterization of the RTD variations divided based on the resistor finger length (see Fig. 3.8 and 3.9), showing the change in resistance at increasing temperatures. Each point at each temperature represents the measured resistance at -1.5 V bias voltage of a sensor belonging to a specific die of specific wafer tested. A number of colored lines, each connecting the markers related to a specific RTD, are drawn to better visualize the response of the devices.

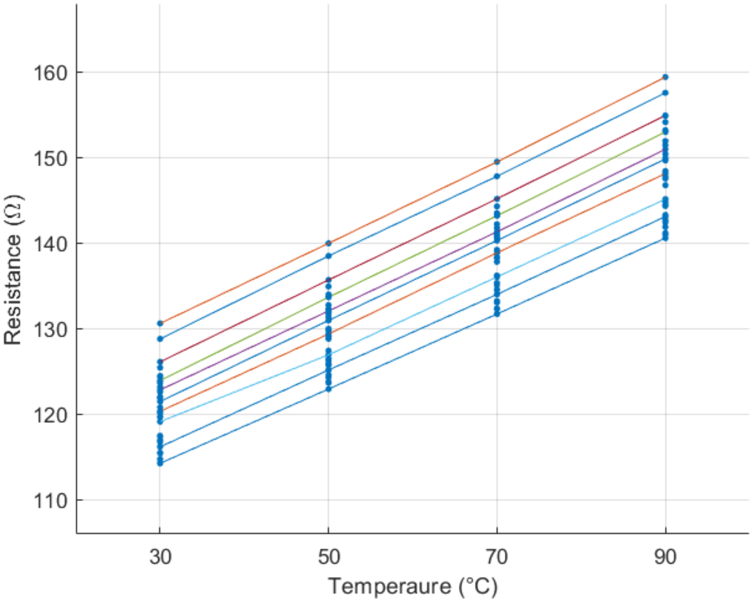

Fig. E.6: Scatter plot of the results deriving from the thermal characterization of the reference RTDs (see Fig. 3.8 and 3.9), which shows the change in resistance at increasing temperatures. Each point at each temperature represents the measured resistance at -1.5 *V* bias voltage of a sensor belonging to a specific die of specific wafer tested. A number of colored lines, each connecting the markers related to a specific RTD, are drawn to better visualize the response of the devices.

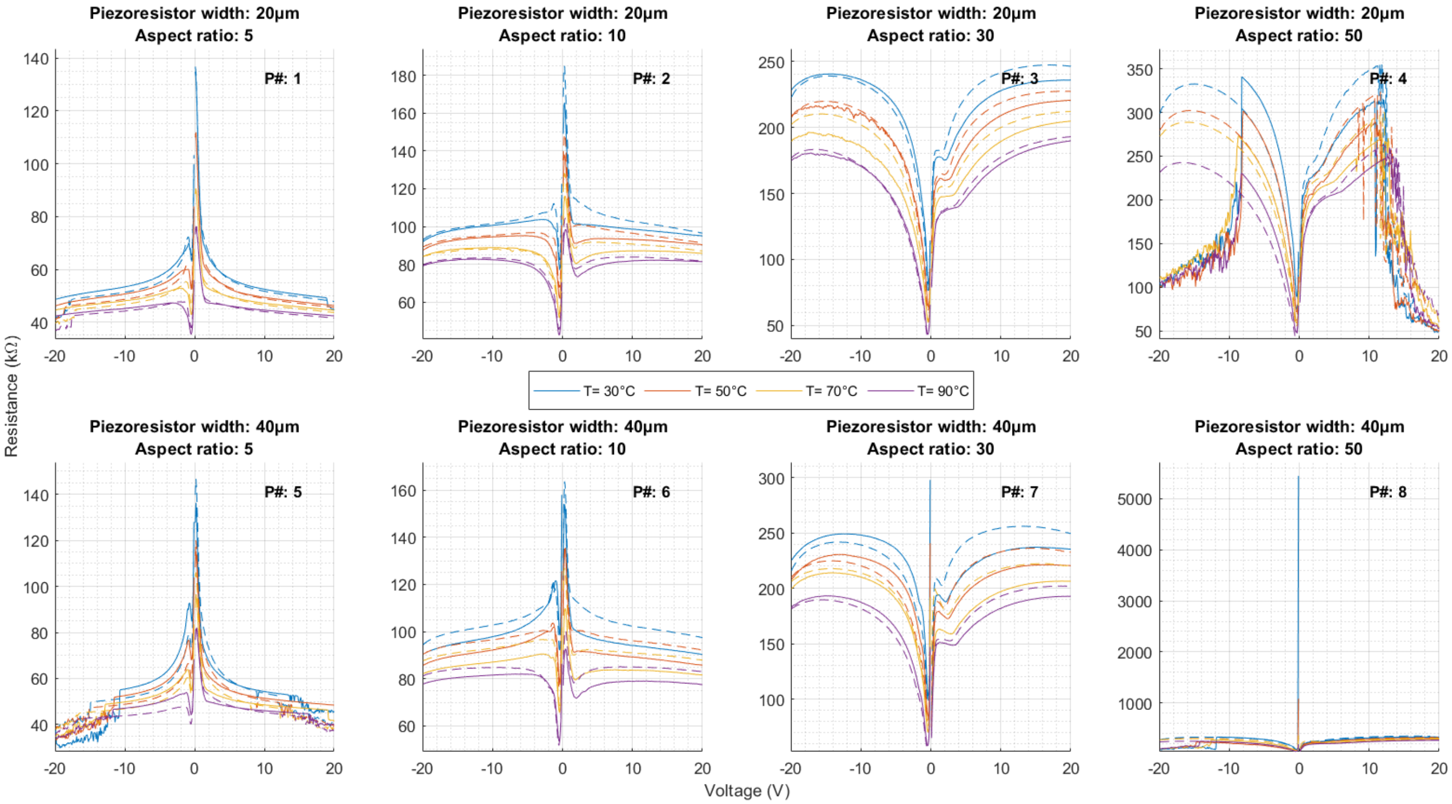

Fig. E.7: Resistance values vs input voltage profile of each piezoresistor located on the *first* wafer tested over the full voltage range and at various temperatures. The full lines are related to the top piezoresistors (horizontal to the primary flat of the wafer), while the intermittent lines indicate the bottom piezoresistors (vertical) (see Fig. 3.7b).

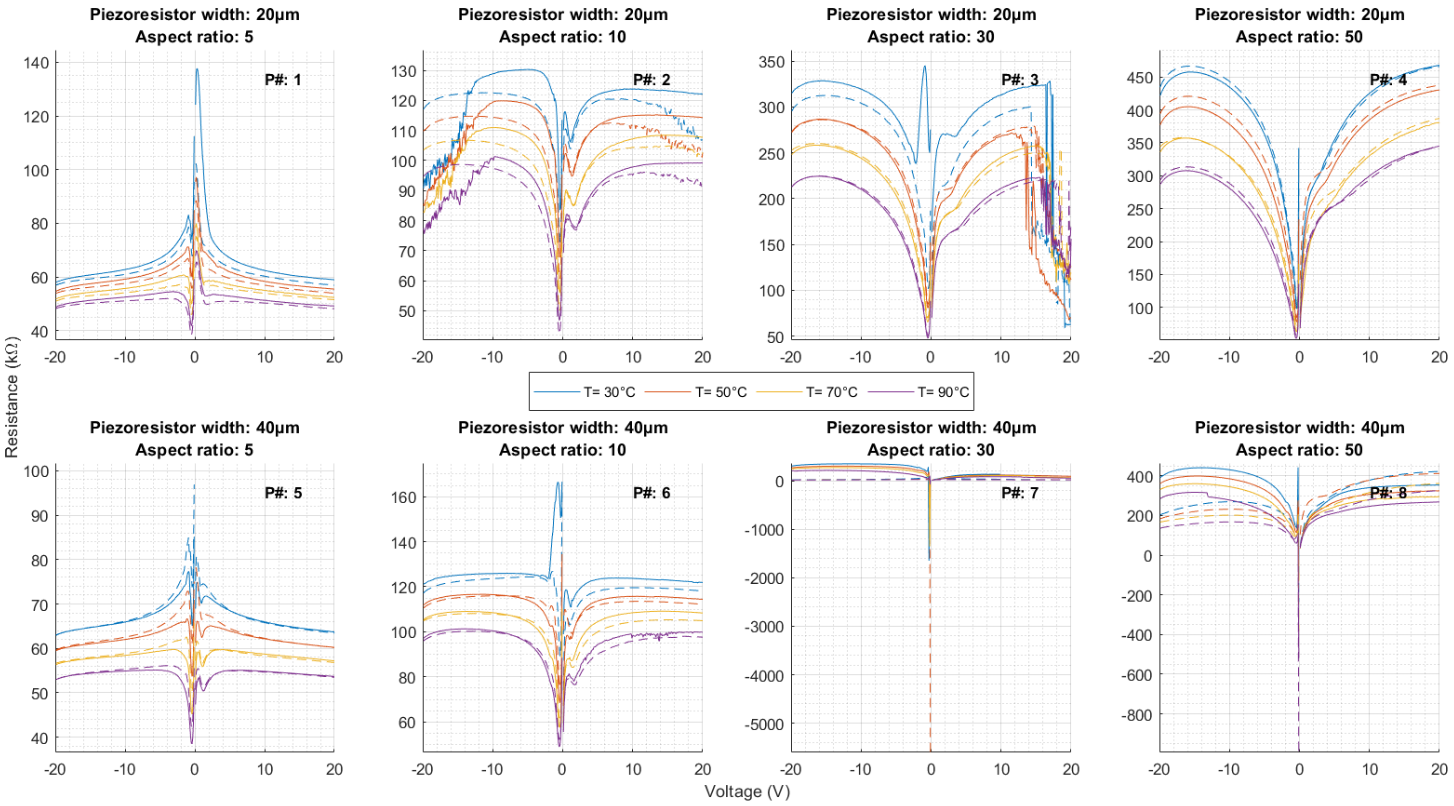

Fig. E.8: Resistance values vs input voltage profile of each piezoresistor located on the *second* wafer tested over the full voltage range and at various temperatures. The full lines are related to the top piezoresistors (horizontal to the primary flat of the wafer), while the intermittent lines indicate the bottom piezoresistors (vertical) (see Fig. 3.7b).

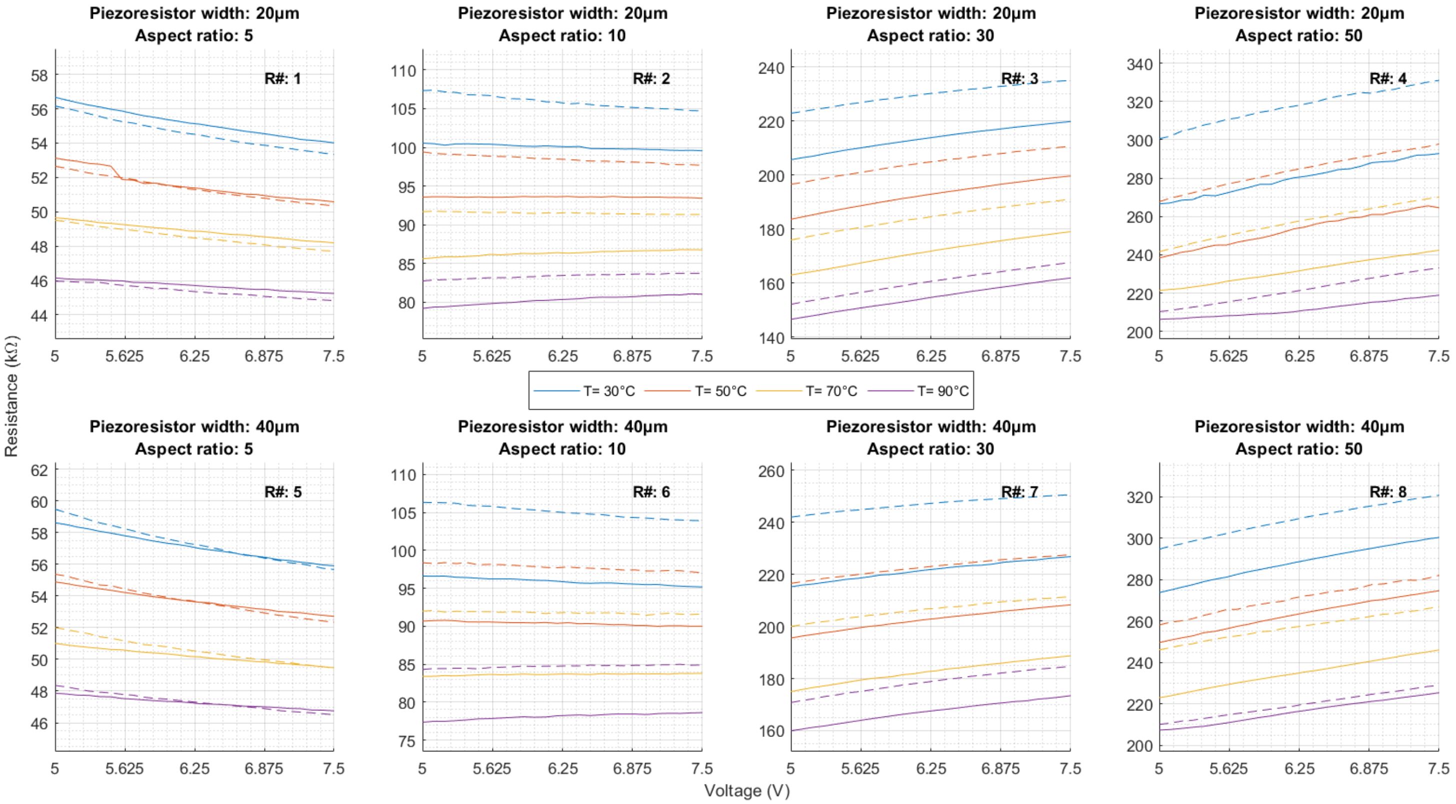

Fig. E.9: Resistance values vs input voltage profile of each piezoresistor located on the *first* wafer tested over the selected voltage range and at various temperatures. The full lines are related to the top piezoresistors (horizontal to the primary flat of the wafer), while the intermittent lines indicate the bottom piezoresistors (vertical) (see Fig. 3.7b).

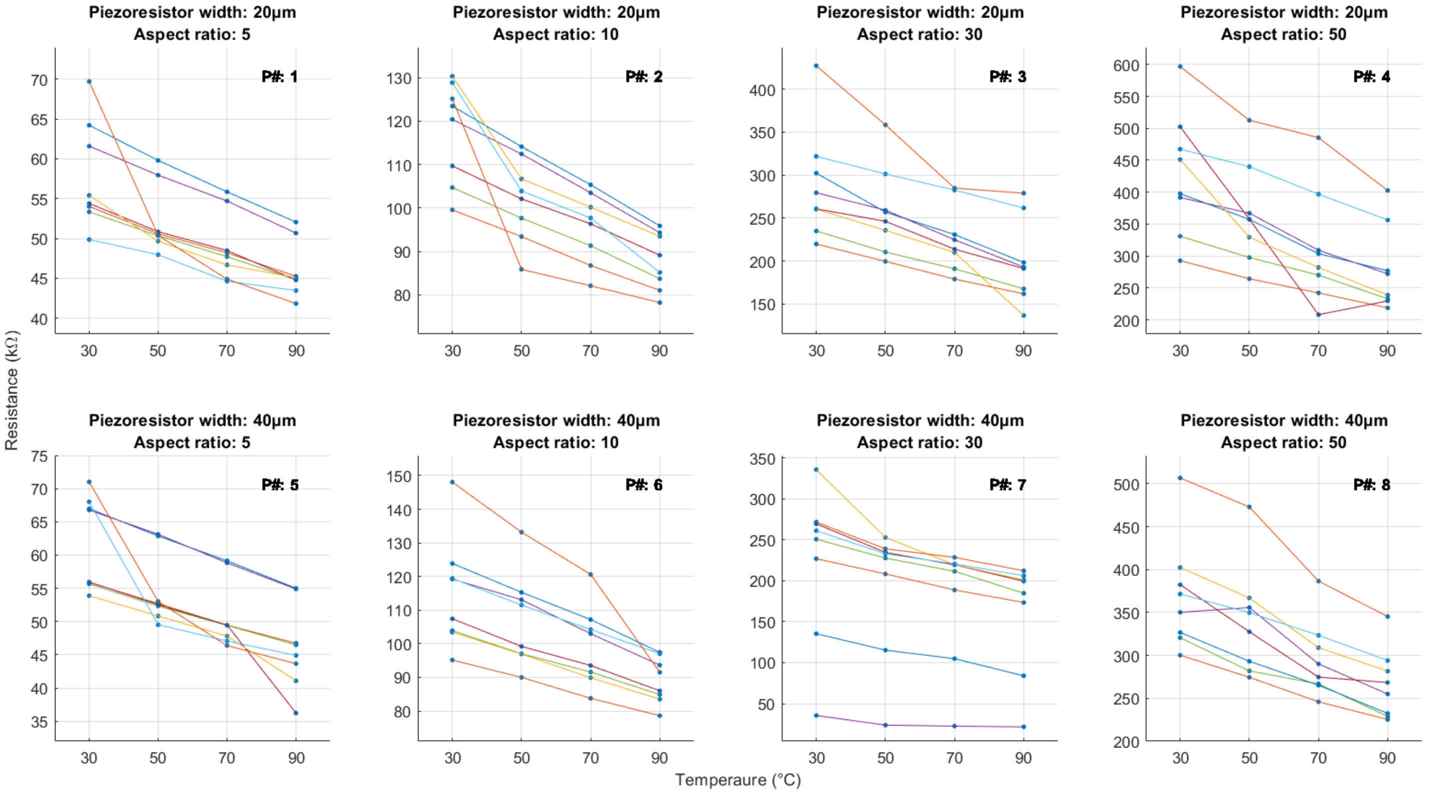

Fig. E.10: Scatter plot of the results deriving from the thermal characterization of the strain sensor variations divided based on the width and aspect ratio (see Fig. 3.8 and 3.9), showing the change in resistance at increasing temperatures. Each point at each temperature represents the measured resistance at +7.5 V bias voltage of a sensor belonging to a specific die of specific wafer tested. A number of colored lines, each connecting the markers related to a specific sensor, are drawn to better visualize the response of the devices.

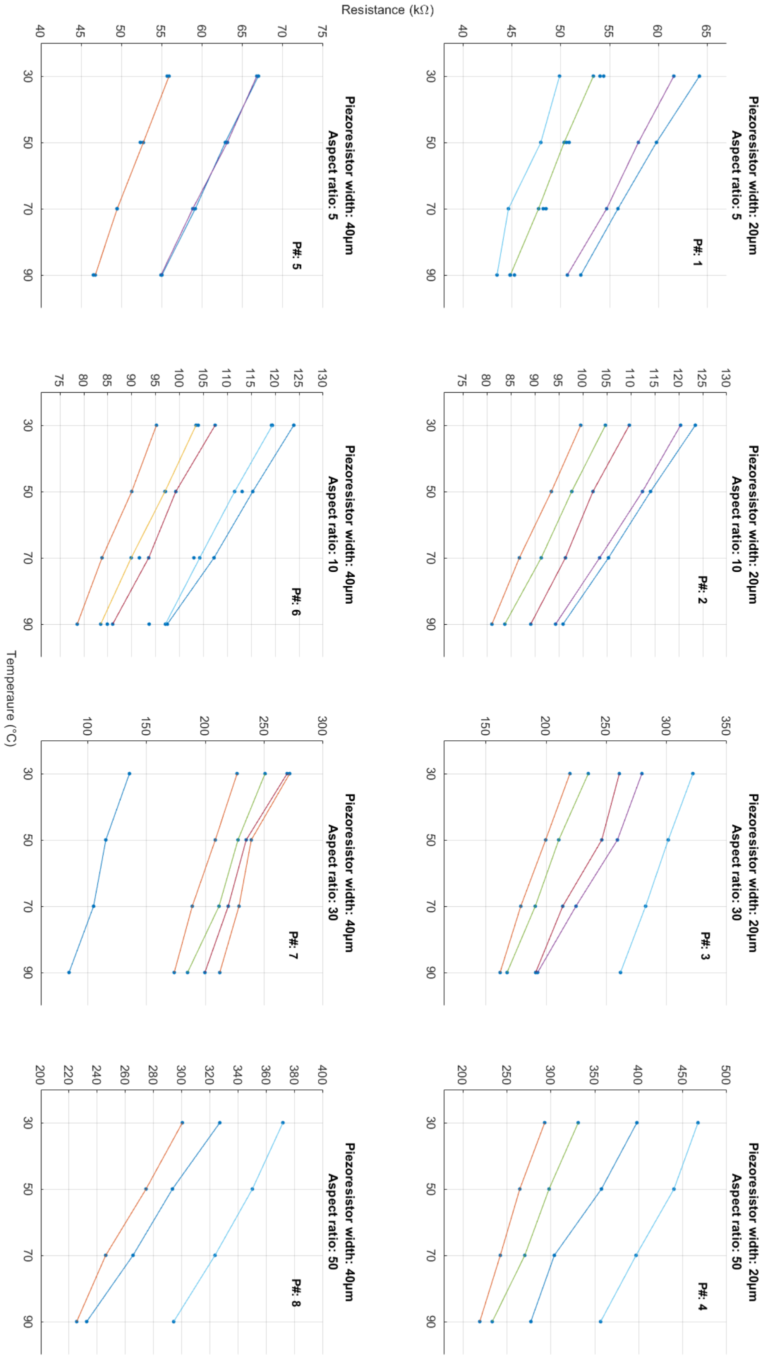

Fig. E.11: Fig. E.10 after the removal of the strongly non-linear resistance profiles.

REFERENCES

[1] F. Ackerman, E. A. Stanton, C. Hope, S. Alberth, J. Fisher, and B. Biewald, *The Cost of Climate Change*, Tech. Rep. (Natural Resources Defense Council (NRDC), 2008) https://www.nrdc.org/sites/default/files/cost.pdf.

[2] E. Vartiainen, G. Masson, C. Breyer, D. Moser, and E. Román Medina, *Impact of weighted average cost of capital, capital expenditure, and other parameters on future utility-scale pv levelised cost of electricity,* Progress in Photovoltaics: Research and Applications **28**, 439 (2020), https://onlinelibrary.wiley.com/doi/pdf/10.1002/pip.3189 .

[3] C. Rollet, *Solar costs have fallen 82% since 2010,* (2020), Date accessed: September 16th, 2021. https://www.pv-magazine.com/2020/06/03/solar-costs-have-fallen-82-since-2010/.

[4] X. Wang and A. Barnett, *The evolving value of photovoltaic module efficiency,* Applied Sciences **9** (2019), 10.3390/app9061227.

[5] IRENA, *Future of Solar Photovoltaic: Deployment, investment, technology, grid integration and socio-economic aspects (A Global Energy Transformation: paper),* Tech. Rep. (International Renewable Energy Agency, Abu Dhabi, 2019) https://irena.org/-/media/Files/IRENA/Agency/Publication/2019/Nov/IRENA_Future_of_Solar_PV_2019.pdf.

[6] *PHOTOVOLTAICS REPORT*, Tech. Rep. (Fraunhofer Institute for Solar Energy Systems, 2020) Date accessed: November 16, 2020. https://www.ise.fraunhofer.de/content/dam/ise/de/documents/publications/studies/Photovoltaics-Report.pdf.

[7] S. Ruehle, *Tabulated values of the Shockley–Queisser limit for single junction solar cells,* Solar Energy **130**, 139 (2016), 10.1016/j.solener.2016.02.015.

[8] J. Ellsmoor, *Renewable energy is now the cheapest option - even without subsidies,* (2019), Date accessed: September 16th, 2021. https://www.forbes.com/sites/jamesellsmoor/2019/06/15/renewable-energy-is-now-the-cheapest-option-even-without-subsidies/?sh=3b755e875a6b.

[9] P. Krogstrup, H. I. Jørgensen, M. Heiss, O. Demichel, J. V. Holm, M. Aagesen, J. Nygard, and A. Fontcuberta i Morral, *Single-nanowire solar cells beyond the Shockley–Queisser limit,* Nature Photonics **7**, 306 (2013), 10.1038/nphoton.2013.32.

[10] *Solar manufacturing cost analysis,* Date accessed: May 8th, 2021. https://www.nrel.gov/analysis/solar-manufacturing-cost.html.

[11] A. Louwen, W. van Sark, R. Schropp, and A. Faaij, *A cost roadmap for silicon heterojunction solar cells,* Solar Energy Materials and Solar Cells **147**, 295 (2016), 10.1016/j.solmat.2015.12.026.

[12] IRENA, *Renewable Power Generation Costs in 2020,* Tech. Rep. (International Renewable Energy Agency, Abu Dhabi, 2021) https://www.irena.org/-/media/Files/IRENA/Agency/Publication/2021/Jun/IRENA_Power_Generation_Costs_2020.pdf.

[13] Fraunhofer ISE, *Current and Future Cost of Photovoltaics. Long-term Scenarios for Market Development, System Prices and LCOE of Utility-Scale PV Systems,* Tech. Rep. (2015) study on behalf of Agora Energiewende. https://www.ise.fraunhofer.de/content/dam/ise/de/documents/publications/studies/AgoraEnergiewende_Current_and_Future_Cost_of_PV_Feb2015_web.pdf.

[14] A. Smets, K. Jäger, O. Isabella, R. Swaaij, van, and M. Zeman, *Solar energy : the physics and engineering of photovoltaic conversion technologies and systems* (UIT, 2016).

[15] B. Subudhi and R. Pradhan, *A comparative study on maximum power point tracking techniques for photovoltaic power systems,* IEEE Transactions on Sustainable Energy **4**, 89 (2013), 10.1109/TSTE.2012.2202294.

[16] L. Barroso, T. Cavalcanti, P. Giesbertz, and K. Purchala, *Classification of electricity market models worldwide,* in *International Symposium CIGRE/IEEE PES, 2005.* (2005) pp. 9–16.

[17] T. AlSkaif, S. Dev, L. Visser, M. Hossari, and W. van Sark, *A systematic analysis of meteorological variables for pv output power estimation,* Renewable Energy **153**, 12 (2020).

[18] K. R. Kumar and M. S. Kalavathi, *Artificial intelligence based forecast models for predicting solar power generation,* Materials Today: Proceedings **5**, 796 (2018), international Conference on Processing of Materials, Minerals and Energy (July 29th – 30th) 2016, Ongole, Andhra Pradesh, India.

[19] P. Mandal, S. Madhira, A. Haque, J. Meng, and R. Pineda, *Forecasting power output of solar photovoltaic system using wavelet transform and artificial intelligence techniques,* Procedia Computer Science **12**, 332–337 (2012).

[20] M. Köntges, S. Kurtz, C. Packard, U. Jahn, K. Berger, K. Kato, T. Friesen, H. Liu, M. Van Iseghem, J. Wohlgemuth, D. Miller, M. Kempe, P. Hacke, F. Reil, N. Bogdanski, W. Herrmann, C. Buerhop, G. Razongles, and G. Friesen, *Review of failures of photovoltaic modules,* (2014).

[21] F. Mavromatakis, E. Kavoussanaki, F. Vignola, and Y. Franghiadakis, *Measuring and estimating the temperature of photovoltaic modules,* Solar Energy **110**, 656 (2014).

[22] C. Buerhop, S. Wirsching, S. Gehre, T. Pickel, T. Winkler, A. Bemm, J. Mergheim, C. Camus, J. Hauch, and C. J. Brabec, *Lifetime and degradation of pre-damaged pv-modules – field study and lab testing,* in *2017 IEEE 44th Photovoltaic Specialist Conference (PVSC)* (2017) pp. 3500–3505.

[23] M. Muttillo, I. Nardi, V. Stornelli, T. de Rubeis, G. Pasqualoni, and D. Ambrosini, *On field infrared thermography sensing for pv system efficiency assessment: Results and comparison with electrical models,* Sensors **20** (2020), 10.3390/s20041055.

[24] T. Malmivirta, J. Hamberg, E. Lagerspetz, X. Li, E. Peltonen, H. Flores, and P. Nurmi, *Hot or not? robust and accurate continuous thermal imaging on flir cameras,* in *2019 IEEE International Conference on Pervasive Computing and Communications (PerCom)* (2019) pp. 1–9.

[25] M. Jankovec, F. Galliano, E. Annigoni, H. Y. Li, F. Sculati-Meillaud, L.-E. Perret-Aebi, C. Ballif, and M. Topič, *In-situ monitoring of moisture ingress in pv modules using digital humidity sensors,* IEEE Journal of Photovoltaics **6**, 1152 (2016).

[26] H. Oldenkamp, B. Litzenburger, L. Podlowski, and I. Jong, *A pv-module integrated sensor for clear, cost effective monitoring,* (2021).

[27] M. Jankovec and M. Topič, *Intercomparison of temperature sensors for outdoor monitoring of photovoltaic modules,* Journal of Solar Energy Engineering **135** (2013), 10.1115/1.4023518, 031012, https://asmedigitalcollection.asme.org/solarenergyengineering/article-pdf/135/3/031012/6323733/sol_135_3_031012.pdf .

[28] C. Hirschl, M. Granitzer, M. Spielberger, W. Muehleisen, M. Kraft, G. Kroupa, and J. Schicker, *Combined experimental and simulatory evaluation of thermal and mechanical loads on pv modules,* (2012).

[29] M. A. Green, E. D. Dunlop, J. Hohl-Ebinger, M. Yoshita, N. Kopidakis, and X. Hao, *Solar cell efficiency tables (version 58),* Progress in Photovoltaics: Research and Applications **29**, 657 (2021), https://onlinelibrary.wiley.com/doi/pdf/10.1002/pip.3444 .

[30] A. Walker, *The physics and technology of submicron MOS devices,* Ph.D. thesis, Department of Electrical Engineering (1994).

[31] J. Pelesko and D. Bernstein, *Modeling MEMS and NEMS* (CRC Press, 2002).

[32] J. C. Gealow, *Impact of Processing Technology on DRAM Sense Amplifier Design*, Master's thesis, Massachusetts Institute of Technology, 77 Massachusetts Avenue, Cambridge, MA 02139, USA (1990).

[33] G. Binnig, H. Rohrer, C. Gerber, and E. Weibel, *Tunneling through a controllable vacuum gap,* Applied Physics Letters **40**, 178 (1982), https://doi.org/10.1063/1.92999 .

[34] J. Cross, R. Opila, I. Boyd, and E. Kaufmann, *Materials characterization and the evolution of materials,* MRS Bulletin **40**, 1019 (2015).

[35] R. Bogue, *Towards the trillion sensors market,* Sensor Review **34** (2014), 10.1108/SR-12-2013-755.

[36] S. Asongu and A. Boateng, *Introduction to special issue: Mobile technologies and inclusive development in africa,* Journal of African Business **19**, 297 (2018), https://doi.org/10.1080/15228916.2018.1481307 .

[37] J. Mössinger, *Software in automotive systems,* IEEE Software **27**, 92 (2010).

[38] V. Dunjko and H. Briegel, *Machine learning & artificial intelligence in the quantum domain: A review of recent progress,* Reports on Progress in Physics **81** (2018), 10.1088/1361-6633/aab406.

[39] J. V. Abellan-Nebot and F. Romero Subirón, *A review of machining monitoring systems based on artificial intelligence process models,* The International Journal of Advanced Manufacturing Technology **47**, 237 (2010).

[40] S. Sagiroglu and D. Sinanc, *Big data: A review,* in *2013 International Conference on Collaboration Technologies and Systems (CTS)* (2013) pp. 42–47.

[41] M. H. Miraz, M. Ali, P. S. Excell, and R. Picking, *A review on internet of things (iot), internet of everything (ioe) and internet of nano things (iont),* in *2015 Internet Technologies and Applications (ITA)* (2015) pp. 219–224.

[42] W. R. Runyan, *Silicon Semiconductor Technology* (McGRAW-HILL, 1965).

[43] T. Markvart, *From steam engine to solar cells: Can thermodynamics guide the development of future generations of photovoltaics?* Wiley Interdisciplinary Reviews: Energy and Environment , n/a (2016).

[44] T. Lipka, L. Moldenhauer, L. Wahn, and H. K. Trieu, *Optofluidic biomolecule sensors based on a-si:h microrings embedded in silicon–glass microchannels,* Opt. Lett. **42**, 1084 (2017).

[45] S. M. Borisov and O. S. Wolfbeis, *Optical biosensors,* Chemical Reviews **108**, 423 (2008), https://doi.org/10.1021/cr068105t .

[46] J. Song, X. Luo, J. S. Kee, K. Han, C. Li, M. K. Park, X. Tu, H. Zhang, Q. Fang, L. Jia, Y.-J. Yoon, T.-Y. Liow, M. Yu, and G.-Q. Lo, *Silicon-based optoelectronic integrated circuit for label-free bio/chemical sensor,* Opt. Express **21**, 17931 (2013).

[47] G. A. Rodriguez, P. Markov, A. P. Cartwright, M. H. Choudhury, F. O. Afzal, T. Cao, S. I. Halimi, S. T. Retterer, I. I. Kravchenko, and S. M. Weiss, *Photonic crystal nanobeam biosensors based on porous silicon,* Opt. Express **27**, 9536 (2019).

[48] G. Mi, C. Horvath, M. Aktary, and V. Van, *Silicon microring refractometric sensor for atmospheric CO2 gas monitoring,* Opt. Express **24**, 1773 (2016).

[49] N. Moser, T. S. Lande, C. Toumazou, and P. Georgiou, *Isfets in cmos and emergent trends in instrumentation: A review,* IEEE Sensors Journal **16**, 6496 (2016).

[50] J. S. Parmar, N. Shafi, and C. Sahu, *A novel multi gate junctionfree gated resistor isfet for ph detection,* in *2019 9th Annual Information Technology, Electromechanical Engineering and Microelectronics Conference (IEMECON)* (2019) pp. 97–101.

[51] T. Karacali, U. C. Hasar, I. Y. Ozbek, E. A. Oral, and H. Efeoglu, *Novel design of porous silicon based sensor for reliable and feasible chemical gas vapor detection,* Journal of Lightwave Technology **31**, 295 (2013).

[52] R. Caroselli, D. Martín Sánchez, S. Ponce Alcántara, F. Prats Quilez, L. Torrijos Morán, and J. García-Rupérez, *Real-time and in-flow sensing using a high sensitivity porous silicon microcavity-based sensor,* Sensors **17** (2017), 10.3390/s17122813.

[53] B. Huy, T. Nguyen, T. A. Nguyen, B. Pham, T. Dang, D. Chi, Q. M. Ngo, R. Coïsson, and P. Hoi, *A vapor sensor based on a porous silicon microcavity for the determination of solvent solutions,* Journal of the Optical Society of Korea **18186010** (2014), 10.3807/JOSK.2014.18.4.301.

[54] M. Suh, *Wearable sensors for athletes,* in *Electronic Textiles,* edited by T. Dias (Woodhead Publishing, Oxford, 2015) Chap. 12, pp. 257 – 273.

[55] M. Victorino, X. Jiang, and C. Menon, *Wearable technologies and force myography for healthcare,* in *Wearable Technology in Medicine and Health Care,* edited by R. K.-Y. Tong (Academic Press, 2018) Chap. 7, pp. 135 – 152.

[56] A. Beinert, M. Imm, J. Benick, F. Becker, S. Seitz, M. Heinrich, O. Paul, S. Glunz, J. Aktaa, U. Eitner, and H. Neuhaus, *Silicon solar cell-integrated stress and temperature sensors for photovoltaic modules,* Progress in Photovoltaics Research and Applications **28**, 717 (2020).

[57] Y. Y. Iossel', É. S. Kochanov, and M. G. Strunskii, *Calculation of Electric Capacitance* ("Energy" - Leningrad branch, 1981).

[58] W. P. Eaton and J. H. Smith, *Micromachined pressure sensors: review and recent developments,* Smart Materials and Structures **6**, 530 (1997).

[59] W. Chen and X. Yan, *Progress in achieving high-performance piezoresistive and capacitive flexible pressure sensors: A review,* Journal of Materials Science & Technology **43**, 175 (2020).

[60] W. Yang, *Design of electrical capacitance tomography sensors,* Measurement Science and Technology **21**, 042001 (2010).

[61] C. G. Xie, A. L. Stott, A. Plaskowski, and M. S. Beck, *Design of capacitance electrodes for concentration measurement of two-phase flow,* Measurement Science and Technology **1**, 65 (1990).

[62] X. Hu and W. Yang, *Planar capacitive sensors - designs and applications,* Sensor Review **30**, 24 (2010).

[63] *Dielectric: Definition of dielectric,* Date accessed: April 8th, 2021. https://www.lexico.com/definition/dielectric.

[64] M. Raven, *Measuring low impedance and skin effect with a gain-phase meter,* Acta Technica CSAV (Ceskoslovensk Akademie Ved) **59**, 303 (2014).

[65] C. L. Roozeboom, M. A. Hopcroft, W. S. Smith, J. Y. Sim, D. A. Wickeraad, P. G. Hartwell, and B. L. Pruitt, *Integrated multifunctional environmental sensors,* Journal of Microelectromechanical Systems **22**, 779 (2013).

[66] C. L. Roozeboom, V. A. Hong, C. H. Ahn, E. J. Ng, Y. Yang, B. E. Hill, M. A. Hopcroft, and B. L. Pruitt, *Multifunctional integrated sensor in a 2×2 mm epitaxial sealed chip operating in a wireless sensor node,* in *2014 IEEE 27th International Conference on Micro Electro Mechanical Systems (MEMS)* (2014) pp. 773–776.

[67] J. Boudaden, M. Steinmaßl, H.-E. Endres, A. Drost, I. Eisele, C. Kutter, and P. Müller-Buschbaum, *Polyimide-based capacitive humidity sensor,* Sensors **18** (2018), 10.3390/s18051516.

[68] Y. Kim, B. Jung, H. Lee, H. Kim, K. Lee, and H. Park, *Capacitive humidity sensor design based on anodic aluminum oxide,* Sensors and Actuators B: Chemical **141**, 441 (2009).

[69] L.Chen and M. Mehregany, *A silicon carbide capacitive pressure sensor for high temperature and harsh environment applications,* in *TRANSDUCERS 2007 - 2007 International Solid-State Sensors, Actuators and Microsystems Conference* (2007) pp. 2597–2600.

[70] W. Cheng, L. Yu, D. Kong, Z. Yu, H. Wang, Z. Ma, Y. Wang, J. Wang, L. Pan, and Y. Shi, *Fast-response and low-hysteresis flexible pressure sensor based on silicon nanowires,* IEEE Electron Device Letters **39**, 1069 (2018).

[71] C. Berggren, B. Bjarnason, and G. Johansson, *Capacitive biosensors,* Electroanalysis **13**, 173 (2001), https://analyticalsciencejournals.onlinelibrary.wiley.com/doi/pdf/10.1002/1521-4109%28200103%2913%3A3%3C173%3A%3AAID-ELAN173%3E3.0.CO%3B2-B .

[72] M. Suster, J. Guo, N. Chaimanonart, and D. Young, *Low-noise cmos integrated sensing electronics for capacitive mems strain sensors,* (2004) pp. 693 – 696.

[73] W. Y. Du, *Resistive, Capacitive, Inductive, and Magnetic Sensor Technologies* (CRC Press, 2014).

[74] G. Douglas C., *Physics,* 4th ed. (Prentice Hall, 1995) table 18 – 1.

[75] L. E. Hollander, G. L. Vick, and T. J. Diesel, *The piezoresistive effect and its applications,* Review of Scientific Instruments **31**, 323 (1960), https://doi.org/10.1063/1.1716967 .

[76] C. Hu, H. Huang, C. Wen, L. Lin, and W. Fang, *Implementation of a flexible silicon-based tactile sensor array,* in *SENSORS, 2010 IEEE* (2010) pp. 1736–1739.

[77] K. Jun and J. Kim, *Fabrication of si membrane for a pressure sensor using the tmah based etching solution,* in *2017 IEEE Sensors Applications Symposium (SAS)* (2017) pp. 1–5.

[78] N. Al Cheikh, C. Coutier, J. Brun, C. Poulain, H. Blanc, and P. Rey, *Characterization of a highly sensitive silicon based three-axial piezoresistive force sensor,* in *2012 International Semiconductor Conference Dresden-Grenoble (ISCDG)* (2012) pp. 183–186.

[79] N. Svedin, E. Stemme, and G. Stemme, *A static turbine flow meter with a micromachined silicon torque sensor,* Journal of Microelectromechanical Systems **12**, 937 (2003).

[80] C. Chu, T. Liu, T. Chen, C. Weng, W. Hsu, and S. Li, *A miniaturized aerosol sensor implemented by a silicon-based mems thermal-piezoresistive oscillator,* in *2017 IEEE 30th International Conference on Micro Electro Mechanical Systems (MEMS)* (2017) pp. 1216–1219.

[81] C. Cai, J. Tan, D. Hua, M. Qin, and N. Zhu, *Piezoresistive temperature sensors fabricated by a surface micromachining cmos mems process,* Scientific Reports **8** (2018), 10.1038/s41598-018-35113-z.

[82] J. Han and M. Meyyappan, *A built-in temperature sensor in an integrated microheater,* IEEE Sensors Journal **16**, 5543 (2016).

[83] M. Mansoor, I. Haneef, S. Akhtar, M. A. Rafiq, A. De Luca, S. Z. Ali, and F. Udrea, *An soi cmos-based multi-sensor mems chip for fluidic applications,* Sensors **16** (2016), 10.3390/s16111608.

[84] C. Pang, H. Bae, A. Gupta, K. Bryden, and M. Yu, *Mems fabry-perot sensor interrogated by optical system-on-a-chip for simultaneous pressure and temperature sensing,* Opt. Express **21**, 21829 (2013).

[85] G. Liu and M. Han, *Fiber-optic gas pressure sensing with a laser-heated silicon-based fabry-perot interferometer,* Opt. Lett. **40**, 2461 (2015).

[86] E. Santolin, I. Junior, V. Corte, J. Cardozo da Silva, and V. de Oliveira, *Thermal monitoring of photovoltaic module using optical fiber sensors,* Journal of Microwaves, Optoelectronics and Electromagnetic Applications **15**, 333 (2016).

[87] Y. Zhang, P. Liu, S. Zhang, W. Liu, J. Chen, and Y. Shi, *High sensitivity temperature sensor based on cascaded silicon photonic crystal nanobeam cavities,* Opt. Express **24**, 23037 (2016).

[88] L. Chen and R. M. Reano, *Compact electric field sensors based on indirect bonding of lithium niobate to silicon microrings,* Opt. Express **20**, 4032 (2012).

[89] N. A. Yebo, S. P. Sree, E. Levrau, C. Detavernier, Z. Hens, J. A. Martens, and R. Baets, *Selective and reversible ammonia gas detection with nanoporous film functionalized silicon photonic micro-ring resonator,* Opt. Express **20**, 11855 (2012).

[90] G. Mi, C. Horvath, and V. Van, *Silicon photonic dual-gas sensor for h2 and co2 detection,* Opt. Express **25**, 16250 (2017).

[91] L. Lei, J. Tang, T. Zhang, H. Guo, Y. Li, C. Xie, C. Shang, Y. Bi, W. Zhang, C. Xue, and J. Liu, *Strain gauge using si-based optical microring resonator,* Appl. Opt. **53**, 8389 (2014).

[92] Z. Ding, P. Liu, J. Chen, D. Dai, and Y. Shi, *On-chip simultaneous sensing of humidity and temperature with a dual-polarization silicon microring resonator,* Opt. Express **27**, 28649 (2019).

[93] M. You, Z. Lin, F. Wang, Y. Bai, X. Li, Y. Su, and J. Liu, *Chip-scale humidity sensor based on a silicon nanobeam cavity,* Opt. Lett. **44**, 5322 (2019).

[94] I. G. Kolobov, W. B. Euler, and I. A. Levitsky, *Optical humidity sensing and ultrasound effect for mesoporous silicon one-dimensional photonic crystals,* Appl. Opt. **49**, 137 (2010).

[95] A. Haapalinna, *Characterization methods for silicon photodiode and silicon subsurface properties,* (2004) Ph.D. Thesis, Helsinki University of Technology.

[96] J. W. Lim, H. Wang, C. H. Choi, H. Kwon, L. N. Quan, W.-T. Park, Y.-Y. Noh, and D. H. Kim, *Self-powered reduced-dimensionality perovskite photodiodes with controlled crystalline phase and improved stability,* Nano Energy **57**, 761 (2019).

[97] J. H. Nam, F. Afshinmanesh, D. Nam, W. S. Jung, T. I. Kamins, M. L. Brongersma, and K. C. Saraswat, *Monolithic integration of germanium-on-insulator p-i-n photodetector on silicon,* Opt. Express **23**, 15816 (2015).

[98] E. Culurciello and P. Weerakoon, *Three-dimensional photodetectors in 3-d silicon-on-insulator technology,* IEEE Electron Device Letters **28**, 117 (2007).

[99] *Optical spectrum analyzer,* .

[100] Keysight Technologies, *Optical spectral analysis,* .

[101] S. Santra, P. K. Guha, S. Z. Ali, I. Haneef, and F. Udrea, *Silicon on insulator diode temperature sensor– a detailed analysis for ultra-high temperature operation,* IEEE Sensors Journal **10**, 997 (2010).

[102] L. Arias, S. Torres, D. Sbarbaro, and O. Farias, *Photodiode-based sensor for flame sensing and combustion-process monitoring,* Appl. Opt. **47**, 5541 (2008).

[103] H. Davy, *Xxix. farther researches on the magnetic phenomena produced by electricity; with some new experiments on the properties of electrified bodies in their relations to conducting powers and temperature,* Philosophical Transactions of the Royal Society of London **111**, 425 (1821), https://royalsocietypublishing.org/doi/pdf/10.1098/rstl.1821.0030 .

[104] L. B. Hunt, *The origin of the platinum resistance thermometer,* Platinum Metals Review **20**, 104 (1980), https://www.technology.matthey.com/article/24/3/104-112/#references .

[105] C. Montgomery, E. Cooper-Balis, S. Semancik, K. Kreider, and J. Geist, *Micro hotplate temperature sensor calibration and bist,* Journal of Research of the National Institute of Standards and Technology **116**, 827 (2011).

[106] k. Ibrahima, Y. Avenas, L. Dupont, and M. Petit, *Realization and characterization of instrumented power diode with aluminum rtd sensor – application to thermal impedance evaluation,* EPE Journal , 1 (2017).

[107] *Resistance thermometers,* in *Temperature Measurement* (John Wiley & Sons, Ltd, 2001) Chap. 4, pp. 85–102, https://onlinelibrary.wiley.com/doi/pdf/10.1002/0470846135.ch4 .

[108] M. Schultz, F. Yang, E. Colgan, R. Polastre, B. Dang, C. Tsang, M. Gaynes, P. Parida, J. Knickerbocker, and T. Chainer, *Embedded Two-Phase Cooling of Large Three-Dimensional Compatible Chips With Radial Channels,* Journal of Electronic Packaging **138** (2016), 10.1115/1.4033309, 021005, https://asmedigitalcollection.asme.org/electronicpackaging/article-pdf/138/2/021005/6141257/ep_138_02_021005.pdf .

[109] M. Dankoco, G. Tesfay, E. Benevent, and M. Bendahan, *Temperature sensor realized by inkjet printing process on flexible substrate,* Materials Science and Engineering: B **205**, 1 (2016).

[110] T. Dinh, H. Phan, A. Qamar, P. Woodfield, N. Nguyen, and D. V. Dao, *Thermoresistive effect for advanced thermal sensors: Fundamentals, design considerations, and applications,* Journal of Microelectromechanical Systems **26**, 966 (2017).

[111] C. Dames, *Resistance temperature detectors,* in *Encyclopedia of Microfluidics and Nanofluidics,* edited by D. Li (Springer US, Boston, MA, 2013) pp. 1–12.

[112] R. Pallás-Areny, *Strain gages,* in *Sensors and signal conditioning* (Wiley, 1991) Chap. 2, p. 81.

[113] J. R. Rice, *Mechanics of solids,* (2017), Date accessed: June 1st, 2021. https://www.britannica.com/science/mechanics-of-solids.

[114] W. Thomson, *Xxxi. the bakerian lecture.-on the electro-dynamic qualities of metals,* Philosophical Transactions of the Royal Society of London **146**, 649 (1856), https://royalsocietypublishing.org/doi/pdf/10.1098/rstl.1856.0031 .

[115] P. K. Stein, *A brief history of bonded resistance strain gages from conception to commercialization,* Experimental Techniques **14**, 13 (1990), https://onlinelibrary.wiley.com/doi/pdf/10.1111/j.1747-1567.1990.tb01474.x .

[116] *Historical review,* in *Technology and Practical Use of Strain Gages With Particular Consideration of Stress Analysis Using Strain Gages* (John Wiley & Sons, Ltd, 2017) Chap. 1, pp. 1–16, https://onlinelibrary.wiley.com/doi/pdf/10.1002/9783433606667.ch1 .

[117] W.-T. Park, *Piezoresistivity,* in *Encyclopedia of Nanotechnology*, edited by B. Bhushan (Springer Netherlands, Dordrecht, 2012) pp. 2111–2117.

[118] A. Fiorillo, C. Critello, and S. Pullano, *Theory, technology and applications of piezoresistive sensors: A review,* Sensors and Actuators A: Physical **281**, 156 (2018).

[119] F. Irgens, *Dynamics,* in *Continuum Mechanics* (Springer Berlin Heidelberg, Berlin, Heidelberg, 2008) pp. 37–81.

[120] F. Irgens, *Deformation analysis,* in *Continuum Mechanics* (Springer Berlin Heidelberg, Berlin, Heidelberg, 2008) pp. 133–181.

[121] P. French and A. Evans, *Piezoresistance in polysilicon and its applications to strain gauges,* Solid-State Electronics **32**, 1 (1989).

[122] P. French, *Polysilicon: a versatile material for microsystems,* Sensors and Actuators A: Physical **99**, 3 (2002), special issue from the papers presented in Symposium J in E-MRS 2001 conference.

[123] A. Beddiaf, K. Fouad, and K. Salah, *The effect of temperature and doping level on the characteristics of piezoresistive pressure sensor,* Journal of Sensor Technology **04**, 59 (2014).

[124] C. L. Dym and I. H. Shames, *Theory of linear elasticity,* in *Solid Mechanics: A Variational Approach, Augmented Edition* (Springer New York, New York, NY, 2013) pp. 1–69.

[125] W. Bludau, A. Onton, and W. Heinke, *Temperature dependence of the band gap of silicon,* Journal of Applied Physics **45**, 1846 (1974), https://doi.org/10.1063/1.1663501 .

[126] Y. Kanda, *Piezoresistance effect of silicon,* Sensors and Actuators A: Physical **28**, 83 (1991).

[127] O. Tufte and D. Long, *Recent developments in semiconductor piezoresistive devices,* Solid-State Electronics **6**, 323 (1963).

[128] J. Ho, T. R. Jow, and S. Boggs, *Historical introduction to capacitor technology,* IEEE Electrical Insulation Magazine **26**, 20 (2010).

[129] A. K. Erenoĝlu, O. Erdinc, and A. Tascikaraoĝlu, *Chapter 1 - history of electricity,* in *Pathways to a Smarter Power System,* edited by A. Tascikaraoĝlu and O. Erdinc (Academic Press, 2019) pp. 1–27.

[130] K. Oyedotun, *Synthesis and characterization of carbon-based nanostructured material electrodes for designing novel hybrid supercapacitors,* Ph.D. thesis (2018).

[131] P. Maheshwari, *Electronic Components and Processes* (New Age International Ltd, 2000).

[132] H. Mehrer, *Diffusion in Solids: Fundamentals, Methods, Materials, Diffusion-Controlled Processes* (Springer Berlin Heidelberg, Berlin, Heidelberg, 2007).

[133] K. Jansen, M. Zhang, L. Ernst, D.-K. Vu, and L. Weiss, *Effect of temperature and humidity on moisture diffusion in an epoxy moulding compound material,* Microelectronics Reliability **107**, 113596 (2020).

[134] J. Crank, *The Mathematics of Diffusion,* 2nd ed. (Oxford University Press, 1990) p. 47.

[135] P. Schubert and J. Nevin, *A polyimide-based capacitive humidity sensor,* IEEE Transactions on Electron Devices **32**, 1220 (1985).

[136] T. A. Wertime, *Pyrotechnology: Man's first industrial uses of fire: The neolithic revolution introduced man to the new energy resources to be had from agriculture and those to be gained by applying fire to fuels and earths,* American Scientist **61**, 670 (1973).

[137] Q. Jiang and Z. Wen, *Fundamentals of thermodynamics,* in *Thermodynamics of Materials* (Springer Berlin Heidelberg, Berlin, Heidelberg, 2011) pp. 1–35.

[138] W. Rohsenow, J. Hartnett, E. Ganic, and Y. Cho, *Basic concepts of heat transfer,* in *Handbook of Heat Transfer* (1997) Chap. 1.

[139] H. D. Baehr, *Introduction. technical applications,* in *Heat and Mass Transfer* (Springer Berlin Heidelberg, Berlin, Heidelberg, 2006) Chap. 1, pp. 1–104.

[140] P. von Böckh and T. Wetzel, *Introduction and definitions,* in *Heat Transfer: Basics and Practice* (Springer Berlin Heidelberg, Berlin, Heidelberg, 2012) pp. 1–15.

[141] W. Rohsenow, J. Hartnett, E. Ganic, and Y. Cho, *Microscale transport phenomena,* in *Handbook of Heat Transfer* (1997) Chap. 8.

[142] H. B. Callen, *Alternative formulations and legendre transformations,* in *Thermodynamics and an Introduction to Thermostatistics* (Wiley, New York, 1985) Chap. 5, pp. 133–137.

[143] W. Demtröder, *Emission and absorption of electromagnetic radiation by atoms,* in *Atoms, Molecules and Photons: An Introduction to Atomic-, Molecular- and Quantum Physics* (Springer Berlin Heidelberg, Berlin, Heidelberg, 2010) pp. 247–288.

[144] H. B. Callen, *Thermodynamics and an introduction to thermostatistics,* (Wiley, New York, 1985).

[145] W. Demtröder, *Atoms, Molecules and Photons: An Introduction to Atomic-, Molecular- and Quantum Physics* (Springer Berlin Heidelberg, Berlin, Heidelberg, 2010).

[146] W. Rohsenow, J. Hartnett, E. Ganic, and Y. Cho, *Microscale transport phenomena,* in *Radiation* (1997) Chap. 7.

[147] S. Pérès and J. Tiberghien, *Tibtech innovations,* Date accessed: January 24th, 2021. https://www.tibtech.com/conductivite.

[148] R. A. Serway and J. W. Jewett, *Current and direct current circuits,* in *Principles of physics: A calculus-based text* (Brooks/Cole, Cengage Learning, 2013) Chap. 21, p. 702.

[149] H. Muro, T. Mitamura, and S. Kiyota, *Determination of electrical properties of n-type and p-type polycrystalline silicon thin films as sensor materials,* Sensors and Materials **18**, 433 (2006).

[150] C.-Y. Lee, W.-Y. Fan, and C.-P. Chang, *A novel method for in-situ monitoring of local voltage, temperature and humidity distributions in fuel cells using flexible multi-functional micro sensors,* Sensors **11**, 1418 (2011).

[151] T. Waber, M. Sax, W. Pahl, S. Stufler, A. Leidl, M. Günther, and G. Feiertag, *Fabrication and characterization of a piezoresistive humidity sensor with a stress-free package,* Journal of Sensors and Sensor Systems **3**, 167 (2014).

[152] M. Bao, *Chapter 4 - electrostatic actuation,* in *Analysis and Design Principles of MEMS Devices,* edited by M. Bao (Elsevier Science, Amsterdam, 2005) pp. 175–212.

[153] B. Okcan and T. Akin, *A low-power robust humidity sensor in a standard cmos process,* IEEE Transactions on Electron Devices **54**, 3071 (2007).

[154] *Oxide growth calculator,* Date accessed: May 4th, 2021. https://cleanroom.byu.edu/oxidetimecalc.

[155] S. Nedelec, D. Mathiot, and M. Gauneau, *Diffusion of boron in polycrystalline silicon,* (1996) pp. 153–156.

[156] P. French, B. van Drieenhuizen, D. Poenar, J. Goosen, R. Mallee, P. Sarro, and R. Wolffenbuttel, *The development of a low-stress polysilicon process compatible with standard device processing,* Journal of Microelectromechanical Systems **5**, 187 (1996).

[157] X.-B. Lu, X. Liu, R.-Y. Chuai, and C.-Z. Shi, *Influence of doping concentration on gauge factor and linearity of polysilicon nanofilms,* Nami Jishu yu Jingmi Gongcheng/Nanotechnology and Precision Engineering **7**, 5 (2009).

[158] *Free online interactive psychrometric chart,* Date accessed: September 14, 2021. http://www.flycarpet.net/en/PsyOnline.

[159] M. R. R. Khan and S.-W. Kang, *Highly sensitive multi-channel idc sensor array for low concentration taste detection,* Sensors (Basel, Switzerland) **15**, 13201 (2015).

[160] K.-P. Yoo, M. J. Lee, K.-H. Kwon, J. Jeong, and N.-K. Min, *Dielectric properties of on-chip-cured polyimide films,* Thin Solid Films **518**, 5986 (2010).

[161] I. Butnaru (former Bacosca), M. Bruma, and S. Gaan, *Phosphine oxide based polyimides: Structure-property relationships,* RSC Adv. **7**, 50508 (2017).

[162] S. Chisca, V. Musteata, I. Sava, and M. Bruma, *Study of dielectric behavior of aromatic polyimide films,* Proceedings of the International Semiconductor Conference, CAS **02**, 325 (2010).

[163] *Mechanical properties of materials,* Date accessed: September 28th, 2021. https://mechanicalc.com/reference/mechanical-properties-of-materials.

[164] J. N. B. Patel, E. Fokuhl, K. S. Prakash, A. Beinert, V. Wesselak, P. Gebhardt, and D. Philipp, *Design and development of solar cell integrated moisture and temperature sensors for photovoltaic modules,* in *38th European PV Solar Energy Conference and Exhibition (6-10 September 2021)* (2021).

[165] J. Zhou, Q. Yi, Y. Wang, and Z. Ye, *Temperature distribution of photovoltaic module based on finite element simulation,* Solar Energy **111**, 97 (2015).

[166] Y. B. Assoa, L. Mongibello, A. Carr, B. Kubicek, M. Machado, J. Merten, S. Misara, F. Roca, W. Sprenger, M. Wagner, S. Zamini, T. Baenas, and P. Malbranche, *Thermal analysis of a bipv system by various modelling approaches,* Solar Energy **155**, 1289 (2017).

[167] J. Oh, B. Rammohan, A. Pavgi, S. Tatapudi, G. Tamizhmani, G. Kelly, and M. Bolen, *Reduction of pv module temperature using thermally conductive backsheets,* IEEE Journal of Photovoltaics **8**, 1160 (2018).

[168] M. Hammami, S. Torretti, F. Grimaccia, and G. Grandi, *Thermal and performance analysis of a photovoltaic module with an integrated energy storage system,* Applied Sciences **7** (2017), 10.3390/app7111107.

[169] M. Ali and M. F. Hossain, *Influence of front and back contacts on photovoltaic performances of p-n homojunction si solar cell: Considering an electron-blocking layer,* International Journal of Photoenergy **2017**, 1 (2017).

[170] A. E.-M. A. Harb, A. Radwan, K. Elsayed, M. Sedrak, and M. Ahmed, *Influence of varying the ethylene-vinyl acetate layer thicknesses on the performance of a polycrystalline silicon solar cell integrated with a microchannel heat sink,* Solar Energy **195**, 592 (2020).

[171] S. Armstrong and W. Hurley, *A thermal model for photovoltaic panels under varying atmospheric conditions,* Applied Thermal Engineering **30**, 1488 (2010).

[172] *Polyimide (PI),* Date accessed: January 11th, 2021. http://www.goodfellow.com/A/Polyimide.html.

[173] *High performance thermally conductive polyimide film: Kapton® mt+,* Date accessed: January 11th, 2021. https://www.dupont.com/products/kapton-mt-plus.html.

[174] *Material property database - material: Polyimide,* Date accessed: January 11th, 2021. https://www.mit.edu/ 6.777/matprops/polyimide.htm.

[175] A. J. Beinert, P. Romer, M. Heinrich, M. Mittag, J. Aktaa, and D. H. Neuhaus, *The effect of cell and module dimensions on thermomechanical stress in pv modules,* IEEE Journal of Photovoltaics **10**, 70 (2020).